UNIVERSITÀ
DEGLI STUDI
FIRENZE

DOCTORAL RESEARCH IN CHEMICAL SCIENCES

CYCLE XXXV

COORDINATOR Prof.ssa Anna Maria Papini

OPTICAL-BASED BIOANALYTICAL ASSAYS FOR DRUGS QUALITY CONTROL AND DIAGNOSTIC APPLICATIONS

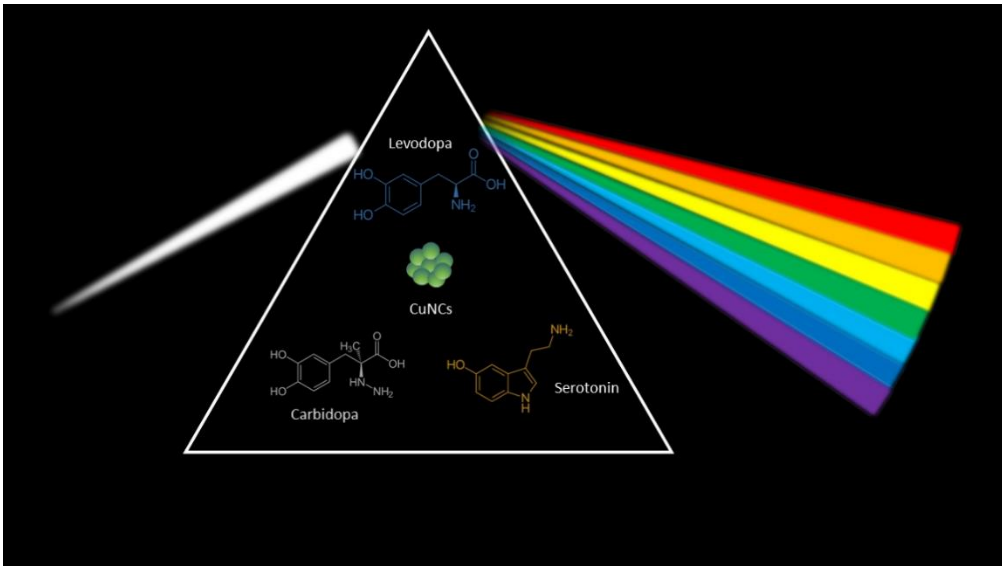

PhD candidate	**Tutor**	**Co-tutors**
Mariagrazia Lettieri	Prof. Simona Scarano	Dr Pasquale Palladino Prof. Maria Minunni

A mia madre

UNIVERSITÀ
DEGLI STUDI
FIRENZE
DICUS
DIPARTIMENTO DI CHIMICA
"UGO SCHIFF"

DOTTORATO DI RICERCA IN
SCIENZE CHIMICHE

CICLO XXXV

COORDINATORE Prof.ssa Anna Maria Papini

OPTICAL-BASED BIOANALYTICAL ASSAYS FOR DRUGS QUALITY CONTROL AND DIAGNOSTIC APPLICATIONS

Settore scientifico disciplinare CHIM/01

Dottoranda	**Tutore**	**Co-tutori**
Lettieri Mariagrazia	Prof. Scarano Simona	Dr Palladino Pasquale
	Simona Scarano	
		Prof. Minunni Maria

Coordinatore
Prof. Papini Anna Maria

Anni 2019/2022

Summary

Summary.. 2
Preface.. 8
Abstract 8
Contents.. 11
Scientific Production 13
    Papers 13
    In-Fieri Material.. 13
    Not-included material (out of PhD project) 14
List of Abbreviations.. 16
1 Introduction to bioanalytical chemistry 20
    1.1 New trends in bioanalytical detection strategies 21
2 Optical-based bioanalytical assays: fundamentals.................................. 28
    2.1 General purpose of biophotonics...28
    2.2 UV-Vis Absorption and Fluorescence in bioanalysis: fundamental principles...30
3 Nanomaterials in bioanalytical applications for diagnostic purposes.......... 36
    3.1 Classification of Nanomaterials...37
    3.2 Nanoparticles, quantum dots, carbon-based and nanocomposites materials in bioanalysis...38
4 Copper nanoclusters and their application for innovative fluorescent detection strategies: an overview 41
    4.1 Abstract...41
    4.2 Introduction 42
    4.3 Synthesis and features of CuNCs 43
    4.4 CuNCs-based detection strategies 48
5 Protein-templated copper nanoclusters for fluorimetric determination of human serum albumin 50
    5.1 Abstract.. 50
    5.2 Introduction 52

5.3 Materials and Methods 53

5.3.1 Chemicals and Reagents 53

5.3.2 Methods and Instrumentation 54

5.3.3 Assay principle 54

5.4 Results and discussions 55

5.4.1 CuNCs synthesis and optical behavior 55

5.4.2 Optimization of parameters for HSA detection 57

5.4.3 Sensitive detection of human serum albumin 59

6 Fluorescence molecules for diagnostic purposes and bioanalytical applications 70

6.1 Fluorophores 70

7 Serotonin-derived fluorophore: a novel fluorescent biomaterial for copper detection in urine 73

7.1 Abstract 73

7.2 Introduction 74

7.3 Materials and methods 75

7.3.1 Chemicals and Reagents 75

7.3.2 Methods and Instrumentation 76

7.4 Results and discussions 78

7.4.1 Process optimization for synthesis of serotonin-derivative 78

7.4.2 Characterization of serotonin derivative by spectroscopy and mass spectrometry 83

7.4.3 Investigation of polymeric properties of serotonin derivative via electrochemical studies 85

7.4.4 Examination of synthesis reaction products of SEDF by Scanning Electron Microscopy techniques 86

7.4.5 SEDF fluorescence quenching by metal ions 87

7.4.6 Copper detection via quenching-based bioanalytical assay 89

7.4.7 Copper detection in human urine samples 91

7.5 Conclusions 93

8 The importance of bioanalytical procedures in drugs quality control 95

8.1 UV-Vis spectrophotometric methods 98

8.2 Colorimetric assays 100

8.3 Colorimetric assays for drug testing 102

9 Melanochrome-based colorimetric assay for quantitative detection of levodopa in co-presence of carbidopa and its application to relevant anti-Parkinson drugs.. 104

9.1 Abstract........ 104

9.2 Introduction 105

9.3 Materials and Methods 107

9.3.1 Chemicals and reagents 107

9.3.2 Methods and Instrumentations........ 108

9.4 Results and discussions 108

9.4.1 Assay principle 108

9.4.2 Influence of pH and Mg^{2+} concentration on color development by levodopa 109

9.4.3 Influence of cation and solvent on color development by natural catecholamine 110

9.4.4 Influence of Mg^{2+} and DMSO on color development by synthetic catecholamine analogues 117

9.4.5 Colorimetric quantification of levodopa in tablets by using melanochrome as molecular probe 118

9.5 Conclusions 120

10 The first observation of melanochrome and indolequinone from catecholamines and their quantification in human urine........ 122

10.1 Abstract........ 122

10.2 Introduction 123

10.3 Materials and Methods 124

10.3.1 Chemicals and Reagents........ 124

10.3.2 Methods and Instrumentations........ 125

10.4 Results and discussions 126

10.4.1 LC–MS/MS Analysis 126

10.4.2 Spectroscopic characterization of products 128

10.4.3 Quantification of levodopa and dopamine in human urine samples 131

10.5 Conclusions 133

11 Colorimetric determination of carbidopa in anti-Parkinson drugs based on 4-hydroxy-3-methoxybenzaldazine formation by reaction with vanillin 135

11.1 Abstract 135

11.2 Introduction 137

11.3 Materials and Methods 139

11.3.1 Chemicals and Reagents 139

11.3.2 Methods and Instrumentations 140

11.4 Results and discussions 141

11.4.1 Assay principle 141

11.4.2 Influence of solvent composition and pH on color development 141

11.4.3 Influence of vanillin concentration, temperature, and heating time on color development 143

11.4.4 Colorimetric quantification of carbidopa in tablets by using of HMOB as molecular probe 144

11.5 Conclusions 147

12 Concluding remarks 149

References 151

Preface

Abstract

The twenty-first century was marked by the scientists' efforts focused on the development of novel tools that allow a precise, reliable chemical quantification of reality. The improvement of detection strategies able to identify the target molecules involved in biological mechanisms, plays a key role in early diagnosis. This has assumed a vital importance, especially in the pandemic situation. Never has analytical chemistry and specifically, bioanalytical chemistry, been more important. It was involved in the direct detection of the virus as well as the relative antibodies, but played a key role also in the validation of vaccines integrity and stability.

Driven by the interest in the design of easy-to-use, low-cost and fast-response diagnostic devices that ensure a continuous monitoring of the patient's health, this thesis aims to the development of innovative and alternative optical-based bioanalytical assays. Two are the approaches commonly involved in bioanalytical applications: point-of-care and laboratory-based approach. The latter, combined with optical methodologies, guarantees excellent clinical accuracy becoming a mainstay in our healthcare system.

Ultraviolet-visible light absorption and fluorescence methods are, among all, the most used techniques in clinical laboratory analysis. The easiness to use, the non-destructive features as well as the possibility of label-free approaches for a direct optical detection render optical methods a powerful tool for bioanalytical investigations. In these last, more frequently is necessary to determine the concentration of small quantities of analyte. For this purpose, nanomaterials have been commonly employed in optical detection strategies to improve the assay's sensitivity. In fact, nanomaterials frequently show extraordinary optical properties that allow them to develop efficient signal enhancement strategies. Here, the interesting photoluminescence properties of a class of nanomaterials, copper nanoclusters (CuNCs), have been deeply examined. Compared to noble metals-based nanomaterials (*e.g.*, silver and gold), CuNCs not only are more easily available and

inexpensive, but also display a unique fluorescent behavior characterized by large Stokes shifts, low toxicity, and high biocompatibility, providing high sensitivity even in complex biological matrices. In this work, the above listed features of CuNCs were applied for the specific and sensitive detection of human serum albumin. The quantitative determination of human serum albumin is of clinical interest in early diagnosis of serious pathological conditions such as albuminuria and albuminemia. Here, copper nanoclusters were used as fluorescent signal indicators. However, it is not always easy to use nanomaterials as fluorophores since they often require huge and long synthetic protocols. Contrarily, fluorescence molecules and dyes can be achieved by means of fast and long synthetic protocols. For this purpose, an interesting novel fluorophore, derived from serotonin self-oxidation and polymerization, was obtained. The fluorophore derived from serotonin showed highly emitting features confirmed by quantum yield calculations. The new biomaterial was characterized by different techniques (*i.e.* spectroscopic, electrochemical and mass spectrometry). The outstanding fluorescent properties of serotonin-derived fluorophore were exploited to develop a quenching-based optical method for Cu(II) quantitative analysis. The concentration of Cu(II) was successfully determined in human urine samples, resulting in a potential diagnostic tool for copper-dependent diseases.

In this dissertation, optical-bioanalytical detection strategies were also applied for drugs active principles estimation. The design of methods for pharmaceutical analysis for the drugs quality control, that is the unambiguous detection of a drug in a pharmaceutical product, is as crucial as its determination in complex matrices, since the pharmaceutical product quality is directly related to the patient’s health. Therefore, the quality of drugs and the identification of counterfeit products must be ensured by performing analytical tests. Among the spectrophotometric methods, colorimetric tests are widely employed in pharmaceutical compounds examination. The identification of drug compounds is generally achieved by exploiting chemical reagents able to selectively react with the drugs functional active principal groups, resulting in a visible change in color. Colorimetric methods, here, were applied for the determination of two active principles in commercial Parkinson’s drugs, levodopa and carbidopa. Levodopa was quantified by exploiting a colorimetric reaction that leads to the purple melanochrome formation, here isolated and stabilized for the first time. Consequently, melanochrome was characterized by means of mass spectrometry techniques. The designed melanochrome-based colorimetric assay was effectively applied to levodopa and dopamine detection in human urinary samples, paving the way for future application in the monitoring of pharmacological therapy in Parkinson's patients. Carbidopa content was also determined in pharmaceutical formulation by using an alternative colorimetric approach based on the selective condensation reaction between the hydrazine group of carbidopa and the formyl functional group of vanillin leading to the formation of yellow 4-hydroxy-3-methoxybenzaldazine.

Definitely, the novel optical-based bioanalytical approaches designed in this research work could have a significant impact on analytical diagnostic tools commonly employed in clinical practice and pharmaceutical analysis improving their availability and applicability.

Contents

The dissertation is divided in 12 section:

- *Section 1.* The role of bioanalytical chemistry in the last century is highlighted focusing on the impact that had on our society. It was paid attention to the importance in the design of novel, low-cost and easy-to-use technologies able to quantify key molecular targets. The main approaches and the trends in the bioanalytical chemistry field are presented.
- *Section 2.* The relevance of optical-based methods as detection strategies is provided. Ultraviolet-visible light absorption and fluorescence methods used in this work to develop optical-based bioanalytical assays are introduced, describing their basic principles.
- *Section 3.* Nanomaterials features and behavior that influence the analytical performance are reported. The classification of nanomaterials is also illustrated. The capability of nanomaterials in the signal enhancement strategies is highlighted.
- *Section 4.* An overview of the copper nanoclusters and their use in fluorescent detection approaches is presented. The synthetic approaches that influence the photoluminescence behavior of copper nanoclusters are explained. The highly emitting properties of copper nanoclusters that provide high sensitivity in sensing strategies are shown.
- *Section 5.* The application of copper nanoclusters for the quantification of human serum albumin is illustrated. The synthesis conditions were optimized to enable a sensitive detection of the target. The outstanding fluorescent properties of copper nanoclusters were exploited to determine human serum albumin concentration in biological matrices representing a promising tool for the diagnosis of albumin-dependent diseases.
- *Section 6.* A brief introduction on the fluorophores, as a valid alternative to use of nanomaterial in bioassays, is presented.

- *Section 7.* Novel fluorescent material derived from serotonin was examined. Different techniques were used to characterize this novel fluorescent material. The photoluminescence properties of serotonin derivative fluorophore were deeply investigated and used for the sensitive detection of copper in human urine samples enabling the applicability in routine clinical practice to facilitate the diagnosis of copper-dependent diseases.
- *Section 8.* The role of bioanalytical methods in drugs analysis and quality control is presented. Analytical methods currently used in the pharmaceutical products control are listed. The importance of optical-based techniques, in particular colorimetric ones, in drugs analysis is pointed out.
- *Section 9.* A colorimetric assay for the detection of levodopa, active principle of Parkinson's drugs, is designed. The colorimetric assay developed exploits the formation of an elusive intermedia of levodopa polymerization reaction, the purple melanochrome. The melanochrome-based assay was used to sensitive, selective and reproducible quantify levodopa in commercially available brand drugs.
- *Section 10.* The melanochrome obtained through the designed colorimetric reaction was characterized by mass spectrometry techniques. The synthesis of melanochrome was applied to levodopa determination in human urine samples offering a novel bioanalytical method for the drugs monitoring in Parkinson's patients.
- *Section 11*. A colorimetric assay for the determination of carbidopa concentration in Parkinson's drugs found on the market, is reported. The colorimetric reaction developed takes advantage of condensation reaction between the hydrazine group from carbidopa and the formyl functional group of vanillin leading to the formation of yellow 4-hydroxy-3-methoxybenzaldazine. This latter enabled the sensitive and selective detection of carbidopa for the quality control of Parkinson's drugs.
- *Section 12.* Concluding remarks are reported.

Scientific Production

Papers

- Lettieri, M.; Palladino, P.; Scarano, S.; Minunni M. Protein-templated copper nanoclusters for fluorimetric determination of human serum albumin, Mikrochim. Acta. 188 (2021) 116. DOI:10.1007/s00604-021-04764-7. IF 6.408.

- Lettieri, M.; Emanuele, R.; Scarano, S.; Palladino, P; Minunni, M. Melanochrome-based colorimetric assay for quantitative detection of levodopa in co-presence of carbidopa and its application to relevant anti-Parkinson drugs, Anal. Bioanal. Chem., vol. 414, no. 4, pp. 1713–1722 (2022) DOI: 10.1007/s00216-021-03804-8. IF 4.478.

- Lettieri, M.; Palladino, P; Scarano, S.; Minunni, M. Copper nanoclusters and their application for innovative fluorescent detection strategies: An overview, Sensors and Actuators Reports. 4 (2022) 100108. DOI: 10.1016/j.snr.2022.100108.

- Lettieri, M.; Scarano, S.; Palladino, P; Minunni, M. Colorimetric determination of carbidopa in anti - Parkinson drugs based on 4 - hydroxy - 3 - methoxybenzaldazine formation by reaction with vanillin, Anal. Bioanal. Chem. (2022). DOI: 10.1007/s00216-022-04256-4. IF 4.478.

In-Fieri Material

- Lettieri, M.; Spinelli, M.; Scarano, S.; Palladino, P.; Minunni, M; Amoresano, A. The first observation of melanochrome and indolequinone from catecholamines and their quantification in human urine. *Submitted.*

- Lettieri, M.; Scarano, S.; Caponi, L., Palladino, P.; Minunni, M; Serotonin-derived fluorophore: a novel fluorescent biomaterial for analytical applications. The sensitive copper ions as an example. *Submitted.*

Not-included material (out of PhD project)

- Pedone, D.; Moglianetti, M.; Lettieri, M.; Marrazza, G.; Pompa, P.P.; Platinum Nanozyme-Enabled Colorimetric Determination of Total Antioxidant Level in Saliva, Anal. Chem. 92 (2020) 8660–8664. DOI:10.1021/acs.analchem.0c01824. IF: 6.986.

- Selvolini, G.; Adumitrachioaie, A.; Lettieri, M.; Hosu, O.; Cristea, C.; Marrazza, G. Electrochemical Sensors Based on Conducting Polymers: Characterization and Applications, in: Lect. Notes Electr. Eng., Springer, 2020: pp. 233–237. DOI:10.1007/978-3-030-37558-4_35.

- Nehra, M.; Lettieri, M.; Dilbaghi, N.; Kumar, S.; Marrazza, G. Nano-biosensing platforms for detection of cow's milk allergens: An overview, Sensors. 20 (2020) 1–21. DOI:10.3390/s20010032. IF: 3.576.

- Lettieri, M.; Hosu, O.; Adumitrachioaie, A.; Cristea, C.; Marrazza, G. Beta-lactoglobulin Electrochemical Detection Based with an Innovative Platform Based on Composite Polymer, Electroanalysis. 32 (2020) 217–225. DOI:10.1002/elan.201900318. IF:3.077.

- Melinte, G.; Hosu, O.; Lettieri, M.; Cristea, C.; Marrazza, G. Electrochemical Fingerprint of Arsenic (III) by Using Hybrid Nanocomposite-Based Platforms, Sensors. 19 (2019) 1–13. DOI:10.3390/s19102279. IF:3.576.

- Bozal-Palabiyik, B.; Lettieri, M.; Uslu, B.; Marrazza, G. Electrochemical Detection of Vascular Endothelial Growth Factor by Molecularly Imprinted Polymer, Electroanalysis. 31 (2019) 1475–1481. DOI:10.1002/elan.201900185. IF:3.007.

- Hosu, O.; Lettieri, M.; Papara, N.; Ravalli, A.; Sandulescu, R.; Cristea, C.; Marrazza, G. Colorimetric multienzymatic smart sensors for hydrogen peroxide, glucose and catechol screening analysis, Talanta. 204 (2019) 525–532. DOI:10.1016/j.talanta.2019.06.041. IF: 6.556.

- Selvolini, G.; Lettieri, M.; Tassoni, L.; Gastaldello, S.; Grillo,M.; Maran, C.; Marrazza, G. Electrochemical enzyme-linked oligonucleotide array for aflatoxin B 1 detection, Talanta. 203 (2019) 49–57. DOI:10.1016/j.talanta.2019.05.044. IF: 6.556.

List of Abbreviations

ACQ	Aggregation-caused Emission Quenching
AIE	Aggregation Induced Emission
APIs	Active Pharmaceutical Ingredients
AU	Artificial Urine
BELISA	Biomimetic Enzyme-linked Immunoassay
BSA	Bovine Serum Albumin
BZ	Benserazide
CARS	Coherent Anti-Stokes Raman Spectroscopy
CD	Carbidopa
CDs	Carbon Dots
CE	Collisional Energy
CNTs	Carbon Nanotubes
Cp	Ceruplasmin
CuNCs	Copper Nanoclusters
CuNPs	Copper Nanoparticles
CV	Cyclic Voltammetry
CV_{av}	Coefficient of Variation average
DA	Dopamine
DHI	6-dihydroxyindole
DHICA	5,6-dihydroxyindole-2-carboxylic acid
DHM	Digital Holographic Microscopy
dsDNA	Double strand DNA
DMAB	p-dimethylaminobenzaldehyde
DTT	Dithiothreitol
EIS	Electrochemical Impedance Spectroscopy
ELISA	Enzyme-linked Immunosorbent Assay
FELISA	Fluorescent Enzyme-linked Immunosorbent Assay
FITC	Fluorescein Isothiocyanate
FLIM	Fluorescence-lifetime Imaging Spectroscopy
FRET	Förster Resonance Energy Transfer
FRAP	Fluorescence recovery after photobleaching
FP	Fluorescent Protein

GFP	Green Fluorescent Properties
GSH	Glutathione
GSPE	Graphite Screen Printed Electrode
HMOB	4-hydroxy-3-methoxybenzaldazine
HPLC	High Performance Liquid Chromatography
HRP	Horseradish Peroxidase
HS	Human Serum
HSA	Human Serum Albumin
ICP-MS	Inductively Coupled Plasma Mass Spectrometry
Ig	Immunoglobulin
IQ	5,6-indolequinone
LFD	Lateral Flow Devices
LiDAR	Light detection and ranging
LD	Levodopa
LOD	Limit of Detection
LOQ	Limit of Quantification
LSPR	Localized Surface Plasmon Resonance
MALDI-TOF/MS	Matrix-assisted laser desorption/ionization- time of flight mass spectrometry
MC	Melanochrome
MIP	Molecular Imprinted Polymer
MRM	Multiple Reaction Monitoring
NE	Norepinephrine
NIR	Near Infrared Region
NMs	Nanomaterials
NMR	Nuclear Magnetic Resonance
NPs	Nanoparticles
NSOM	Near-field scanning optical microscopy
PALM	Photo-Activation Localization Microscopy
PD	Parkinson’s Disease
PDT	Photodynamic Therapy
PL	Photoluminescence
PEI	Polyethyleneimine
PoC	Point of Care
PVP	Polyvinyl Pyrrolidone
PSE	Polyserotonin
RT-PCR	Real-time Polymerase Chain Reaction
UV-Vis	Ultraviolet-visible

QDs	Quantum Dots
Q.Y.	Quantum Yield
TERS	Tip-enhanced Raman Scattering
TRITC	Tetramethyl Rhodamine-isothiocyanate
TPA	Two-photon Absorption
SD	Standard Deviation
SE	Serotonin
SEDF	Serotonin Derivative Fluorophore
SELEX	Systematic Evolution of Ligands By Exponential Enrichment
SERS	Surface enhanced Raman scattering
SPR	Surface Plasmon Resonance
STED	Stimulated Emission Depletion Microscopy
STORM	Stochastic Optical Reconstruction Microscopy
ssDNA	Single strand DNA
WD	Wilson's diseases

1

Introduction to bioanalytical chemistry

“If you cannot measure it, you cannot improve it”. This citation by Lord William Thomson Kelvin synthesizes how it is important to monitor physical and chemical quantities that surround our world, not just to know and to study it but also to intervene to improve it. In this regard, over the past decade, the way we diagnose diseases has changed drastically. Certainly, the recent COVID-19 pandemic situation had a strong impact on the development of alternative quantification strategies to ensure the continuous monitoring of the patient's health.

The efforts of the scientists have increasingly been moving towards more accessible and cost-effective technologies able to quantify molecular targets crucial in biological activity. In this scenario, bioanalytical methods represent a mainstay for the analysis and detection of multiple and different types of targets. Two different approaches are usually involved in bioanalytical applications: *point of care* (PoC) and *laboratory-based* approaches (Fig. 1.1). *Point of care* diagnostic methods (*i.e.,* pregnancy test, lateral flow assays, glucometer) perform rapid on-site testing, they are pocket-sized, easy-to-use, and low-cost. Despite these numerous advantages, they could lack in specificity, sensitivity, and often the concentration of targets is below the limit of detection. These frequently results in false negative responses. In contrast, *laboratory-based* technologies guarantee better clinical accuracy providing more reliable results. However, the instrumentation is often costly and bulky and requires complicated experimental set up and expert personnel to perform the analysis. Therefore, the design of a cheap, portable, and user-friendly device that can support laboratory-testing methodologies at the point of care could revolutionize the diagnosis and therapy methods. The application of optical techniques in bioanalysis could represent an invaluable tool for the realization of point of care devices which exploit assays usually applied in laboratory-based technologies.

This thesis aims to address some of the existing limitations imposed by the sophisticated common analytical techniques proposing valid optical-based analytical approaches. These last could lead to significant changes in terms of costs, time, sample pretreatment, easy-to-use, compared to conventional highly sophisticated analytical approaches usually involved in pharmaceutical analysis and molecular clinical diagnosis.

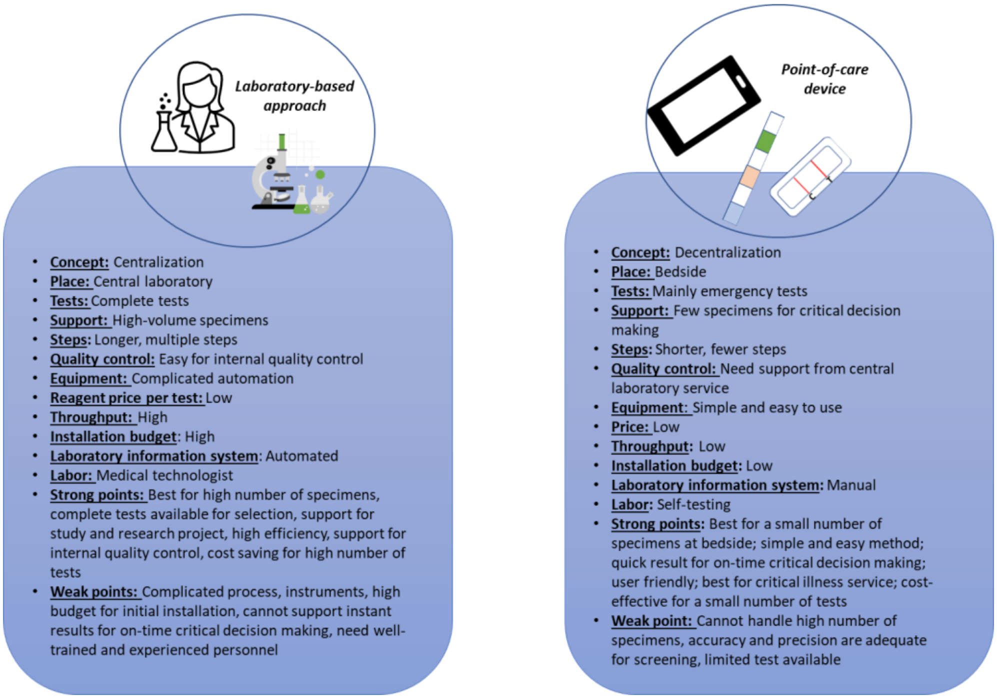

- **Concept:** Centralization
- **Place:** Central laboratory
- **Tests:** Complete tests
- **Support:** High-volume specimens
- **Steps:** Longer, multiple steps
- **Quality control:** Easy for internal quality control
- **Equipment:** Complicated automation
- **Reagent price per test:** Low
- **Throughput:** High
- **Installation budget:** High
- **Laboratory information system:** Automated
- **Labor:** Medical technologist
- **Strong points:** Best for high number of specimens, complete tests available for selection, support for study and research project, high efficiency, support for internal quality control, cost saving for high number of tests
- **Weak points:** Complicated process, instruments, high budget for initial installation, cannot support instant results for on-time critical decision making, need well-trained and experienced personnel

- **Concept:** Decentralization
- **Place:** Bedside
- **Tests:** Mainly emergency tests
- **Support:** Few specimens for critical decision making
- **Steps:** Shorter, fewer steps
- **Quality control:** Need support from central laboratory service
- **Equipment:** Simple and easy to use
- **Price:** Low
- **Throughput:** Low
- **Installation budget:** Low
- **Laboratory information system:** Manual
- **Labor:** Self-testing
- **Strong points:** Best for a small number of specimens at bedside; simple and easy method; quick result for on-time critical decision making; user friendly; best for critical illness service; cost-effective for a small number of tests
- **Weak point:** Cannot handle high number of specimens, accuracy and precision are adequate for screening, limited test available

Figure 1.1. *Laboratory-based approach vs point of care device. Adapted from Ref.*[1].

1.1 New trends in bioanalytical detection strategies

The field of bioanalysis is a relatively young science that started to flourish in the late twenty-first century. Bioanalytical chemistry arises from the need to monitor novel markers and analytes [2]. It is defined as a sub-discipline of analytical chemistry including a wide research area and analytical activities, from human health screening (medical, clinical, food, and pharmaceutical analysis) to forensic analysis and from basic biochemistry studies to special apparatus development [3]. The aim of bioanalytical chemistry is to quantify a plethora of target molecules which usually include xenobiotics (*e.g.* biological molecules, drugs and their metabolites) and biotics (macromolecules such as proteins, DNA, metabolites)[4]. The constant research and discovery of novel biomarkers greatly affect the design of the bioanalytical method. The latter could lead invalid test results if the choice of biomarker is not appropriate. In addition, the selection of suitable biomarkers has a great impact also on the time, cost, specificity, and sensitivity of the diagnostic test development, especially when a disease is characterized by more than one biomarker. An excellent biomarker can lead to an early diagnosis of disease to prevent severe adverse reactions. For all the above reasons, the research that combines novel and effective biomarkers with easy assays is in considerable expansion. In order to ensure an ultra-sensitive quantification, most bioanalytical technologies are based on the single target molecule determination [5–7]. Meanwhile, the simultaneous identification of several biomarkers, *i.e.*, the multiplexed approach, is a promising tool to describe the molecular signature of a disease. Numerous examples of multiplexed technologies are reported in literature [8–10], and several of these employ nanomaterials (NMs) thanks to their brightness, photostability, size-dependent optoelectronic properties, and nanoscale interface, as detailed in section 3[11–16].

Taking into account these considerations, the trends in bioanalytical chemistry have been driven towards microfabrication techniques which facilitate the production of portable and cheap devices that quantify and use small amounts of analyte [17]. The current major topics in bioanalytical science include *wearable biosensors, home-testing kits, 3D printed systems, paper* and *smartphone-based devices* (Fig.1.2).

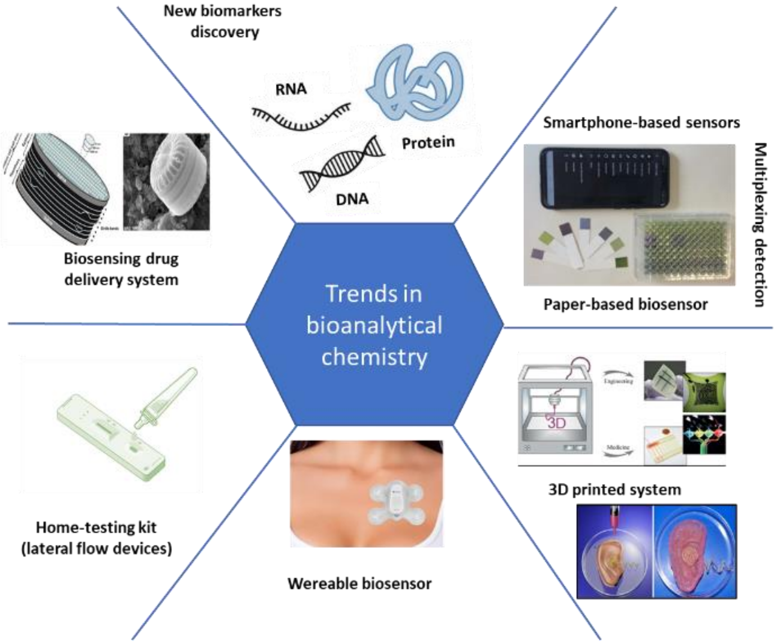

Figure 1.2. *Trends in bioanalytical chemistry: smartphone-based sensors, multiplexing detection and paper based biosensor* [18]*; 3D printed systems* [19], *wearable biosensors* [20], *home-testing kits, drug delivery biosensing based systems* [21] *and discovery of novel biomarkers. The figures were adapted with permission of Elsevier. V.B.*

Undoubtedly, biosensors were the first technology to be developed that observe the cornerstones of the concept of miniaturization. Nowadays, the biosensors occupy our everyday life and are actively part of the market [22]. As we all know, biosensors were created for real-time monitoring of patients' state of health to reduce the hospitalization rate. In order to implement the biosensors portability and the continuous monitoring of diagnostic parameters, *wearable biosensors* were designed by using three-dimensional (3D) printing [23]. Wearable devices are not yet widespread enough to be commercialized. Surely, they are one of most relevant emerging tendency in bioanalytical field for the near future, but they present some limitations, such as reliability of detection for over extended periods, stability of the bio-recognizer, body fluid transport through the device, sensor biofouling, and long-term self-powered operation, which still need to be overcame. The scientists are continuously working on the innovative wearable technologies since the growing demand for non-invasive and real-time quantification of various biochemical markers in the human body fluid. This leads to significant progress in the current healthcare infrastructure for the global population. Wearable biosensors are characterized by the capability to perform accurate health data collection and to be connected remotely to the personal health professional, allowing the monitoring of the health progress checking the patient health status. This approach greatly reduces the hospitalization avoiding crowding in the hospital. Wearable biosensors are usually tattoo, patch, gloves, clothing and implants (Fig. 1.3).

The new trend in wearable technology are biosensing-drug delivery systems. They are the perfect combination between biosensors and drug delivery technology. They consist in the monitoring of disease’s biomarker and, subsequently, release the required therapeutic dose [24]. An example of a biosensing-drug delivery device is represented by a patch able to mimic the pancreas activity. This patch consists of microneedles preloaded with insulin, which quickly release the drug when it detects high levels of blood sugar, and the release of insulin decreases when blood glucose returns to normal [25].

Among the emerging bioanalytical technologies, the *3D-printing* is very promising [26]. The ability to manufacture geometrically complex and highly flexible objects in a short period of time, with minimum waste, make the 3D-printing method one of the most novel eco-friendly technologies.

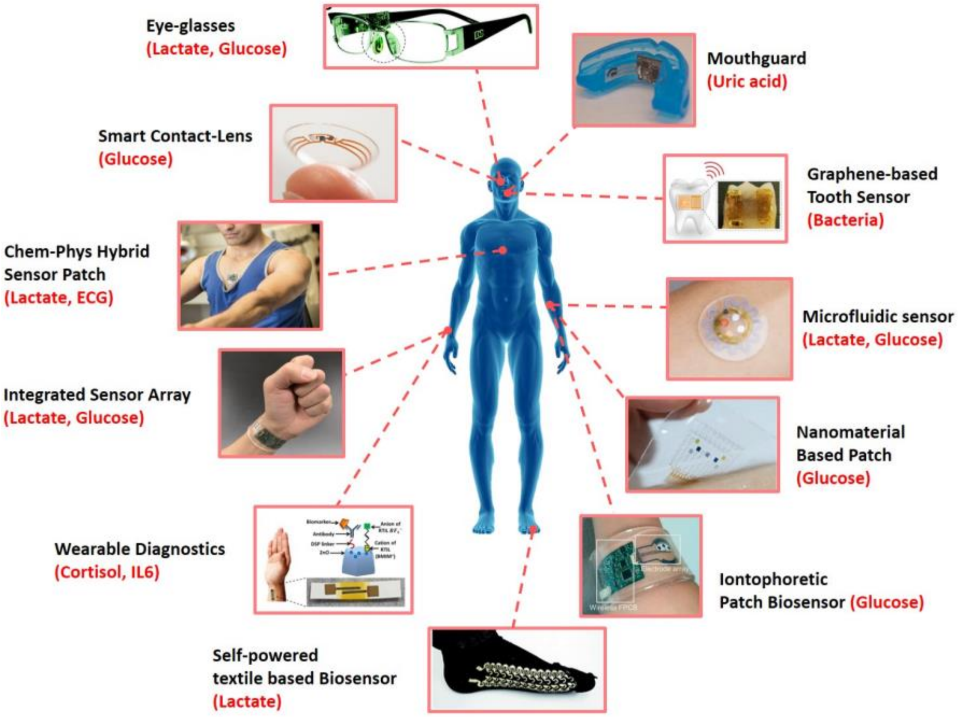

Figure 1.3. *Examples of most common wearable biosensors. The figure was adapted from Ref.* [27] *with permission of Springer Nature.*

Thanks to the 3D-printing systems some researchers at the University of Minnesota developed a system able to print biosensors on living organs [28]. In this study, a hydrogel-based sensor was applied on the pig's lung surface to provide the continuous spatial mapping of the organ deformation via electrical impedance tomography. Unfortunately, 3D-printer systems are still not common to use in bioanalytical applications since the performances are not comparable to that of biosensors technologies. Surely, in the last period, the number of scientific works which involve the use of this technology has grown. This means that three-dimensional-printing will become an applicable technology in the foreseeable future. Concerning the environmentally friendly platforms, *paper-based substrates* occupy a prominent position. Paper is a clean/green material that replaces the use of glass or plastic. This satisfies the global concern for sustainable development. For these reasons, paper-based devices properties are applied in different fields *i.e.* detection of multi-analytes using a combination of different techniques and different paper properties, integrated system for pre-treatment and sample analysis, strong capillary action and biocompatibility [29].

Smartphones-based technologies are powerful instruments for on-site analysis since their potential use as sensitive platforms. More and more preliminary information for a screening analysis are obtainable by smartphone-based devices [30]. These devices work improving the direct identification of physical quantities monitoring the most relevant diagnostic parameters employing inexpensive equipment. The easy and low-cost configuration of mobile diagnostic devices enable their global use also in low-resource countries and underdeveloped areas taking smartphone-based sensors everyone’s reach devices. The smartphone can be used in two different ways: as a detector, in this case the camera is used to identify the signal output; as an interface for an instrument to control and display the test results and the experimental setups on the screen. The latter configuration is common in available commercial devices (*e.g.,* glucometers, ethylometers, abuse drugs detection strips). The diversity of detectors, *i.e.,* color (absorbance and reflectance); luminescence (bio, electro and photo-chemiluminescence and fluorescence); SPR (surface plasmon resonance) and electrochemical-based detection combined with smartphone [31] allow their applicability in diverse sensing area such as healthcare [32], food safety [33], environmental monitoring [34], drug analysis [35] and biosecurity [36].

Despite the high scientific and commercial impact that will have this novel research field, some significant difficulties need to be overcome. For instance, matrix and real sample analysis lead to high inaccuracy in target determination. This is due to the big quantity of interference substances that influence the performance of the smartphone sensors. Conventional devices are not or less affected by this problem. In fact, the results obtained through instruments, like portable photometers, are not still comparable to that of smartphone platforms where also the repeatability of measurements could be compromised. The efforts of the scientific community are currently focusing on the enhancement of this promising technology addressing the mentioned flaws. The integration of biorecognition processes in the smartphone devices is a current challenge in the ideation of standalone smartphone-based biosensors that can be easily operated by self. The continuous monitoring of some important health biomarkers could be guaranteed by the development of sensing devices integrated in gadgets like smartwatches or contact lenses [37]. The wireless network also enables a direct connection with the emergency services for a rapid response in urgent cases. No shortage of applications of smartphone platforms in the quality food control field, especially, to monitor safety indicators. In the future, it will be possible to view the results through QR code scanning [38].

An additional widespread trend for bioanalysis are the *home-testing kits* [39]. They are especially lateral flow devices (LFD) that ensure the self-testing without the help of skilled professionals [40]. The home-self tests unify analytical platforms and medical diagnostic concepts in a simplified way to create highly autonomous devices. More of these tests are commercially available as in the case of pregnancy test [41], cholesterol [42] and oral anticoagulation monitoring [43] or of HIV [44] and Malaria diagnosis [45] not forgetting COVID-19 [46] tests which have been an important resource to fight the disease.

As seen, there are an infinity of applications and possibilities in the use of bioanalytical assays, each one related to the real need. Therefore, these devices will be a powerful point of care and lab on a chip tools [47] for the next generation technology for detecting and monitoring countless analytes.

Unfortunately, as explained above, PoC devices sometimes provide not reliable data [48]. For these reasons, *laboratory-based technologies* are frequently required to provide more accuracy of data that assure a precise diagnosis. In this regard, laboratory-based technologies which imply optical-based instrumentations, play a key role in health care analysis. Let us think about of how the invention of Bradford [49] or Folin-Ciocalteu assays [50], ELISA test [51] or whatever microplate-based methods [52] or even fluoroimmunoassays [53], had a global impact on bioanalysis for clinical purposes. In this context, herein, they were realized different optical-based bioanalytical methods. This dissertation analyzes optical-based bioassays which eventually exploit nanomaterials focusing especially in detection strategies applied for the pharmaceutical analysis.

2

Optical-based bioanalytical assays: fundamentals

Among the laboratory-based technologies, optical assays are a mainstay in our healthcare system. Tests like real-time polymerase chain reaction (RT-PCR), employed in the diagnosis of coronavirus [54], are now part of our everyday life for routine analysis of relevant biomarkers. Thereby, the design of smart bioanalytical assays with the capability of accurate and reliable diagnosis could help to decrease probability of harm, minimize clinical intervention and the costs of medical treatments improving long-term public health. This requires the development and implementation of new suitable detection strategies to estimate potential risk factors and their effects on health, identification of early symptoms of diseases or monitoring the progress of treatment. Nowadays, a remarkable attention is toward the optical diagnostics given by their huge potentiality for real-time non-invasive analyte detection [55]. This is due to the prominent advantage of the non-destructive quality of optical techniques as well as the possibility to avoid the use of labels for a direct optical detection [56]. Additionally, they do not require physical contact with the sample and this represents a precious element also for in vivo analysis [57]. Optical bioanalytical assays provide plenty of information even to the molecular level. Light interaction with biomatter is an incredible resource to deduce biological mechanisms. That is why optical diagnostic technology together with novel biophotonics science can have a huge impact on clinical practice.

2.1 General purpose of biophotonics

Biophotonics is an emerging multidisciplinary research area, embracing all light-based technologies applied to the study of biological systems [58]. Photonics is the science that investigates the interaction of light, over the whole spectrum from ultraviolet through the visible and the infrared to the terahertz region, with matter.

This implies phenomena such as emission, absorption, reflection, that involve the detection, modification or creation of radiation from biomaterials, cells, tissues and organisms that are the focus of the biophotonics studies. The controlled use of light has already revolutionized the approaches applied to the early recognition of diseases [59]. The enormous advantage of the use of light is the non-invasive treatment of the samples that allows the manipulation of tissues and cellular structures without any damage. This contributes to extending the application fields of biophotonic ranging from life science to environmental science. The interaction between light and biological systems enabled to explore cellular processes at molecular level to understand diseases in order to develop target therapies and to proceed to an early diagnosis.

Why is light a suitable tool in biomedical applications? With light is possible the macromolecular and subcellular manipulation since it ensures the object's observation on a scale from several nanometers to centimeters. The use of ultrashort light pulses of femtosecond lasers enables the high precision and long monitoring of extremely fast cellular processes. Furthermore, optical methods can be combined with numerous non-optical approaches like nanotechnology *(e.g.*, nanoparticles, nanocapsules, nanostructures) and microsystem technology (*e.g.*, integrated microoptics, microfluidics). It must also be considered the practical advantages that optical methods offer due to compact and inexpensive instrumentations employed during the analyses. The versatility of optical technologies enables the examination of morphological (scattering, absorption and reflection measurements), chemical (fluorescence and Raman investigations) and mechanical features (holography, optical trapping, doppler spectroscopy and dynamic light scattering studies).

As anticipated, biophotonics covers a broad range of applications [58]: biomedical research; pharmacological research (*i.e.* drug development, for example, target evaluation, high-throughput screening (HTS) and/or high-content screening (HCS) of drug candidates, drug delivery); laboratory tests, PoC diagnostics; clinical diagnostics, therapy and therapy control; regenerative medicine; environmental monitoring, food safety; quality process control (*i.e.* controlling composition and quality of pharmaceuticals, nutrition and cosmetics); security applications (*i.e.*

detection of harmful biological and chemical substances and weapons). The optical techniques used in biophotonics applications are divided into:

- Spectroscopy applications: absorption (THz, microwaves, IR, UV–Vis); emission (all fluorescence methods one-photon/multi-photon fluorescence, FRET, FRAP, FLIM, FLIP); elastic and inelastic light scattering (e.g., Rayleigh, Raman, CARS, SRS, SERS, TERS, Mie, LIDAR).
- Light Microscopy: fluorescence microscopy (observing autofluorescence or using fluorescence labels, *e.g.*, proteins), including sub-diffraction techniques (optical nanoscopy, *e.g.*, STED, NSOM, PALM/STORM, structured illumination) and 3D imaging techniques (*e.g.*, confocal and multi-photon excitation microscopy); Raman microscopy (CARS, SRS, TERS); other contrast methods (phase contrast microscopy, digital holographic microscopy (DHM)).

In the studies reported here, spectroscopy methods were widely applied for the development of optical-based bioanalytical detection strategies. In particular, absorption and fluorescence methods were used for the development of novel easy bioanalytical methods.

2.2 UV-Vis Absorption and Fluorescence in bioanalysis: fundamental principles

More than 90 % of clinical laboratory analyses are performed by operating ultraviolet-visible (UV-Vis) light absorption and fluorescence methods. The common thread among these spectroscopic techniques is the signal derived from photoexcitation of the chemical species. The scalable, rapid, portable, versatile, non-destructive and easy-to-use approach render them among the most used analytical methods for bioanalytical purposes. Additionally, a large variety of biomolecules absorb UV-Vis light and can be identified by using spectrophotometry studies. Photometric techniques are ubiquitous in the examination of biological and chemical species. By applying the Lambert-Beer equation, it becomes easy to quantify analytes if they absorb photons within a specific wavelength range. Some experimental artefacts can compromise the UV-Vis analysis, limiting its application. For instance, the choice of the solvent that could influence the electronic properties of the dye, as well as the material used to perform the UV-Vis measurements (*e.g.*, cuvette, microplate, slide, etc) and undesired light scattering could lead to baseline distortion and generate problems in the spectra interpretation. However, these are small flaws with respect to the several advantages that spectrophotometric analysis offers. The UV-Vis spectrum of a molecule represents its “fingerprint” from which, a multitude of useful information, about the nature of the examined molecule, can be extrapolated. An important point in bioanalytical approaches is the analysis of biological matrices. All chemical species in solutions contribute to absorption, including interfering species. Fortunately, many approaches such as multivariate calibration or classification, difference spectrophotometry, and derivative absorption spectroscopy operate to minimize the background effect. As a result, UV-Vis measurements are generally suitable also for the bioanalysis of complex biological samples. Moreover, different UV-Vis instrumental configurations guarantee its applicability in various areas. The most common optical configuration includes single- and double-beam arrangements. The target detection takes place by means of photomultiplier or a photodiode array. The bioanalytical assays combined with absorption measurements are based on chemical transformations and interactions for producing light-absorbing chromophores and for this are very sensitive and specific in the target analysis. According to the examined sample and to the field of application, different experimental set ups are employed. Solid and semi-solids samples are analyzed through diffuse reflectance or fiber optic probes. The combination with separation techniques, like electrophoresis or chromatography enables flow injection analysis in the diagnostic and environmental field. Despite the high quantities of information that can be deduced from the analysis of the UV-Vis spectrum, structural data are lacking and fluorescence studies are required.

Fluorescence spectroscopy is more sensitive about two orders of magnitude than spectrophotometry. Fluorescence is the emission of light accompanying the relaxation of a singlet excited state to the ground state [60]. The photoluminescence (PL) emission is measured during the irradiation since the excitation phenomenon takes a few seconds. The spectrofluorometer set up arrangement (light source and the detector at 90 °C) reduces the problem derived to the background. The instrumental response is proportional to the intensity of the excitation light.

PL techniques are very sensitive and suitable for analytes at low concentration. Through the study of fluorescence behavior, it is even possible to obtain information on the characteristics of a single molecule. Fluorophores, fluorogenic compounds, and fluorescence molecules are usually employed for the exploration of complex molecular systems. Fluorescence methods are also used as imaging tools to visualize biochemical processes. It is necessary to know physicochemical, photophysical, and photochemical properties of the fluorophores, quenchers and analyte to develop an efficient bioanalytical spectrofluorimetric method. An important parameter which is evaluated in a fluorescence study is the quantum yield (Q.Y.) (ϕ_{FL}). It gives information on the fluorescence efficiency of the examined system and represents the ratio between the number of photons absorbed and emitted.

Fluorescence investigations play a key role in diagnostic applications since various simultaneous readouts such as emission intensity, lifetime of the excited state of the fluorophore, anisotropy, and spectral characteristics can be obtained. A relevant drawback of fluorescence techniques is the application of turbid media analysis leading to light scattering phenomena. This is verified mostly in no diluted human samples such as human tissue or blood. Furthermore, some samples can be photolyzed by photoexcitation phenomena. As a result, photodegradation can occurs involving the formation of toxic products. This problem can be overcome by using diluted samples. In this case, the fluorescence response is linearly correlated with the concentration of the fluorophore. A multitude of fluorescence phenomena can be exploited for diverse applications. For example, by using the FRET (Förster resonance energy transfer) process it is possible to establish the position and the dynamics of two fluorophores in a biological system. In the bioanalytical field, FRET-based assays are applied prevalently in the study of the biorecognition events (*e.g.,* DNA hybridization, ligand–receptor binding, etc). The molecular aggregation also leads to fluorescence emission (AIE aggregation induced emission) or quenching phenomena (ACQ aggregation-caused emission quenching). AIE is frequently employed in ultrasensitive sensing experiments but it also represents an important tool for biomolecular imaging. The excimers (excited dimers) and exciplexes (excited complexes) formation enable to understand an incredible variety of biophysical properties *i.e.*, excited-state dynamics of DNA. Moreover, a broad range of fluorescent dyes are helpful for multiphoton excitation investigation. For instance, two-photon absorption (TPA) combined with the use of NIR light are frequently used as photoactive drugs and to penetrate deeper into tissues for bioimaging purposes. These are only a few examples in which photoluminescence phenomena are applied as investigation tools in bioanalysis.

In detail, we report below the bioanalytical applications in which spectrofluorimetry and spectrophotometry techniques are employed (Table 2.1). As shown, UV-Vis and fluorescence spectroscopy techniques are daily used in clinical laboratories. The growing interest in these bioanalytical methods was born in recent periods where the direct fast detection of pathogenic targets enabled the monitoring of the spread of several diseases. In fact, the use of optical laboratory methods in identification and direct detection of the coronavirus and in vaccine development and validation was essential. That is why the research is now focused on the implementation of optical-based tests used in diagnostic laboratories. The aim is to improve the sensitivity of the tests by exploiting, for instance, nanomaterials, synthetic receptors (*e.g.*, molecular imprinted polymers) or labels. UV-Vis and fluorescence signal detection combined with these approaches are promising tools for future applications in different areas such as in personalized medicine and theranostic [61].

Table 2.1. *Some of the most employed spectrophotometric and spectrofluorimetric assays in bioanalytical diagnostic applications. Adapted from Ref.* [62].

Assay	Analyte	Method
Spectrophotometric assays for biomolecules	*Protein*	Folin-Ciocalteu
		Biuret
		Bicinchoninic acid
		Coomassie Brilliant Blue
		Tyr, Trp: 278 nm; peptide bond: 190 nm
	Carbohydrate	Phenol, H_2SO_4
		Anthrone, H_2SO_4
	Amino acids	Ninhydrin
		Cupric salts
	Cys and thiolates	Ellman’s reagent, (5,50-dithiobis-(2-nitrobenzoic acid)
	Coenzymes	FAD: 438 nm, NADH: 340 nm, NAD+: 260 nm
	Carotenoids	Direct (420, 450 and 480 nm)
	Porphyrins	Direct
	Glucose	Glucose oxidase, peroxidase, o-dianisidine
	DNA	Diphenylamine
		Direct (260 nm)
	RNA	Bial
	Cholesterol	Cholesterol oxidase, peroxidase, 4-aminoantipyrine, phenol
Enzyme-based spectrophotometric assay	*Bilirubin*	Malloy-Evelyn
	Cholesterol	Kinetic: cholesterol oxidase
	Glucose	Hexokinase (NAD^+/NADH)

	Lactate dehydrogenase	Kinetic: lactate pyruvate
	Urea	Kinetic: (NAD^+/NADH)
	Triglycerides	Kinetic: glycerol 3-phosphate oxidase
Immunoassays	*Biomolecules*	ELISA
	Biomolecules	BELISA
	Biomolecules	FELISA
Fluoroimmunoassays	Ca^{2+}	Intensity change (single fluorescent protein (FP) sensor) or FRET based
		Intensity change or spectral shift in dye
	Kinase activity	Change in localization (nucleus versus cytoplasm) of single FP reporter
	NADH/ NAD^+	Conformational change of single FP fused to NADH/ NAD^+-sensing domain
	Cell cycle stages	Fucci (fluorescent, ubiquitination-based cell cycle indicator)
	CDK2-based localization change	Change in localization (nucleus versus cytoplasm) of single FP reporter

3

Nanomaterials in bioanalytical applications for diagnostic purposes

Efficient signal enhancement strategies are frequently indispensable in a bioanalytical approach. At this aim, nanomaterials (NMs), and their unique optical, electrochemical and magnetic properties, are commonly employed for signal amplification in countless detection systems [63–66].

Bioanalytical procedures take numerous advantages in the use of NMs. The nano-sized structures (1-100 nm) and the exceptionally large specific surface areas improve the sensitivity of the assay and enable its miniaturization. The versatility and the nano-tailored features of NMs allow their use in different kinds of detection methods, suitable for each specific application. Thereby, nanomaterials had a large scale impact in bioanalytical sciences through the fabrication of novel nano devices, nanotools, nanosensors and nanosorbents expanding the nanoworld [67]. Nowadays, NMs are totally embedded in a number of analytical procedures [68]. Quality, such as the high surface-to-volume ratios allows a high loading of receptors or signaling molecules enhancing the surface functionalization of NMs. This and other features like small size, high stability, enhanced control of light spectrum and excellent chemical reactivity make the NMs a powerful tool for bioanalysis. Numerous are the uses of NMs in optical-based bioanalytical methods due to their ability to manage the light [69]. The majority of optical properties of NMs depend on the chemical composition and the size/geometry of nanostructures. For instance, NMs can show fluorescent behavior or UV-Vis absorption wavelength or even a plasmon band. These spectroscopic features are influenced by the chemistry of the NMs and are ordinarily applied in detection strategies [70–72]. As a matter of fact, luminophores and signal reporters are generally NMs possessing fluorescent features. On the other hand, NMs with proper size can generate reflectance and scattering phenomena usable, for example, in surface enhanced Raman scattering (SERS)-based assays [73]. Of course, electrochemical, magnetic, catalytic, mechanical, and thermal properties of nanomaterials are also exploited in various analytical detection strategies, but they will not be the focus of this discussion.

The optical features of NMs will be treated in depth below since, in this thesis, a class of nanomaterials (copper nanoclusters) were fabricated to develop an optical bioanalytical detection strategy for protein detection in human specimens. More are the nanomaterials which are actively part of nanoscience. Accordingly, a classification is needed and is reported in the following paragraph.

3.1 Classification of Nanomaterials

NMs are classified according to diverse criteria based on their size, morphology and chemical composition [74]. Depending on their dimensionality and shape, NMs are firstly divided into four classes: zero- (0D), one- (1D), two- (2D) and three (3D)-dimensional nanomaterials. 0D NMs like quantum dots (QDs), spherical NMs (*i.e.* NPs), clusters, cubes, nanorods, polygons, metal and core-shell have size below 100 nm; 1D are materials with one dimension not in nanoscale and include metallic, polymeric, ceramic, nanotubes, and nanorods filament or fibers, nanowires, and nanofibers. 2D class contains single-layered and multi-layered, crystalline or amorphous, thin films, nanoplates, and 3D nanomaterials are prevalently nanotubes, fullerenes, pillars and all of that configurations which combine multiple nanocrystals in different directions. The morphology also influences the characteristics of such NMs. In particular, NPs can be uniform (*i.e.*, isometric) or inhomogeneous that lead to agglomerate formation (*e.g.*, cluster). NPs agglomerates show diverse chemistry and electromagnetic properties with great possibility to functionalize the surface. Examples of NPs with different morphology are nanorods, nanostars, nanocubes or nanohelices. The last classification of NMs is based on the chemical composition of nanomaterials. Carbonaceous NMs are composed mainly of carbon *e.g.*, fullerenes or graphene. Metallic NMs are formed by metals like silver, copper, iron, gold, etc. Then, branched dendrimers and nanocomposite NMs are also included in this classification since they possess electrical or thermal conductivity. Finally, also QDs differ for the chemical and electronic properties since they are tiny semiconductor particles of few nanometers with quantum mechanics behavior. In Figure 3.1 a scheme which synthetizes the classification of nanomaterials, is reported.

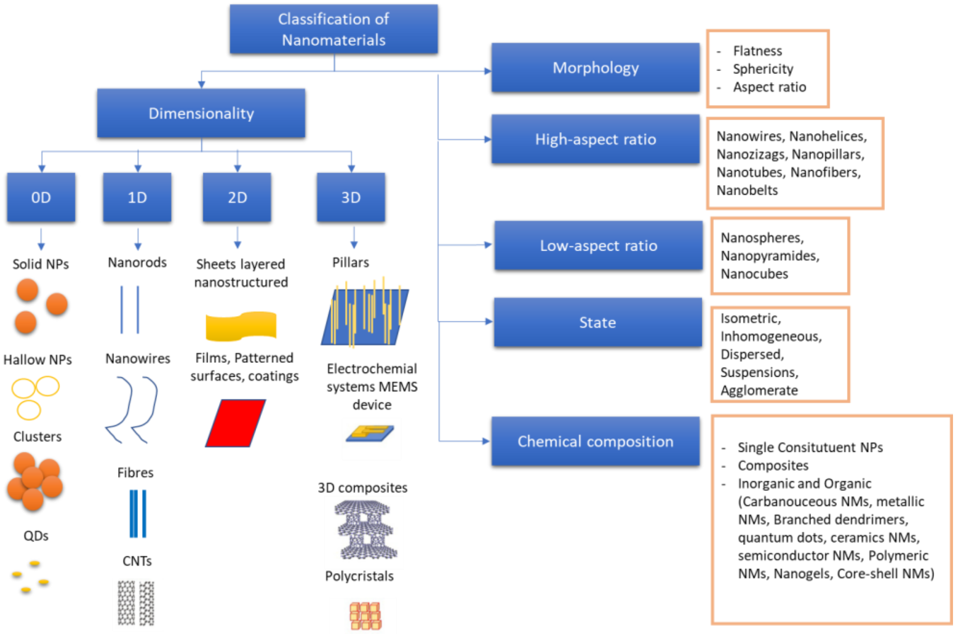

Figure 3.1. *A synthetic scheme of NMs classification. The figure was adopted from reference* [74].

The most widespread nanomaterials generally applied in bioanalytical studies (*e.g.*, photothermal cancer therapy, diagnostic, biosensors, drug delivery, imaging) are nanoparticles, quantum dots, carbon dots (CDs), graphene, carbon nanotubes (CNTs), and nanocomposites materials.

3.2 Nanoparticles, quantum dots, carbon-based and nanocomposites materials in bioanalysis

NPs with different size, shape or chemical composition (*e.g.* metal or oxide NPs) are already involved in bioanalytical measurements [75]. One of the most common applications of NPs in bioanalytical tests is their use as *quantitation tags* [76]. Thereby, NPs have the role to identify a target through the quantification of themselves or a measurable parameter. This arises from the need to eliminate organic fluorophores or radioactive labeling which have some drawbacks like the toxicity or the high cost. This paves the way to the development of novel signal reporters. NPs act also as *substrates* in solution multiplexed bioassays in which NPs functionalized with nucleotide sequences are able to recognize the target sequences [77]. Another relevant role of NPs in bioanalysis is that of *signal transducer* where the aggregation phenomenon of NPs is employed to detect, for example, immunoglobulins (Ig) in whole blood [78]. Since the huge versatility in the application of NPs, the research is moving into the improvement of the development of purchasable nanoparticles to more include them in routine bioanalysis protocols.

QDs are highly luminescent zero-dimensional (1-20 nm) semiconductor fluorescent nanoparticles. The quantum confinement effect of QDs is used as a analyte quantification system [79]. However, large amounts of QDs are required for high signal amplification. This can be achieved by surface engineering of the QDs [80]. The high quantum yields, photostability, large Stokes shift, wide excitation spectrum, large biochemically accessible surface area, good biocompatibility, and long fluorescence lifetime allow the enormous QDs use in life sciences area such as cancer diagnosis [81] or photodynamic therapy (PDT) [82].

High mechanical properties, relevant chemical stability, low density, remarkable emission properties, great electrical and heat conductivity, and large surface area which provides higher binding capacity are the key properties of carbon nanotubes, carbon dots, and graphene oxide that are used in bioanalytical field [83]. In carbon-based NMs electron transfer effect is applied to improve the signal enhancement.

Nanocomposite materials are solid materials composed by diverse phases, one of these with dimensions less than 100 nm [84]. Composite materials improve the adsorption capacity of the material through several types of interactions, *e.g.*, electrostatic interactions or n-π interactions. This offers high surface area by means of binding capacity improvement with positive impact in numerous analytical sensing platforms.

As seen, measurable improvements in performance of analytical tests (*i.e.* sensitivity, decrease in detection limits) are guaranteed when different kinds of NMs are adopted. The extraordinary advantages involved in the use of NMs were exploited also in more of diagnostic applications [85] such as bioimaging [86], target therapy [87], drug delivery [88], biological labeling [89], pathogenic bacteria detection [90], biomolecules and molecules recognition [91], sensors and biosensors design [92], etc. As a matter of fact, in this research work the outstanding properties of a class of NMs, copper nanoclusters, were deeply investigated and they were used for the development of an optical-based bioanalytical approach for diagnostic purposes *i.e.*, human albumin (HSA) detection. In the following section, properties and applications of CuNCs are treated in detail.

4 Copper nanoclusters and their application for innovative fluorescent detection strategies: an overview

Sensors and Actuators Reports 4, (2022) 100-108 – **DOI:** 10.1016/j.snr.2022.100108.

4.1 Abstract

Nanomaterials have revolutionized the design of the detection strategies, and nowadays nanoparticles are extensively employed in innovative assays for the selective and sensitive detection of a large variety of analytes. Recently, a new nanomaterials category, namely nanoclusters (NCs), is rapidly emerging. These nanostructures offer great advantages in terms of stability and ease of fabrication. The increasing interest in NCs applications, well represented by the wide bibliography reporting on gold and silver NCs, opens new perspectives for copper nanoclusters (CuNCs). Compared to noble metals, CuNCs not only are more easily available and inexpensive, but also display unique photoluminescent properties with large Stokes shifts, low toxicity, and high biocompatibility, providing high sensitivity even in complex biological matrices. In this work, some relevant aspects of the application of CuNCs to various detection strategies are presented, reporting the main features that define the most interesting CuNCs properties, and focusing on CuNCs as a promising functional nanomaterial for the development of innovative fluorescent-based platforms.

Keywords: Copper nanoclusters, CuNCs synthetic approach, CuNCs-based assays, fluorescence detection strategies.

4.2 Introduction

There is a need in bioanalytical chemistry of simple, easy, sensitive, and inexpensive assays. In the last years, nanomaterials have been used to improve bioassays' analytical performances, mainly in terms of detection limits. Metal or carbon nanostructures have been applied to Surface Plasmon Resonance (SPR) coupled to nucleic acids or protein based biosensing [93,94] or used in fluorescent-based measurements such as quantum dots (QDs). Recently, a new category of nanomaterials, namely nanoclusters (NCs), is rapidly attracting the interest of bioanalytical chemists for the important fluorescence features applied to the development of bioassays.

Metal nanoclusters (MNCs) are exciting and versatile nanomaterials with intermediate properties between isolated metal atoms and metal nanoparticles (MNPs). To date, the majority of the sensing strategies based on MNCs exploit noble metals, *e.g.*, silver (AgNCs)[95] and gold (AuNCs) [96].

Thanks to their low toxicity and high biocompatibility, in the last decade, copper nanoclusters (CuNCs) were successful used in biomedical and biological fields for *in vitro* and *in vivo* applications [97–100], including molecular diagnostics, nanotheranostic, and environmental analysis. Furthermore, copper is less expensive and more accessible on earth than noble metals, positively impacting on NCs-based systems development. CuNCs appear as excellent substitutes of QDs and organic dyes, thanks to high quantum yield (QY), photostability [101], and large Stokes shifts [102]. The outstanding fluorescence and catalysis features of CuNCs are size-dependent [103], limited by definition to few-to-tens atoms, and diameters within 1 nm, leading to a quantum-like behavior with discrete HOMO-LUMO electronic transitions [104].

The first reports on the formation of fluorescent CuNCs nanoclusters were proposed in 1998 by Zaho and Balogh and co-workers [105,106]. They used a class of monodisperse polymeric macromolecular compounds (dendrimers) as template triggering metal ion reduction which stabilize formed metal clusters, avoiding their aggregation [107]. Other useful templates are nucleic acids [108], proteins [109], peptides [110], and small molecules [111], which reduce copper ions and inhibit the formation of aggregates by steric hindrance [112]. CuNCs were used as sensing probes (enhancing or quenching their fluorescence) to achieve the high-sensitive determination of small and macromolecules even in complex real matrices. First studies reported the Pb^{2+} ions detection by using BSA as template for copper clustering and CuNCs fluorescence quenching to reveal Pb^{2+} presence in solution [113]. Since then, CuNCs were used for quali-quantitative molecular targets' analysis [114–118], pH determination [119–122], or biological imaging [123–125]. The coupling of CuNCs with a biological recognition element, enabled the development of fluorescence-based platforms characterized by good detection range and detection limit, great stability, and selectivity, which are of great importance in bioanalysis to develop simple and ultrasensitive strategies for biomolecular targets. In this framework, the use of peptides, proteins [126], single (ssDNA), double stranded (dsDNA) [127], and hairpins DNA[128], has been reported [129].

4.3 Synthesis and features of CuNCs

4.3.1 Experimental parameters that influence fluorescence of CuNCs

The fluorescent properties of CuNCs depend on their nanometric dimensions (Fig.4.1) and, similarly to NPs, can be tuned by working on the synthesis conditions (metal and template concentration/type, reducing agent, solvent, pH, temperature, growth time, *etc.*), generating atomically precise entities [130]. The emission energy (E_g) of CuNCs depends on Fermi energy of the bulk metal (E_{fermi}) and the number of atoms in single clusters (n), according to equation $E_g=E_{fermi}/n^{1/3}$ [130,131], with the emission wavelengths (λ) spanning from the visible to the near-infrared (NIR) region. Consequently, NCs represent a link between optical properties of a single atom, with discrete electronic transitions between the occupied *d* bands and the Fermi level, and those of nanoparticles, exhibiting localized surface plasmon resonance (LSPR) [132–136]. The core size is directly proportional to the quantity of the reducing agent used during the synthesis but inversely proportional to fluorescence intensity. In particular, fluorescence is limited to NCs with less than ten copper atoms that can be obtained using very low percentages of reducing agent with respect to stoichiometric amount of copper ($\alpha < 0.1$) [137].

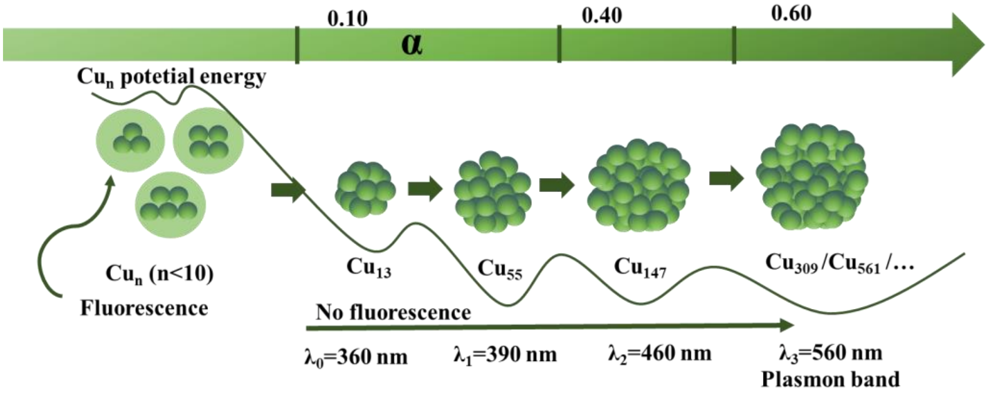

Figure 4.1. *The influence of the reducing agent-to-copper ratio (α) on CuNCs size (n) and absorption band (λ). Size changes proportionally with α values, whereas photoluminescence is observed when the number of atoms (n) is smaller than 10. The estimated wavelengths (λ) for each cluster and the trend of potential energy are reported* [137].

Coordination of ligands to the metal core [138] and pH influence both the photoluminescence (PL) of the CuNCs. In particular, electron-rich or electron donor groups, like -SH, –COOH, -NH$_2$ and –OH, increase the emission intensity and fluorescence lifetime of CuNCs [139,140]. Moreover, pH changes lead to CuNCs emission and excitation peaks shifts due to protonation/deprotonation mechanisms [141], inducing aggregation, emission enhancement, and impacting on CuNCs growth [142]. For example, alkaline pH favors disulfide bonds breaking within the protein scaffold, stabilizing CuNCs by thiol groups coordination [143]. Thanks to the CuNCs pH sensibility, pH sensors are reported [144–147] in the range from 2.0 to 13.2.

Solvents also influence CuNCs PL spectra, due to interactions among the ground state, the excited state, and solvent molecules [148,149]. In particular, CuNCs fluorescence spectra show lower number of peaks and greater Stokes shift in solvents with higher polarity, but the fluorescent emission intensity is higher when CuNCs are dispersed in solvents with lower polarity [150].

4.3.2 Synthetic strategies of copper nanoclusters

Top-down and bottom-up approaches are leading strategies to obtain photoluminescent CuNCs (Fig. 4.2). Top-down synthesis is based on CuNPs resizing to obtain smaller CuNCs; this approach is very laborious [151,152] while the bottom-up one, simple and mostly used, involves the reduction of metal atoms, followed by their aggregation into clusters, often in presence of a stabilizing agent. Different procedures including electrochemical [153], sonochemical [154], photo-reduction [155], microwave-assisted [124], and template-based synthesis [156] are used in the bottom-up approach. In electrochemical methods, an anode is used as the metal ions source that are reduced at the cathodic surface to metal atoms forming aggregates or nanoclusters stabilized by using surfactants [157]. The sonochemical method is a green and easy synthetic method, exploiting ultrasounds derived from acoustic cavitation [158]. Its limitation is the low quantity of metal atoms obtained, which impairs the following nanoclusters' growth. In photo-reduction synthesis, the production of NCs is induced directly by UV radiation [155]. The microwave-assisted method produces rapid CuNCs crystallization due to homogenous and fast heating [157]. The most used approach is the template-assisted one, allowing a facile, fast, cheap, and green synthesis of nanoclusters by using a template to control the kinetics of copper ions reduction, tuning CuNCs size and shape, and preventing their aggregation [159]. Micro and macromolecules like polymers, oligonucleotides, proteins, peptides, and small molecules have been adopted as scaffolds to induce the controlled nucleation of copper nanoclusters as detailed in the following paragraphs.

Nucleotide sequences as templates

Copper ions interact with nucleotide bases through the coordination of the negatively charged phosphodiester backbone [160]. The length and the nucleic acid sequence of the dsDNA template strongly influence the CuNCs synthesis and photoluminescence properties [161]. Firstly, random dsDNA was initially exploited for the CuNCs synthesis. Subsequently, it was noticed that a remarkable fluorescent signal improvement was obtained by using polyT ssDNA or poly(AT-TA) dsDNA, where adenine and thymine represent the nucleation site for reduction of Cu(II) to Cu(0) and its clustering to CuNCs. This mechanism is impaired by adopting cytosine and guanine rich sequences likely due to strong copper complexation that could limit copper reduction. Summarizing, ssDNA containing poly(thymine) sequences [162–

164], dsDNA with AT-rich domains, as well as long oligonucleotide sequences [165,166], in presence of a reducing agent (usually ascorbic acid), favor the formation of high fluorescent CuNCs with an excitation wavelength at 340 nm and an emission peak around at 600 nm. Besides the stabilizing effect and its influence on the CuNCs photoluminescent properties, nucleotide sequences may also possess specific molecular recognition ability, that can be exploited in solution assays to selectively bind different analytes [167,168], like for the aptamers that are nucleic acid sequences (DNA or RNA) able to bind a target molecule [169,170]. They are obtained *in vitro* after a selection process by exponential enrichment (SELEX) or non-SELEX approaches[171,172]. DNA is a privileged scaffold for the synthesis of CuNCs also because it can be used for a rapid detection of genetic alteration [173], differently from classic genetic tests that usually require long analysis time [174].

Proteins and peptides as templates

Proteins and peptides are often used as templates for building stable and biocompatible CuNCs, requiring mild conditions for the synthesis [175] .They contain several functional groups, like amine-, thiol- and carboxyl groups, which initiate the complexation through electrostatic forces. Amine- and carboxyl groups coordinate copper ions while thiol groups contribute to the reduction and stabilization of CuNCs. Thus, the diversity of the amino acid sequence affects the final CuNCs properties. A conventional protein-CuNCs synthesis implies the use of various additives that alter the protein structure by breaking the disulfide bonds, like dithiothreitol (DTT) [176], H_2O_2 [177], hydrazine hydrate [178], and NaOH [179]. So far, different protein templates have been explored to synthesize luminescent CuNCs. For instance, bovine serum albumin (BSA) leads to high QY fluorescent CuNCs [167,168,180]. Bustos et al. produced blue emitting CuNCs (610 nm) with high photostability with a decrease of only 15% in emission signal after 50 min [168]. Other proteins, such as human serum albumin (HSA)[181,182], lysozyme [183,184], ovalbumin [185], papain [186,187], transferrin [188] and trypsin [146] have been also applied as templates for CuNCs production. Although proteins are preferred as templates for the presence of multiple active sites that favor the reduction and the accumulation of copper ions promoting the CuNCs growth, few studies report the use of peptides as template [189,190]. For example, Tang and co-workers prepared stable and well water-dispersed CuNCs by reducing copper chloride with ascorbic acid in the presence of a short peptide template Cys-Cys-Cys-Asp-Leu, highlighting the importance of $CuCl_2$-to-peptide molar ratio (1:4) in the formation of CuNCs [189].

Polymers as templates

Dendrimers, *i.e.*, highly ordered branched polymers with different size and the chemical structure, are the most exploited templates to produce very stable CuNCs [105,191]. Polyvinyl pyrrolidone (PVP)-CuNCs were applied to develop a FRET-based assay in solution (named sensor) for the micromolar detection of glutathione (GSH) in human serum with performances comparable to HPLC [192]. Polyethyleneimine (PEI) was also used as scaffold for facile one-pot synthesis of water soluble CuNCs applied to Fe^{2+} detection in tap, river water, and urine, with very good analytical performances, *i.e.*, micromolar level concentration and 100% recovery [193]. Furthermore, CuNCs were incorporated into composite polymer films by reduction of copper ions in a hydrogel network with 30% QY, opening to possible applications in heterogeneous phase assays/sensors [194].

Small molecules as templates

Small molecules, containing thiolates and carboxylates groups, like glutathione (GSH) and cysteine, act as reducing, protecting, and capping agents to stabilize CuNCs through to a facile one-step green synthetic approach [195–199]. Glutathione was exploited also for its ability to coordinate metal cations like aluminum ions that guide the self-assembly of nanoclusters resulting in the formation of CuNCs with controllable size and retained bright luminescence in neutral conditions [200,201]. Many authors took advantage of the easy and cheap synthesis of copper nanoclusters by using small molecules as templates [202–205]. Additional small molecules like 4-methylthiophenol and 4-chlorothiophenol were also applied to synthesize CuNCs able to sensitively detect different kinds of target molecules like tetracycline (LOD 40 nM)[206].

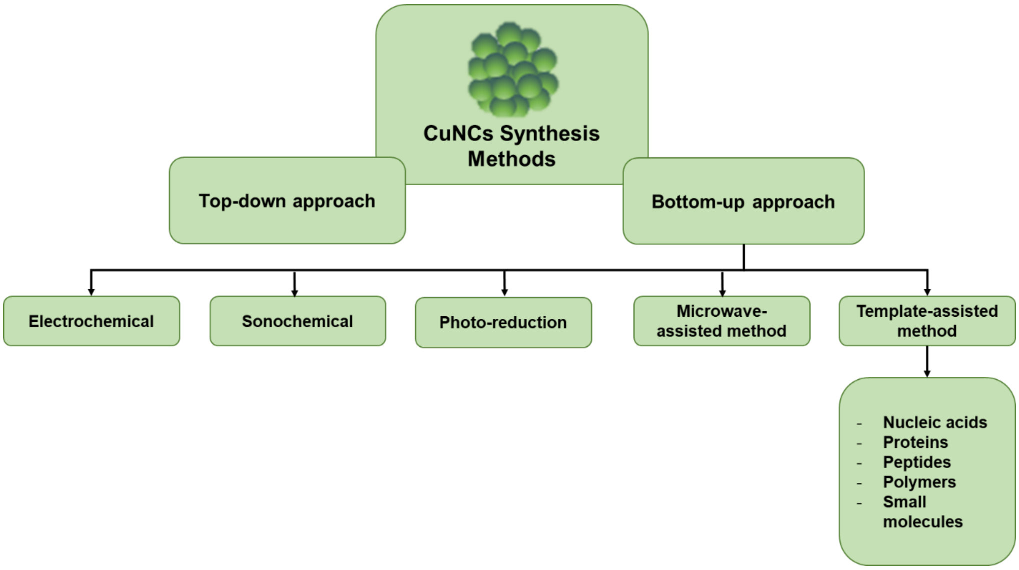

Figure 4.2. *Synthetic strategies of copper nanoclusters.*

4.4 CuNCs-based detection strategies

CuNCs were exploited as sensing probes in solution since they are able to detect different types of targets, from ions to macromolecules (*i.e.*, proteins, DNA, enzyme, etc.) [207]. Numerous publications are related to the integration of noble metal nanomaterials in bioanalytical assays development [208–211], leading to remarkable improvement in bio-detection processes.

Generally, an efficient detection system should be characterized by the following properties: stability, selectivity towards the analyte, reproducibility, desired sensitivity, a null or minimal sample pre-treatment. Moreover, to ensure the development of a potential commercial device, the assay should be simple, cheap, and able to perform rapid analysis making it suitable as a PoC test [212–214].

Copper nanoclusters employed as signal transducers in “sensors” design lead great advantages in the assay performance, such as high selectivity, sensitivity, low detection limits, and wide detection range. Typically, when the bioreceptor is associated with CuNCs, the binding event leads to a fluorescence signal variation depending on analyte concentration [215–217].

Most bioanalytical applications that exploit CuNCs involve the use of oligonucleotide sequences as bioreceptors (*i.e.* capture/ signal probe) and as template for CuNCs growth [218]. On the other hand, detection strategies which employ protein as a template is an unexplored field that could be a promising tool for diagnostic purposes. Herein, protein-templated CuNCs were used for the determination of human serum albumin. The details related to the design of the CuNCs-based assay development are reported in the following section.

5 Protein-templated copper nanoclusters for fluorimetric determination of human serum albumin

Mikrochim. Acta. 188, (2021) 116 – **DOI:** 10.1007/s00604-021-04764-7

5.1 Abstract

Copper nanoclusters (CuNCs) are attractive for their unique optical properties, providing sensitive fluorescent detection of several kinds of targets even in complex matrices. Their ability in growing on suitable protein and nucleic acid templates make CuNCs efficient optical reporters to exploit in bioanalysis. In this work, we report the specific and sensitive determination of human serum albumin (HSA) in human serum (HS) and urine via CuNCs fluorescence. HSA is the most abundant protein in plasma, and plays a key role in the early diagnosis of serious pathological conditions such as albuminuria and albuminemia. Recently, HSA has become clinically central also as a biomarker to assess severity, progression, and prognosis of various cancers. We report the controlled and reproducible growth of CuNCs directly on the target analyte, HSA, which results in a fine dose-dependent fluorescent emission at 405 nm. The protocol is optimized in water, then applied to serum and urine specimens, without matrix pretreatment. The method linearly responds within the whole concentration of clinical interest, with a sensitivity of $1.8 \pm 0.1 \times 10^{-3}$ g L^{-1} and $0.62 \pm 0.03 \times 10^{-3}$ g L^{-1} in serum and urine, respectively, and excellent reproducibility (CV_{av}% ca. 3% for both). Both the parameters result lower than other reference techniques. Moreover, the assay is designed to have a single protocol working for both the matrices, with recovery efficiency of 95% (HS) and 96% (urine). The stability of the fluorescence after CuNCs formation was tested over three days, displaying good results higher in urine than in serum.

Keywords: Copper Nanoclusters, Human serum albumin, Fluorescence, Label-free assay.

5.2 Introduction

Human serum albumin (HSA), the most abundant protein in human blood (35-50 g L^{-1}), is a multi-domain protein able to bind different endogenous and exogenous macromolecules. Therefore, the key role of HSA consists in carrying many biomolecules and, consequently, in modulating oncotic blood pressure [219]. In addition, HSA is a notable biomarker of many diseases such as cancer [220], liver disorders [221] (*i.e.* cirrhosis or hepatitis), rheumatoid arthritis [222], diabetes, hypertension, kidney and cardiovascular diseases [223,224]. In particular, low HSA concentration in human serum and high HSA values in urine denote two important pathological states known respectively as albuminemia and albuminuria [225,226]. As a whole, the accurate determination of HSA in different biological specimens plays a critical role both from a diagnostic and a prognostic point of view. In the past, precipitation-based methods were commonly applied to detect albumin [227]. Presently, a large number of analytical methods (*i.e.* immunochemical, dye-binding, chromatographic, spectroscopic, and electrophoresis-based methods) are reported in literature for the accurate estimation of HSA [217,228,229]. For HSA detection in blood, electrophoretic technique represents the first choice [230], whereas immunonephelometry and immunoturbidimetry are preferred for HSA determination in urine samples [231,232]. There is a lack, therefore, of a method allowing HSA determination in these two specimens through the same procedure, *i.e.* in a matrix-independent manner. Moreover, most of the analytical methods proposed so far, taken together, suffer from some disadvantages because they are often expensive, time-consuming, and laborious, requiring in some cases (*e.g.,* electrophoretic investigations) many pre-analytical steps and the use of synthetic dyes. In this framework, here we present a low cost and rapid method for the accurate and selective determination of HSA, both in human serum and urine, without the need for any sample pre-treatment (except dilution for human serum). The outstanding properties of copper nanoclusters (CuNCs) [189] were exploited to develop an assay able to directly detect albumin-templated CuNCs by fluorescence. As far as we know, this is the first report on the use of CuNCs for the selective albumin detection for clinical diagnostics. Differently from metallic nanoparticles, widely employed in bioanalytics, metallic nanoclusters are still poorly explored for such applications. However, in recent years, the unique fluorescent properties of CuNCs, such as high quantum yield, photostability, and large Stokes shifts, enabled their frequent use in numerous bioanalytical assays [126,233]. In addition, remarkable features such as low toxicity and good biocompatibility allow the use of CuNCs as fluorophores for biolabeling and bioimaging [234], representing an alternative to the quantum dots and organic dyes. However, two works referred to CuNCs and HSA [143,235]. In the first, bilirubin is quantified in urine and human blood samples by the quenching induced by the analyte upon its interaction with red fluorescent CuNCs synthesized by using HSA as a template [143]. In the second, Chen et al. quantified HSA in plasma by following the reduction of fluorescence of poly(thymine)-templated copper nanoparticles (CuNPs) due to HSA that inhibits the CuNPs formation [235]. Differently from above reported turn-off fluorescence strategies, here we report for the first time that HSA-templated CuNCs are able to directly detect and quantify HSA itself by a turn-on strategy that exploits the selective growth of CuNCs on the albumin template. The optimized experimental conditions only require the addition of Cu(II) and NaOH aliquots to the serum/urine sample, followed by 1-3 hours of incubation at 55 °C. The blue emitting HSA-templated CuNCs allow detecting HSA with high sensitivity, selectivity, and reproducibility in serum and urine specimens without any pretreatment, except 1:300 dilution of serum in water. Serum dilution allowed the processing of serum and urine samples within the same calibration range, but could be tailored on the basis of specific testing requirements. The excellent analytical performances of the developed assay represent a valid alternative to current screening techniques, paving the route toward an effective and innovative method for HSA detection in clinical diagnostics.

5.3 Materials and Methods

5.3.1 Chemicals and Reagents

Copper sulfate ($CuSO_4$) and sodium hydroxide (NaOH) were from Thermo Fisher Scientific (Parma, Italy). Human serum albumin (HSA), human serum from male AB

(HS) and human IgG were purchased from Merck (Milan, Italy). Artificial urine (AU) was from LCTech GmbH (Obertaufkirchen, Germany). High Select™ HSA/Immunoglobulins (IgG, IgA, IgM, IgD, and IgE) Depletion Mini Spin Columns used for selectivity studies were from Thermo Fisher Scientific (Rodano, MI). The columns were used by following the manufacturer's instructions.

5.3.2 Methods and Instrumentation

HSA-CuNCs were synthesized in water, serum, or urine samples, by incubation at 55 °C (Thermomixer comfort, Eppendorf, VWR International, Milan). Fluorescence experiments were performed with Spectrofluorometer FP-6500 (Jasco, Easton, Pennsylvania, USA) and absorbance measurements were recorded by using Thermo Scientific™ Evolution™ 201/220 UV-Visible Spectrophotometer (Rodano, MI). Data management was performed by using OriginLab (Origin Pro 8.5.1) software. In order to define the proper excitation wavelength, λ_{ex} were scanned from 325 nm to 450 nm, by using an interval of 10 nm. Experimental conditions: 1.5 g L^{-1} HSA-CuNCs, wavelength range 200-650 nm, integration time 60 s, spectral bandwidth 1 nm, scan speed 100 nm min^{-1}. This step allowed us to establish the best conditions for fluorescence measurements, *i.e.* λ_{ex}= 325 nm and λ_{em}= 405 nm (emission bandwidth 5 nm, excitation bandwidth 5 nm, data pitch 1 nm, scanning speed 100 nm min^{-1}, sensitivity low). The same operative conditions were used for water, serum, and urine samples.

5.3.3 Assay principle

HSA-templated CuNCs were synthesized starting from the protocol proposed by Goswami et al.[113], with some modifications. 1 mL of 0.02 mol L^{-1} $CuSO_4$ water solution is added to 5 mL of standard HSA (15 g L^{-1} in water or matrix), obtaining a sudden turbid-light blue coloring. The solution is then stirred for 2 min at room temperature and then adjusted at pH 11.5 (30 µL, 5 mol L^{-1} NaOH), changing the color in limpid-purple. Subsequently, the sample is stirred at 500 rpm for 3 hours at 55 °C, showing finally a brown color. The fluorescent HSA-templated CuNCs do not require any purification step. All the measurements were performed at 25 °C in triplicates, at least. The same protocol is used for water, serum, and urine samples, except for 1:300 serum dilution in water, which permits it to work within the same calibration range for both the matrices. The linear trend of the assay in HS was first evaluated by the standard addition method, since it naturally contains physiological HSA (ca. 35-50 g L^{-1}). To this aim, a series of equal HS aliquots were prepared, adding to each a different concentration of HSA (standard in water, concentration range 0-0.50 g L^{-1}). The fluorescence emission intensity of the samples was measured in triplicate both just after the reaction ended (intraday variation) and for the three consecutive days (inter-day standard deviation), by subjecting the samples to a daily freeze/thaw cycle before fluorescence measurement.

5.4 Results and discussions

5.4.1 CuNCs synthesis and optical behavior

The experimental procedure optimized to synthesize HSA-CuNCs gave highly photoluminescent nanoclusters in an easy, quick, and cheap manner (Fig. 5.1). Advantageously, this protocol does not require purification steps or the use of reducing agents nor toxic substances as reported by other procedures [236,237]. This simplifies the detection of compounds of interest in complex biological matrices, such as urine, human serum, human blood, etc. The mechanism of nanoclusters formation involves principally amine-, thiol- and carboxyl groups of HSA that acts as template and triggers the formation and stabilization of the nanoclusters by using $-NH_2$ and -COOH groups for the coordination of Cu(II), while the –SH groups allow the reduction mediated by alkaline pH of copper ions to metallic Cu atoms, which aggregate in stable nanoclusters.

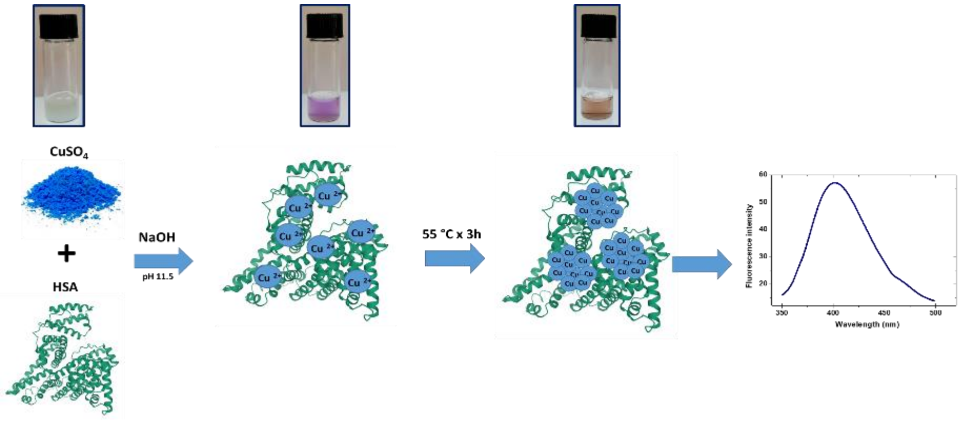

Figure 5.1. Schematic illustration of the experimental steps involved in HSA-CuNCs synthesis.

The absorption spectra of HSA-CuNCs obtained in water show a main peak at 280 nm, due to aromatic amino acids, and a second peak, weaker, at 325 nm, characteristic of copper nanoclusters, as previously reported [113] (Fig. 5.2). The absence of the characteristic localized surface plasmon resonance (LSPR) band of copper nanoparticles between 500 nm and 600 nm [238] confirms the effective formation of nanoclusters while avoiding the presence of bigger nanoparticles.

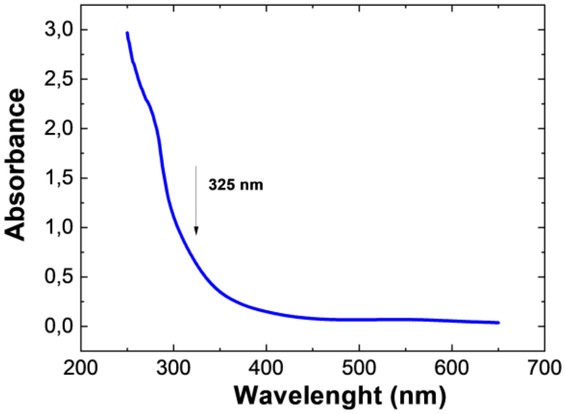

Figure 5.2. UV-vis absorption spectrum of HSA-CuNCs in water solution.

The maximum intensity of fluorescence emission (Fig. 5.3A) was obtained by using λ_{ex}=325 nm, with the emission peak centered at 405 nm, as reported elsewhere [113]. Accordingly, when the fluorescence at 405 nm was examined, the excitation spectrum of HSA-CuNCs exhibited a sharp peak at 325 nm, and both show a clear dose-response trend as a function of HSA concentration in solution (Fig. 5.3B). For this reason, all fluorescence measurements were performed employing λ_{ex} = 325 nm and λ_{em} = 405 nm. The smaller shoulder at about 375 nm, particularly evident at low analyte concentrations, is due to the Raman scatter peak, which depends on solvent and excitation wavelength [239].

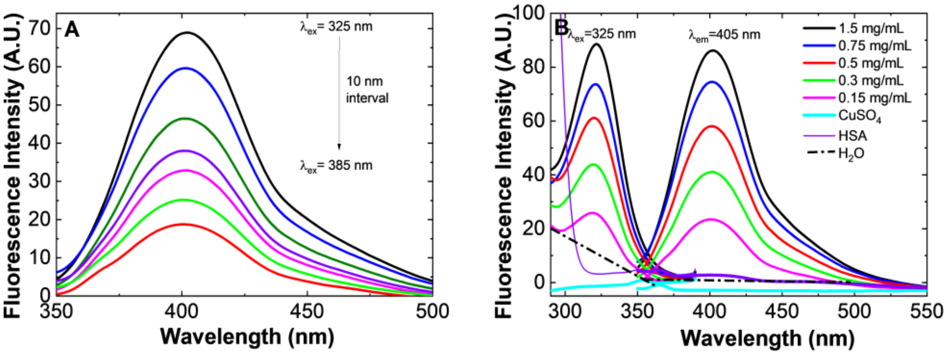

Figure 5.3. *HSA-CuNCs in water: A) emission spectra at different excitation wavelengths. B) emission and excitation spectra at different HSA concentrations. Dashed line is the blank sample (H_2O).*

5.4.2 Optimization of parameters for HSA detection

The photoluminescent properties of CuNCs strongly depend on the medium pH and, in particular, an alkaline pH is necessary for their formation. At pH 7.0, Cu(II) is reduced to Cu(I), which binds the protein structure to form the metalloprotein complex. Subsequently, when the pH is raised close to 12.0, copper ions are further reduced to metallic copper (Cu(0)) that leads to the initiation of the nucleation and growth of the clusters [113]. To optimize the CuNCs formation, the pH influence was carefully evaluated by preparing several aqueous HSA-CuNCs solutions at pH ranging from 9.0 to 13.0. The maximum luminescence signal was reached at pH 11.5 (see Fig. 5.4), presumably due to the enhancement of the reducing properties of albumin thiol groups, which promote the effective formation of copper nanoclusters. This pH value was thus kept for all the following experiments.

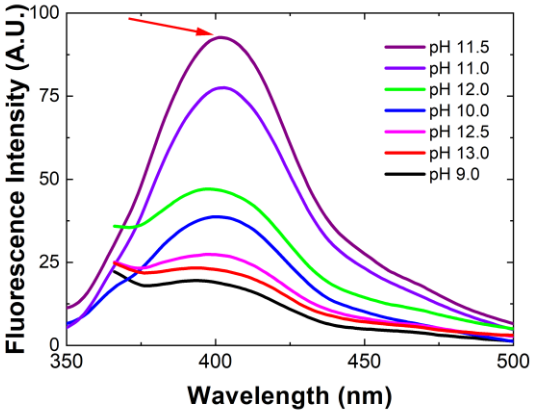

Figure 5.4. *Emission spectra of HSA-CuNCs in water solutions at different pH values, ranging from 9.0 to 13.0. The arrow indicates the maximum fluorescent signal corresponding to the pH adopted during the CuNCs synthesis.*

We also investigated the ability of the method in giving valuable responses in the shortest possible time with the aim to improve the current protocols in diagnosing and monitoring hypoalbuminemic and microalbuminuric patients. For this purpose, the Cu(II)/HSA mixtures were incubated from 1 to 7 h at 55 °C, monitoring the fluorescence signal evolution. As shown in Fig. 5.5, the highest fluorescent emission was obtained after 3 h, reaching a plateau stage for a longer incubation time, followed by a decrease of the signal around 7 h. Therefore, 3 h was chosen as the best incubation time for CuNCs formation, which is shorter than reaction times from 5 h to 8 h previously reported for HSA-CuNCs formation [240,241]. However, these results may foresee the possibility of shortening the incubation time to ca. 1 h, reinforcing the real applicability of the method in clinical settings. We also explored the possible influence of the stirring speed (200, 500, 1000 and 1400 revolutions per minute (rpm)) during the formation of the clusters, finding that this parameter does not affect the final CuNCs fluorescence intensity (data not shown). The CuNCs obtained with the optimized protocol show excellent fluorescence stability up to 4 months of storage at room temperature and/or after multiple freezing/thawing steps (data not shown).

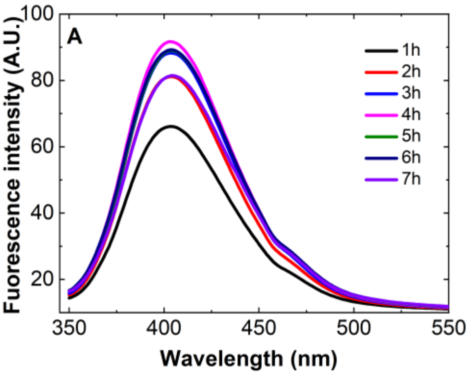

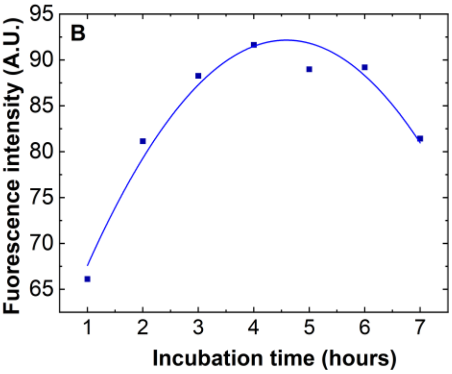

***Figure** 5.5. Time evolution of the fluorescence emission spectra during the CuNCs formation in water solution.*

5.4.3 Sensitive detection of human serum albumin

5.4.3.1 HSA detection in water solution

Preliminary studies were carried out in milliQ water in order to study the calibrator in ideal conditions. To this aim, the fluorescence spectra of HSA-CuNCs formed in solution upon different concentrations of HSA, were recorded (Fig. 5.6 A), showing the clear dose-response of the peak centered at 405 nm (with a minor shoulder at 460 nm) that was exploited to infer the standard HSA calibration within the range 0.03-1.50 g L^{-1} (Fig. 5.6 B). It shows a very well correlated (R^2 = 0.994) linear response (y = 96.6x-1.4) up to 0.5 g L^{-1} (Fig. 5.6 B), with a slight deviation at higher concentrations of HSA (data not shown). The limit of detection (LOD) obtained was 2.48 ± 0.07 x 10^{-3} g L^{-1} (LOD=3*SD_{blank}/slope), with an average coefficient of variation (CV_{av}%) of 5%.

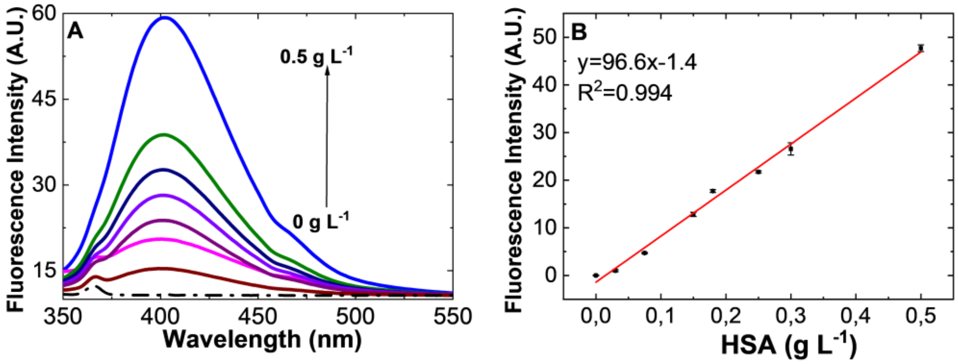

Figure 5.6. *HSA-CuNCs fluorescence in water: A) Emission spectra at different HSA concentrations. Dashed line is the blank sample (H_2O). B) Calibration plot of CuNCs fluorescence intensity at 405 nm versus HSA concentration after blank subtraction. The error bars represent the triplicate measurements (intraday standard deviation).*

The inter-day stability of HSA-CuNCs in water was also investigated. After CuNCs formation, the samples were stored at -20 °C, and then subjected to a 3-days of freeze/thaw cycles, giving the fluorescence data reported in Fig. 5.7A. The overall variability, expressed as CV_{av}% over all the data collected over the 3 days (7 concentration points for each calibration, each point in triplicate, see Fig. 5.7 B) resulted in 9%, confirming the good reproducibility of the measurements despite the freeze/thaw cycles the samples were subjected to. The overall recovery of fluorescence intensity at the second and the third day resulted in 92% and 70%, respectively, compared to the intraday results.

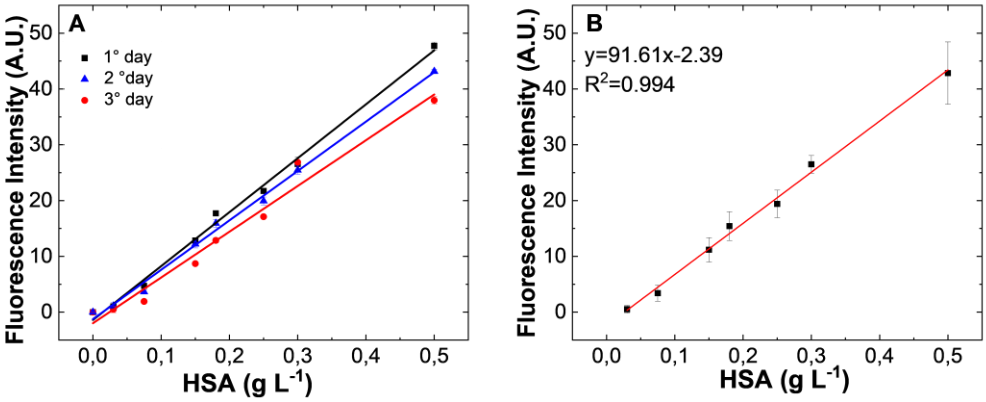

Figure 5.7. *Figure A) Calibration plots of HSA determination in milli Q water, over three different days (error bars represent the intraday triplicate measurements). B) Cumulative inter-day calibration curve*

corresponding to the average of the fluorescence measurements carried out over 3 different days (error bars represent the interday triplicate measurements). The relative calibration plots equation and R^2 are reported in Table 5.1. Fluorescence intensity values were obtained by the subtraction of blank fluorescence signal (H_2O).

Table 5.1 *Calibration plots equation and R^2 values of calibration plots reported in Figure5.7.*

		Calibration plot equation	***R^2 values***
Figure 5.7 A	***1° day (black)***	*y=96.6x-1.4*	*0.994*
	2° day (blue)	*y=88.5x-1.2*	*0.994*
	3° day (red)	*y=82.0x-2.0*	*0.970*
Figure 5.7 B	***Cumulative 1°-3° days***	*y=91.6x-2.4*	*0.994*

5.4.3.2 HSA detection in human serum

The blue emitting HSA-CuNCs were successfully applied to albumin quantification in untreated human serum (except 1:300 water dilution), where HSA values lower than 35 g L^{-1} define a pathological state known as hypoalbuminemia [225]. The patients suffering from analbuminemia, in which the HSA level is less than 1 g L^{-1}, are rare [225]. However, both hypoalbuminemia and analbuminemia may be signs of severe liver, kidney, or gastrointestinal diseases, as well as cancer evolution [242–244], and all require the accurate determination of albumin. Albumin is the most abundant protein in human serum with physiological concentrations generally between 35 - 50 g L^{-1} [225]. Therefore, to obtain its absolute estimation, we first applied the standard addition method to assess the linear dose-response trend in the matrix. Due to the high albumin concentration in human serum with respect to our calibration range, a 1:300 dilution of the serum sample is preliminary performed. Then, known increasing concentrations of standard HSA were spiked (0.03 – 0.50 g L^{-1} final concentration range) to six aliquots of the same serum sample. CuNCs formation was finally carried out simultaneously on all the aliquots following the protocol optimized in water, and the fluorescence responses were recorded (Fig. 5.8). Also in this case, we confirmed the presence of a well-defined peak centered at 405 nm (with a minor shoulder at 460 nm). As evidenced in water, the overall optical response is thus related to the endogenous HSA in the sample plus the contribution of the spiked standard HSA. An excellent linear correlation ($R^2 = 0.999$) allowed us to fit the data and extrapolate the concentration of serum HSA, which resulted in 48.0 ± 1.8 g L^{-1}. The CV_{av}% resulted in 3%, highlighting the excellent reproducibility of the proposed assay.

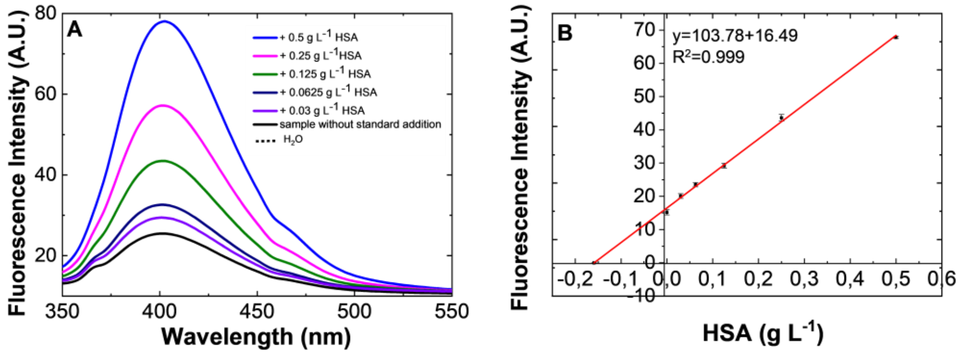

Figure 5.8. HSA-CuNCs in human serum: A) Emission spectra at different HSA concentrations. Dashed line is the blank sample (HSA-depleted serum). B) Calibration plot corresponding to the quantitative determination of HSA by using the standard addition method. Fluorescence intensity values, in the calibration plot, were obtained by the subtraction of blank fluorescence signal (HSA-depleted serum). The error bars represent the intraday standard deviation calculated on three replicates.

The inter-day variability of the method was estimated over three days, as previously performed in water, to assess the possibility of storing the processed serum samples until the analysis (Fig. 5.9).

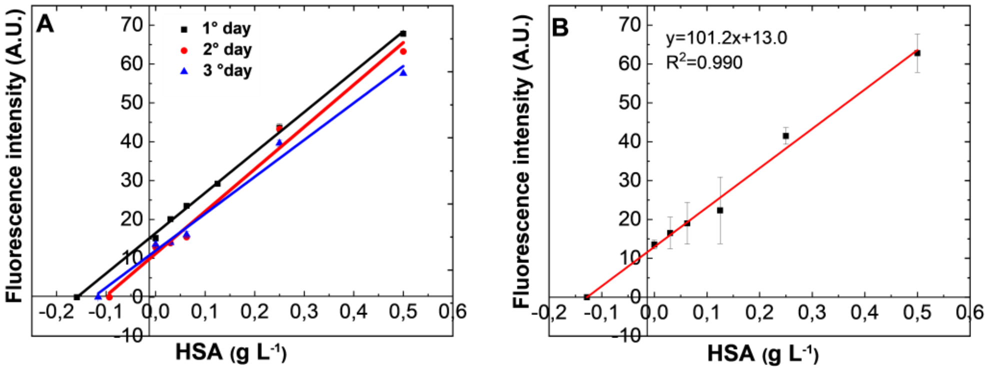

Figure 5.9. A) Calibration plots of HSA determination in human serum, over three different days (error bars represent the intraday triplicate measurements). B) Cumulative inter-day calibration curve corresponding to the average of the fluorescence measurements performed in 3 different days (error bars represent the interday triplicate measurements). The relative calibration plot equation and R^2 are

reported in Table 5.2. Fluorescence intensity values were obtained by the subtraction of blank fluorescence signal (HSA-depleted serum).

Table 5.2 *Calibration plots equation and R^2 values of calibration plots reported in Figure 5.9.*

	Day	***Calibration plot equation***	***R^2 values***
Figure 5.9 A	***1° day (black)***	*y=103.8x+16.5*	*0.999*
	2° day (red)	*y=108.6x+11.2*	*0.982*
	3° day (blue)	*y=94.9x+12.0*	*0.985*
Figure 5.9 B	***Cumulative 1°-3° days***	*y=101.2x+13.0*	*0.990*

In this case, the overall CV_{av}% averaged on all the collected data resulted significantly higher than that obtained in water (19%), although the most marked effect of signal decrease was observed between the first and second day. Due to the complexity of the matrix, the observed progressive decrease could be reasonably ascribed to some serum components that interfere with fluorescence stability over time. However, data up to 0.25 g L^{-1} of the second and the third day show recovery values on all the concentrations of 80% and 73%, respectively. This could indicate a stabilization of the fluorescence after the first 24 h and/or the first freeze/thaw cycle, that should be investigated for longer times. The selectivity of the CuNCs-based fluorescent assay was first tested by considering that the protein portion of human serum other than albumin is predominantly composed of immunoglobulins. Therefore, we reproduced the assay on immunoglobulin solutions to assess the absence of their contribution in the final fluorescent signal. Fig. 5.10A shows that the fluorescent spectra recorded in the IgGs solutions are comparable to a blank solution. Moreover, we have excluded possible interference due to other matrix components by using separation columns to remove HSA and immunoglobulins from samples and also such depleted samples have given negligible response (see Fig. 5.10B), confirming the selectivity of the method.

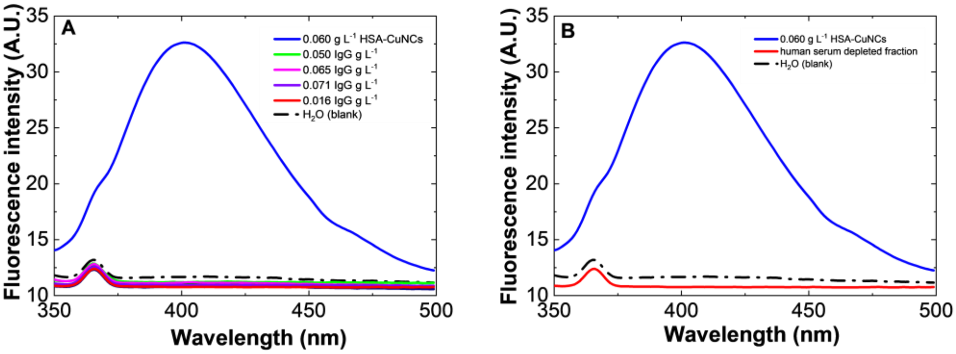

Figure 5.10. *A) Fluorescent spectra of different IgG concentrations in comparison with HSA-CuNCs fluorescent emission signal (blue line). B) Spectrum of samples obtained after separation of diluted human serum (1:300) on High Select™ HSA/Immunoglobulin Depletion Mini Spin Columns. The depleted fraction of human serum (red line), in which HSA and immunoglobulins were removed, did not show fluorescence at 405 nm characteristic of HSA-CuNCs solution (blue line), appearing superimposable to milli Q water (blank) emission response (black dashed line).*

5.4.3.3 HSA detection in urine

Albuminuria consists in release of a large quantity of albumin in urine as a consequence of kidney damage. The mild form of albuminuria is known as microalbuminuria and is characterized by low HSA values in urine, *i.e.* 0.02-0.2 g L^{-1}, whereas higher values are associated with the severe condition called macroalbuminuria [5]. Cardiovascular and kidney diseases, such as hypertension and diabetes mellitus, are closely related to micro and macroalbuminuria [5, 6]. To demonstrate the applicability of the method also to the urine matrix, artificial urine samples were added with increasing standard HSA concentrations, and the CuNCs growth was conducted as above for water and serum. Differently from serum, urine does not contain physiological HSA, therefore a classical dose-response calibration was carried out by testing urine samples fortified with HSA in the range 0.01-0.50 g L^{-1} (Fig. 5.11). Fig. 5.11 A displays the intensity evolution of CuNCs fluorescence upon HSA increase. Differently from water and serum, spectra recorded in urine show two minor peaks at higher wavelengths with respect to the main emission peak (Fig. 5.11A).

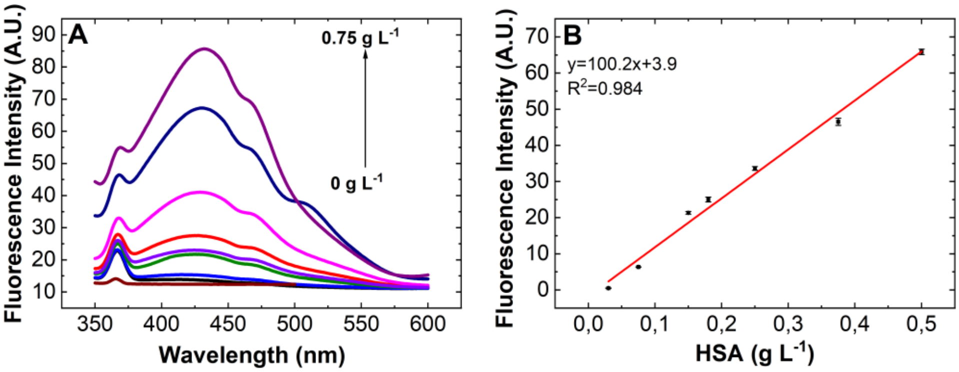

Figure 5.11. *HSA-CuNCs in artificial urine: A) Emission spectra at different HSA concentrations. Dashed line is the blank sample (unspiked urine). B) Calibration plot of standard HSA in artificial urine. Fluorescence intensity values were obtained by the subtraction of the blank (unspiked urine). The error bars represent the triplicate measurements (intra-day standard deviation)*

Moreover, the latter appears red-shifted to ca. 425 nm, likely due to the fact that in this case the matrix is not subjected to dilution in water as above reported for serum. The calibration curve, described by the equation y = 100.2x + 3.9, correlates with a R^2 value of 0.984 giving a LOD of 0.62 ± 0.03 x 10^{-3} g L^{-1} and a CV_{av}% = 3%. The best linear correlation was obtained up to 0.50 g L^{-1}, after that a loss of linearity is clearly visible (data not shown). Considering the clinical range of interest, the assay showed its ability in detecting with high precision and accuracy even microalbuminuria condition. The inter-day standard deviations display an averaged calibration curve with a very similar trend and a CV_{av}% of 10 % (Fig. 5.12). The recovery efficiency, inferred by comparing the fluorescence responses obtained over the three days, resulted in 98% and 90% for the second and the third day, respectively.

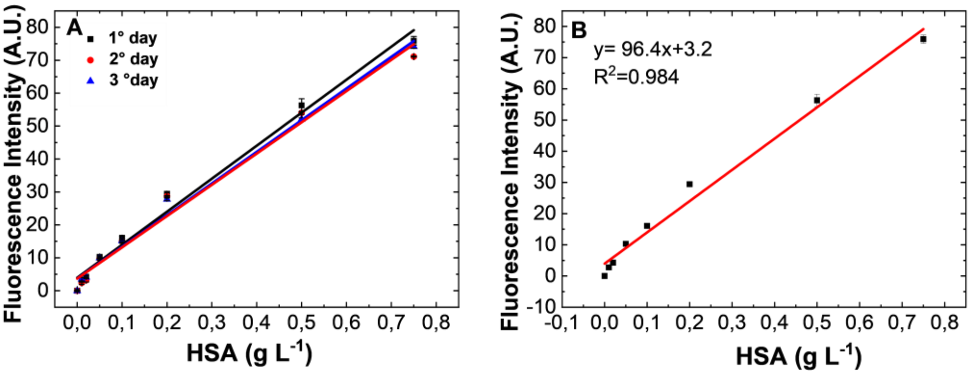

Figure 5.12. *A) Calibration plots corresponding of HSA determination in urine, over three different days (error bars represent the intraday triplicate measurements). B) Cumulative inter-day calibration curve corresponding to the average of the fluorescence measurements performed over 3 different days (error bars represent the interday triplicate measurements). The relative calibration plot equation and R^2 are reported in Table 5.3..*

Table 5.3. *Calibration plots equation and R^2 values of calibration plots reported in Figure 5.12.*

	Day	***Calibration plot equation***	***R^2 values***
Figure 5.12 A	***1° (black)***	*y=100.2x+3.9*	*0.984*
	2° (red)	*y=94.9x+3.7*	*0.980*
	3° (blue)	*y=96.2x+3.7*	*0.988*
Figure 5.12 B	***Cumulative 3 days***	*y=94.4x+3.2*	*0.984*

5.4.3.4 Performance of the assay in serum and urine

To reinforce the validity of the developed method, we compared the dose-response curves obtained in both the matrices by testing a serial dilution of serum and urine containing the same HSA content (serum and urine absorbance and fluorescence spectra are reported in Fig. 5.13).

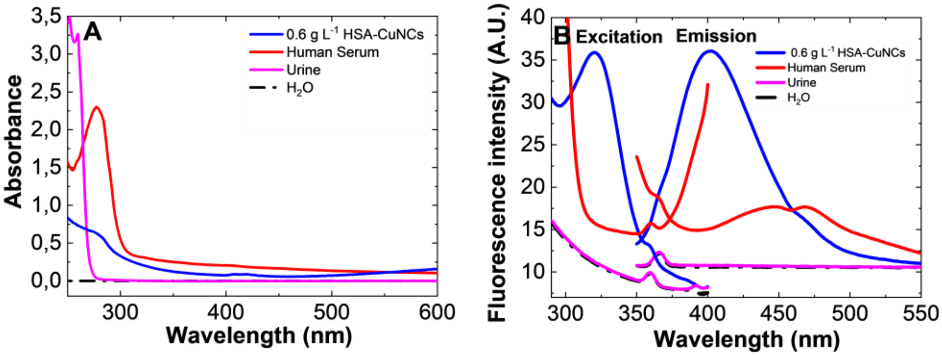

Figure 5.13. *A) Absorbance spectra of: HSA-CuNCs (blue line) where the peak at 320 nm (due to CuNCs formation, see Section 3.1) and 280 nm (due to aromatic compounds) were observed; human serum (red line, diluted 1:300) where the peak due to aromatic amino acid at 280 nm appeared; urine (pink line) and water (black dashed line). B) Fluorescence spectra of: HSA-CuNCs (blue line) in which the emission and the excitation peak are clearly illustrated; human serum (red line, diluted 1:300); urine (pink line) and water (black dashed line). Note as the analyzed matrices, urine and human serum, does not interfere under UV light used as excitation wavelength (325 nm).*

In the case of HS, we diluted a sample of known HSA concentration to 0.50 g L^{-1}; to directly compare the responses, an undiluted aliquot of urine was spiked with the same HSA concentration and the same serial dilutions were performed and tested for both the matrices. As reported in Fig. 5.14, a very good overlapping of the dynamic ranges over the tested conditions is found within the whole range of concentration. In these conditions, the limit of detection in serum can be also directly extrapolated, resulting in 1.8 ± 0.1 x 10^{-3} g L^{-1} , with a CV_{av}%=3%. This result enables HSA detection at concentrations lower than those achieved by reference techniques [245,246]. In addition, recovery has been calculated for all the urine and human serum spiked samples by comparison with the calibration curve of HSA in milli Q water. A recovery value of 95 % for human serum and of 96 % for urine were obtained.

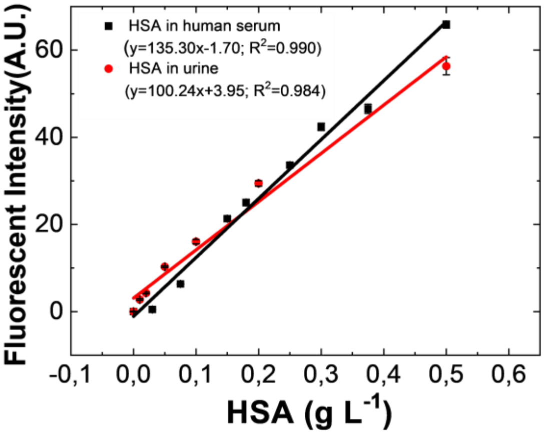

Figure 5.14. *Analytical performance of HSA detection assay in human serum (black line) and urine (red line). The respective blanks (HSA-depleted serum for HS, and unspiked urine for urine samples) were subtracted to the fluorescence signals. Fluorescence values are reported as the mean value ± intraday standard deviation) calculated on three replicates.*

5.4.3.5 Assay performance compared to other nanomaterials-based methods

The CuNCs-based assay developed was finally compared to other nanomaterial-based methods reported in literature for HSA detection (Table 5.4). Despite the declared LODs referred to standard solutions display better performances in all the cases, no information about the performances obtained in human serum and urine is reported (except for Huang et al.[247]), and none of them shows the possibility of applying the assay to both the matrices by the same protocol. Since from a clinical point of view the lowest concentration of interest for HSA in urine (in serum the interest goes to the relative variation of physiological levels) is around 0.02 g L^{-1}, the reported LODs play a marginal role in the evaluation of a realistic application of the method for clinical purposes. Moreover, some detection methods, such as SERS and ELSD, are far from being considered simple since they require multiple synthesis steps for the nanomaterials involved in the protocol and expensive instrumentation. Finally, a CuNCs-based platform is cheaper than gold- and silver-based nanomaterials, since Cu(II) salts are less expensive than the relative Au(III) and Ag(I) ones. In this framework, the assay here developed allows us to achieve a step forward in its application in clinical settings.

Table 5.4. *Nanomaterial-based methods for the determination of HSA .*

Probe	**Method**	**LOD**	**Speci-ficity**	**Matrix**	**Referen-ces**
HSA-templated copper nanoclusters (CuNCs)	Spectro-fluorimetry	$2.48 \pm 0.07 \times 10^{-3}$ g L^{-1} (in H_2O); $1.8 \pm 0.1 \times 10^{-3}$ g L^{-1} (in human serum) $0.62 \pm 0.03 \times 10^{-3}$ g L^{-1} (in urine)	Yes	Artificial urine Human serum	This work
Poly(thymine)-templated copper nanoparticles (CuNPs)	Spectro-fluorimetry	8.2×10^{-11} g L^{-1} (in buffer solution)	Yes	Human serum	[235]
Gold Nanoparticles (AuNPs)	Colorimetry	9.3×10^{-5} g L^{-1} (in urine)	Yes	Artificial Urine	[247]
Gold “pearl necklace” (Au PNNs)	Surface-enhanced Raman scattering (SERS)	4.6×10^{-6} g L^{-1} (in buffer solution)	Yes	Artificial Urine	[248]
Nanoporous gold (NPG)	SERS	0.1×10^{-9} g L^{-1} (in buffer solution)	-	-	[249]

Gold Nanorods (AuNR)	Surface Plasmon resonance (SPR)	-	-	Artificial Urine	[250]
AuNPs	Evaporative light scattering detection (ELSD)	21.0 ng (in buffer solution)	-	Human serum	[251]
Silver Nanoparticles (AgNPs)	Localized surface plasmon resonance (LSPR)	1.0×10^{-6} g L^{-1} (in buffer solution)	Yes	Urine	[252]

5.4.3.6 Conclusions

A novel CuNCs-based assay for the fluorescent detection of HSA in urine and human serum is reported. Both the matrices are successfully analyzed by the same protocol, without significant pretreatment (except for a 1:300 dilution of serum in water), and high selectivity. The whole protocol is performed within 3 hours, but it could be further reduced down to one hour, in line with clinical requirements. The sensitivity of the CuNCs-based assay resulted higher than other diagnostic methods, *i.e.* 0.03-1.00 g L^{-1} in serum, and 0.01-0.75 g L^{-1} in urine, with excellent intraday variability (3%). Despite at this development stage we have demonstrated its applicability to reinforced matrices, we foreseen that the method could be further validated for its application in clinical diagnostics with improved accuracy, shorter times, and very low costs with respect to current available assays. To the best of our knowledge, this is the first example of an assay for HSA able to work in serum and urine without the need of a matrix-dependent protocol and very similar analytical performances.

6

Fluorescence molecules for diagnostic purposes and bioanalytical applications

In the previous chapter, the importance of nanostructures in bioanalytical applications was highlighted. Especially, in the diagnostic field, where efficient alternative and innovative analysis methods could lead significant improvement in the healthcare system. The diagnostic purposes fueled the development of this thesis. In this regard, an interesting novel fluorescent material was investigated. Above, it was shown as the photoluminescence properties of CuNCs were exploited to determine HSA concentrations in human biological fluids in order to identify albuminuria cases. Fluorescent nanomaterials are increasingly used due to their photostability and the possibility to cover a wide range of emission wavelengths changing size or chemical composition of the nanomaterial. Nanoparticles, nanoclusters, and quantum dots are frequently used as fluorophores for their relevant luminescence [60]. However, it is not always easy to use NMs as fluorophores since they often require huge and long synthetic protocols. Contrarily, most fluorescent molecules or fluorescent dyes do not need to be synthesized. They are often available in nature and, consequently, they are among the most immediately available fluorophores.

6.1 Fluorophores

Fluorescent dyes are a relevant diagnostic tool and an active part of the healthcare system. For example, fluorescence-based diagnose are fast and noninvasive methods which employ endogenous (*e.g.* aromatic amino acids) or exogenous (*e.g.* porphyrins) molecules for imaging of precancerous and cancerous tissues in many locations [253]. These methods are applied in many fields like oncology, dermatology, laryngology, pulmonology, gynecology, and gastroenterology. Fluorescent compounds work as sensing probes not only for imaging techniques but also to identify and quantify a wide range of target molecules, from small analytes *e.g.* small ions [254] or drugs [255] to high dimension molecules like biomolecules [256] or cells [257]. This is feasible thanks to the high intrinsic sensitivity of fluorescence compared to other techniques that rely on light absorption measurements. This phenomenon is explained by the different excitation and emission wavelengths that enable it to completely filter out the excitation light without blocking the emitted fluorescence. It is for this reason that fluorophores are applied in many areas of study in which low detection limits are necessary.

In the planning of bioanalytical fluorescent assays, it is crucial to previously know the specific excitation and emission wavelength of the fluorophore. This guarantees the sensitive detection of the target under examination. Another important factor that influences the detection strategy is the photostability and phototoxicity of the fluorescent dye. The first refers to the ability to preserve fluorescence (*i.e.*, to resist photobleaching) after cycles of excitation and emission. Instead, phototoxicity involves the production of toxic species after the exposure to low or high wavelength lights used. This phenomenon usually leads to reactive oxygen species that could damage the analyzed human samples.

The most common synthetic fluorescent dyes are rhodamine-B, cyanine (Cy3 and Cy5), fluorescein isothiocyanate (FITC), tetramethyl rhodamine-isothiocyanate (TRITC) and variations of Alexa Fluor® [60]). Many varieties of fluorescent proteins, obtained by using biotechnology techniques, are also widely diffused as fluorescent probes. They cover a large photoluminescence spectrum that ranges from green to blue, red, and yellow. An example is represented by the green fluorescent protein (GFP), the first fluorescent protein to be described and one of the most used in cell studies. Frequently, fluorescent dyes are conjugated with other molecules, such as antibodies, allowing the detection of the target structure or molecule. In this case, the detection of the analyte is performed indirectly. Therefore, the non-fluorescent molecule is analyzed after being detected upon specific interaction with a fluorophore dye. For example, ethidium bromide intercalates DNA duplexes and RNA molecules, generating a measurable signal.

It must be taken into account that the use of a synthetic dye is not always the best choice when a bioanalytical assay is developed. The primary reason is due to the high cost of synthetic fluorophores. In addition, fluorescence probes are commonly toxic molecules. On the other hand, the ability to generate fluorescence is not common in all molecules because their structure may preferably allow for energy loss in a non-radiative pathway after light excitation. However, such compounds that have resonant ring structures, like aromatic molecules, exhibit incredible spontaneous fluorescence properties. These molecules are also known as intrinsic or natural fluorophores. Intrinsic protein fluorescence originates from the aromatic amino acids tryptophan, tyrosine, and phenylalanine. The indole groups of tryptophan residues are the dominant source of UV absorbance and emission in proteins. The indole ring plays an important photochemical and photobiological role in the photoreactions of proteins.

In this study, the fluorescence properties of an indole derivative compound, serotonin, were thoroughly investigated. The unexpected emission signal of this compound was exploited to develop a fluorescent-based detection strategy able to determine copper concentration and to facilitate the diagnosis of copper-dependent diseases.

7

Serotonin-derived fluorophore: a novel fluorescent biomaterial for copper detection in urine

7.1 Abstract

We took advantage of the fluorescent features of a serotonin-derived fluorophore to develop a simple and low-cost assay for copper in urine. The quenching-based fluorescence assay linearly responds within the concentration range of clinical interest in buffer and in artificial urine, showing very good reproducibility ($CV_{av}\% = 4\%$ and 3%) and low detection limits (16.33 ± 0.72 µg L^{-1} and 22.56 ± 1.00 µg L^{-1}). The Cu(II) content was also estimated in human urine samples, showing excellent analytical performances ($CV_{av}\% = 1\%$), with a limit of detection of 59.14 ± 3.41µg L^{-1}, and a limit of quantification of 96.97 ± 11.36 µg L^{-1}, which are below the reference value for pathological Cu(II) concentration. The assay was successfully validated through mass spectrometry measurements. To the best of our knowledge, this is the first example of copper ions detection exploiting the fluorescence-quenching of a biopolymer, offering a potential diagnostic tool for copper-dependent diseases.

Keywords: serotonin, urine analysis, fluorescence quenching, copper detection, copper-dependent diseases, copper poisoning.

7.2 Introduction

Herein, we propose a first example of the potential diagnostic applicability of a novel fluorescent biomaterial derived from serotonin (SE), a neurotransmitter involved in multiple important physiological processes like memory, learning, anxiety, depression, cognition, vomiting, and vasoconstriction [258]. Very few studies describe the formation of serotonin (SE) oligomers [259–262], including polyserotonin (PSE) obtained using horseradish peroxidase (HRP) [262], and serotonin-based nanoparticles (PSE-NPs) [259,260], as multifunctional material for free radical scavenging, bioelectrical, and biomedical applications. In this paper, the highly emitting SE-derivative fluorophore (SEDF, $\lambda_{ex,}$= 350 nm, λ_{em}= 450 nm) was obtained simply by heating the scarcely-fluorescent SE monomer at alkaline pH (Fig. 7.1A). SEDF was characterized by means of UV-Vis spectroscopy and mass spectrometry (matrix-assisted laser desorption/ionization-time of flight mass spectrometry, MALDI-TOF/MS). The fluorescent properties of SEDF were outstanding also compared with polymers obtained by using other endogenous neurotransmitters (polydopamine and polynorepinephrine) [263,264], stimulating the development of a fluorescence quenching-based bioanalytical method for the determination of copper in human urine. The concentration of copper ions in the human body regulates many physiological functions, acting as a cofactor of numerous enzymes, *e.g.*, dopamine β-hydroxylase, tyrosinase and cytochrome c oxidase [265]. Copper contributes to cellular and tissue growth, working also as an antioxidant [266]. However, an excess of this heavy metal leads to protein structure modification, interfering with the exchange of zinc in metalloproteins, and compromising most cellular functions [267]. Recently, it was demonstrated that an accumulation of Cu(II) affects the activity of dopaminergic neurotransmitters, potentially leading to neurodegenerative disorders like Parkinson’s and Alzheimer’s disease [268,269] and mental issues, including anxiety, depression, language and cognitive impairment [270]. Accordingly, there is always the need for sensitive detection of copper ions in biological fluids. The fluorescence quenching-based bioassay, here developed, allowed the detection of Cu(II) in human urine without any pretreatment of the real matrix. The analytical performances of the fluorescence detection strategy were firstly evaluated by determining Cu(II) in buffer and in artificial urine. Then, based on these results, we proceeded to determine Cu(II) concentration in human urine samples obtaining excellent repeatability of the measurements ($CV_{av}\% = 1\%$) and a LOQ value of 96.97 ± 11.36 $\mu g\ L^{-1}$ which would be sufficient to detect the early stage of diseases associated with Cu(II) accumulation, such as chronic liver disease, acute hepatitis, and, primarily, Wilson's disease (WD), a rare inherited disorder that can lead to excess storage of copper in the liver, brain, and other organs [271,272]. In particular, patients who suffer from WD have high urinary copper values between c.a. 200 to 400 µg per day [273,274]. Values of Cu(II) higher than 100 µg per day are strongly indicative of this disease [272]. Common diagnostic assays for WD are based on ceruloplasmin (Cp) concentration and, on hepatic and urinary Cu(II) detection [272,275]. However, the Cp test is inaccurate in free Cu(II) estimation, whereas the evaluation of hepatic copper requires an invasive procedure and, often, the heterogeneous Cu(II) distribution within the liver leads to false negative results. Differently, the experimental procedure here developed for copper estimation would be non-invasive, fast, very simple, green and low-cost, if compared to reference instrumental approach for copper quantification in urine samples, such as inductively coupled plasma mass spectrometry (ICP-MS) [276], here used to validate the fluorescence method. We propose a valid alternative to the current analytical diagnostic techniques for copper-dependent diseases. In addition, SEDF, here described for the first time, appears as a promising biomaterial for many future applications.

7.3 Materials and methods

7.3.1 Chemicals and Reagents

Serotonin ($C_{10}H_{12}N_2O$), tris(hydroxymethyl)aminomethane ($C_4H_{11}NO_3$), sodium hydroxide (NaOH), hydrochloric acid (HCl), sodium chloride (NaCl), potassium chloride (KCl), lithium chloride (LiCl), and magnesium chloride ($MgCl_2$) were obtained from Thermo Fisher Scientific (Parma, Italy). Barium chloride ($BaCl_2$), copper sulfate ($CuSO_4$), bismuth (III) nitrate ($Bi(NO_3)_3$ x $5H_2O$), aluminum chloride ($AlCl_3$), zinc (II) sulphate ($ZnSO_4$ x $7H_2O$), cadmium (II) sulfate ($CdSO_4$ x $8H_2O$), mercury chloride ($HgCl_2$), silver chloride (AgCl), gold(III) chloride ($HAuCl_4$ x $3H_2O$), nickel(II) chloride ($NiCl_2$ x $6H_2O$) chloroplatinic acid solution (H_2PtCl_6), Palladium (II) oxide (PdO), iron (III) chloride ($FeCl_3$ x $6H_2O$), potassium permanganate ($KMnO_4$), potassium chromate ($K_2Cr_2O_7$), cobalt (II) chloride ($CoCl_2$ x $6H_2O$), ruthenium (IV) oxide (RuO_2), acetonitrile (C_2H_3N), DHB (2,5-Dihydroxy Benzoic acid, $C_7H_6O_4$), glutamic acid (1 μM, $C_5H_9NO_4$), glucose (2 μM, $C_6H_{12}O_6$), ascorbic acid (2 μM,$C_6H_8O_6$), hypoxanthine (9 μM, $C_5H_4N_4O$), uric acid (4.5 μM, $C_5H_4N_4O_3$), creatinine (4 μM, $C_4H_7N_3O$), urea (0.5 M, CH_4N_2O), sodium citrate (2 μM, $Na_3C_6H_5O_7$), trifluoroacetic acid (TFA, $C_2HF_3O_2$), quinine sulfate ($C_{40}H_{50}N_4O_8S$), and sulfuric acid (H_2SO_4) were purchased from Merck (Milan, Italy). Artificial urine (AU) was from LCTech GmbH (Obertaufkirchen, Germany).

Urine samples: the assay was tested on human urines (see ethical standard*). Samples were chosen among those destined for destruction at the Clinical Pathology Laboratory of the University Hospital in Pisa and pseudonymized. Spiked samples were eventually obtained and tested. Fluorescence measurements and ICP-MS experiments on urine samples were performed in the Clinical Pathology Laboratory of the University Hospital in Pisa.

7.3.2 Methods and Instrumentation

Temperature-controlled synthesis reaction of SEDF was performed by using Thermomixer comfort (Eppendorf, VWR International, Milan). Fluorescence experiments were performed with fluorometer FP-6500 (Jasco, Easton, Pennsylvania, USA) by using as excitation and emission wavelength λ_{ex}= 350 nm and λ_{em}= 450 nm, respectively (emission bandwidth: 10 nm; excitation bandwidth: 5 nm; data pitch: 1 nm; scanning speed: 100 nm min^{-1}; sensitivity: low) and microplate readers Fluoroskan Ascent (Thermo Fisher Scientific, Milan) by selecting as filter pair λ_{ex}= 390 nm and λ_{em}= 460 nm corresponding to excitation and emission wavelengths, respectively. The absorbance measurements were obtained by using SPECTROstar^{nano} UV-Visible Spectrophotometer (Ortenberg, Germany) in 1.0 cm quartz cells at 20 °C. MALDI-TOF spectrometry measurements were performed with MALDI-TOF/TOF Ultraflex III (Bruker Daltonics, Milan) mass spectrometer. Mass measurements were performed by mixing the samples in 1:1 ratio with 20 ng μL^{-1} DHB (2,5-Dihydroxy

Benzoic acid) as matrix dissolved in 70 % of acetonitrile, 25 % trifluoroacetic acid and 5 % ethanol. Mass spectra were acquired in positive-ion mode.

Serotonin-derived fluorophore was synthesized in a few easy steps. 2 g L^{-1} of serotonin solution were prepared in a 10 mM TRIS buffer pH 9.00. Then, the sample was heated at 60 °C for 2 h. After the synthesis reaction at a controlled temperature, the sample was left for 10 min at room temperature, then centrifuged 2 times for 10 min at 10000 g, and the supernatant was finally collected and stored at 4 °C after the addition of 5 mM HCl.

The fluorescence quantum yield (Q.Y.) of SEDF was estimated by using quinine sulfate dissolved in 0.1 M H_2SO_4 as a fluorescence reference standard of known quantum yield (QY_{ref}), as reported by Lakowicz [277]. The quantum yield of SEDF was calculated using the following equation:

$$QY = QY_{ref} \frac{\eta^2}{\eta_{ref}^2} \frac{I}{A} \frac{A_{ref}}{I_{ref}}$$

where η is the refractive index of the solvent, I is the integrated fluorescence intensity and A is the absorbance at the excitation wavelength of SEDF. The subscript r*ef* indicates the same parameters for the reference fluorophore, in this case quinine sulfate. The absorbances at the wavelength of excitation (350 nm) were kept at A=0.05 in order to avoid inner filter effects and ensure linear response on the intensity.

Copper concentration was estimated via a fluorescence quenching-based method. Stock Cu(II) solutions were prepared in 10 mM Tris pH 9.00 and in artificial urine. Then, different volumes of copper solution were added to the serotonin-derived fluorophore solution, that is the reactant solution. The solution was mixed, and the fluorescence signal recorded. The decrease of fluorescence in dependence of copper concentration was expressed as F_0/F, where F_0 is the fluorescence of serotonin-derived fluorophore without any metal addition and F is the fluorescence recorded after the copper addition, in buffer, artificial urine, and real urine samples.

The validation of the quenching-based method was performed by determining Cu(II) content in urine samples by using Agilent Technologies 7900 ICP-MS (Santa Clara, CA, USA), equipped with an ASX-500 Series autosampler and a peristaltic pump for sample injection. The analyses were preceded by autotuning, which is an automated software routine that can optimize instrumental parameters to obtain the maximum level of sensitivity correlated with the maximum performance in terms of polyatomic interferences removal, and the acquisitions made use of the following parameters: carrier gas flow rate 0.80 L min^{-1} (Ar), Aerosol dilution flow rate 0.50 L min $^{-1}$ (Ar), plasma gas flow rate (15 L min^{-1} (Ar)), collision gas flow rate 4.3 x 10^{-3} L min^{-1} (He), RF power 1550 W, stabilization time 20 s, peak pattern 3 point, replicates 3, sweeps per replicate 100, peristaltic pump speed 0.1 rps. System control and data acquisition and processing were carried out by the MassHunter 5.1 Workstation® version software. For the pre-analytical procedure a 10000 µg L^{-1} stock solution of Agilent TraceCERT® standard mix, including copper (63Cu), was diluted in deionized water to prepare an initial calibration curve ranging from 0 to 2500 µg L^{-1}. The curve was then diluted 1:10 using a dilution solution made of water: 1-butanol=98.5:1.5 added with Triton X100 (Sigma Aldrich), 10 µl L^{-1}, and Tetramethylammonium hydroxide (TMAH, Sigma Aldrich), 100 µl L^{-1}, to achieve the final range of 0 - 250 µg L^{-1}. The calibration points were: 0 – 0.1 – 0.2 – 0.5 – 1 – 2 – 5 – 10 – 20 – 50 – 100 – 200 – 250 µg L^{-1}. Each calibration point was added with the appropriate amount of an internal standard mix to achieve the same final concentration in both the submitted samples and in the curve. Two quality control points were added to attest the accuracy of the analysis. Urines, previously centrifuged at 1230 rcf for 15 min to remove the sediment, were analyzed diluted 1:100 in the dilution solution and added with the appropriate amount of the internal standard mix. The internal standard used for the quantification of copper in these samples was Germanium (72Ge).

7.4 Results and discussions

7.4.1 Process optimization for synthesis of serotonin-derivative

We obtained a fluorescent serotonin-derived fluorophore (SEDF) upon the self-oxidation of the serotonin monomer heated at 60 °C for 2 h at pH 9.00 (Fig. 7.1)[259]. The supernatant exhibited outstanding photoluminescence properties after the optimization of several experimental parameters such as pH, reaction time, and starting monomer concentration. In detail, the influence of pH was evaluated between 2.00 and 12.00. Solutions of SEDF excited at 350 nm showed spectra with a λ_{max} about 400 nm at pH 2.00-4.00, 425 nm at pH 6.00-7.00, and 450-475 nm at pH 8.00-12.00. The intensity of fluorescence emission λ_{em}= 450 nm was strongly reduced at pH below 6.00 or above 11.00 (see Figs. 7.1B and 7.1C). Moreover, highly basic conditions led to heterogeneous mixtures (Fig. 7.1D) with large scattering phenomena (data not shown). Among the other pH conditions enabling the spontaneous oxidation of SE, the mild alkaline buffer at pH 9.00 gave the best reproducibility, as evident from the lower standard deviation values (Fig. 7.1C).

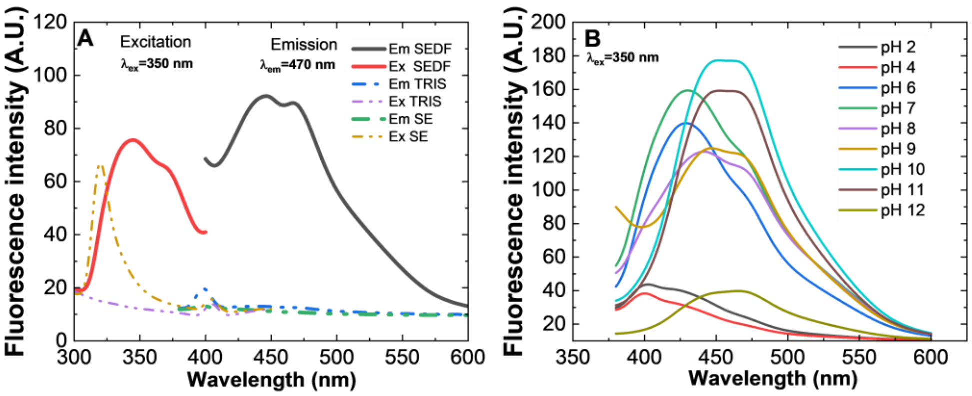

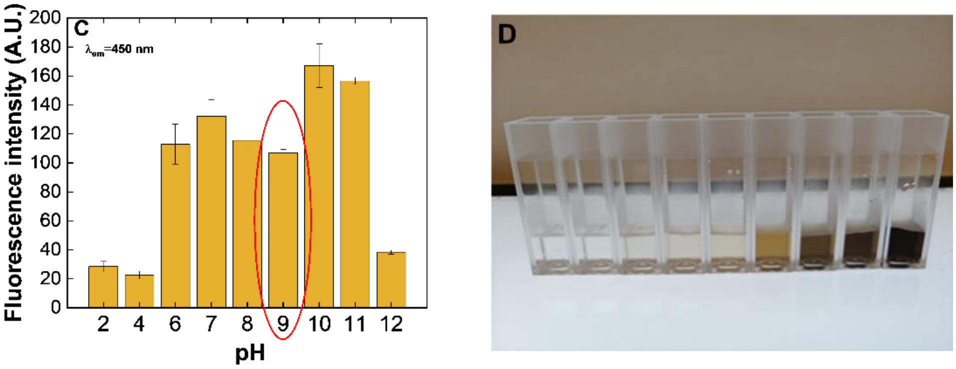

Figure 7.1. *Fluorescence excitation and emission spectra (λ_{ex}= 350 nm, λ_{em}= 450 nm) of serotonin-derivative fluorophore (thick line) and serotonin (dashed line) (A). Influence of pH on SE-derivatives fluorescence emission spectra (B), fluorescence emission at 450 nm (C). Pictures of 2 g L^{-1} serotonin solution heated at 60 °C for 2 hours in 10 mM TRIS at pH ranging from 2.00 to 12.00 (left to right) (D).*

Subsequently, we evaluated the influence of temperature and reaction time on SE self-oxidation at pH 9.00 (Fig. 7.2). The fluorescence emission of the serotonin-derivatives increased with the temperature from 40 °C to 90 °C for 2 h. However, 60 °C condition resulted the best in terms of fluorescence intensity (FI) and reproducibility (Figs. 7.2A and 7.2B). Conversely, the emission signal of the SE monomer (λ_{ex}=250 nm; λ_{em}=340 nm) decreases over time (Fig. 7.2C). The large difference between SE and SEDF emission spectra (Fig. 7.1A) agrees with the monomer-to-oligomer transformation. The fluorescent peak of SEDF at 450 nm is clearly visible after the first 30 min of reaction at 60 °C, reaching the maximum intensity after 1 h and then decreasing (Fig. 7.2D). However, the best reproducibility was achieved after 2 h of reaction (Fig. 7.2E).

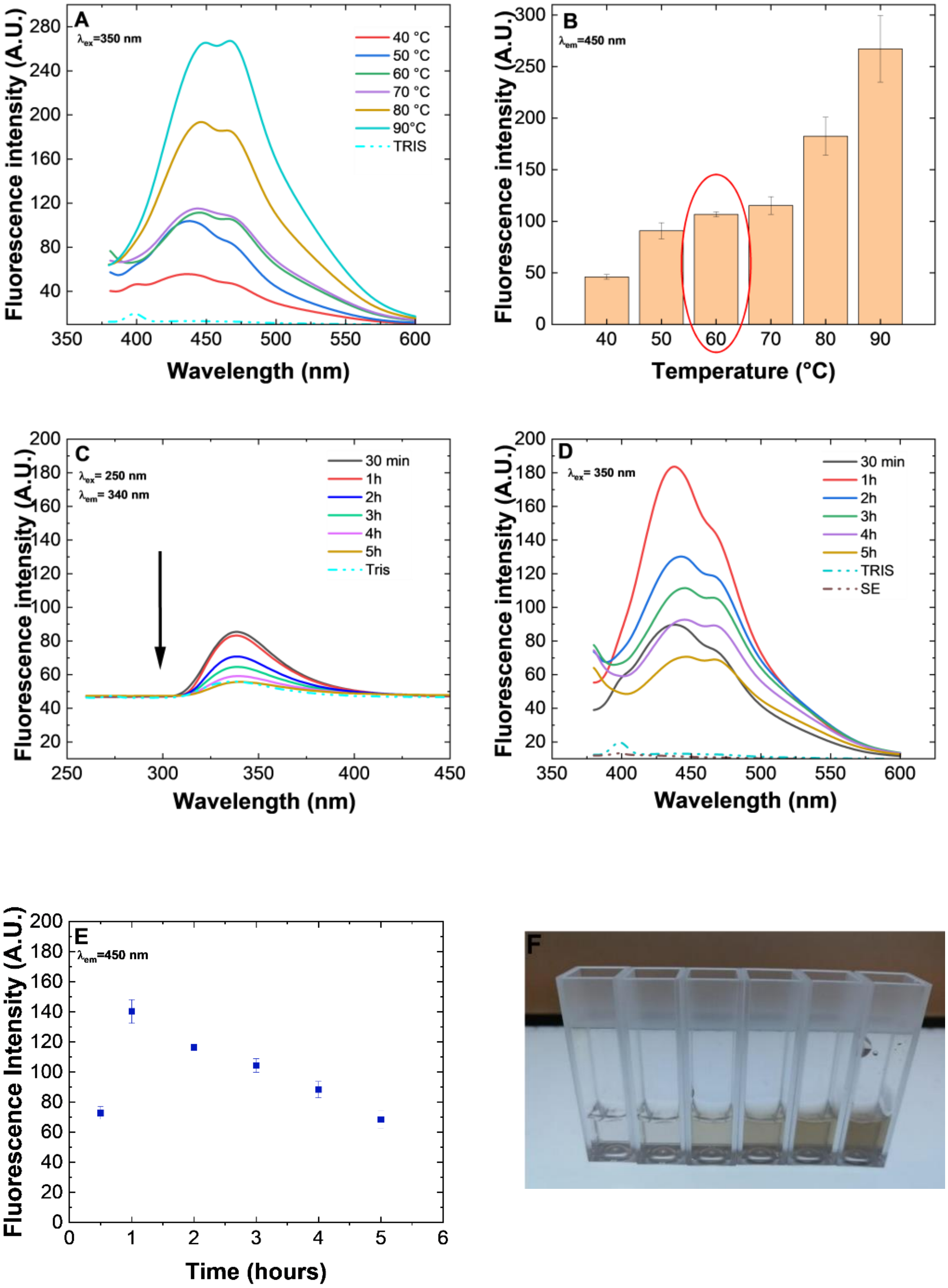

Figure 7.2. *Influence of temperature and reaction time on the fluorescent SE-derivatives in 10 mM Tris HCl at pH 9.00 upon excitation at 350 nm. Emission spectra (A) of samples obtained heating SE between 40 °C to 90 °C for 2 h, and corresponding fluorescence emission response at 450 nm (B). Emission spectra of serotonin monomer (C). The emission spectra of SEDF samples (D) obtained heating SE at*

60 °C between 30 min and 5 h, with the corresponding emission response at 450 nm (E) and the samples' image (F).

Finally, it was investigated the influence of SE monomer concentration on fluorescence of the SE derivative (Fig. 7.3), obtaining that the signal intensity increased almost linearly with the monomer concentration up to 0.5 g L^{-1}, and then reaching a maximum at 2 g L^{-1} SE, which was fixed as the monomer concentration for the following experiments.

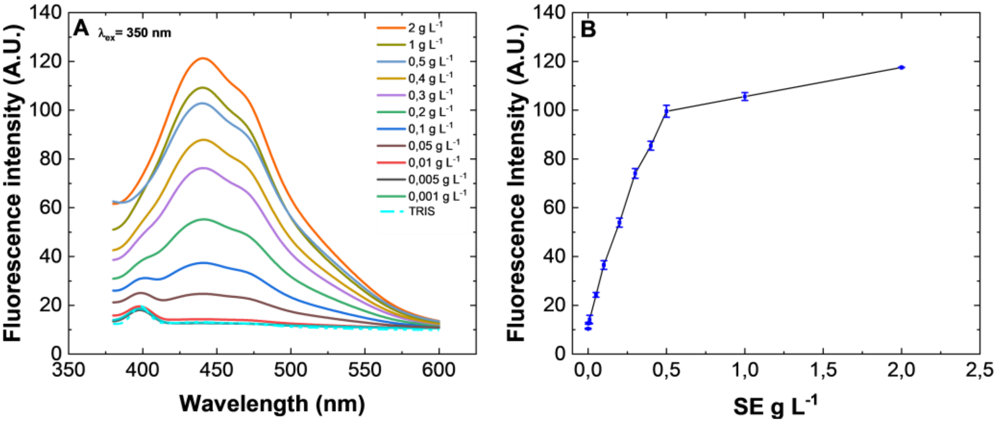

Figure 7.3. *Influence of serotonin monomer concentrations (0.001 g L^{-1} - 2 g L^{-1}) on emission signal of the serotonin-derivative fluorophore synthesized after 2 h at 60 °C in alkaline conditions (pH 9.00). Fluorescence emission spectra upon excitation at 350 nm (A) and corresponding fluorescence emission intensity at 450 nm (B). The error bars represent the standard deviation (n =4).*

The synthetic product was stabilized by adding 5 mM of HCl that stopped the oxidation process. The samples preserve about 100% of the fluorescent properties up to 4 h, decreasing to 75% after one month (Fig. 7.4).

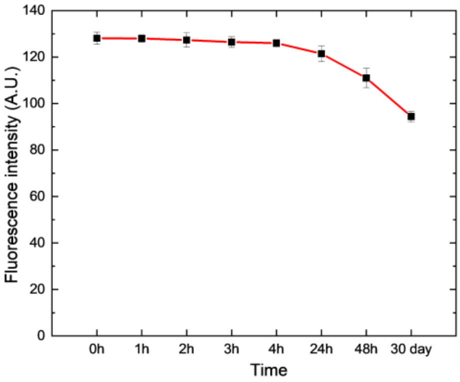

Figure 7.4. *Fluorescence stability over time for SE-derivative fluorophore (SEDF) obtained heating 2 g* L^{-1} *serotonin at 60 °C for 2 h in 10 mM TRIS at pH 9. The fluorescence intensity at 450 nm* (λ_{ex} *=350 nm) was measured up to one month.*

7.4.2 Characterization of serotonin derivative by spectroscopy and mass spectrometry

The quantum yields of the polymers were estimated by performing fluorescence and absorbance measurements (see Section 7.3.2). The QY of SEDF resulted in 0.025 in water, which was higher than the QY reported for polyserotonin obtained enzymatically (0.017) [262], and also higher than the QY here calculated for polydopamine (0.019) and polynorepinephrine (0.008), confirming the good fluorescent properties of conjugated serotonin. Spectrophotometric properties of SEDF were examined and compared to that of the serotonin monomer (Fig. 7.5). The π - π^* electronic transitions are responsible for the UV-absorbance of both molecules below 300 nm. The absorbance peaks of the serotonin monomer are typical of colorless indole derivative solutions with maximum absorbance values at 280 nm and 300 nm, thus the solution appears colorless by the naked eye. Conversely, the SEDF solution under visible light is brown in color with a λ_{max} = 470 nm indicative of a larger conjugated system. Few works refer to a SE-dimer [278,279], while others report about the oligomer obtained through electrochemical oxidation of serotonin [280–282].

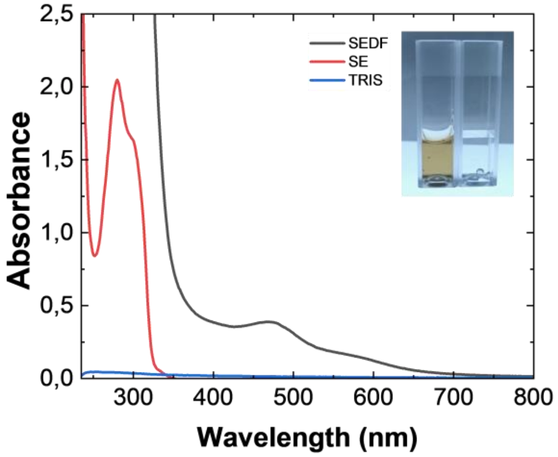

Figure 7.5. UV-Vis Absorption spectra of SE (red line, right cuvette) and SEDF (black line, left cuvette) obtained heating 2 g L^{-1} SE at 60 °C for 2 h in 10 mM TRIS at pH 9 (blue line).

In order to understand the nature of the serotonin derivative obtained here, we performed mass spectrometry experiments, in particular by MALDI-TOF/TOF instrumentation. Several peaks are highlighted in Fig. 7.6 (*m/z* 176.689; 350.978; 502.098, and 672.180) that are compatible with monomeric, dimeric, trimeric, and tetrameric structure, respectively, possibly due to the linkage between the benzene rings (4-4’ and 4-7’).

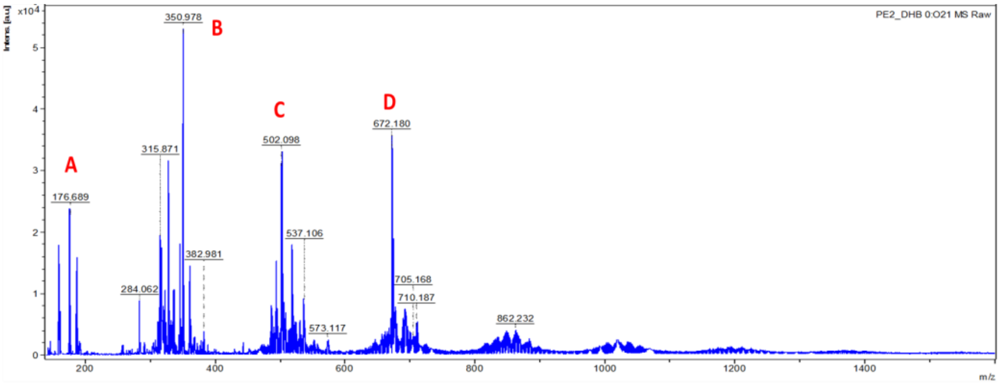

***Figure 7.6.** MALDI-TOF/TOF mass spectrum of SE-derivative fluorophore (SEDF) obtained heating 2 g L^{-1} SE at 60 °C for 2 h in 10 mM TRIS at pH 9.00. m/z values compatible with: SE monomer (A), dimer (B), trimer (C) and tetramer (D) structures (red notation).*

7.4.3 Investigation of polymeric properties of serotonin derivative via electrochemical studies

The polymeric properties of the serotonin derivative were explored by electrochemical studies. To this aim, serotonin solution was not stabilized through HCl addition enabling the oxidation and polymerization process. Therefore, 8 µL of serotonin solution was deposited on the GSPEs working electrode surface and incubated overnight. Subsequently, electrochemical measurements were performed. The bare GSPEs and GSPEs modified with serotonin solution (SE/GSPEs) were characterized by CV using 5 mM $[Fe(CN)_6]^{4- /3-}$ as redox probe at different scan rates (25, 50, 75, 100, 150 mV s^{-1}). The redox peaks height of SE/GSPEs were higher than that of bare GSPEs demonstrating the polymer film formation on the electrode surface (Fig. 7.7A and B). This was confirmed also by the calculation of the electroactive area by applying the Randles-Sevcik equation. The Fig. 7.7C clearly illustrates a higher electroactive area for SE/GSPEs than bare GSPEs. This highlighted the formation of a conductive polymer. In order to confirm this hypothesis, Electrochemical Impedance Spectroscopy (EIS) investigations were carried out using 5 mM $[Fe(CN)_6]^{4- /3-}$ as a redox probe. The Nyquist plots reported in the Fig. 7.7D showed that the charge transfer resistance (R_{ct}) decreases for GSPEs modified with serotonin solution. This is further evidence of the polymeric film formation on the electrode surface starting from the SE monomer solution that reduces the electron transfer from the redox probe solution to the electrode surface.

Finally, the oxidative-reductive properties of the polymer derived from the SE solution were investigated by performing CV measurements using 0.1 M KCl showing a prominent oxidation peak with a potential of 0.301 V (data not shown). This demonstrated the reductive properties of the polymer derived from serotonin.

These electrochemical studies highlighted that the conductive properties of the polymer derived from serotonin can be exploited to develop novel electrochemical-based platforms. In addition, the easy polymerization synthesis (*i.e.* 12 h at room temperature) paves the way for different future applications of this novel polymer.

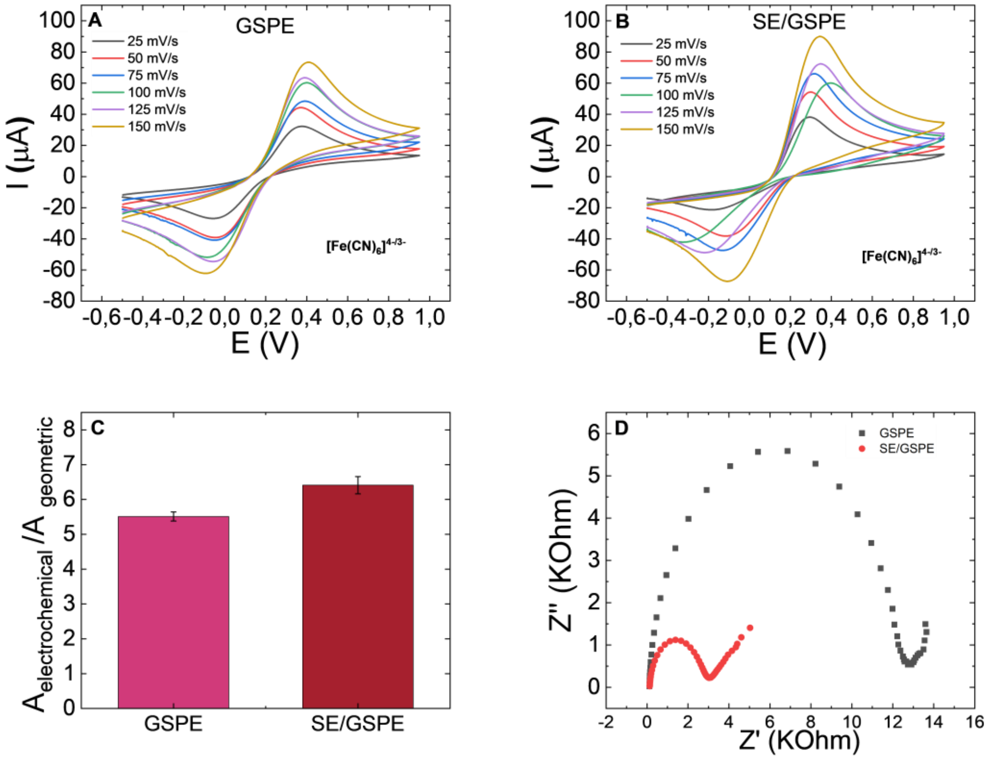

Figure 7.7. *Cyclic voltammetry characterization of the A) bare GSPEs and B)GSPEs modified with SE solution (SE/GSPEs) (potential range from −0.5 V to +0.5 V) at different scan rates (25, 50, 75 and 125 mV s^{-1}) in 5.0mM $[Fe(CN)_6]^{4-/3-}$ equimolecular mixture in 0.1M KCl and relative C) electroactive area. D) Nyquist plots of bare GSPE (black) and SE/GSPE (red) in 5.0mM $[Fe(CN)_6]^{4-/3-}$ equimolecular mixture in 0.1M KCl.*

7.4.4 Examination of synthesis reaction products of SEDF by Scanning Electron Microscopy techniques

In order to achieve the maximum photoluminescence intensity from the SEDF, two centrifugation cycles were necessary to remove the non fluorescent part. After the centrifugation at 10000 g for 15 minutes, the solution appeared composed by two distinguished parts, a soluble part on the top of the solution, known as supernatant and an insoluble part on the bottom *i.e.* pellet. The photoluminescent SEDF with low molecular weight remained in the supernatant, whereas the insoluble part, with high molecular weight, precipitated to form the pellet. The latter did not show fluorescent behavior. For this reason, we used SEM technique to understand the nature of the pellet. We found that the insoluble part was composed by microparticles of PSE with a mean diameter of about 300 nm (Fig. 7.8). We decided to discard the no photoluminescent microparticles because they are not useful to our scope. However, the PSE microparticles could be useful for further future studies.

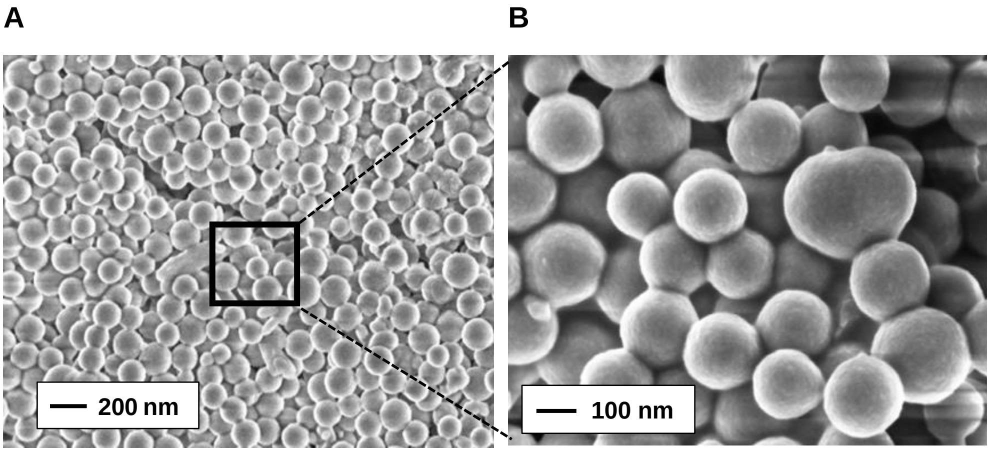

Figure 7.8. *SEM A) micrograph and B) magnification of PSE microparticles. SEM analyses were performed at CSGI (Center for Colloid and Surface Science), Department of Chemistry "Ugo Schiff", University of Florence in collaboration with Prof. Emiliano Fratini and by Dr Giovanni Ferraro.*

7.4.5 SEDF fluorescence quenching by metal ions

To evaluate the possible influence of solution composition on SEDF fluorescence, we tested several solutions (0.5 mM) of alkaline, alkaline earth metals (Fig. 7.9A), and transition metals (Fig. 7.9B and C). It is clear from the graphs that alkaline and alkaline earth metal did not affect the fluorescence signal, whereas, among the heavy species, Au(III), $Cr_2O_7^{2-}$, Fe(III), and Cu(II) largely quenched the fluorescence of SEDF (Figs. 7.9C), in agreement with literature that reports on fluorescence quenching of indole derivatives by copper ions and a few other metals [277,283,284]. Fe(III) exhibited a prominent fluorescence quenching, as previously observed for fluorescent derivatives of dopamine used to quantify iron [285,286]. The fluorescence quenching was also large for Au(III) and $Cr_2O_7^{2-}$ ions but associated with low data reproducibility, also due to the formation of gold nanoparticles.

Based on these results, and considering that, to the best of our knowledge, there are no studies on copper ions detection exploiting the fluorescence-quenching of biopolymers, we decided to apply this method to real urine samples, where the presence of large amounts of copper ions would be indicative of a pathological condition (see below), whereas the concomitant presence of the other quenching ions is insignificant [287,288]. Accordingly, we also evaluated the interference of the main organic compounds in urine on SEDF fluorescence quenching. As shown in Figure 7.9D, urea, uric acid, creatinine and citrate, in the physiological concentration ranges [289], do not lead to a fluorescence quenching. This was also true for glucose, hypoxanthine, glutamic acid and ascorbic acid at concentration that determines pathological state. Accordingly, we proceeded to determine Cu(II) concentration in buffer solution, artificial urine, and human urine samples.

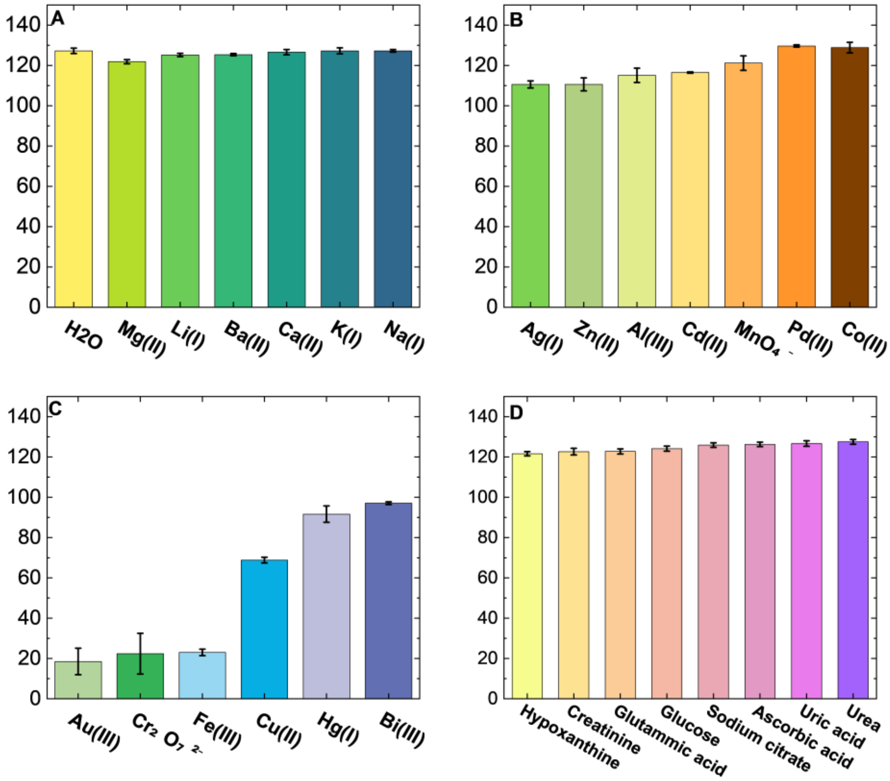

Figure 7.9. *Fluorescence of SEDF in 10 mM TRIS pH 9.00 after the addition of 0.5 mM of alkaline and alkaline earth metals (A), transition metals (B, C), and organic compounds occurring in urine (D).*

7.4.6 Copper detection via quenching-based bioanalytical assay

Copper is a key trace element involved in numerous physiological functions like cardiovascular integrity, lung elasticity, enzymatic function, aerobic metabolism, neovascularization, neuroendocrine function, etc [266]. However, an excessive copper concentration in body fluids is toxic and indicative of serious pathological states. The homeostasis of copper is regulated by the liver, which removes the excess of copper via bile. For this reason, in patients who suffer from copper-dependent diseases the copper excretion pattern changes dramatically. As a result, high urinary copper concentration is an important diagnostic biomarker for several conditions like hepatitis, cancer and pregnancy playing a fundamental role in diagnosis of Wilson diseases. WD is a genetic disorder due to the inactivation of copper transporter (ATP7B) resulting in hepatic copper overloads [265]. Different clinical studies showed that the rate of Cu(II) excretion in patients with WD changes from patient to patient. For instance, hepatic and neurological patients and also pharmacological therapy with penicillamine involve high urinary copper (up to 9000 μg per day) [272]. In general, the threshold of urinary copper that determines the pathological state is 100 μg per day [272]. However, patients with WD show urinary Cu(II) values between c.a. 200 to 400 μg per day [273,274]. This means that an analytical method for the sensitive urinary copper estimation which covers a broad range of Cu(II), is required. ICP-MS is the reference method actually employed in clinical laboratories analysis for the evaluation of copper in urine samples [276]. However, it requires a high-cost instrumentation and samples pre-treatment. Here, we propose an inexpensive, fast and simple quenching-based bioanalytical assay for the urinary copper determination in human urine samples, exploiting the fluorescence of SEDF. SEDF fluorescence spectra and dose-response plots in buffer and in artificial urine (AU) samples are reported in Fig. 7.10. The fluorescence signal was reported as F_0/F, where F_0 is the fluorescence intensity of SEDF, and F is the emission signal of SEDF after the copper addition. The fluorescence intensity at 450 nm after the Cu(II) addition was plotted versus Cu(II) concentration in the range of 0.05-0.5 mM. It can be noted a common linear trend with remarkable analytical performance (Table 7.1) both in buffer and in AU samples, as confirmed by the correlation coefficient $R^2 = 0.990$ for both and by linear fitting equations $F_0/F = 4.68\times[Cu(II)] + 0.87$ used for Cu(II) detection in buffer and $F_0/F = 3.38\times[Cu(II)] + 0.93$ for AU. The excellent assay reproducibility was highlighted by low variability ($CV_{av}\% = 4\%$ for buffer and 3% for AU), with a LOD of 16.33 ± 0.72 $\mu g\ L^{-1}$ and a LOQ of 54.42 ± 2.41 $\mu g\ L^{-1}$ in buffer solution and 22.56 ± 1.00 $\mu g\ L^{-1}$ and 75.19 ± 3.38 $\mu g\ L^{-1}$ in AU (where LOD = $3\times SD_{blank}/slope$ and LOQ = $10\times SD_{blank}/slope$) (Table 7.1). Notably, the LODs and LOQs calculated are below the threshold value of copper that determines the pathological state of Wilson's diseases (100 µg per day), stimulating us to apply this assay to human urine samples.

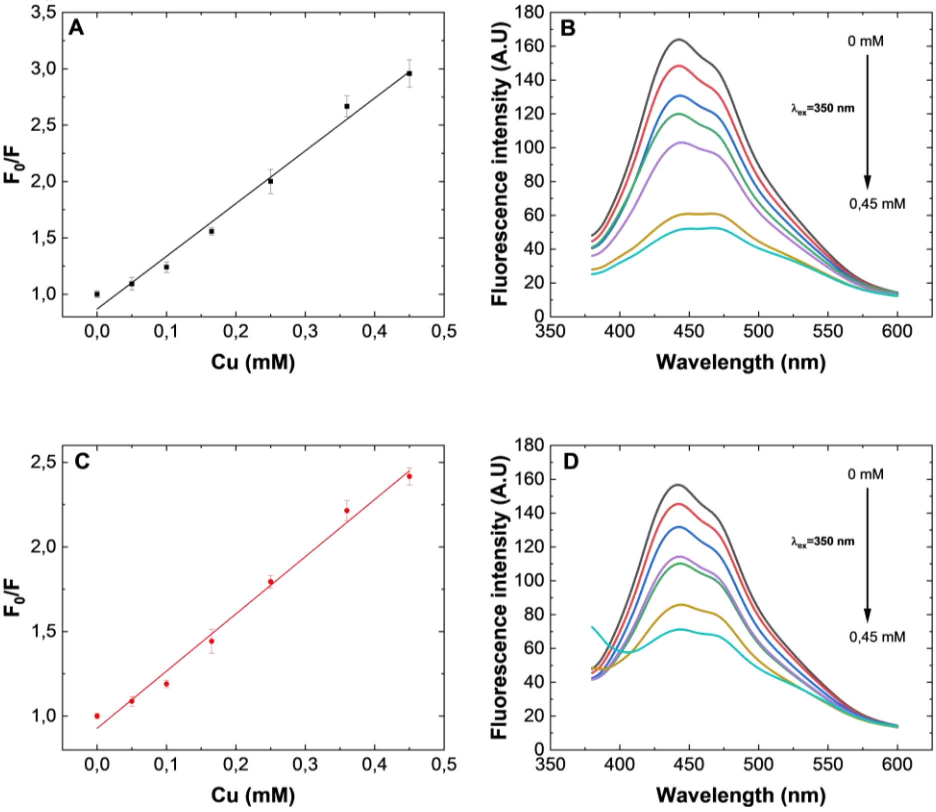

Figure 7.10. *Fluorescence spectra and the relative calibration plots of SEDF after copper ions addition in buffer (A and B) and in artificial urine samples (C and D). The fluorescence intensity was recorded at 450 nm (λ_{ex} 350 nm). The fluorescence signal is reported as F_0/F, where F_0 is the emission intensity of SEDF, and F is the emission signal of SEDF after the copper addition. The quenched emission signal of*

SEDF (F_0/F) was plotted versus Cu(II) concentration. The error bars represent the standard deviation (n =4). The analytical parameters are reported in the table below (Table 7.1).

Table 7.1. *Linear fitting parameters obtained by Cu(II) detection in buffer and in AU. The corresponding fluorescent quenched signal of SEDF was measured at λ_{em}= 450 nm (λ_{ex} 350 nm) after Cu(II) addition.*

** LODs and LOQs are reported in µg L^{-1} to compare them to the clinical thresholds of Cu(II) that determine the pathological state i.e. 100 µg/24h.*

Matrix	***m (mM)***	***LOD (µM)***	***LOQ (µM)***	***LOD (µg L^{-1})****	***LOQ (µg L^{-1})****	***R^2***	***CV_{av}%***
Buffer *y=4.68x+0.87*	*4.68 ± 0.24*	*0.26 ± 0.01*	*0.85 ± 0.04*	*16.33 ± 0.72*	*54.42 ± 2.41*	*0.990*	*4*
AU *y=3.38x+0.92*	*3.38 ± 0.15*	*0.35 ± 0.01*	*1.18 ± 0.05*	*22.56 ± 1.00*	*75.19 ± 3.38*	*0.990*	*3*

7.4.7 Copper detection in human urine samples

With the aim to design a bioassay for the urinary Cu(II) quantification for clinical purposes, we transferred our experiments in ELISA-type 96-wells microplates, allowing the simultaneous analysis of different human urine samples. This reduces the turnaround time for the analysis and results in a potential positive impact on the patient's management. The other advantage offered by the method, here developed, is the direct analysis of the urine samples without any pretreatment.

Urine samples were preliminarily assayed by ICP-MS to determine their starting Cu(II) physiological concentration, resulting in the nM range. Among them, the urine sample n. 3 was selected to be used as a calibrator in the real matrix by Cu(II) standard additions (red line in Fig. 7.11), since its Cu(II) level represents a mean value within the series. The CV_{av}% (1%) and the slope reported in the Table 7.2 highlighted the high reproducibility and sensitivity of the method, even in the complex real matrix, with LOD of 59.14 ± 3.41 µg L^{-1} and LOQ of 96.97± 11.36 µg L^{-1}.

After that, each urine sample was spiked with different known Cu(II) concentrations (0.05 mM; 0.20 mM and 0.40 mM, see Table 7.3) to evaluate the ability of detecting the Cu(II) in real samples, *i.e*, potentially pathological ones. In detail, to 100 µL of each reinforced urine sample, 1800 µL of SEDF solution were added, and the corresponding fluorescent signal was finally measured (Table 7.2 and Fig. 7.11). The same spiked samples were analyzed in parallel by ICP-MS, the gold standard for Cu(II) detection in clinical diagnostics.

Despite the complexity and the variability of the analyzed urine samples, the results clearly highlighted a very good accuracy of the assay with respect to the calibrator, even if the urine n. 2 showed a slightly higher variability likely due to the marked turbidity and the darker color of the sample. This allows us to foresee the realistic applicability of the method as a diagnostic tool, even considering that it is able to cover the broad range of Cu(II) concentration expected in this type of patients.

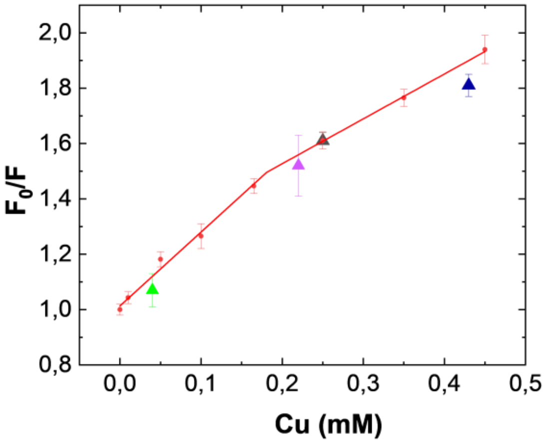

Figure 7.11. *Calibration of Cu(II) in human urine (sample 3, red points and fitting) and its quantification in the four urine samples, indicated with different colors (sample 1 green, sample 2 violet, sample 3 black and sample 4 blue). The fluorescent signal is reported as F_0/F at λ_{em} = 450 nm (λ_{ex} = 350 nm) versus Cu(II) concentration, where F_0 is the emission intensity of SEDF, and F is the emission signal of SEDF after the copper addition. The error bars represent the standard deviation (n =4). The analytical parameters of the calibration are reported in Table 7.2 and were obtained by using the piecewise linear fitting implemented in the Originlab software.*

Table 7.2. *Linear fitting parameters obtained by Cu(II) detection in buffer and in AU. The corresponding fluorescent quenched signal of SEDF was measured at λ_{em}= 450 nm (λ_{ex} =350 nm) after Cu(II) addition.*

** LODs and LOQs are reported in µg L^{-1} to compare them to the clinical thresholds of Cu(II) that determine the pathological state i.e. 100 µg/24h.*

Calibration curve: F_0/F= 1+ k [Cu(II)]

Matrix	***[Cu] (mM)***	***k (mM) (slope)***	***LOD (µM)***	***LOQ (µM)***	***LOD* (µg L^{-1})***	***LOQ * (µg L^{-1})***	***R^2***	***CV_{av}%***
Urine	*0 - 0.165*	*2.61± 0.15*	*0.93± 0.05*	*3.1 ± 0.18*	*59.14 ± 3.41*	*96.97± 11.36*	*0.997*	*1*
	0.25– 0.45	*1.64± 0.14*						

Table 7.3. Comparison of Cu(II) concentration in reinforced urine samples obtained by the quenching-based method and ICP-MS, the "gold standard" method for the urinary copper determination. The relative fluorescent signals of the four samples were reported in Fig. 7.11 with respect to the urine calibrator.

Urine sample n.	Spiked [Cu(II)]	Fluorescence signal (F_0/F)	[Cu(II)] via quenching-based method	[Cu(II)] determined via ICP-MS (reference method)	Recovery (%)
1	0.05 mM	1.07 ± 0.06	0.04 mM ± 0.02	0.03 mM	133 %
2	0.20 mM	1.52 ± 0.11	0.22 mM ± 0.01	0.21 mM	105 %
3	0.20 mM	1.61 ± 0.03	0.25 mM ± 0.01	0.22 mM	114 %
4	0.40 mM	1.81 ± 0.04	0.43 mM ± 0.01	0.49 mM	88 %

7.5 Conclusions

In this study, the outstanding properties of a novel serotonin-derived fluorophore were successfully exploited for the first time for urinary Cu(II) determination via a quenched-based bioanalytical method. Different techniques were applied to characterize this novel material. The experimental conditions were optimized to obtain the highest emission signal and to improve the assay sensitivity and reproducibility. The calculated quantum yield confirms the remarkable photoluminescence behavior of this new emerging serotonin derivative, probably due to its oligomeric structure, as confirmed by mass spectrometry measurements. Firstly, copper ion concentration was quantified in buffer and in artificial urine obtaining very low variability, high sensitivity and low LODs and LOQs values. Then, the assay was applied to estimate Cu(II) concentration in human urine samples from volunteers, and finally validated by ICP-MS obtaining very good recovery values. The resulting excellent analytical performances in the real matrix are well represented by the CV_{av}% of 1 % and LOD of 59.14 ± 3.41 μg L^{-1} and LOQ of 96.97± 11.36 μg L^{-1} . These values are below the threshold of urinary Cu(II) that determines the pathological state of WD (100 μg per day), enabling the applicability of the method for Cu(II) measurement in routine clinical practice.

8

The importance of bioanalytical procedures in drugs quality control

The importance of bioanalysis in drug discovery and drug development is well known. The role of bioanalysis in the drug development is prevalently related to the quantitative estimation of drugs and their metabolites in biological media to evaluate the bioequivalence, pharmacokinetic, pharmacodynamic and toxic effects. However, also the development of methods for pharmaceutical analysis to drug quality control (qualitative and quantitative analysis, purity testing, chiral separation, pro-drugs and stoichiometric determination) plays a significant role. In fact, the unambiguous detection of a drug in a pharmaceutical product is as crucial as determination in complex matrices, because the pharmaceutical product quality is directly related to patient health.

In brief, the process of drug development starts with investigation of a molecule able to interact with biological components to generate a response that leads to therapeutic effect in the cure of disease. The compound, which was selected as drug candidate, also called active pharmaceutical ingredients (APIs), undergoes safety tests and experiments to understand the distribution of the drug in the body, the metabolization process and the absorption in the bloodstream. Then, *in vitro* studies are performed followed by animal testing. Once these preclinical tests are passed, clinical trials on patients are carried out and if they are successfully completed the drugs are launched on the market [290]. Analytical methods and procedures are essential for each of these steps involved in drug development, *i.e.,* understanding the physical and chemical stability of the drug, impact on the selection and design of the dosage form, and assessing the stability of the drug molecules. On the other hand, the pharmaceutical product may develop impurities at various stages of its fabrication. This could generate enormous risk to patients' health. As a result, quantification and identification of impurities considered above to establish toxic threshold and the discrimination of these impurities from that of the API, are mandatory stages.

As a consequence, the quality of drugs must be ensured by performing analytical tests. The selection of the appropriate methods of quality control is essential in the pharmaceutical industry to the efficacy of the drugs but mostly for patients' safety. The development of bioanalytical methods for pharmaceutical formulation involves the procedure that enables to measure and identify the drug.

Analytical techniques are important tools also for the identification of counterfeit drugs. These last are widespread especially in underdeveloped countries where the quality monitoring is impracticable given by the lack of specific analytic infrastructure [291]. On the other hand, the problem is not exclusively limited to developing countries since the high cost of biotechnologically APIs product, lifestyle medication, traditional herbal medicines and dietary supplements pushed the industrialized areas to falsify pharmaceutical formulations.

The World Health Organization (WHO) defines counterfeit drugs with the following definition [292]: "A counterfeit drug is one which is deliberately and fraudulently mislabeled with respect to identity and/or source. Counterfeiting can apply to both branded and generic products and counterfeit products may include products with the correct ingredients or with the wrong ingredients, without active ingredients, with insufficient active ingredient". The cause of the presence of counterfeit drugs is due mainly to the lack of robust information regarding the prevalence of fake drugs globally, traditional herbal medicines and to the presence of websites that sell discount medicines bypassing the doctor-patient relationship and could supply consumers with counterfeit medications [293]. Counterfeit drugs are a really common, important public health problem. The presence of "false" active ingredients can lead to harmful consequences such as to mask important clinical signs and to cause adverse effects whose origin would not be apparent to the clinicians. Usually, "false" active ingredients are molecules able to simulate the organoleptic characteristics and the effect of the real active principle.

The decision of the analytical method to use for drug estimation depends on the information sought by the investigators, the chemical properties of the analyte, concentrations, sample matrix, cost of the analysis method and instruments, cost per sample, time of the analysis, quantitative or qualitative measurement, precision, and necessary equipment. A plethora of analytical methods are available for the quantitative determination of drugs that include titrimetric, chromatographic, spectroscopic, electrophoretic, and electrochemical techniques. In Table 8.1 are reported the percentage use of these techniques in drug analysis according to the edition of European (The European Pharmacopoeia and Council of Europe, 2002) and US (United States Pharmacopoeia, 2004) pharmacopoeias.

Table 8.1.*Proportion of various analytical methods prescribed for the assay of bulk drug materials in Ph. Eur. 4* [294] *and USP XXVII* [295]. *Adapted from reference* [296].

Method	***Ph. Eur. 4 (%)***	***USP 27 (%)***
HPLC	15.5	44
GC	2	2.5
Titration	69.5	40.5
Acid-base	57.5	29.5
Aqueous mixtures	21	5.5
Indicator	6.5	4.5
Potentiometric	14.5	1
Non-aqueous	36.5	24
Indicator	9.5	14
Potentiometric	27	10
Redox (Iodometry, Nitritometry, etc.)	6.5	5.5
Others (complexometry, argentometry, etc.)	5.5	5.3
UV–vis spectrophotometry	9.5	8.5
Native absorption	8.5	6.5
Colorimetry based on chemical reactions	1	2

Microbiological assay (antibiotics)	3	2.5
Other (IR, NMR, polarimetry, fluorimetry, atomic absorption spectroscopy, polarography, gravimetry etc.)	0.5	2

Separation techniques like thin layer chromatography (TLC), high performance liquid chromatography (HPLC), gas chromatography (GC), and capillary electrophoresis (CE) are fully established and have been added to almost all monographs of the major pharmacopoeias, *e.g.* the European Pharmacopoeia (Ph. Eur.) [297], Japanese Pharmacopoeia [298] and the United States Pharmacopoeia (USP)[299]. However, for more applications chromatography methods are really sophisticated requiring time consuming analysis and expensive instrumentation. For instance, to decide if a sample is counterfeit or not, simple colorimetric tests could suffice. As a consequence, UV-Vis spectrophotometric tests are useful tools for drugs examination.

8.1 UV-Vis spectrophotometric methods

Spectrophotometric methods occupy an important place in pharmacopoeias. These methods are based on two important properties of pharmaceutical products: the natural UV absorption of chromophore groups which allows their direct determination and the use of a derivatization reaction that leads to a detectable product in the ultraviolet region. The quantitative determination of the drug active principle occurs through the measurement of the reflection or transmission properties of a material as a function of wavelength. The precision and the accuracy of the UV-Vis method as well as the speed, economic and simplicity of the procedures make this method suitable for the analysis of pharmaceutical dosage [300].

However, spectral overlapping of molecules in pharmaceutical formulations could compromise the UV-Vis analysis. Derivative spectrophotometry (calculation and plot one of the mathematical derivatives of spectral curve [301]) intervenes to overcome this drawback. Sometimes, it could be necessary to obtain low detection and quantification limits (in the range of ng mL^{-1} and pg mL^{-1}). These values are hard to obtain by using spectrophotometric techniques. Luminescence spectroscopy is applied in solving this kind of problem. Luminescence measurements allow the selective and sensitive determination of a wide range of pharmaceutical ingredients. As a result, fluorimetric methods are also commonly used for pharmaceutical drugs quality control.

Despite these trivial limitations, absorbance measurements for drugs estimation has increased rapidly over the last year, as highlighted in Table 8.2.

Table 8.2. *Some of more relevant UV-Vis spectrophotometric assays applied for drug estimation. The table was adapted from reference* [244,302].

Reagent	***Drug name***	λ_{max}	***Rif.***
4-aminobenzenesulfonic acid	Labetalol	395	[303]
p-Chloranilic acid	Enalapril	534	[304]
m-Cresol	Acetaminophen	640	[305]
7,7,7,8-Tetracyanoquinodimethane	Alendronate sodium	743; 840	[306]
Iodine	Flunarizine dihydrochloride; Aripiprazole	380; 400	[307]; [308]
Potassium iodide and potassium iodate	Irbesartan	402	[309]
Ninhydrin	Pregabalin	530	[310]
Ascorbic acid	Lisinopril	760	[311]
Folin-Ciocalteu phenol	Oxcarbazepine Ampicillin, amoxicillin, and carbenicillin	760 750, 770, 750	[312], [313]
Tris Buffer	Diclofenac sodium	284, 305	[314]
Sodium metavanadate	Diltiazem HCl	750	[315]

Bromothymol blue	Rasagiline mesylate	414	[316]
Cu (II) & eosin	Carbinoxamine	538	[317]
KMnO4 in alkaline medium	Metoprolol	610	[318]
p-chloranilic acid	Quetiapine fumarate	520	[319]

In particular, between the spectrophotometric tests, colorimetric tests are enormously employed for drug compound examination. Easy identification of drug compounds is achieved by using chemical reagents, reacting with specific functional groups of the drugs, resulting in a visible change in color.

8.2 Colorimetric assays

For over a century, the potentialities of colorimetric assays have been extensively explored. Thanks to the improvement of miniaturized technology, the high visibility of colorimetric techniques was reached mostly in the last two decades where paper-based analytical devices and image capture instruments played a key role. This is clearly illustrated in Figure 8.1 where is evident the impressive increase of the number of publications regarding colorimetric assays since 2000.

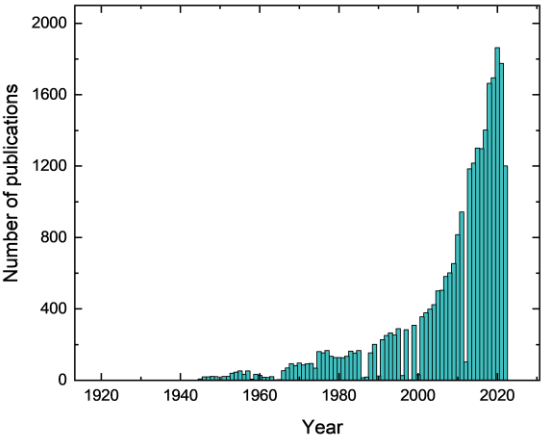

Figure 8.1. Number of publications in the bioanalytical field related to "colorimetric assays" (Pub med database).

This trend could be explained by the general simplicity of the tests and by the fabrication and enhancement of various technologies for the color detection to meet the demands of making qualitative, semi-quantitative, and fully quantitative analyses of multiple analytes. For this purpose, cameras, scanners, and smartphones are consistently employed.

The development of colorimetry occurred between 1800 and 1900 with the first colorimetric assays reported in 1838 by Lampadius [320] for the identification of copper and nickel in a cobalt-ore and the presentation of Beer's Law [321] followed by the development of the first photometer and its distribution [322]. As noticeable from the studies reported in literature, the first colorimetric approaches were related prevalently to the estimation of inorganic species [322,323]. For instance, Dehm in 1865 produced the first commercial system for copper identification that revolutionized the analytical strategies usually applied for the copper detection [324]. It is obvious as colorimetric methods were spread already in the 800's. The perception of colors, the identification of different tones and intensities are the first abilities acquired by humans. Color in chemistry has always been the most fascinating and exploited aspect. The changing in color in a chemical reaction shows that a transformation has occurred. In fact, the scientists immediately exploited the colorimetric properties of chemical reactions to correlate the color intensity with the concentration of the products involved in that reaction. The selective colorimetric reactions became a powerful tool for qualitative analysis before the definition of color vision theory proposed in 1853 by Herman von Helmholtz and Clerk Maxwell [325]. Colorimetric detection is based on electromagnetic radiation that interacts with matter producing different phenomena like light absorption, reflection, dispersion, refraction, etc. The light source, the detection mode of radiation after interaction with the object and the detector are the main factors that influence a colorimetric analysis in terms of sensitivity and detectability. The quantification of an analyte in colorimetric analysis takes place through the interaction of visible radiation with a colorful product in a solvent or a solid substrate and the resulting reflection, transmission or absorbance radiation produced by this phenomenon. Absorbance is the most common modality used in colorimetry and it is based on the intensity of monochromatic radiation absorbed by the analytes from a light beam. Through the correlation of analyte concentration with its absorbance, reflectance, or transmission properties it is possible to obtain a calibration curve that enables the quantification of the examined analyte. The only aspect to pay attention is the saturation phenomenon due to high sample concentration which results in non-linear calibration curves. Despite this, different devices based on colorimetric reactions are routinely employed in analysis for their simplicity, affordability, ease to operate and the well-known colorimetric reactions employed. These features were exploited for the design of novel devices like paper-based, lateral flow test strips or microfluidic strips that are applied prevalently in point of care testing [326]. The criteria required for the design of PoC devices, such as size and portability for the realization of on-site testing and healthcare management, are fully satisfied by colorimetric tests. In these cases, the colorimetric measurements are performed by detecting color intensity signals by robust image sensors such as a complementary metal oxide semiconductor camera or charge coupled device. Therefore, the concentration of the analyte is calculated, and the quantification of samples achieved.

The constant research and innovation of procedures, devices, and theories for colorimetric measurements enabled the application of colorimetry in different fields such as that of, environmental [327], food [328] and bioanalytical [329]. In this regard, numerous are the applications of colorimetric assays in the bioanalytical field especially in drug testing. The details are reported in the following paragraph.

8.3 Colorimetric assays for drug testing

Colorimetric methods are widely used for drug estimation. Laboratory color tests are useful for qualitative analysis of many organic functional groups and inorganic species. They involve the use of chemical reagents able to react with active principle functional groups producing a visible change in color of the tested solution. These colorimetric methods applied for drugs testing are usually based on a complex-formation reaction, oxidation-reduction process or a catalytic effect. Colorimetric tests are described in many pharmacopoeia monographs since the chemistry of these assays usually employed standard test tubes or spotting plates without avoiding the complex laboratory setup. Portable field kits utilizing colorimetric techniques have long been the choice of investigators for quickly identifying poor quality medicines and to identify the absence of the active ingredient [330]. A big variety of detection devices are designed for on-field colorimetric detection to identify APIs and counterfeit medicines. An example is represented by the Global Pharma Health Fund (GPHF) Minilab® [331] which consists of a mini-laboratory to help developing countries detect at least 85 different essential medicines by thin-layer chromatography. Another important example consists in the paper test cards serving as screening tools to indicate potential low-quality antimalarial medicines [332]. This demonstrates that such tests for active principle determination are very suitable for being used in pharmacies or in field laboratories where basic laboratory inventories demand for a high grade of simplicity.

It is important to note that colorimetric methods are regularly used for drugs estimation. For instance, the blue tetrazolium assay is used for the determination of corticosteroid drug formulations [300,333]. The colorimetric approach is also applied for the determination of cardiac glycosides and is presented in European Pharmacopoeia [297]. Another relevant example described in pharmacopeial monograph consists in the precipitation of halide ions using silver nitrate or the formation of colored azo dyes by converting primary aromatic amines into diazonium ions and coupling them with *e.g.* 2-naphthol [334]. The primary results obtained by using this type of simple and low cost assays are mainly qualitative. For this reason, colorimetric tests are widely used for drug screening. However, false positives due to the low specificity of the testing protocols can alter the results of the analysis. Typically, this occurs when a molecular scaffold has a similar molecular structure of the active principle that leads to the colorimetric response in APIs from the same chemical group or when certain “impurities” are added.

Despite this disadvantage, colorimetric techniques remain the most inexpensive, simple, fast methods for drug analysis which could improve the methods used by the pharmaceutical companies. For this reason, this thesis focuses on drug detection to ensure the quality of pharmaceutical products and to recognize counterfeit drugs that are widespread especially in low-income countries.

9

Melanochrome-based colorimetric assay for quantitative detection of levodopa in co-presence of carbidopa and its application to relevant anti-Parkinson drugs

Anal. Bioanal. Chem. 414, (2022) 1713–1722 – **DOI**:10.1007/s00216-021-03804-8.

9.1 Abstract

In this work is reported the selective detection and quantification of levodopa in co-presence of carbidopa. The method took advantage of the spontaneous oxidation and color development of levodopa at basic pH here driven by alkaline earth cations and co-solvent in solution. We have shown for the first time the generation and stabilization of the purple melanochrome from levodopa, by using magnesium acetate and dimethyl sulfoxide, which was here exploited for the development of a quantitative colorimetric assay for the active principle ingredient in commercial drugs for the treatment of Parkinson's disease. The calibration curves of levodopa in the two tablet formulations, containing carbidopa as decarboxylase inhibitor, showed a common linear trend between 10 mg L^{-1} and 40 mg L^{-1} with levodopa alone or in combination with carbidopa in standard solutions, with very good reproducibility (CV_{av}%, 3.3% for both brand and generic drug) and very good sensitivity, with limit of quantification about 0.6 mg L^{-1} in any case. The colorimetric method here developed is very simple and effective, appearing as a rapid and low-cost alternative to other methodologies, involving large and expensive instrumentations, for drug estimation and quality control of pharmaceutical formulations.

Keywords: carbidopa, colorimetry, drug analysis, levodopa, melanochrome, Parkinson.

9.2 Introduction

Parkinson’s disease (PD), like many human neurodegenerative disorders, is related to dopaminergic neuron disruption upon pH-dependent oxidative conversion of neurotransmitters like dopamine (DA) into cytotoxic molecules [335–337] and protein misfolding and aggregation, eventually causing neuronal death [338]. Unfortunately, there is no cure for PD, but several medications, dependent on the stage and the age at disease onset, may improve the quality of life of patients, starting from the pharmacological treatment of motor symptoms, *i.e.*, rigidity, bradykinesia, and tremor [339]. Particularly effective, although fluctuating and transitory, appears the administration of levodopa (LD) as molecular precursor of DA that, being unable to cross the blood-brain barrier, cannot be directly taken as a medicine. However, to avoid LD metabolization prior to reach the brain, anti-Parkinson drugs always contain a decarboxylase and/or catechol-O methyltransferase inhibitor like carbidopa (CD), benserazide (BZ), or entacapone, which also reduces side effects associated to LD therapy [340]. In this framework, several methods were developed for LD determination in presence of adjuvants and impurities in such drugs by means of chromatography [341], electrochemistry and electrophoresis [342–344], spectrophotometry [344,345,354,346–353], and NMR [355]. Literature about colorimetric determination of LD in pharmaceutical formulations is not very vast although representing an advantageous alternative, for easiness, rapidity, and low-cost, to the other methodologies requiring large instrumentation. These visible spectroscopy researches were based on LD chemical or enzymatic oxidation, for example, by using KIO_4 or tyrosinase to form the aminochrome (λ_{max}= 480 nm) [344,346], or 4,5-dioxygenase to form betaxanthin pigment (λ_{max} = 430 nm) [308], or Au^{3+} to form gold nanoparticles (λ_{max} = 520 nm) [352]; other strategies were based on LD derivatization with a dye to form a colored adduct, for example, by using 4-aminoantipyrine (4-AAP) (λ_{max} = 454 nm) [353].

Simple colorimetric quantitative assays are thus welcome for fast, simple, and low-cost drug estimation with several potential applications including quality control of pharmaceutical formulations, illicit drug testing, and monitoring in advanced drug delivery systems and personalized drug dosing [356].

Here, we obtained for the first time the generation and stabilization of the elusive purple melanochrome [357] from levodopa and dopamine (λ_{max} about 585 nm) without the use of chemical oxidant, enzyme, transition metal ions, or dye conjugation. This achievement inspired the analytical study of the O_2/pH-driven oxidation of some fundamental neurotransmitters (LD, DA, NE), and two synthetic analogues (CD, BZ) either one found in combination with LD in pharmaceutical formulations for the treatment of Parkinson's disease (Fig. 9.1), reporting the modulation of the color development, corresponding to different stages of molecular oxidation prior to self-polymerization, in dependence of alkaline earth cation and co-solvent concentration. The generation of the purple color was found only from levodopa and dopamine, instead obtaining yellow solutions for norepinephrine and benserazide, and uncolored solutions for carbidopa in the same conditions. Therefore, we focused our investigations on the selective detection and quantification of LD in some anti-Parkinson tablet formulations (see "Materials and Methods") where levodopa is in co-presence of carbidopa at a mass ratio of 4:1 (LD 200 mg + CD 50 mg), together with numerous excipients. We optimized the solvent composition and experimental conditions for the selective detection and quantification of LD also in pharmaceutical formulations, after tablet dissolution, by using for the first time the purple stage of catecholamine oxidation here obtained as a colorimetric probe. The modulation of purple color intensity upon oxidation was explored up to 1 g L^{-1} for LD, following a dose-response trend, with a superimposable, selective, and linear colorimetric response for levodopa alone, after proper dilution between 10 mg L^{-1} and 40 mg L^{-1}, and in combination with carbidopa as for some anti-Parkinson drugs with a very good data reproducibility and sensitivity, appearing a valuable tool for rapid and low-cost point of care testing of LD content in such formulations.

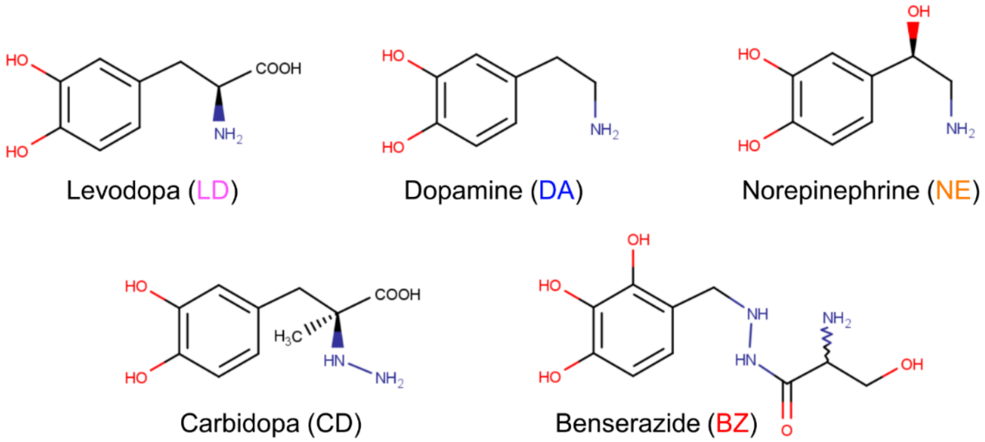

Figure 9.1.*Structural representation of some natural catecholamines levodopa (LD), dopamine (DA), norepinephrine (NE), and their synthetic analogues carbidopa (CD) and benserazide (BZ).*

9.3 Materials and Methods

9.3.1 Chemicals and reagents

Sodium acetate trihydrate (NaOAc, $(CH_3COO)Na \cdot 3H_2O$), magnesium acetate tetrahydrate ($Mg(OAc)_2$, $(CH_3COO)_2Mg \cdot 4H_2O$), calcium acetate monohydrate ($(Ca(OAc)_2$, $(CH_3COO)_2Ca \cdot H_2O$), barium acetate ($Ba(OAc)_2$, $(CH_3COO)_2Ba$), ammonium chloride (NH_4Cl), hydrochloric acid (HCl), dimethyl sulfoxide (DMSO, C_2H_6OS), methanol (MeOH, CH_3OH), acetonitrile (MeCN, CH_3CN), levodopa (LD, $C_9H_{11}NO_4$), dopamine hydrochloride (DA, $C_8H_{11}NO_2 \cdot HCl$), norepinephrine (NE, $C_8H_{11}NO_3$), carbidopa (CD, $C_{10}H_{14}N_2O_4$) and benserazide hydrochloride (BZ, $C_{10}H_{15}N_3O_5 \cdot HCl$) have been purchased from Sigma-Aldrich (Milan, Italy). Brand drug Sinemet (200 mg levodopa, 50 mg carbidopa, 35 mg excipients) has been obtained from MSD (Rome, Italy) and its pharmaceutical alternative (generic drug) Hexal (200 mg levodopa, 50 mg carbidopa, 194 mg excipients) has been produced by Sandoz (Basel, Switzerland). All chemicals were of analytical reagent grade and used as received without any further purification. All solutions have been prepared using water obtained from Milli-Q Water Purification System (resistivity $\geq$ 18 MΩcm) (Germany, www.merckmillipore.com).

9.3.2 Methods and Instrumentations

Levodopa, dopamine, norepinephrine, carbidopa, and benserazide have been dissolved in HCl 1 M to obtain 100 g L^{-1} stock solutions. Stock solutions of a brand drug and the generic drug containing 5 g L^{-1} of levodopa have been prepared by stirring for 10 minutes one tablet (200 mg LD, 50 mg CD) in 4 mL of 1 M HCl, then adding 36 mL of DMSO and continuing stirring at 37 °C. The brand drug dissolved in 20 minutes giving a transparent orange solution, whereas the generic drug required 50 minutes, resulting in yellow suspension. The working solutions in DMSO, H_2O, and salts have been prepared within 24 hours from tablet dissolution, as further detailed in Results and Discussions section. Absorbance measurements have been performed in 1.0 cm cuvette at 20 °C by using a UV-Visible Spectrophotometer Evolution™ 201/220 from Thermo Scientific™ (Rodano, Milan, Italy).

9.4 Results and discussions

9.4.1 Assay principle

The O_2/ pH-induced non-enzymatic oxidation and self polymerization of catecholamines was recently exploited to generate biocompatible nanometric films with several applications ranging from (bio)analytical chemistry to materials science [215,358–365], using for example dopamine [359,360], norepinephrine [362,363], and levodopa [366], as functional monomers. Typically, catecholamine spontaneous oxidation is achieved at basic pH, which gives a black/brown polymer with a broad absorbance spectrum, including the visible region, with thickness and, consequently, absorbance intensity also depending on temperature, buffer concentration, and starting amount of catecholamine monomer [364,367]. Exploring unusual conditions for the growth of a polydopamine film, we noticed the different oxidation behaviors of catecholamines in dependence of alkaline earth cations in solution at a high millimolar range, leading to distinct colors corresponding to different stages of monomer oxidation, cyclization, and rearrangement, naturally occurring prior to polymerization. For levodopa (LD) and dopamine (DA), we obtained purple/blue color solutions ascribable to melanochrome formation, an elusive intermediate stage of catecholamine polymerization isolated by enzymatic oxidation [357,368], and tentatively identified as the dimer of indolequinone (Fig. 9.2) [369–372]. Consequently, we explored the chemical determinants of color development for some fundamental neurotransmitters (LD, DA, NE), and two synthetic analogues (CD, BZ) (Fig. 9.1), by changing cation, pH, ionic strength, and co-solvent concentration as detailed in the following sections, focusing the study on the detection of LD in combination with CD that, like BZ, is found in pharmaceutical formulations for the treatment of Parkinson's disease, whereas the other catecholamines here investigated (DA and NE) are not included in such drugs.

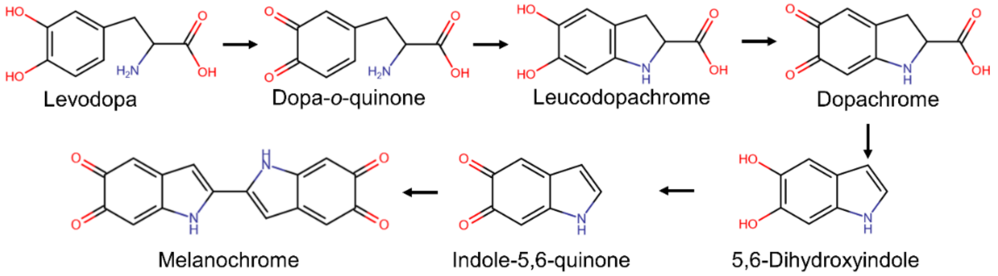

Figure 9.2. *Schematic representation of melanochrome synthetic pathway analogue to Raper-Mason pathway for the biosynthesis of melanin* [368–370]. *The oxidation of levodopa produces dopa-o-quinone, which gives leucodopachrome upon cyclization. The subsequent oxidation leads to dopachrome that rearranges to 5,6-dihydroxyindole, before to be oxidized to indole-5,6-quinone that dimerizes forming melanochrome.*

9.4.2 Influence of pH and Mg^{2+} concentration on color development by levodopa

Preliminary experiments on 96-well microplates were devoted to determining the influence of pH and magnesium salt concentration on melanochrome formation by oxidation of levodopa solution in H_2O/DMSO (1:1). Data were acquired by using a filter-based plate reader, reporting the absorbance at 595 nm (Fig. 9.3), *i.e.*, the best available optical filter for melanochrome detection. Absorbance values of levodopa solutions in 150 mM Mg^{2+} increased with pH (Fig. 9.3A), as expected for metal coordination by catechol moiety. However, the best condition was achieved at pH 9.4, due to high absorbance, lowest CV_{av}% (2.2%), and the absence of any precipitation that instead occurred at higher pH, where the solutions turned cloudy and orange (data not shown). Analogously, we observed that the absorbance values of levodopa solutions at pH 9.4 increased with Mg^{2+} concentration up to 150 mM (Fig. 9.3B), representing the best condition also in terms of CV_{av}% (1.9%). Accordingly, pH 9.4 and 150 mM Mg^{2+} were identified as the optimal conditions for any further experimental investigation.

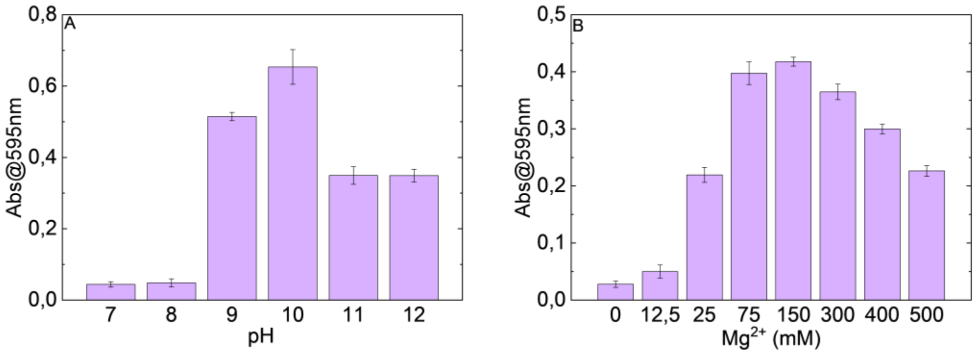

Figure 9.3. *Levodopa color development in dependence of pH A) and B)concentration of* $Mg(OAc)_2$ *in* NH_4Cl *at 20 °C on 96-well microplates. LD was solubilized at fixed final concentration of 0.20 g* L^{-1} *in* H_2O*/DMSO (1:1) a in presence of 150 mM* Mg^{2+} *acetate salt and 150 mM* NH_4Cl *at several pH values, or in presence of* Mg^{2+} *acetate salt and* NH_4Cl *up to 500 mM at pH 9.4. The absorbance values at 595 nm were acquired 15 min after mixing by using a filter-based microplate reader. Each bar represents the mean ± SD of 4 replicates.*

9.4.3 Influence of cation and solvent on color development by natural catecholamine

Here, we investigated the O_2/pH-induced oxidation [361] of levodopa (LD), dopamine (DA), and norepinephrine (NE) at fixed final concentration of 0.20 g L^{-1} in water or water/co-solvent in presence of 150 mM Na^{+}, Mg^{2+}, Ca^{2+}, or Ba^{2+} acetate salt and 150 mM NH_4Cl at pH 9.4. We showed the main role of cations and solvent in regulation of catecholamine oxidation. Remarkably, dopamine and levodopa solutions in DMSO/H_2O (1:1) containing magnesium salt stood out for the appearance of a purple/blue color (λ_{max} = 580–590 nm) at 20 °C, reaching the maximum absorbance after 15 min. It is worth to note that the similarity of levodopa and dopamine spectra and color here described was a consequence of their common synthetic pathway reported in Fig. 9.2, sharing the stages of the generation of 5,6-dihydroxyindole, and the oxidation to indole-5,6-quinone that dimerizes virtually forming the same melanochrome. DMSO could act as further oxidant; nevertheless, the purple color here ascribed to melanochrome formation [357,368–372] were also obtained by using methanol/ water (1:1) as solvent for levodopa (Fig. 9.4A) and dopamine (Fig. 9.4B) solutions, or acetonitrile/water (1:1) for dopamine only (Fig. 9.4B), likely underlines the main influence of these solvents on pKas and on the oxidation potentials of catecholamines and their derivatives [373–375].

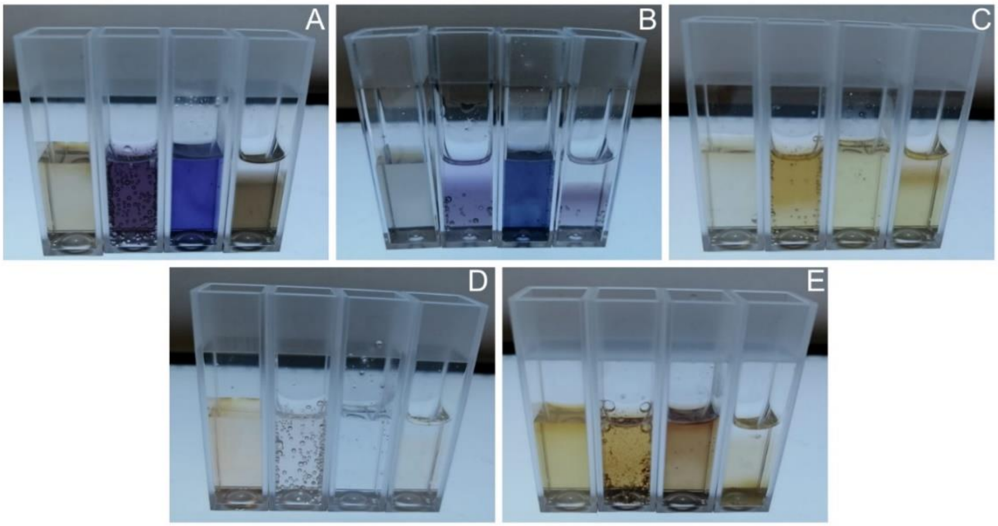

Figure 9.4. *Color development in dependence of solvent. Dopamine (A), levodopa (B), norepinephrine (C), carbidopa (D), and benserazide (E) were solubilized at final concentration of 0.20 g* L^{-1} *in 150 mM* $Mg(Ac)_2$ *and 150 mM* NH_4Cl *at pH 9.4 in* H_2O, CH_3OH/H_2O *1:1,* $DMSO/H_2O$ *1:1 and* CH_3CN/H_2O *1:1 (from the left to the right of each picture). Photos were acquired at 20°C after 15 min solution mixing.*

Finally, DMSO was selected as the only co-solvent since it is non-flammable, less harmful, and less volatile among the tested ones. Differently from levodopa and dopamine, norepinephrine solution resulted yellow (λ_{max} = 410 nm) in the same conditions, likely due to the additional hydroxyl group in the ethyl chain when compared with dopamine and levodopa (Fig. 9.1 and Fig. 9.4C), which confers peculiar properties to this catecholamine and its polymers as reported elsewhere [362,366]. Figure 9.5 displays the colored solutions and the corresponding absorption spectra for natural catecholamines upon addition of 150 mM alkaline earth cations in water and water/DMSO mixture at pH 9.4.

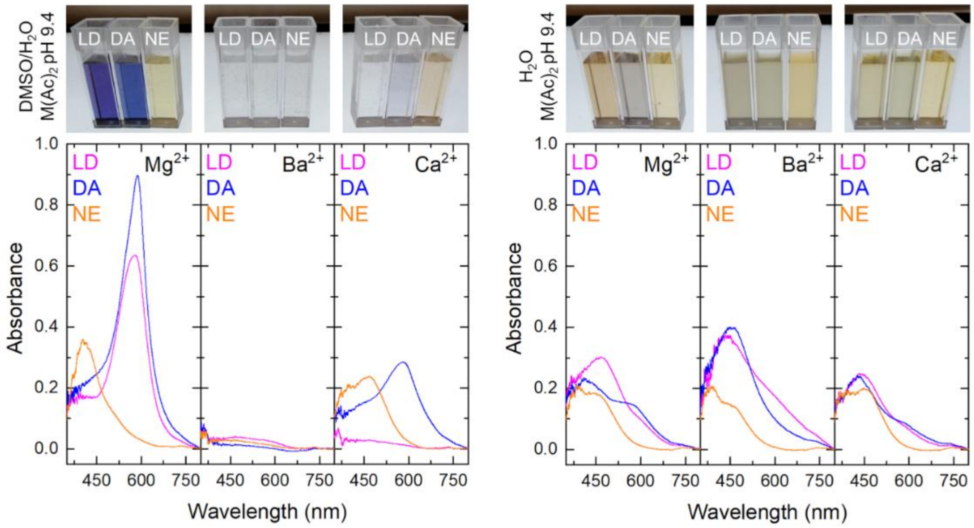

Figure 9.5. *Natural catecholamines color development in dependence of Mg^{2+}, Ba^{2+}, and Ca^{2+} at basic pH and fixed solvent composition. Levodopa (LD), dopamine (DA), and norepinephrine (NE) solubilized at 0.4 g L^{-1} in DMSO HCl 10 mM (left panels), or H$_2$O (right panels), and mixed with an equal volume of 300 mM Mg(OAc)$_2$, Ba(OAc)$_2$, and Ca(OAc)$_2$ in 300 mM NH$_4$Cl pH 9.4. Images and spectra have been acquired at 20 °C, 15 min after mixing.*

In the absence of the co-solvent, for any cation and catecholamine explored, the main absorption peak was around 440‑470 nm due to formation of dopa-, dopamine-, and norepinephrine-chrome, corresponding to yellow-orange solutions (Fig. 9.5 right panels, and Fig 9.4). Differently, water/DMSO mixtures in presence of 150 mM Mg^{2+} (to a minor extent with 150 mM Ca^{2+}, and without any color development with 150 mM Ba^{2+}) generated brilliant purple/blue colors for LD and DA, with a maximum absorbance around 580‑590 nm (melanochrome), and yellow-orange solutions for NE (Fig. 9.5 left panels). Moreover, increasing concentration of DMSO up to 50% v/v, in presence of 150 mM Mg^{2+}, led to red shift for LD and DA solutions due to conversion of yellow dopa- and dopamine-chrome to deeper blue/purple color of melanochrome according to the scheme reported in Fig. 9.2, whereas the NE solutions stayed yellow (Fig. 9.6) due to different reactivity. These colors were formed in 15 min, but solutions became darker with time, up to formation of black precipitate after 3 days (Figs. 9.7 and 9.8). No color development and no precipitation was observed during 3 days for water/DMSO mixtures of any catecholamine in presence of 150 mM Na^{+} at pH 9.4

(Fig. 9.9, lower panels), whereas the same solutions became darker in absence of DMSO (Fig. 9.9, upper panels), underling the capability of DMSO to slow down the kinetics of oxidation of these neurotransmitters here followed by using the absorbance at 415 nm in Fig. 9.10, elsewhere reported as characteristic of catecholamine polymerization [217].

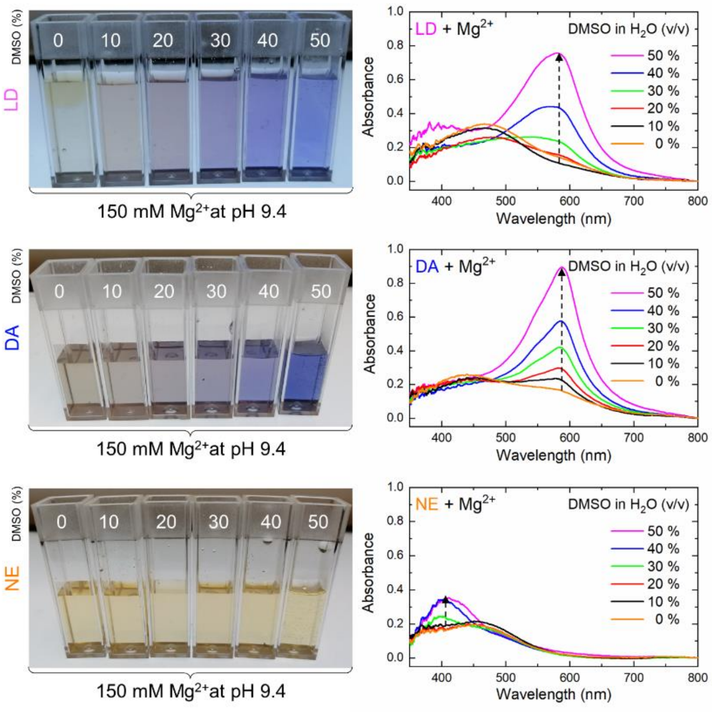

Figure 9.6. *Natural catecholamines color development in dependence of DMSO at basic pH and at fixed magnesium salt concentration. Levodopa (LD), dopamine (DA), and norepinephrine (NE) solubilized at 0.4 g L^{-1} in DMSO HCl 10 mM, or H_2O, and mixed with $Mg(OAc)_2$ in NH_4Cl at pH 9.4 to obtain different percentage in volume of DMSO in H_2O from zero to 50% as indicated by the arrow. Images and spectra have been acquired at 20 °C, 15 min after mixing.*

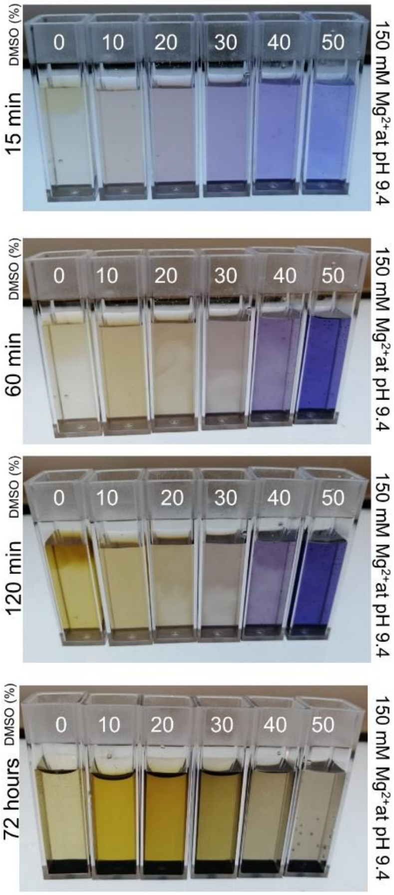

Figure 9.7. *Levodopa color development over time in dependence of DMSO at basic pH at fixed magnesium salt. LD was solubilized at final concentration of 0.20 g L^{-1} in 150 mM Mg(Ac)$_2$ and 150 mM NH$_4$Cl at pH 9.4 in presence of a different percentage in volume of DMSO in H$_2$O from zero to 50%. Photos were acquired at 20 °C after 15 min, 60 min, 120 min, 72 hours solution mixing.*

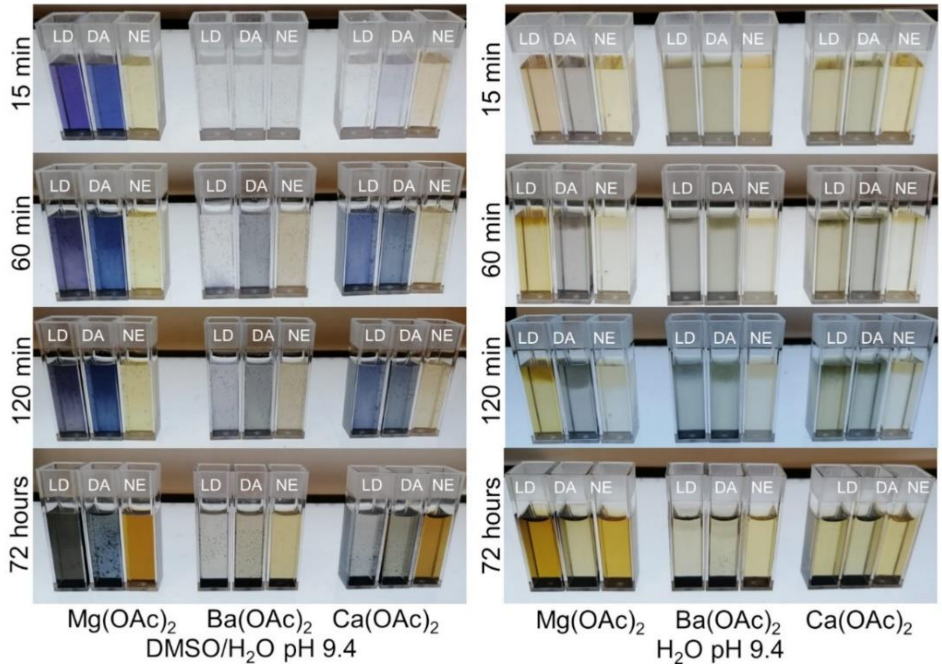

Figure 9.8. *Natural catecholamines color development over time in dependence of alkaline earth cation at basic pH. Levodopa (LD), dopamine (DA), and norepinephrine (NE) were solubilized at final concentration of 0.20 g* L^{-1} *in 150 mM* Mg^{2+}, Ba^{2+}, *or* Ca^{2+} *acetate and 150 mM* NH_4Cl *at pH 9.4, in DMSO/*H_2O *1:1 (left panels), or* H_2O *(right panels). Photos were acquired at 20 °C after 15 min, 60 min, 120 min, 72 hours solution mixing.*

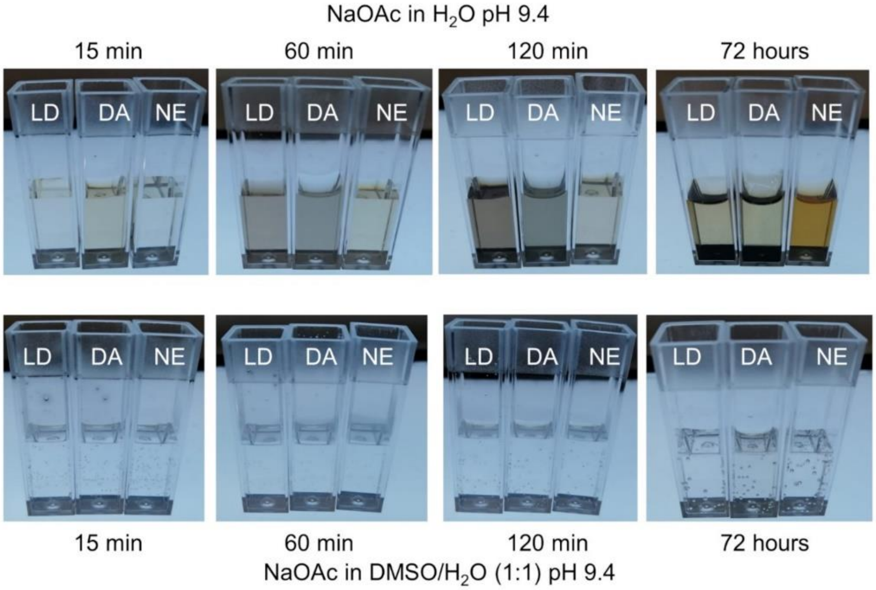

Figure 9.9. *Natural catecholamines color development in dependence of NaOAc at basic pH at fixed solvent over time. Levodopa (LD), dopamine (DA), and norepinephrine (NE) were solubilized at final*

concentration of 0.20 g L^{-1} in 150 mM Na^{+} acetate at pH 9.4 in H$_2$O (upper panels), or DMSO/H$_2$O 1:1 (lower panels). Photos were acquired at 20 °C after 15 min, 60 min, 120 min, 72 hours, solution mixing.

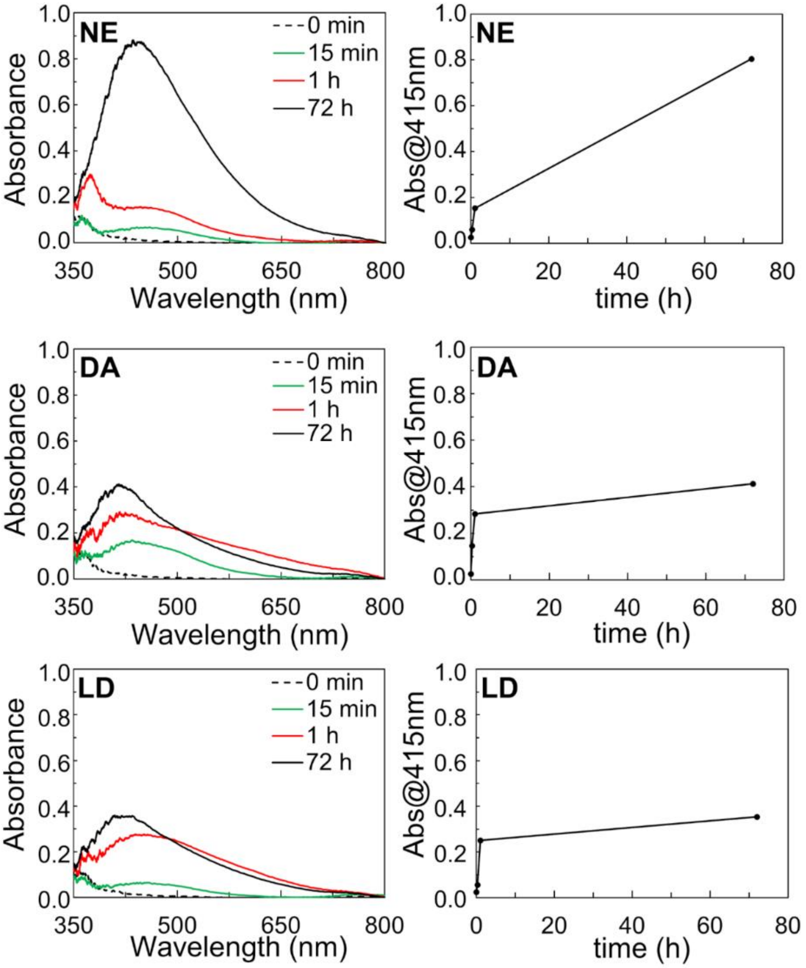

Figure 9.10. *Kinetics of oxidation of natural catecholamines in aqueous solutions without DMSO at basic pH at 20 °C. Visible spectra (left panels) and absorbance values at 415 nm (right panels) for NE, DA, and LD solutions as described in Fig. 9.8.*

9.4.4 Influence of Mg^{2+} and DMSO on color development by synthetic catecholamine analogues

On the base of the results reported above, aiming to finally selectively detect and quantify levodopa directly in pharmaceutical formulations, we evaluated the colorimetric behavior of two levodopa-decarboxylase inhibitors, carbidopa (CD) and benserazide (BZ), as possible interferents, taken singularly; CD and BZ are structurally related to endogenous catecholamines (Fig. 9.1), largely, but never together, present in levodopa tablets for the treatment of Parkinson's disease, whereas the other catecholamines here investigated, *i.e.*, dopamine and norepinephrine, are not included in such pharmaceutical formulations and, therefore, cannot interfere with the assay. We thus analyzed DMSO/water 1:1 (v/v), solutions of CD or BZ at constant concentration of Mg^{2+} (150 mM $Mg(OAc)_2$ solutions at pH 9.4) (Fig. 9.11); this was the selected condition to obtain the purple color development in presence of levodopa and thus used to explore the behavior of its analogues, eventually co-present in formulations. First, we analyzed CD and BZ solutions singularly to evaluate the assay applicability to binary solutions of LD and CD or BZ. In the case of BZ, a yellow solution (λ_{max} = 430‑450 nm) was produced at any percentage of DMSO tested, becoming darker at 50% DMSO. Accordingly, BZ was not further studied in this paper, requiring additional selectivity investigations and improvement for the application of such a method to drugs containing both LD and BZ. Differently, CD solutions showed an orange/pink color (λ_{max} = 400 and 480 nm) decreasing in intensity with increasing amount of co-solvent, becoming uncolored (λ_{max} = 360 nm) at 50% DMSO. Such peculiar behavior for CD among all the natural and synthetic molecules here studied, *i.e.*, the absence of any color development at high DMSO concentration, encouraged to test the approach here described in solutions containing both LD and CD as preliminary step for quantifying LD in pharmaceutical formulations also containing CD (see after).

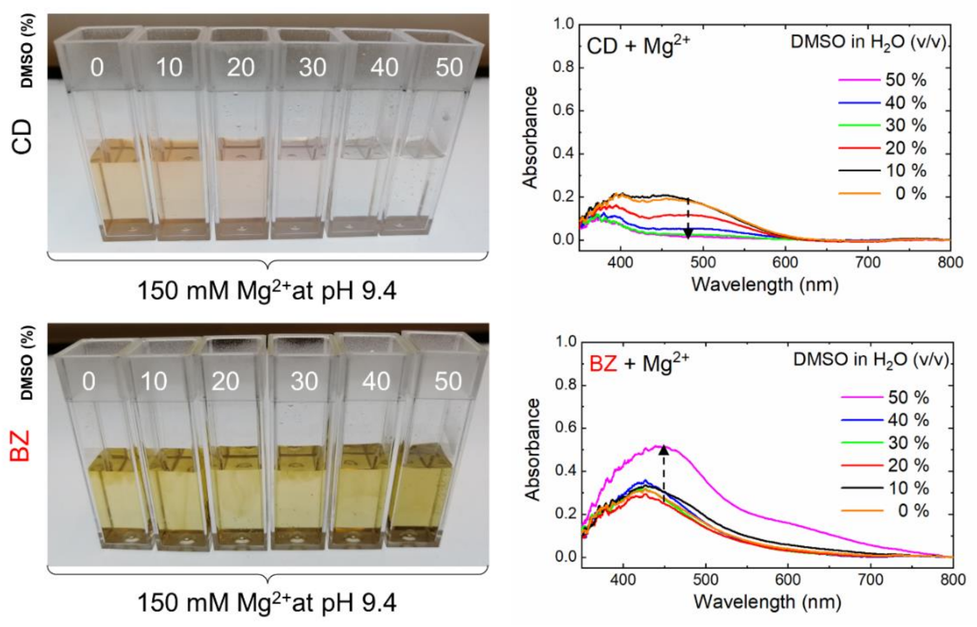

Figure 9.11. *Synthetic catecholamine analogues color development in dependence of DMSO at basic pH at fixed magnesium salt concentration. Carbidopa (CD) (upper panels) and Benserazide (BZ) (lower panels) were solubilized at 0.4 g* L^{-1} *in DMSO HCl 10 mM, or* H_2O*, and mixed with* $Mg(OAc)_2$ *in* NH_4Cl *at pH 9.4 to obtain a final concentration of 0.20 g* L^{-1} *with different percentage in volume of DMSO in* H_2O *from zero to 50% as indicated by the arrow. Images and spectra were acquired at 20 °C, 15 min after mixing.*

9.4.5 Colorimetric quantification of levodopa in tablets by using melanochrome as molecular probe

The best conditions here determined for color development from LD solutions, *i.e.*, 150 mM $MgAc_2$ in presence of 150 mM NH_4Cl at pH 9.4 in water/dimethyl sulfoxide 1:1 (v/v), were also applied to CD and LD+CD binary solutions with mass ratio of 4:1 as indicated in pharmaceutical formulations here used. The spectrophotometric analysis of LD and CD standard solutions showed (Fig. 9.12) a very clear concentration-dependent signal at 585 nm only for LD (black circles), giving the largest absorbance increase up to 40 mg L^{-1}, considered as the limit of linearity for the LD curve in Fig. 9.12 (left panel), and reaching a plateau at higher concentration. CD solutions (white circles), instead, did not show any absorption at this visible wavelength over the entire concentration range, as expected from uncolored solution already observed at high (50%) DMSO concentrations as reported in Fig. 9.11. Therefore, the developed colorimetric assay was applied to the binary mixture

(LD+CD 4:1), as simplified model, and validated by using commercially available levodopa/carbidopa tablets (the real samples) containing 200 mg of levodopa and 50 mg of carbidopa (from the package leaflet of tablets) as the large number of generic formulations appeared during the worldwide shortage of brand drug in 2010-2011 [376,377]. Figure 9.12 (right panel) shows the superposition of calibration curves for the standard solutions of LD alone (black circle), LD+CD 4:1 mixtures (black and white circles), and both the brand drug (blue circles) and the generic drug (red circles). All data were fitted according to the linear equation A @ 585nm = $m \times C$, (1), where m represents the slope of the melanochrome absorbance at 585 nm. The excellent test performances were also highlighted by the fitting parameters reported in Table 9.1, indicating very limited, if any, matrix effect despite the numerous excipients (see experimental section), also excluding any interference of CD with the assay in such conditions. The assay reproducibility between 10 mg L^{-1} and 40 mg L^{-1}, expressed as CV_{av}%, was 3.7% for LD, and 3.3% for LD+CD 4:1 mixture, brand drug, and generic drug. Other fitting parameters are reported in Table 9.1, including the limit of quantification found to be about 0.6 mg L^{-1} (3 μM) even in target matrices represented by tablets.

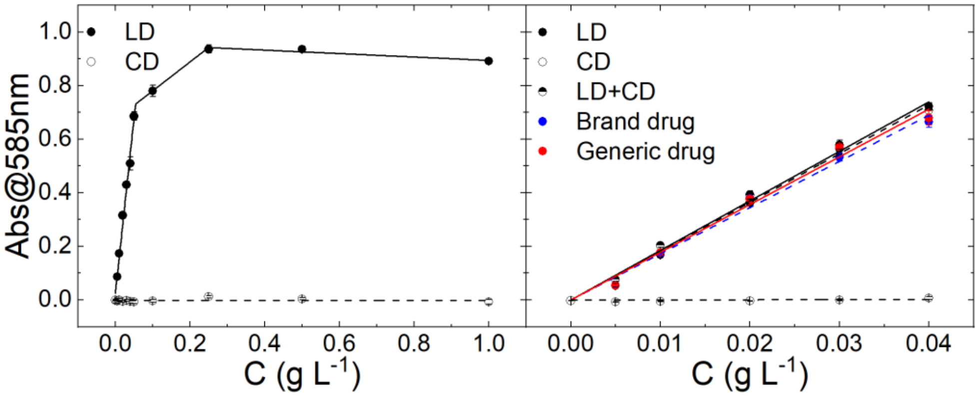

Figure 9.12. *Levodopa quantification curves up to 1 g L^{-1} (left) or 40 mg L^{-1} (right). Levodopa (LD, black circles), carbidopa (CD, white circles), LD+CD 4:1 mixture (black and white circles), brand drug (blue circles), and generic drug (red circles) were solubilized separately in DMSO/H_2O 1:1 (v/v) with 150 mM $Mg(OAc)_2$ and 150 mM NH_4Cl pH 9.4. Absorbance at 585 nm was acquired at 20 °C after 15 min of solution mixing. Each point represents the mean ± SD of 4 replicates. Absorbance data in the right panel were fitted according to linear equation 1.*

Table 9.1 *Linear fitting parameters for levodopa quantification.*

Sample	m (L g^{-1})	LOD (mg L^{-1})	LOQ (mg L^{-1})	R^2	CV_{av} %*
LD	18.19 ± 0.35	0.184 ± 0.036	0.615 ± 0.119	0.996	3.7
LD+CD	18.49 ± 0.42	0.181 ± 0.041	0.605 ± 0.138	0.993	3.3
Brand drug	17.24 ± 0.44	0.195 ± 0.051	0.649 ± 0.167	0.992	3.3
Generic drug	17.81 ± 0.51	0.188 ± 0.054	0.628 ± 0.182	0.990	3.3
*Calculated between 10 mg L^{-1} and 40 mg L^{-1}					

9.5 Conclusions

The main discovery behind the focus of this paper was the synergistic capability of dimethyl sulfoxide and magnesium cation to trigger and stabilize the purple melanochrome formation for natural catecholamines levodopa and dopamine only, likely modulating the pKas and the oxidation potentials of these natural neurotransmitters. In the same conditions, instead, norepinephrine and benserazide displayed yellow solutions, and the synthetic analogue carbidopa appeared uncolored. These results inspired the subsequent application of the optimized protocol to some pharmaceutical formulations for the treatment of patients with Parkinson's disease, which contain levodopa in presence of carbidopa at fixed ratio 4:1. The analytic colorimetric method here developed allowed the selective detection and quantification of the active substance, levodopa, in co-presence of a decarboxylase inhibitor, carbidopa, achieving a superimposable matrix- and carbidopa-independent colorimetric response with a common linear dynamic trend with high reproducibility in target matrices (CV_{av}%, 3.3% for brand drug and the generic drug) and very good sensitivity, with limit of quantification found to be 0.6 mg L^{-1}. Accordingly, this simple colorimetric method requiring just proper dissolution and dilution of pharmaceutical formulations could be used for rapid (15 min) and low-cost point of care testing of the LD content of drug tablets, resulting potentially useful for high-throughput analysis of brand and generic levodopa drugs. In addition, these results could represent a first step for a fast and non-invasive therapeutic drug monitoring of levodopa and its metabolites in specimens from patients with Parkinson's disease treated with such drugs in clinical practice. In this perspective, we proceeded our studies by applying the melanochrome-based colorimetric assay to levodopa quantification in human specimens. In addition, the observation of melanochrome, here stabilized and synthesized for the first time, prompted us to characterize it by means of mass spectrometry. The details related to these investigations are illustrated in the following section.

10

The first observation of melanochrome and indolequinone from catecholamines and their quantification in human urine

10.1 Abstract

In the section 9 we referred about the capability of magnesium cation in dimethyl sulfoxide at basic pH to favor the development of purple/blue color in presence of levodopa and dopamine due to formation of melanochrome, described as a dihydroxyindole/indolequinone conjugate, and yellow color in presence of norepinephrine, due to formation of 5,6-indolequinone. These molecules are elusive and, up to now, indirectly characterized species from the catecholamines polymerization pathway. Here, instead, we used the first enzyme-free synthesis and stabilization of soluble melanochrome and 5,6-indolequinone from catecholamines to elucidate the time-dependent formation and molecular weight by the direct examination of such compounds by means of mass spectrometry and UV-Vis. UV-Vis confirmed the presence of melanochrome with the same molecular weight of the enzymatic oxidation of dopamine and levodopa. Contrarily, norepinephrine in the same conditions gave the 5,6-indolequinone only. These results could facilitate the quantification of catecholamines in Parkinson's disease, enhancing the mass spectrometry imaging of their networks within the fine structures of a brain, as well as monitoring the LD-based pharmacological therapy of such disorder by colorimetric analysis of urine, helping to develop more effective pharmacological treatments of motor symptoms due to the deterioration dopaminergic neurons.

Keywords: levodopa, dopamine, melanochrome, Parkinson's, 5,6-indolequinone, norepinephrine.

10.2 Introduction

Parkinson’s disease (PD) is confirmed by post-mortem observation of Lewy bodies inside nerve cells and analysis of the selective deterioration of dopaminergic neurons, *i.e.*, the cause of motor symptoms and tremor [378]. The pharmacological treatment of PD is based on levodopa (LD) that crosses the blood-brain barrier and then restores the dopamine (DA) concentration in the brain, improving, momentarily, the quality of life of patients [379,380]. In section 9, we have reported the development of a colorimetric assay for the selective detection and quantification of levodopa in co-presence of carbidopa in some pharmaceutical formulations for the treatment of Parkinson’s patients [381]. Summarizing, the method was based on the discovery of the capability of magnesium cation in dimethyl sulfoxide to trigger the development of purple/blue color in presence of levodopa or dopamine, whereas this color was absent in the same environment for natural norepinephrine and for synthetic analogues carbidopa and benserazide. We ascribed the purple/blue color to melanochrome formation, an elusive intermediate stage of catecholamine polymerization previously generated by enzymatic oxidation of LD, 5,6-dihydroxyindole (DHI), or 5,6-dihydroxyindole-2-carboxylic acid (DHICA) [368,370–372,382,383] and described as biindolyls isomers generated from the nucleophilic attack of DHI molecule to the electrophile molecule 5,6-indolequinone (IQ) [370–372]. The uncertainties regarding the precise structure of melanochrome arose from its high instability and complete insolubility when obtained with previous methods that required the chemical reduction and the acetylation of the colored precipitate to achieve soluble fractions for the analyses, impairing the direct investigation of the molecule [370–372]. Analogously, any previous attempt to isolate and characterize the 5,6-indolequinone molecule failed, and indirect chemical evidence of an indolequinone formation was obtained by oxidation of analogues model molecules with protected reactive positions that conferred a longer stability to the transient intermediates [384–388]. Here, instead, we took the advantage of the first enzyme-free synthesis and stabilization of soluble melanochrome (λ_{max} 540-600 nm) derived from the naturally occurring neurotransmitters DA and LD, and 5,6-indolequinone (λ_{max} 340-360 nm) derived from norepinephrine (NE), in Mg^{2+}/DMSO at basic pH. Accordingly, it was possible to shed light on their molecular weights and time evolution by the direct examination of such compounds by means of LC-MS/MS-based analysis and by UV-Vis spectroscopy, confirming the molecular weight indicated for the enzymatic product for the purple/blue melanochrome [370]. The melanochrome was the main reaction product, with a m/z value 293.1 $[M+H]^+$, for synthesis starting from dopamine or levodopa, although with slightly different kinetics, therefore, indicating the decarboxylation of the latter monomer during the synthesis. Differently, according to an m/z value 147.2 $[M+H]^+$ and the UV-Vis spectra, we found that the reaction product of NE in the same condition was mainly the IQ, without melanochrome formation, underlining the main influence of the β-hydroxyl group on the oxidative pathway of NE. The time-dependent oxidation of each catecholamine was described by visible spectroscopy, recording the absorbance values over time at 340 nm, which is associated with IQ formation and 590 nm, which is associated with melanochrome. We believe that stable species generation and quantification in situ here characterized represents a promising 'self-staining' tool to enhance the selective mass spectrometry imaging of catecholamines (DA, LD and NE) networks within the fine structures of a brain affected by Parkinson's disease [389,390], hope-fully contributing to understand the molecular basis of such disorder and helping to develop more effective pharmacological treatments of the symptoms. Finally, we sensitively determined levodopa (LODs 2.00 mg L^{-1}) and dopamine (LOD 4.00 mg L^{-1}) concentrations in human urine samples taking advantage of purple melanochrome synthesis. This confirmed the validity of the melanochrome-based colorimetric method as responsive detection strategies for levodopa and dopamine quantification. This could represent an invaluable tool for the monitoring of levodopa therapy.

10.3 Materials and Methods

10.3.1 Chemicals and Reagents

Magnesium acetate tetrahydrate ($Mg(OAc)_2$, $(CH_3COO)_2Mg \cdot 4H_2O$), ammonium chloride ($NH_4Cl$), hydro-chloric acid (HCl), dimethyl sulfoxide (DMSO), levodopa (LD, $C_9H_{11}NO_4$), dopamine hydrochloride (DA, $C_8H_{11}NO_2 \cdot HCl$) and norepinephrine

(NE, $C_8H_{11}NO_3$) were purchased from Sigma-Aldrich (Milan, Italy). Artificial urine (AU) was from LCTech GmbH (Obertaufkirchen, Germany).

Urine samples: the assay was tested on human urines (see ethical standard*). Samples were chosen among those destined for destruction at the Clinical Pathology Laboratory of the University Hospital in Pisa and pseudonymized. Spiked samples were eventually obtained and tested. Absorbance measurements on urine samples were performed in the Clinical Pathology Laboratory of the University Hospital in Pisa.

* The use of pseudonymized biological samples destined for destruction has been approved by the local Ethics Committee (CEAVNO), Pisa, Italy (13/02/2020) *

10.3.2 Methods and Instrumentations

Standard solutions 1000 µg L^{-1} of levodopa, dopamine and norepinephrine were prepared in 0.1 M HCl. Standard mixtures for quantitative analysis were prepared by serial dilution of each catecholamine in a proper buffer (150 mM $Mg(Ac)_2$, NH_4Cl at pH 9.4 in DMSO:H_2O 1:1(v:v)). The same buffer was used to dilute 1:4:4 (v/v) artificial urine or human urine samples from volunteers that did not assume levodopa-based drugs. The urine samples were spiked with a known amount of catecholamine spanning from 5.0 to 50.0 mg L^{-1} to simulate post-drug administered urine specimens.

Absorbance studies were performed at 25 °C by using Ocean View VIS-NIR (Maybachstrasse, Germany). The samples were analyzed in cuvettes with optical path length of 1.0 cm. Time-dependent studies were performed on levodopa, dopamine, or norepinephrine standard mixtures, recording the visible spectra from 0 minutes to 144 minutes. Absorbance measurements of spiked urine samples were performed in 96-wells microplate by using Thermo Scientific Multiskan GO Microplate Spectrophotometer (Fisher scientific, Rodano (MI)).

The LC-MS/MS analysis were performed by injecting 1 µL of standard mixtures of norepinephrine, levodopa, and dopamine via HPLC autosampler of 6420 triple quadrupole system with a HPLC 1100 series binary pump from Agilent Technologies (Milano). Samples were eluted (starting 1 min after injection) with a linear gradient consisting of eluent A (0.1% formic acid and 5 mM ammonium formate in water) and eluent B (0.1% formic acid and 5 mM ammonium formate in methanol) from 10 to 80% of eluent B in 4 min at a flow rate of 200 mL min^{-1}. The column was re-equilibrated at initial conditions for 4 min with eluent A. A mass spectrometry method analysis based on Multiple Reaction Monitoring (MRM) tandem mass spectrometry was set up to analyze the samples, by using a turbo ion spray source operating in positive and ion mode.

10.4 Results and discussions

10.4.1 LC–MS/MS Analysis

Dopamine standard mixture at 50 µg L^{-1} was used for optimization of the MRM transitions of melanochrome (MC), while an analogue norepinephrine solution was used for the optimization of IQ analysis. Samples were automatically tuned, accurately selecting ionization polarity, production, and collision energy (CE). A MS/Full Scan analysis was performed to find precursor ions of the target molecules. Subsequently, the selection of tandem mass spectral parameters improved the precursor ion detection. Finally, fragmentation experiments were performed at different collision energy (CE) for identification of the products of reaction (see Table 10.1). Figure 10.1A reports the MRM transitions of LD, where the coelution of the selected precursor/fragment ion pairs can be observed, using the most intense one for quantification, and the others as qualifiers of the products. Figure 10.1B shows the chromatogram of LD and melanochrome, the latter eluting before LD. Finally, Figure 10.1C indicates the formation of IQ molecule whereas neither NE monomer nor melanochrome were detected.

Table 10.1. *Results of LC-MS/MS analysis with MRM parameters in positive ion mode.*

Molecule	[1][M+H]$^+$	Product ions	[2]CE
DA	154.1	137.2	10
		91.1	25
		65.2	35
LD	198.1	152.1	10
		139.0	15
		135.0	15
		107.0	35
		79.0	35
[3]MC	293.1	214.9	15
		136,9	15
		121.9	25
		58.9	30
NE	170.1	107.1	15
		135.0	15
		151.8	15
[4]IQ	147.2	103.2	10
		73.9	20

[1]Precursor ion; [2]CE, Collision energy (eV); [3]Melanochrome from DA or LD; [4]IQ from NE

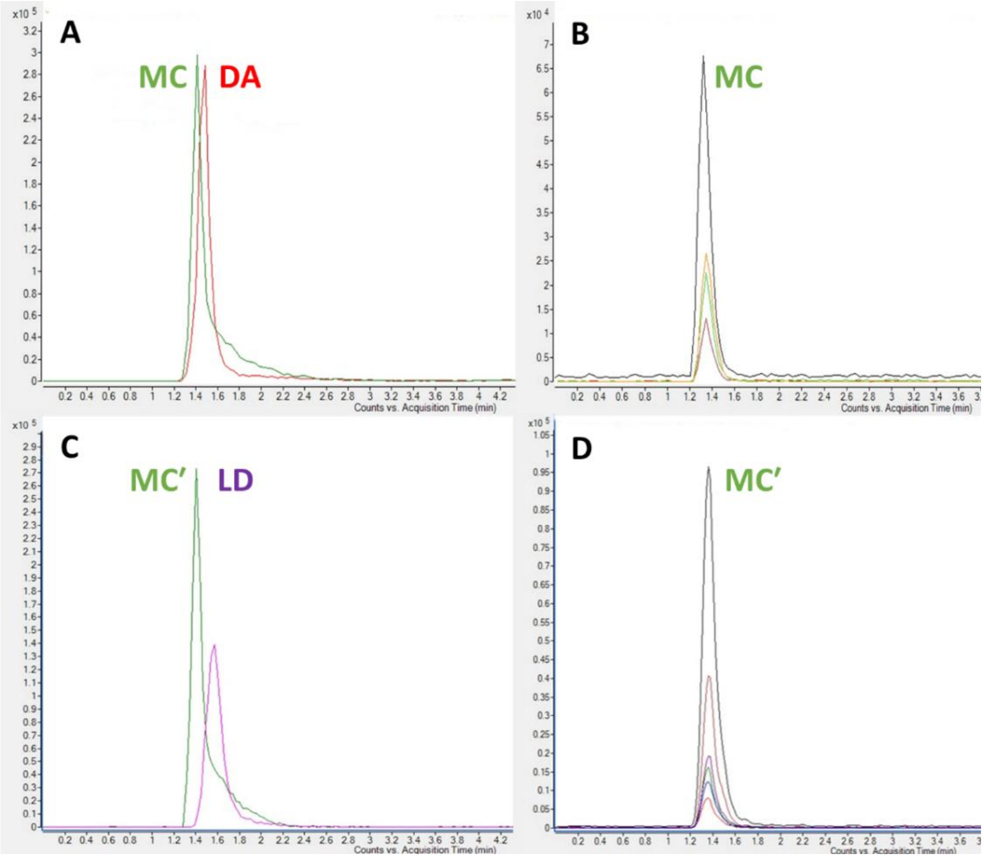

Figure 10.1.. MRM chromatograms of catecholamine standards DA (A) and LD (C) and correspondent melanochrome transitions (B, D).

10.4.2 Spectroscopic characterization of products

The comparison of the UV-Vis spectra indicates that the products of the oxidation of dopamine (Figure 10.2A) and levodopa (Figure 10.2B) in Mg^{2+}/DMSO at basic pH are strictly related, although not identical in shape and relative intensity of the bands, and very different from the products of the oxidation of norepinephrine in the same conditions (Figure 10.2C). Dopamine products gave a broad absorbance with a main peak in the visible region corresponding to the λ_{max} value found for the blue 2,2'-DHI-dimer (590-600 nm) [10], plus a barely visible shoulder at the λ_{max} value, previously associated to the purple 2,4'- and 2,7'-DHI-dimer (540 nm) as well as to the melanochrome formed by levodopa oxidation [368,370–372,382,383]. Spectra from levodopa were similar but the two visible peaks are almost equal in intensity. Notably, these soluble purple/blue molecules were obtained directly by DA and LD dissolution in a proper solvent system without enzymatic and chemical oxidation, transition metals, or the acetylation of 5,6-dihydroxyindoles, previously required to achieve soluble fractions of melanochrome for the analyses [370–372]. Differently, very low absorbance resulted for NE in the spectral region associated to melanochrome formation, showing instead a larger absorbance band with less defined λ_{max} value about 340-360 nm (Figures 10.2C and 2F). However, this broad band covers the visible region, conferring a yellow color to the solutions. A similar peak at 340-360 nm appeared also after oxidation of DA and LD, reaching roughly the 50% (Figure 10.2A) or 100% (Figure 10.2B) of the corresponding melanochrome absorbance, respectively. According to literature data and results from mass spectrometry (see above) the absorbance band with a λ_{max} about 340-360 nm was ascribed to IQ, here appearing stable, differently from any previous characterization attempt confined to 5,6-dihydroxyindole analogues presenting substituents at the reactive positions of the indole ring [382,384–388]. Finally, the melanochrome formation appears faster for LD than DA (Figures 10.2D and 10.2E, respectively), reaching a plateau after 1 hour or reaction at 25 °C for LD only. Considering the equal boundary conditions here explored for synthesis and analysis, in terms of concentrations, temperature, solvents, ionic strength, and pH, we ascribed the differences between spectra in Figure 10.2 to different abundance of reaction products that depend on the substituents of the catecholamine monomer, *i.e.*, the α-carboxylic group for LD, and the β-hydroxyl group for NE. These results on DA and LD, in fact, agree with previous studies on DHI and DHICA, where the oxidative coupling led to several melanochrome isomers, with the same m/z, with different kinetics of formation [387,390–392]. Analogously, our results on NE oxidation agree with the evidence in literature that this neurotransmitter, although was able to generate synthetic or natural melanins, as DA and LD, evades the melanochrome formation through a different oxidative pathway [393,394]. Although out of the scope of this paper, our results could give further insights into the biological route to melanins. In fact, the large amount of IQ here detected for NE oxidation underlined that IQ formation is not sufficient for the melanochrome synthesis. In fact, considering that the formation of the 2,2'-, 2,4'-, and 2.7'-biindolyls, *i.e.*, the melanochrome isomers, previously isolated by oxidation of DHI [370–372,390], was associated to the nucleophilic attack of DHI molecule to the electrophile molecule IQ, it is possible that in our conditions the redox equilibrium of indole derivatives upon NE oxidation is largely dominated by IQ, largely limiting the nucleophilic reagent concentration and, thus, impairing the melanochrome formation. More importantly, the generation and quantification here demonstrated for the peculiar species derived from fundamental neurotransmitters could represents a facile 'self-staining' tool to improve the selective mass spectrometry imaging of their networks within the brains affected by Parkinson's disease [395], therefore contributing to a better understanding of molecular anomalies responsible for such disorder and the effectiveness of the related pharmacological treatment.

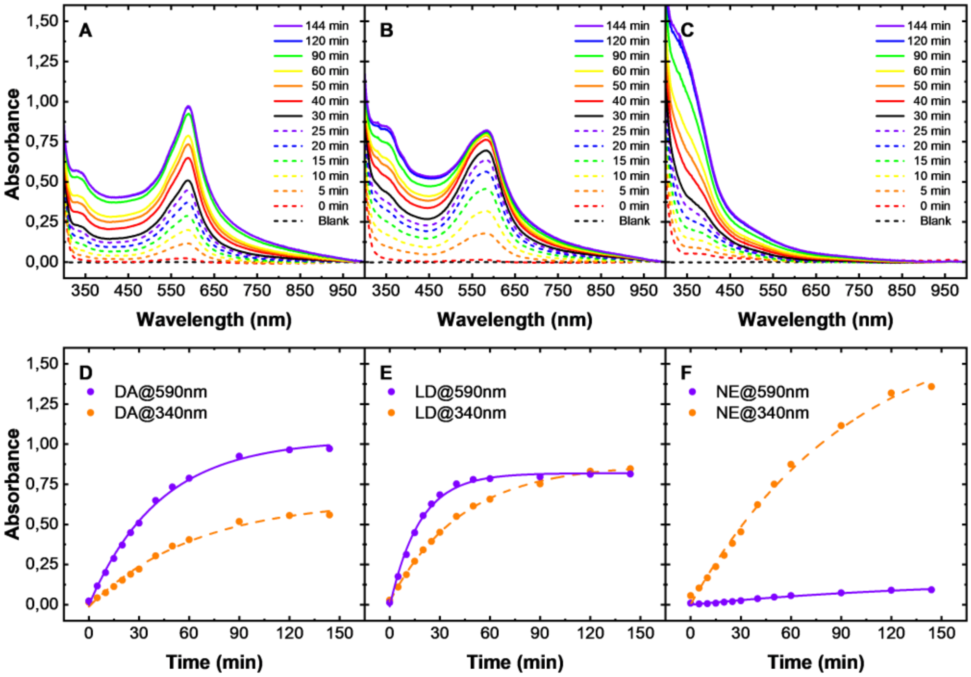

Figure 10.2. *Time-dependent oxidation of natural catecholamines 0.2 g L^{-1} in DMSO:H_2O 1:1 (v/v) in presence of 150 mM Mg(Ac)$_2$, 150 mM NH_4Cl at pH 9.4 and 25 °C between 2 min to 144 min. UV-Vis spectra (upper panels) and absorbance values (lower panels) at 340 nm (orange circles/dashed line) and 590 nm (purple circles/dashed lines) for dopamine (A-D), levodopa (B-E), and norepinephrine (C-F).*

10.4.3 Quantification of levodopa and dopamine in human urine samples

The monitoring of pharmacological therapy of Parkinson's disease plays a key role in evaluation of how the patients respond to it. In patients that receive long-term levodopa therapy, particularly in elderly patients, the drug compliance may be an important cause of variation in drug response [396]. Frequently, the dosage could result inappropriate generating toxic effects. This often occurs in subjects that take less than their prescribed dose, increasing inappropriately their dosage. In reducing problems with drug therapy, related to treatment success, failure or toxicity, regularly assessing patients' drug therapy is among the most important aspects of patient care. This ensures that patients take their medications as prescribed, proactively identify the adverse reactions as they occur, and assess therapeutic effectiveness. This is significant also for pharmaceutical companies to ensure that patients obtain the greatest benefit and suffer the least harm from their medicines. For these reasons, a simple, low-cost and non-invasive method that guarantees the monitoring of drug treatment on Parkinson's subject, is necessary.

The melanochrome-based colorimetric assay, here developed, was able to sensitively, selectively and reproducibly detect levodopa in human urine samples. Concentration between 3.00 mg L^{-1}- 50 mg L^{-1} of levodopa and dopamine, are usually found in Parkinson's patients undergoing pharmacological therapy [397,398]. The presence of DA in urine is due to exogenously-administered of LD that is converted to DA in peripheral tissues [399]. In this regard, the melanochrome-based colorimetric assay was applied for the detection of LD e DA in human urine.

The assay was performed in a 96-wells microplate to process different samples simultaneously, reducing the analysis time. The experimental procedure that ensures LD quantification in urine, was firstly optimized in artificial urine (AU). Different ratios between AU samples containing LD, $Mg(Ac)_2$ and DMSO were adopted to evaluate which of them enabled the maximum absorbance signal. The following volume ratios were examined: 0.5:0.5:0.5, 1:1:1, 1:2:2, 1:4:4, and 1:10:10 corresponding to AU:$Mg(Ac)_2$:DMSO. A visible purple color, due to melanochrome formation, that results in the highest absorption and therefore in LD and DA sensitive detection, was obtained for the volume ratio of 1:4:4. This volume ratio was applied for the following experiments. In order to evaluate the matrix effect on the LD detection, LD was primarily quantified in artificial urine samples obtaining the linear calibration plot reported in Figure 10.3.

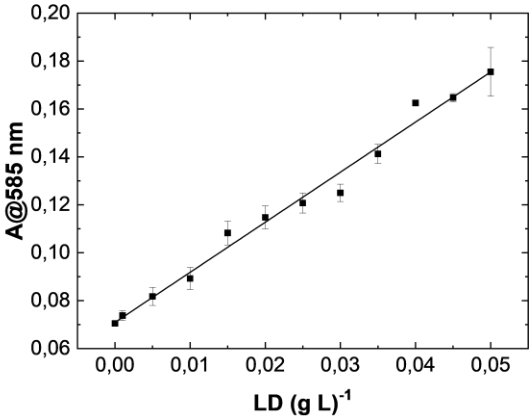

Figure 10.3. *Calibration plot relative to levodopa quantification in human urine samples. The absorbance signal was recorded at 585 nm after 15 minutes and was plotted versus levodopa concentration. The linear fitting parameters are reported in the Table 10.1.*

Table 10.1 *Linear fitting parameters for LD detection in artificial urine.*

Sample	***m (L g^{-1})***	***LOD (mg L^{-1})***	***LOQ (mg L^{-1})***	***R^2***	***CV_{av} (%)****
LD	*2.09 ± 0.08*	*1.65 ± 0.06*	*5.50 ± 0.20*	*0.986*	*3*

Based on these preliminary results, we proceeded to determine LD and DA concentration in human urine samples. For the analysis, spiked LD and DA human urine samples were used. Then, $Mg(Ac)_2$ and DMSO were added to urine samples containing LD or DA according to the volume ratio 1:4:4. The absorbance measurements were performed after 15 minutes of reaction, reading the absorbance values at 585 nm [381]. As shown in the Figure 10.4, and the analytical parameters reported in Table 10.2, levodopa and dopamine were successfully quantified showing CV_{av}% values of 6 % and 4 % respectively, and a LOD of 2.00 mg L^{-1} for LD and 4.00 g L^{-1} for DA, observing the reference values of LD and DA usually find in Parkinson's patients. As expected from the spectra in Figure 10.2C, NE did not generate the purple color. The excellent analytical performance, here obtained, confirms that the melanochrome-based colorimetric method is completely matrix-independent.

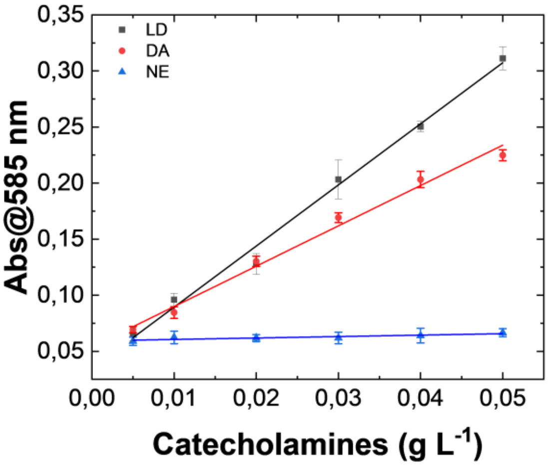

Figure 10.4. *Calibration plots of levodopa (black line), dopamine (red line), and norepinephrine (blue line) relative to their quantification in human urine. Absorbance signals were recorded at 585 nm after 15 minutes. The linear fitting parameters are reported in the table below (Table 10.2).*

Table 10.2 *Linear fitting parameters for LD and DA detection in human urine.*

Sample	*m (L g^{-1})*	*LOD (mg L^{-1})*	*LOQ (mg L^{-1})*	*R^2*	*CV_{av} (%)*
LD	*5.45 ± 0.20*	*2.00 ± 0.10*	*8.10 ± 0.03*	*0.992*	*6*
DA	*3.60 ± 0.10*	*4.00 ± 0.10*	*12.3 ± 0.34*	*0.990*	*4*

10.5 Conclusions

We have determined the molecular weight of soluble melanochrome from dopamine and levodopa, confirming for both catecholamines the formation of purple/blue biindolyl molecules, previously indicated for the elusive enzymatic product of oxidation of these neurotransmitters. Moreover, we found that norepinephrine in the same condition gave only the 5,6-indolequinone monomer, previously characterized only for analogues model molecules. These results could give further insights into the synthetic route to melanins, contributing to understanding the molecular basis of disorders associated with neurotransmitter depletion. Recently, chemical modification of phenolic and primary amine functional groups enabled the mapping of the dopamine and serotonin pathways, together with other neurotransmitters, metabolites, and amino acids [384]. In this framework, the procedure here described should offer a new more selective analytical tool for dopamine pathway characterization implementing the highly sensitive mass spectrometry imaging of ex-vivo tissue specimen from the human brain [385], towards more effective attempts in pharmacological treatment of motor symptoms of Parkinson's disease. Finally, the synthesis of melanochrome was successfully exploited for levodopa and dopamine detection in human urine samples. The remarkable analytical performance of the melanochrome-based colorimetric assay, in terms of sensitivity, reproducibility (CV_{av}% 6 for LD and 4 % for DA) and selectivity, confirmed that the developed assay was completely matrix-independent. The obtained LODs observed the threshold values of LD and DA content usually found in human urine of Parkinson's patients under drug therapy. Therefore, the melanochrome-based colorimetric assay could facilitate drug monitoring in Parkinson's patients. As a result, the melanochrome assay could represent a promising tool for the clinical practice in the management of pharmacological therapy in Parkinson's subjects.

11

Colorimetric determination of carbidopa in anti-Parkinson drugs based on 4-hydroxy-3-methoxybenzaldazine formation by reaction with vanillin

Anal. Bioanal. Chem. 414 (2022) 6911–6918 – **DOI**: 10.1007/S00216-022-04256-4

11.1 Abstract

In this work is reported the selective colorimetric detection and quantification of carbidopa, an inhibitor of aromatic amino acid decarboxylase, in the co-presence of levodopa as dopamine precursor in pharmaceutical formulations for the treatment of Parkinson's disease. The method is based on the selective condensation reaction between the hydrazine group from carbidopa and the formyl functional group of vanillin, a natural flavoring agent, in acidified alcoholic solution. The yellow color development (λ_{max} ~ 420 nm) due to the formation of 4-hydroxy-3-methoxybenzaldazine (HMOB) was observed for carbidopa only, whereas levodopa, lacking the hydrazine group, did not color the solution, as expected. The calibration curves for two tablet formulations of levodopa in combination with carbidopa (4:1) were superimposable with levodopa/carbidopa (4:1), as well as carbidopa alone, in standard solution, *i.e.*, the excipients and additives did not interfere with carbidopa determination, corresponding to a mean recovery about 105%. The linear dynamic range was between 5.00 and 50.0 mg L^{-1} with very good reproducibility within this range (CV_{av}% about 3-4%) and very good sensitivity, with limits of quantification of about 1 mg L^{-1}. The colorimetric method developed here is very simple, inexpensive, and effective for drug estimation and quality control of pharmaceutical formulations.

Keywords: Anti-Parkinson drugs, Vanillin, Benzaldazine, Levodopa, Carbidopa, Colorimetry.

11.2 Introduction

As already mentioned, the pharmacological treatment of PD is based on levodopa (LD), which is the molecular precursor of DA, together with carbidopa (CD), which works as peripheral inhibitor of aromatic amino acid decarboxylase, avoiding the conversion of LD in DA prior to crossing the blood–brain barrier, thus largely reducing the dose, and the resulting side effects, of levodopa to be administered. Several methods were developed for CD determination in presence of LD in such drugs by means of chromatography [400], electrochemistry and electrophoresis [342,344], spectrophotometry [350,351,401], and NMR [355]. In section nine it was reported the selective detection and quantification of levodopa in co-presence of carbidopa in these commercial drugs for the treatment of PD. The method was based on the generation and stabilization of the purple melanochrome (λ_{max} ~ 585 nm) from levodopa by using magnesium acetate and dimethyl sulfoxide [381]. Here, instead, it is reported the detection and quantification of carbidopa for the same tablet formulations, exploiting the well-known and selective reactivity of the hydrazine group of carbidopa with an (aromatic) aldehyde. At the same time, the levodopa, lacking the hydrazine group, forms only an imine and leaves the solution not colored at acidic pH. It was decided to use vanillin (4-hydroxy-3-methoxybenzaldehyde), observing the yellow color development (λ_{max} ~ 420 nm) due to formation of 4-hydroxy-3-methoxybenzaldazine by reaction with carbidopa (Fig. 11.1). The same azine was previously obtained by the condensation of free hydrazine molecule with vanillin: (a) as a probe to develop a colorimetric hydrazine dosimeter [402]; (b) as a Schiff base ligand to generate biologically active transition metal complexes [403]; (c) as side-products [404]. Moreover, an analogous azine was obtained by reaction of carbidopa with p-dimethylaminobenzaldehyde (DMAB) for spectrofluorimetric determination of carbidopa in monkey plasma [405]. However, being vanillin a well-known water soluble and naturally occurring flavoring agent used in food industries [406,407], although adverse effects can occur due to chemical reactivity, it appears a safer and convenient alternative to the synthetic and low water-soluble DMAB. Based on this, it was decided to develop a colorimetric quantitative assay for CD estimation, offering a simple, fast, and low cost alternative to the other methodologies requiring large instrumentation, for control of pharmaceutical formulations also in advanced drug delivery systems [356]. It was explored the chemical determinants of color development for CD by changing vanillin concentration, solvent composition and pH, heating temperature and time, as detailed in the following sections, focusing the study on the detection of CD in combination with LD as found in some pharmaceutical formulations (Sinemet and Hexal) for the treatment of parkinsonism.

Major efforts were devoted to obtaining large, selective, and reproducible color development from CD solutions, avoiding at the same time both the possible interference from the pharmaceutical additives and the spontaneous oxidation and polymerization of LD, typical of catecholamines, which gives rise to a black/brown polymer with a broad absorbance spectrum, including the visible region, therefore potentially affecting the colorimetric assay [360,361,364,365]. We found the generation of the yellow color from carbidopa and uncolored solutions for levodopa in the same buffer conditions, irrespective of the notable redox properties of LD [381]. Therefore, we focused our investigations on the selective detection and quantification of CD in some anti-Parkinson tablet formulations at a mass ratio of 4:1 (LD 200 mg + CD 50 mg), together with numerous excipients. The modulation of yellow color intensity upon vanillin reaction was explored up to 200 mg L^{-1} LD and 50.0 mg L^{-1} CD. The calibration curves for two tablet formulations were superimposable to levodopa/carbidopa (4:1), as well as to CD alone, showing a linear dynamic range between 50.0 and 5.00 mg L^{-1} of CD with very good reproducibility within this range and a good mean recovery of CD for both drugs. Data were acquired by using a common microplate reader, underlining the affordability of the method for drug estimation and quality control of pharmaceutical formulations. Furthermore, based on the very good sensitivity, for brand and generic drugs, this assay could pave the way for future research into therapeutic monitoring areas for carbidopa-based medications.

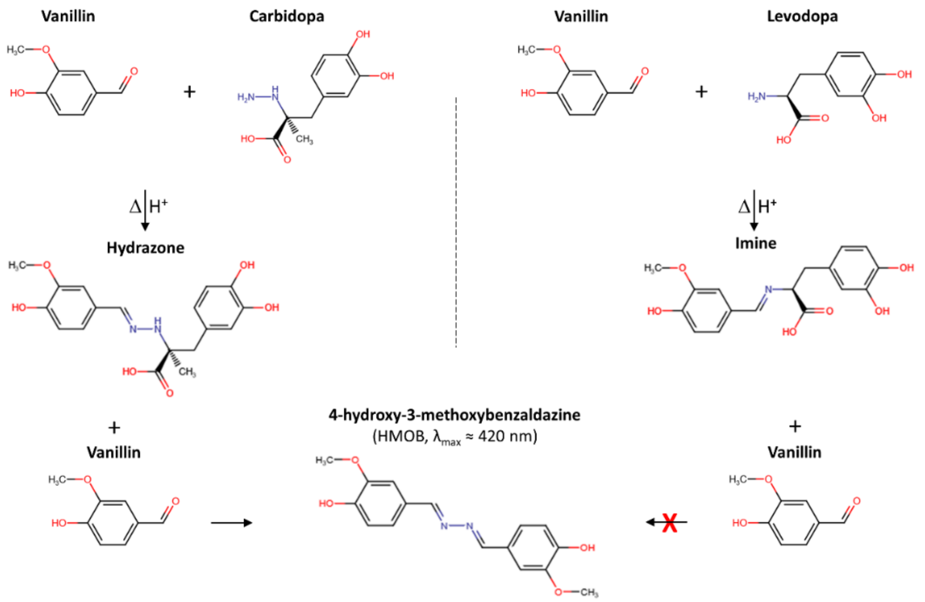

Figure 11.1.*Scheme of condensation reactions of vanillin with carbidopa and levodopa. Carbidopa hydrazide functional group produces a hydrazone that further reacts with an excess of vanillin to form the 4-hydroxy-3-methoxybenzaldazine (HMOB), with a maximum visible absorbance about 420 nm (yellow). Levodopa amine group produces an imine that cannot generate the azine, leaving the solution uncolored at acidic pH.*

11.3 Materials and Methods

11.3.1 Chemicals and Reagents

Carbidopa (CD, (2S)-3-(3,4-dihydroxyphenyl)-2-hydrazinyl-2-methylpropanoic acid), levodopa (LD, (2S)- 2-amino-3-(3,4-dihydroxyphenyl)propanoic acid), vanillin (4-hydroxy-3-methoxybenzaldehyde), acetonitrile (MeCN), ethanol (EtOH), dimethyl sulfoxide (DMSO, methylsulfinylmethane), methanol (MeOH), and hydrogen chloride (HCl) were purchased from Sigma-Aldrich (Milan, Italy). Brand drug Sinemet (200 mg levodopa, 50 mg carbidopa, 35 mg excipients) was obtained from MSD (Rome, Italy), and its pharmaceutical alternative (generic drug) Hexal (200 mg levodopa, 50 mg carbidopa, 194 mg excipients) was produced by Sandoz (Basel, Switzerland). All chemicals were of analytical reagent grade and used as received without any further purification. All solutions were prepared using water obtained from Milli-Q Water Purification System (resistivity ≥ 18 MΩcm) (Germany, www. merckmillipore. com).

11.3.2 Methods and Instrumentations

Carbidopa and levodopa were dissolved in HCl 1.00 M to obtain 100 g L^{-1} stock solutions. Stock solutions of a brand drug and the generic drug containing 5.00 g L^{-1} of levodopa were prepared by stirring for 10 minute one tablet (200 mg LD, 50 mg CD) in 40.0 mL of 1.00 M HCl. The working solutions were prepared within 24 h from tablet dissolution. The samples were heated by using thermomixer to control time and temperature of the reaction. All the solutions in different solvents (acetonitrile, methanol, ethanol, water, dimethyl sulfoxide, and EtOH:H_2O mixtures) contained 50.0 mg L^{-1} 1 (0.221 mM) of CD and 10.0 mM vanillin. The same CD and vanillin concentrations were used for EtOH:H_2O (1:1) solutions containing HCl 5 mM, 50 mM, or 500 mM. In all these cases the absorbance spectra were acquired after 4 h at 70 °C. The condition of CD 50.0 mg L^{-1} in EtOH/H_2O 1:1 with HCl 0.500 M at 70 °C was applied also to different vanillin concentrations (0.00, 1.25, 2.50, 5.00, 10.0, 20.0 mM) for 4 h: vanillin 10.0 mM at 30 °C, 40 °C, 50 °C, 60 °C, 70 °C, 80 °C for 4 h; vanillin 10.0 mM at 70 °C for 15, 30, 60, 120, 240 min. For calibration curves, each concentration of CD, LD + CD 4:1, or pharmaceutical formulations was in HCl 1.00 M, and added then to vanillin 20.0 mM in ethanol, obtaining the final sample solutions in EtOH:H_2O 1:1, HCl 0.500 mM and vanillin 10.0 mM. The limit of detection (LOD) and the limit of quantification (LOQ) were calculated based on the standard deviation (SD) of the mean of the blank values, as $3 \times SD/m$ and $10 \times SD/m$, respectively, where m indicates the slope of the calibration curve. The assay reproducibility is reported as (mean) coefficient of variation (CV_{av}). Absorbance spectra were acquired in disposable polystyrene 96-well microtest plates (Sarstedt, Milan, Italy) by using iMark™ microplate visible absorbance reader with optical filters (Bio- Rad, Milan, Italy), as well as in 1.0 cm cell by using a UV‑Visible Spectrophotometer Evolution™ 201/220 from Thermo Scientific™ (Rodano, Milan, Italy).

11.4 Results and discussions

11.4.1 Assay principle

Pioneering works described the reaction between hydrazine and an acidified alcoholic solution of p-dimethylaminobenzaldehyde (DMAB), resulting in the development of a characteristic yellow color that was used for the quantitative determination of hydrazine and hydrazide derivatives [405,408,409]. More in general, the reactivity of the hydrazine, or hydrazide group, allows the formation of hydrazone by 1:1 by condensation with an aldehyde [402,410,411]. The hydrazone can further react with an aldehyde to form an azine [403–405,412,413] with several applications, ranging from material chemistry to medicinal chemistry [413]. When the aldehyde is aromatic, like a benzaldehyde derivative, the product of condensation resulted colored and fluorescent, depending on several factors, including the ring substitutions and solvent polarity [405,412]. Levodopa, instead, can give an aldimine (Schiff base) by amine/aldehyde condensation reaction, but cannot lead to azine formation, lacking the hydrazine group and therefore leaving the solution not colored at acidic pH, whereas at basic pH, LD, as other catecholamines (dopamine, norepinephrine, methyldopa), can form yellow unstable aminochrome derivatives [337,381,414,415]. Grounded on this, we decided to develop a colorimetric assay for carbidopa quantification based on the reaction of an excess of vanillin (4-hydroxy-3-methoxybenzaldehyde) with the hydrazide group of carbidopa at acidic pH to generate the yellow 4-hydroxy-3-methoxybenzaldazine (HMOB, λ_{max} ~ 420 nm in ethanol/water solution) and 3,4-dihydroxyphenylacetone in Fig. 11.1 [416,417].

11.4.2 Influence of solvent composition and pH on color development

Several experimental parameters of HMOB formation were tested here by using a spectrophotometer or a microplate reader for visible absorbance detection. Firstly, the role of solvent composition and pH on carbidopa/vanillin reaction at 70 °C for 4 h was evaluated for 50.0 mg L^{-1} (0.221 mM) of CD in presence of a large excess of vanillin (10.0 mM) by using absorbance spectra acquired in quartz cuvettes. Figure 11.2A shows that the absorbance of the solution decreased with the polarity of the solvent, reaching the largest values for acetonitrile or methanol, and the lowest values for H_2O

or DMSO. Pure ethanol appeared as a good compromise between sensitivity and health risk. Accordingly, we decided to continue the method development based on ethanol:water solutions. Figure 11.2B reports the results of the same reaction for different compositions of EtOH:H_2O as a solvent system. The color development was proportional to ethanol content, as expected from Fig. 11.2B. Interestingly, absorbance spectra for EtOH:H_2O 3:7 and 1:1 appeared almost superimposable, and this aspect resulted very useful to develop a robust assay with a minimal dependence on possible variation of solvent composition. Therefore, we focused on EtOH:H_2O (1:1) solvent system, exploring the dependence of the reaction on the acidity of the solution. Figure 11.2C shows the large intensity increase obtained incrementing the HCl content from 5 to 500 mM, with a λ_{max} about 420 nm.

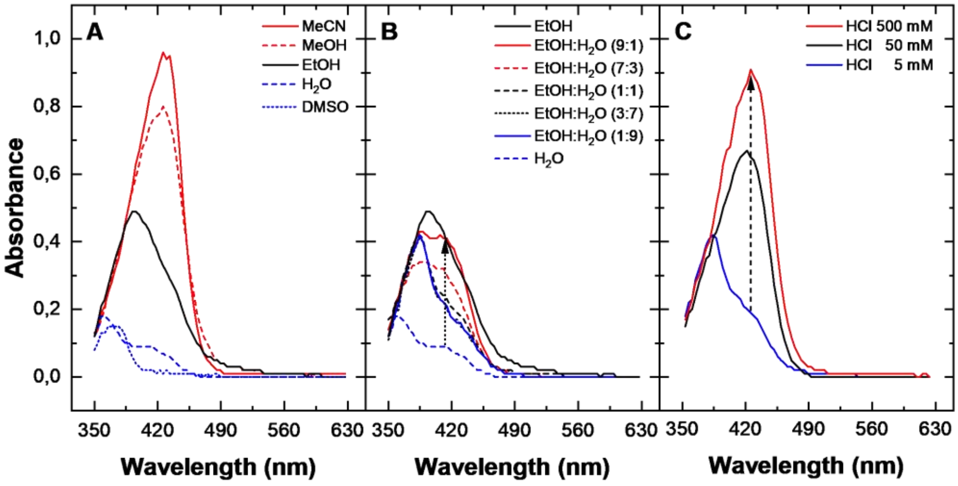

Figure 11.2. *Influence of solvent composition and pH on color development. All the solutions contain 50.0 mg L^{-1} (0.221 mM) of CD and 10.0 mM vanillin reacted for 4 h at 70 °C. A) Absorbance spectra in acetonitrile (MeCN, red line), methanol (MeOH, red dashes), ethanol (EtOH, black line), water (H_2O, blue dashes), dimethyl sulfoxide (DMSO, blue dots). B) Absorbance spectra for different EtOH:H_2O compositions, from neat water (H_2O, blue dashes) to neat ethanol (EtOH, black line). C) Absorbance spectra in EtOH:H_2O (1:1), containing 5 mM (blue line), 50 mM (black line), or 500 mM (red line) HCl.*

11.4.3 Influence of vanillin concentration, temperature, and heating time on color development

Subsequent measurements were performed by using iMark™ Microplate Absorbance Reader determining the absorbance values for 0.200 mL solutions in disposable polystyrene 96-well microtest plates at 415 nm, *i.e.*, the available optical filter closest to the absorbance λ_{max} about 420 nm. Figure 11.3 shows the results of the experiments for CD 50.0 mg L^{-1} dissolved in EtOH /H_2O 1:1 with HCl 0.500 M. Figure 11.3A shows the effect of vanillin concentration (0.00, 0.50, 2.5, 4.4, 10.0, 20.0 mM) on color development after 4 h at 70 °C. The color change was almost undetectable by vanillin addition up to 5.00 mM; a large absorbance increase occurred for vanillin between 5.00 and 10.0 mM, and further increase for vanillin at 20 mM. Considering that carbidopa is fixed at 50.0 mg L^{-1} (0.221 mM), this results underlining the need of a large excess of vanillin to obtain the condensation reaction described in Fig. 11.1, which is responsible for HMOB formation and color development. Vanillin at 10 mM appears as the best concentration in terms of data reproducibility (CV% 1.1). Figure 11.3B shows that the absorbance recorded at 415 nm increases with the temperature, reaching the maximum at 70 °C, and then falling at 80 °C. Although the reproducibility is very good at any temperature, 70 °C appeared the best choice (CV% 2.9). Finally, Fig. 11.3C reports the absorbance of the CD solutions that increased with the heating time up to 2 h, and then decreased up to 4 h in these conditions. Data reproducibility was very good for carbidopa at any reaction time. However, the advantage of using 4 h for color development was clear when we applied the same procedure to levodopa/carbidopa as mixed standards or in real drugs (Fig. 11.3C). In detail, apart from LD alone that gave no color development, as expected, all mixtures containing CD gave rise to yellow solutions but with a much worse reproducibility and faster kinetics with respect to carbidopa alone. Such discrepancy among the absorbance values decreased at 2 h, reaching a minimum after 4 h, as evident from the data superposition in Fig. 11.3C for CD, LD + CD, brand drug, and generic drug, indicating this reaction time as the best option to build a calibration curve to estimate the carbidopa concentration in pharmaceutical formulation, as detailed below.

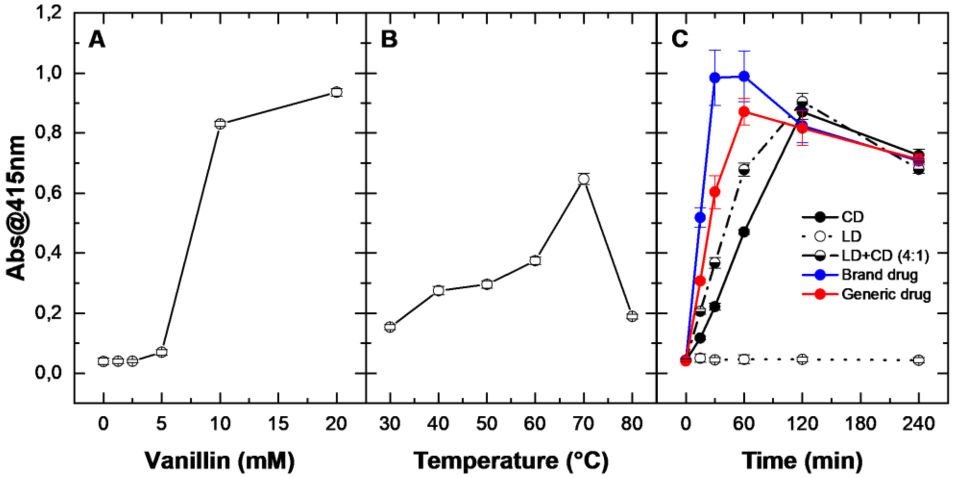

Figure 11.3. *Influence of vanillin concentration, temperature, and heating time on color development. Absorbance at 415 nm for CD 50.0 mg L*$^{-1}$ *samples dissolved in EtOH/*H_2O *1:1 with HCl 0.500 M. (**A**)Vanillin 0.00, 1.25, 2.50, 5.00, 10.0, 20.0 mM after 4 h at 70 °C. (**B**) Vanillin 10.0 mM at 20 °C, 30 °C, 40 °C, 50 °C, 60 °C, 70 °C after 4 h. (**C**) Vanillin 10.0 mM at 70 °C after 15, 30, 60, 120, 240 min in presence of carbidopa (CD, black circles), levodopa (LD, white circles), LD + CD 4:1 (half black circles), brand drug (blue circles), and generic drug (red circles). Each point represents the mean ± SD of 4 replicates.*

11.4.4 Colorimetric quantification of carbidopa in tablets by using of HMOB as molecular probe

The firsts experiments were performed by obtaining the calibration curves reported in Figure 11.4A. As shown, the curves did not superimpose due to the high concentrations of excipients that influenced the analysis. This means that the previously adopted experimental conditions (10.0 mM vanillin in presence of 0.05 M HCl in EtOH at 70 °C for 15 minutes) did not enable the selective quantification of CD since the method was conditioned by the matrix effect. This drawback was completely overcome by working on the experimental parameters (Figure 11.4B).

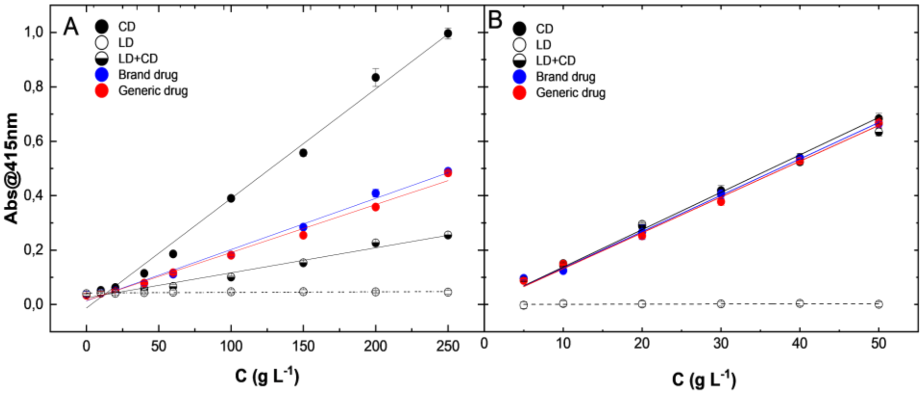

Figure 11.4. Colorimetric calibration plots. Absorbance values at 415 nm for sample solutions in A) EtOH with HCl 0.05 M and 10.0 mM vanillin after 15 minutes at 70°C B) EtOH/H_2O 1:1 with HCl 0.500 M and vanillin 10.0 mM after 4 h at 70 °C. Carbidopa (CD, black circles), levodopa (LD, white circles), LD + CD 4:1 (half black circles), brand drug (blue circles), and generic drug (red circles). The explored concentration range was between 5.00 and 50.0 mg $L^{-1}$for CD, and between 20.0 and 200 mg L^{-1} for LD alone or in combination with CD. Each point represents the mean ± SD of 4 replicates. Data were fitted according to linear Eq. 1. The linear fitting parameters are reported in the table below (Table 11.1).

Table 11.1. Linear fitting parameters for carbidopa at 415 nm. Where m is the slope of the calibration curve. LOD, limit of detection, LOQ, limit of quantification. CV_{av}, mean coefficient of variation calculated between 0.005 and 0.050 g L^{-1}.

Sample	**m (L g^{-1})**	**LOD (mg L^{-1})**	**LOQ (mg L^{-1})**	**R^2**	**CV_{av} (%)**
CD	*13.7 ± 0.2*	*0.399 ± 0.005*	*1.330 ± 0.018*	*0.996*	*4.2*
LD+CD	*13.2 ± 0.3*	*0.184 ± 0.005*	*0.615 ± 0.015*	*0.987*	*3.5*
Brand drug	*13.4 ± 0.2*	*0.215 ± 0.003*	*0.778 ± 0.010*	*0.996*	*3.7*
Generic drug	*13.2 ± 0.2*	*0.399 ± 0.005*	*1.140 ± 0.019*	*0.995*	*3.4*

The best experimental parameters for HMOB formation and the concomitant color development from CD solutions in terms of sensitivity and reproducibility were identified here as 10.0 mM vanillin in presence of 0.500 M HCl in EtOH/H_2O 1:1 (v/v) at 70 °C for 4 h (Fig. 11.4B). Accordingly, these parameters were fixed to selectively detect CD in co-presence of LD, as for the pharmaceutical formulations for the treatment of parkinsonism. Figure 11.4B reports the final calibration curves for CD (black circle), LD (white circles), the binary mixture of pure components (LD + CD 4:1) (black and white circles), brand drug (blue circles), and the generic drug (red circles). In detail, LD standard solutions did not show any absorption at 415 nm over the entire concentration range here explored, as expected due to the absence of the hydrazine group, preventing the synthesis of the HMOB (Fig. 11.1). Differently, the LD + CD 4:1 mixture, which represents a simplified model of commercial drugs, and the levodopa/carbidopa tablets, which represent the real samples, containing 200 mg of levodopa and 50 mg of carbidopa, together with the excipients (see "Materials and methods"), all gave colored solutions, as for CD standard solutions. After blank subtraction, data corresponding to CD between and 50.0 mg L^{-1} were fitted according to the linear equation

Abs @415nm= m x C (1)

where m indicates the slope of the HMOB absorbance at 415 nm. The excellent performances of the assay are well highlighted by the superposition of the curves, due to the almost identical slope values reported in Table 11.1.

Moreover, the analytical parameters from data fitting underline the absence of the matrix effect, due to the different formulations of such drugs, as well as the absence of interference from LD in such conditions, leading to a very good assay reproducibility and promising sensitivity (CV_{av}% 3.7 and 3.4; LOD 0.215 ± 0.003 mg L^{-1} and 0.342 ± 0.006 mg L^{-1} for carbidopa in brand and generic drugs, respectively). Finally, Table 11.2 reports the recovery estimated by using the absorbance values for carbidopa alone with respect to pharmaceutical formulations at the corresponding nominal concentration of CD, obtaining a mean recovery value of 104.6% and 105.3% for brand and generic drugs, respectively, over the entire range of calibration.

Table 11.2. *Absorbance values at 415 nm (Fig. 11.4) and corresponding CD recovery in drugs.*

CD (mg L^{-1})	***Abs@415nm CD***	***Abs@415nm Brand drug***	***Recovery (%)***	***Abs@415nm Generic drug***	***Recovery(%)***
5.0	0.093 ± 0.010	0.096 ± 0.005	96.4	0.088 ± 0.007	105.7
10.0	0.143 ± 0.009	0.124 ± 0.007	115.3	0.149 ± 0.010	96.0
20.0	0.289 ± 0.011	0.265 ± 0.027	109.1	0.252 ± 0.011	114.7
30.0	0.419 ± 0.018	0.406 ± 0.016	103.2	0.378 ± 0.013	110.8
40.0	0.539 ± 0.016	0.538 ± 0.004	100.2	0.527 ± 0.003	102.3
50.0	0.683 ± 0.020	0.664 ± 0.008	102.9	0.668 ± 0.018	102.2
Mean (%)			104.6		105.3

11.5 Conclusions

Carbidopa was added to levodopa and commercialized under the name of Sinemet since 1975, which represents the gold standard for the care of parkinsonism and generating, together with several other levodopa/carbidopa formulations, millions of prescriptions per year [418,419]. Here, it was reported the development of a colorimetric assay for the detection and quantification of carbidopa in such medications. The method is based on selective condensation reaction between carbidopa and vanillin, observing the yellow color development due to formation of HMOB, irrespective of levodopa content. The modulation of yellow color intensity upon vanillin reaction was explored up to 200.0 mg L^{-1}LD and 50.0 mg L^{-1} CD. The calibration curves for two tablet formulations were superimposable to levodopa/carbidopa (4:1), as well as to CD alone, showing a linear dynamic range between 50.0 mg L^{-1} and 5.00 mg L^{-1} of CD with very good reproducibility within this range (CV_{av}%, 3 - 4%) and good mean recovery (105%). Data were acquired by using a common microplate reader, underlining the affordability of the method, appearing as an effective tool for drug estimation and quality control of pharmaceutical formulations. Moreover, considering that about 30% of carbidopa excreted in urine from patients that received an oral dose of such substance is not metabolized [417], the very good sensitivity of the assay, with limit of quantification about 1 mg L^{-1} for commercial drugs, stimulates a perspective study on non-invasive therapeutic monitoring of carbidopa-based medications in human excretion.

12

Concluding remarks

In this work, optical-based bioanalytical detection strategies for drugs quality control and diagnostic applications, were presented. In order to overcome the limitations imposed by the high-cost and benchtop instrumentation currently used in the analysis laboratories, valid easy-to-use and low cost alternative bioanalytical assays were proposed. In recent years, it has become increasingly important to simplify the analysis methods, especially to give rapid responses in the diagnosis. Ultraviolet-visible light absorption and fluorescence techniques help to pursue this goal. Fluorescence and absorbance measurements are a part of the daily routine of any laboratory. These optical methods enable to obtain a large amount of information in a few steps and, often, without any sample pre-treatment. In the bioanalytical field, fluorescence and absorbance measurements play an essential role in the sensitive detection of different target molecules. This thesis took advantage of optical methods to design novel bioassays able to quantify pharmaceutical products and key targets to disease diagnosis.

With the aim to improve the sensitivity of the bioanalytical assays, the optical properties of a class of nanomaterials, CuNCs, were exploited. Primary, the fluorescent features of CuNCs were deeply investigated. Then, CuNCs were used to quantify the human serum albumin in biological matrices. However, it may be difficult to synthesize photoluminescence nanomaterials. As a consequence, sometimes, the use of fluorescent molecules or fluorescent dyes become necessary. Here, for the first time, a novel fluorophore derived from serotonin was obtained. This novel fluorophore was characterized by different techniques. The highly emitted behavior of the fluorophore derived from serotonin are applied for copper quantification in human urine via a quenching-based method.

The optical-based bioanalytical detection strategies were also applied to active principle determination of Parkinson’s drugs, levodopa and carbidopa. The identification of these pharmaceutical compounds was achieved by using selective colorimetric reactions for the drugs functional active principal group. This results in a visible change in color that enables the quantification of the active principles in the pharmaceutical formulations. The concentration of levodopa in Parkinson’s drugs was determined exploiting the formation reaction of purple melanochrome. Melanochrome was synthetically obtained for the first time and for this was examined via mass spectrometry. Then, the melanochrome-based colorimetric assay was successfully applied to determine levodopa and dopamine concentrations in human urine samples. Finally, carbidopa was also selectively quantified by exploiting a colorimetric reaction that led to the formation of the yellow 4-hydroxy-3-methoxybenzaldazine.

The optical-based approaches, here developed, could improve the analytical methods commonly applied in clinical laboratories practice. The use of CuNCs and serotonin-derived fluorophore could, respectively, make faster diagnosis of albuminuria and copper-dependent diseases. This could have a great impact on the monitoring of a patient's state of health. Furthermore, optical methods are among the best suited tools for being miniaturized. For this reason, novel smart devices, *i.e.*, PoC, which allows the continuous monitoring of a patient's health, could be easily developed. The colorimetric reaction, here studied, could be applied to the design of paper-based devices enabling drugs direct and fast detection, also in human specimens. This could simplify the current drugs quality control, the identification of counterfeit drugs and it could represent an invaluable tool for the monitoring of drug therapy in Parkinson’s patients. Ultimately, the characterization of melanochrome and its related species could be exploited as a ‘self-staining’ tool to enhance the selective mass spectrometry imaging of dopamine, levodopa and norepinephrine. This could hope-fully contribute to understanding the molecular basis of such disorders and helping to develop more effective pharmacological treatments of the symptoms.

References

1. Tongtoyai, J.; Tientadakul, P.; Chinswangwatanakul, W.; Opartkiattikul, N. Establishment and implementation of an internal quality assessment program for point-of-care glucose testing at the largest public university hospital in Thailand. *Point Care* **2012**, *11*, 37–41.
2. Ferreira, V. G.; Feitor, J. F.; Almeida, M. B.; Cardoso, D. R.; Carrilho, E. What Is Bioanalytical Chemistry? Scientific Opportunities with Immediate Impact. *Tools Trends Bioanal. Chem.* **2022**, 1–24.
3. Labuda, J.; Bowater, R. P.; Fojta, M.; Gauglitz, G.; Glatz, Z.; Hapala, I.; Havliš, J.; Kilar, F.; Kilar, A.; Malinovská, L.; Sirén, H. M. M.; Skládal, P.; Torta, F.; Valachovič, M.; Wimmerová, M.; Zdráhal, Z.; Hibbert, D. B. Terminology of bioanalytical methods (IUPAC Recommendations 2018). *Pure Appl. Chem.* **2018**, *90*, 1121–1198.
4. Saylor, R. A.; Lunte, S. M. Role of Bioanalytical Chemistry in the Twenty-First Century. *Tools Trends Bioanal. Chem.* **2022**, 25–51.
5. Lettieri, M.; Hosu, O.; Adumitrachioaie, A.; Cristea, C.; Marrazza, G. Beta-lactoglobulin Electrochemical Detection Based with an Innovative Platform Based on Composite Polymer. *Electroanalysis* **2020**, *32*, 217–225.
6. Selvolini, G.; Lettieri, M.; Tassoni, L.; Gastaldello, S.; Grillo, M.; Maran, C.; Marrazza, G. Electrochemical enzyme-linked oligonucleotide array for aflatoxin B 1 detection. *Talanta* **2019**, *203*, 49–57.
7. Torrini, F.; Palladino, P.; Baldoneschi, V.; Scarano, S.; Minunni, M. Sensitive ‘two-steps’ competitive assay for gonadotropin-releasing hormone detection via SPR biosensing and polynorepinephrine-based molecularly imprinted polymer. *Anal. Chim. Acta* **2021**, *1161*, 338481.
8. Cady, N. C.; Tokranova, N.; Minor, A.; Nikvand, N.; Strle, K.; Lee, W. T.; Page, W.; Guignon, E.; Pilar, A.; Gibson, G. N. Multiplexed detection and

quantification of human antibody response to COVID-19 infection using a plasmon enhanced biosensor platform. *Biosens. Bioelectron.* **2021**, *171*, 112679.

9. Li, Y.; Cu, Y. T. H.; Luo, D. Multiplexed detection of pathogen DNA with DNA-based fluorescence nanobarcodes. *Nat. Biotechnol.* **2005**, *23*, 885–889.
10. Cai, S.; Pataillot-Meakin, T.; Shibakawa, A.; Ren, R.; Bevan, C. L.; Ladame, S.; Ivanov, A. P.; Edel, J. B. Single-molecule amplification-free multiplexed detection of circulating microRNA cancer biomarkers from serum. *Nat. Commun.* **2021**, *12*, 1–12.
11. Kim, H. J.; Ahn, H.; Kim, H.; Park, D.; Lee, J. S.; Lee, B. C.; Kim, J.; Yoon, D. S.; Hwang, K. S. Nanoparticle-based multiplex biosensor utilising dual dielectrophoretic forces for clinical diagnosis of Alzheimer's disease. *Sensors Actuators B Chem.* **2022**, *355*, 131288.
12. Lee, S.; Crulhas, B. P.; Suvakov, S.; Verkhoturov, S. V.; Verkhoturov, D. S.; Eller, M. J.; Malhi, H.; Garovic, V. D.; Schweikert, E. A.; Stybayeva, G.; Revzin, A. Nanoparticle-Enabled Multiplexed Electrochemical Immunoassay for Detection of Surface Proteins on Extracellular Vesicles. *ACS Appl. Mater. Interfaces* **2021**, *13*, 52321–52332.
13. Qu, J. H.; Peeters, B.; Delport, F.; Vanhoorelbeke, K.; Lammertyn, J.; Spasic, D. Gold nanoparticle enhanced multiplexed biosensing on a fiber optic surface plasmon resonance probe. *Biosens. Bioelectron.* **2021**, *192*, 113549.
14. Wu, W.; Liu, X.; Shen, M.; Shen, L.; Ke, X.; Cui, D.; Li, W. Multicolor quantum dot nanobeads based fluorescence-linked immunosorbent assay for highly sensitive multiplexed detection. *Sensors Actuators, B Chem.* **2021**, *338*, 129827.
15. Liu, H.; Cai, P.; McHugh, K. J.; Perkinson, C. F.; Li, L.; Wang, S.; Wang, W.; Jiao, M.; Luo, X.; Jing, L. Aqueous synthesis of bright near-infrared-emitting Zn-Cu-In-Se quantum dots for multiplexed detection of tumor markers. *Nano Res. 2022 159* **2022**, *15*, 8351–8359.
16. Pandey, P.; Shin, K.; Jang, A. R.; Seo, M. K.; Hong, W. K.; Sohn, J. I. Highly

sensitive multiplex-detection of surface-enhanced Raman scattering via self-assembly arrays of porous AuAg nanoparticles with built-in nanogaps. *J. Alloys Compd.* **2021**, *888*, 161504.

17. Agrawal, A.; Keçili, R.; Ghorbani-Bidkorbeh, F.; Hussain, C. M. Green miniaturized technologies in analytical and bioanalytical chemistry. *TrAC Trends Anal. Chem.* **2021**, *143*, 116383.
18. Hosu, O.; Lettieri, M.; Papara, N.; Ravalli, A.; Sandulescu, R.; Cristea, C.; Marrazza, G. Colorimetric multienzymatic smart sensors for hydrogen peroxide, glucose and catechol screening analysis. *Talanta* **2019**, *204*, 525–532.
19. Khosravani, M. R.; Reinicke, T. 3D-printed sensors: Current progress and future challenges. *Sensors Actuators, A Phys.* **2020**, *305*, 111916.
20. Zhu, P.; Peng, H.; Rwei, A. Y. Flexible, wearable biosensors for digital health. *Med. Nov. Technol. Devices* **2022**, *14*, 100118.
21. Dolatabadi, J. E. N.; de la Guardia, M. Applications of diatoms and silica nanotechnology in biosensing, drug and gene delivery, and formation of complex metal nanostructures. *TrAC Trends Anal. Chem.* **2011**, *30*, 1538–1548.
22. Arunrao Polshettiwar, S.; Devidas Deshmukh, C.; Motilal Baheti, A.; Shivdas Wani, M.; Bompilwar, E.; Jambhekar, D.; Choudhari, S.; Tagalpallewar, A.; Satish Polshettiwar, C. A. Recent Trends on Biosensors in Healthcare and Pharmaceuticals: An Overview. *Int. J. Pharm. Investig.* **2021**, *11*, 131–136.
23. Sharma, A.; Badea, M.; Tiwari, S.; Marty, J. L. Wearable Biosensors: An Alternative and Practical Approach in Healthcare and Disease Monitoring. **2021**, *26*.
24. Meng, E.; Sheybani, R. Insight: implantable medical devices. *Lab Chip* **2014**, *14*, 3233–3240.
25. Yu, J.; Wang, J.; Zhang, Y.; Chen, G.; Mao, W.; Ye, Y.; Kahkoska, A. R.; Buse, J. B.; Langer, R.; Gu, Z. Glucose-responsive insulin patch for the regulation of blood glucose in mice and minipigs. *Nat. Biomed. Eng.* **2020**, *4*,

499.

26. Praveena, B. A.; Lokesh, N.; Buradi, A.; Santhosh, N.; Praveena, B. L.; Vignesh, R. A comprehensive review of emerging additive manufacturing (3D printing technology): Methods, materials, applications, challenges, trends and future potential. *Mater. Today Proc.* **2022**, *52*, 1309–1313.
27. Kim, J.; Campbell, A. S.; de Ávila, B. E. F.; Wang, J. Wearable biosensors for healthcare monitoring. *Nat. Biotechnol.* **2019**, *37*, 389–406.
28. Zhu, Z.; Park, H. S.; McAlpine, M. C. 3D printed deformable sensors. *Sci. Adv.* **2020**, *6*, 5575–5592.
29. Hou, Y.; Lv, C. C.; Guo, Y. L.; Ma, X. H.; Liu, W.; Jin, Y.; Li, B. X.; Yang, M.; Yao, S. Y. Recent Advances and Applications in Paper-Based Devices for Point-of-Care Testing. *J. Anal. Test.* **2022**.
30. Rateni, G.; Dario, P.; Cavallo, F. Smartphone-based food diagnostic technologies: A review. **2017**, *17*.
31. Huang, X.; Xu, D.; Chen, J.; Liu, J.; Li, Y.; Song, J.; Ma, X.; Guo, J. Smartphone-based analytical biosensors. *Analyst* **2018**, *143*, 5339–5351.
32. Majumder, S.; Deen, M. J. Smartphone Sensors for Health Monitoring and Diagnosis. *Sensors 2019, Vol. 19, Page 2164* **2019**, *19*, 2164.
33. Lu, Y.; Shi, Z.; Liu, Q. Smartphone-based biosensors for portable food evaluation. *Curr. Opin. Food Sci.* **2019**, *28*, 74–81.
34. Sumriddetchkajorn, S.; Chaitavon, K.; Intaravanne, Y. Mobile-platform based colorimeter for monitoring chlorine concentration in water. *Sensors Actuators B Chem.* **2014**, *191*, 561–566.
35. Faham, S.; Golmohammadi, H.; Ghavami, R.; Khayatian, G. A nanocellulose-based colorimetric assay kit for smartphone sensing of iron and iron-chelating deferoxamine drug in biofluids. *Anal. Chim. Acta* **2019**, *1087*, 104–112.
36. Sumriddetchkajorn, S.; Intaravanne, Y. Data-nonintrusive photonics-based credit card verifier with a low false rejection rate. *Appl. Opt. Vol. 49, Issue 5, pp. 764-771* **2010**, *49*, 764–771.

37. Liu, J.; Geng, Z.; Fan, Z.; Liu, J.; Chen, H. Point-of-care testing based on smartphone: The current state-of-the-art (2017–2018). *Biosens. Bioelectron.* **2019**, *132*, 17–37.

38. Xu, Y.; Liu, Z.; Liu, R.; Luo, M.; Wang, Q.; Cao, L.; Ye, S. Inkjet-printed pH-sensitive QR code labels for real-time food freshness monitoring. *J. Mater. Sci.* **2021**, *56*, 18453–18462.

39. Christodouleas, D. C.; Kaur, B.; Chorti, P. From Point-of-Care Testing to eHealth Diagnostic Devices (eDiagnostics). *ACS Cent. Sci.* **2018**, *4*, 1600–1616.

40. Mak, W. C.; Beni, V.; Turner, A. P. F. Lateral-flow technology: From visual to instrumental. *TrAC Trends Anal. Chem.* **2016**, *79*, 297–305.

41. Minaretzis, D.; Tsionou, C.; Tsandoulas, E. Clinical evaluation of a sensitive urine pregnancy test in the gynecological emergencies. *Eur. J. Obstet. Gynecol. Reprod. Biol.* **1991**, *39*, 123–126.

42. Crawford, M. L.; Collier, B. B.; Bradley, M. N.; Holland, P. L.; Shuford, C. M.; Grant, R. P. Empiricism in Microsampling: Utilizing a Novel Lateral Flow Device and Intrinsic Normalization to Provide Accurate and Precise Clinical Analysis from a Finger Stick. *Clin. Chem.* **2020**, *66*, 821–831.

43. Ryan, F.; O’shea, S.; Byrne, S. The reliability of point-of-care prothrombin time testing. A comparison of CoaguChek S® and XS® INR measurements with hospital laboratory monitoring. *Int. J. Lab. Hematol.* **2010**, *32*, e26–e33.

44. Ibitoye, M.; Frasca, T.; Giguere, R.; Carballo-Diéguez, A. Home testing past, present and future: Lessons learned and implications for HIV home tests. *AIDS Behav.* **2014**, *18*, 933–949.

45. Mens, P. F.; van Amerongen, A.; Sawa, P.; Kager, P. A.; Schallig, H. D. F. H. Molecular diagnosis of malaria in the field: development of a novel 1-step nucleic acid lateral flow immunoassay for the detection of all 4 human Plasmodium spp. and its evaluation in Mbita, Kenya. *Diagn. Microbiol. Infect. Dis.* **2008**, *61*, 421–427.

46. Stohr, J. J. J. M.; Zwart, V. F.; Goderski, G.; Meijer, A.; Nagel-Imming, C. R.

S.; Kluytmans-van den Bergh, M. F. Q.; Pas, S. D.; van den Oetelaar, F.; Hellwich, M.; Gan, K. H.; Rietveld, A.; Verweij, J. J.; Murk, J. L.; van den Bijllaardt, W.; Kluytmans, J. A. J. W. Self-testing for the detection of SARS-CoV-2 infection with rapid antigen tests for people with suspected COVID-19 in the community. *Clin. Microbiol. Infect.* **2022**, *28*, 695–700.

47. Shrivastava, S.; Trung, T. Q.; Lee, N. E. Recent progress, challenges, and prospects of fully integrated mobile and wearable point-of-care testing systems for self-testing. *Chem. Soc. Rev.* **2020**, *49*, 1812–1866.

48. Jiang, N.; Tansukawat, N. D.; Gonzalez-macia, L.; Ates, H. C.; Dincer, C.; Der, F. G.; Tasoglu, S.; Yetisen, A. K. Low-Cost Optical Assays for Point-of-Care Diagnosis in Resource- Limited Settings. **2021**.

49. Kielkopf, C. L.; Bauer, W.; Urbatsch, I. L. Bradford Assay for Determining Protein Concentration. *Cold Spring Harb. Protoc.* **2020**, *2020*, pdb.prot102269.

50. Hudz, N.; Yezerska, O.; Shanaida, M.; Sedláčková, V. H.; Wieczorek, P. P. Application of the Folin-Ciocalteu method to the evaluation of Salvia sclarea extracts. **2019**, *66*, 209–215.

51. Adnan, N.; Khandker, S. S.; Haq, A.; Chaity, M. A.; Khalek, A.; Nazim, A. Q.; Kaitsuka, T.; Tomizawa, K.; Mie, M.; Kobatake, E.; Ahmed, S.; Ali, nor A. A.; Khondoker, M. U.; Haque, M.; Jamiruddin, M. R. Detection of SARS-CoV-2 by antigen ELISA test is highly swayed by viral load and sample storage condition. *Expert Rev. Anti. Infect. Ther.* **2021**, *20*, 473–481.

52. Kalogerakis, G. C.; Boparai, H. K.; Yang, M. I.; Sleep, B. E. A high-throughput and cost-effective microplate reader method for measuring persulfates (peroxydisulfate and peroxymonosulfate). *Talanta* **2022**, *240*, 123170.

53. Chen, Z. J.; Wu, H. L.; Shen, Y. D.; Wang, H.; Zhang, Y. F.; Hammock, B.; Li, Z. F.; Luo, L.; Lei, H. T.; Xu, Z. L. Phosphate-triggered ratiometric fluoroimmunoassay based on nanobody-alkaline phosphatase fusion for sensitive detection of 1-naphthol for the exposure assessment of pesticide

carbaryl. *J. Hazard. Mater.* **2022**, *424*, 127411.

54. da Silva Ferreira, B. I.; da Silva-Gomes, N. L.; da Costa Nunes Pimentel Coelho, W. L.; da Costa, V. D.; de Souza Carneiro, V. C.; Kader, R. L.; Amaro, M. P.; Villar, L. M.; Miyajima, F.; Alves-Leon, S. V.; de Paula, V. S.; Leon, L. A. A.; Moreira, O. C. Validation of a novel molecular assay to the diagnostic of COVID-19 based on real time PCR with high resolution melting. *PLoS One* **2021**, *16*, 1–17.
55. Monnier, J.; Tognetti, L.; Miyamoto, M.; Suppa, M.; Cinotti, E.; Fontaine, M.; Perez, J.; Orte Cano, C.; Yélamos, O.; Puig, S.; Dubois, A.; Rubegni, P.; del Marmol, V.; Malvehy, J.; Perrot, J. L. In vivo characterization of healthy human skin with a novel, non-invasive imaging technique: line-field confocal optical coherence tomography. *J. Eur. Acad. Dermatology Venereol.* **2020**, *34*, 2914–2921.
56. Gauglitz, G. Direct optical detection in bioanalysis: An update. *Anal. Bioanal. Chem.* **2010**, *398*, 2363–2372.
57. Al-madani, H.; Du, H.; Yao, J.; Peng, H.; Yao, C.; Jiang, B.; Wu, A.; Yang, F. Living Sample Viability Measurement Methods from Traditional Assays to Nanomotion. *Biosensors* **2022**, *12*, 453.
58. Yeh, Y.; Krishnan, V. V Introduction to Biophotonics. **2018**, *1*, 1–11.
59. Popp, J. Translational biophotonics for clinical routine. *Biophotonics Biomed. Microsc.* **2020**, *11575*, 1157503.
60. Albrecht, C. Joseph R. Lakowicz: Principles of fluorescence spectroscopy, 3rd Edition. *Anal. Bioanal. Chem. 2007 3905* **2008**, *390*, 1223–1224.
61. Kim, H.; Beack, S.; Han, S.; Shin, M.; Lee, T.; Park, Y.; Kim, K. S.; Yetisen, A. K.; Yun, S. H.; Kwon, W.; Hahn, S. K. Multifunctional Photonic Nanomaterials for Diagnostic, Therapeutic, and Theranostic Applications. *Adv. Mater.* **2018**, *30*, 1701460.
62. Alberto, J. *Tools and Trends in Bioanalytical Chemistry*; Tools Trends Bioanal. Chem.; 2022.
63. Pirzada, M.; Altintas, Z. Nanomaterials for Healthcare Biosensing

Applications. *Sensors 2019, Vol. 19, Page 5311* **2019**, *19*, 5311.

64. Rawtani, D.; Rao, P. K.; Hussain, C. M. Recent advances in analytical, bioanalytical and miscellaneous applications of green nanomaterial. *TrAC Trends Anal. Chem.* **2020**, *133*, 116109.

65. Qing, T.; Feng, B.; Zhang, P.; Zhang, K.; He, X.; Wang, K. Beyond native deoxyribonucleic acid, templating fluorescent nanomaterials for bioanalytical applications: A review. *Anal. Chim. Acta* **2020**, *1105*, 11–27.

66. Yilmaz, E.; Sarp, G.; Uzcan, F.; Ozalp, O.; Soylak, M. Application of magnetic nanomaterials in bioanalysis. *Talanta* **2021**, *229*, 122285.

67. Soldado, A. B.; Suárez, P. L.; Fernández-Argüelles, M. T.; Sanz-Medel, A.; Costa-Fernández, J. M.; Trapiella-Alfonso, L. (Bio)Analytical Nanoscience & Nanotechnology. *Encycl. Anal. Chem.* **2022**, 1–31.

68. Valentini, F.; Palleschi, G. Nanomaterials and Analytical Chemistry. *Anal. Lett.* **2008**, *41*, 479–520.

69. Fu, B.; Sun, J.; Cheng, Y.; Ouyang, H.; Compagnini, G.; Yin, P.; Wei, S.; Li, S.; Li, D.; Scardaci, V.; Zhang, H. Recent Progress on Metal-Based Nanomaterials: Fabrications, Optical Properties, and Applications in Ultrafast Photonics. *Adv. Funct. Mater.* **2021**, *31*, 2107363.

70. Shao, B.; Xiao, Z. Recent achievements in exosomal biomarkers detection by nanomaterials-based optical biosensors - A review. *Anal. Chim. Acta* **2020**, *1114*, 74–84.

71. Ullah, N.; Mansha, M.; Khan, I.; Qurashi, A. Nanomaterial-based optical chemical sensors for the detection of heavy metals in water: Recent advances and challenges. *TrAC Trends Anal. Chem.* **2018**, *100*, 155–166.

72. Mahmoudpour, M.; Ezzati Nazhad Dolatabadi, J.; Torbati, M.; Homayouni-Rad, A. Nanomaterials based surface plasmon resonance signal enhancement for detection of environmental pollutions. *Biosens. Bioelectron.* **2019**, *127*, 72–84.

73. Schwartzberg, A. M.; Zhang, J. Z. Novel optical properties and emerging applications of metal nanostructures. *J. Phys. Chem. C* **2008**, *112*, 10323–

10337.

74. Saleh, T. A. Nanomaterials: Classification, properties, and environmental toxicities. *Environ. Technol. Innov.* **2020**, *20*, 101067.

75. Penn, S. G.; He, L.; Natan, M. J. Nanoparticles for bioanalysis. *Curr. Opin. Chem. Biol.* **2003**, *7*, 609–615.

76. Science ; Chan, P.; Nie, W. C. W.; Taylor, S.; Fang, J. R.; Nie, M. M.; Shenton, S. M.; Davis, W.; Mann, S. A.; Elghanian, S.; Storhoff, R.; Mucic, J. J.; Letsinger, R. C.; Mirkin, R. L.; Mucic, C. A.; Storhoff, R. C.; Mirkin, J. J.; Letsinger, C. A.; Mitchell, R. L.; Mirkin, G. P.; Harma, R. L.; Lehtinen, H.; Takalo, P.; Lovgren, H.; Giunchedi, T.; Conte, P.; Chetoni, U.; Saettone, P.; Adler, M. F.; Jayan, J.; Melia, A.; Bourel, C. D.; Rolland, D.; Leverge, A.; Genetet, R.; Shibata, B.; Yano, S.; Yamane, T.; Shibata, M.; Taniguchi, S.; Yano, T. Conjugation of Biomolecules with Luminophore-Doped Silica Nanoparticles for Photostable Biomarkers. *J. Sol-Gel Sci. Technol* **1998**, *281*, 4988.

77. Han, M.; Gao, X.; Su, J. Z.; Nie, S. Quantum-dot-tagged microbeads for multiplexed optical coding of biomolecules. *Nat. Biotechnol. 2001 197* **2001**, *19*, 631–635.

78. Hirsch, L. R.; Jackson, J. B.; Lee, A.; Halas, N. J.; West, J. L. A whole blood immunoassay using gold nanoshells. *Anal. Chem.* **2003**, *75*, 2377–2381.

79. Yang, E.; Zhang, Y.; Shen, Y. Quantum dots for electrochemiluminescence bioanalysis - A review. *Anal. Chim. Acta* **2022**, *1209*, 339140.

80. Fenzl, C.; Hirsch, T.; Baeumner, A. J. Nanomaterials as versatile tools for signal amplification in (bio)analytical applications. *TrAC - Trends Anal. Chem.* **2016**, *79*, 306–316.

81. Kumar, A.; Singh, K. R.; Ghate, M. D.; Lalhlenmawia, H.; Kumar, D.; Singh, J. Bioinspired quantum dots for cancer therapy: A mini-review. *Mater. Lett.* **2022**, *313*, 131742.

82. Chen, J.; Wu, W.; Zhang, F.; Zhang, J.; Liu, H.; Zheng, J.; Guo, S.; Zhang, J. Graphene quantum dots in photodynamic therapy. *Nanoscale Adv.* **2020**, *2*,

4961–4967.

83. Mathew, T.; Sree, R. A.; Aishwarya, S.; Kounaina, K.; Patil, A. G.; Satapathy, P.; Hudeda, S. P.; More, S. S.; Muthucheliyan, K.; Kumar, T. N.; Raghu, A. V.; Reddy, K. R.; Zameer, F. Graphene-based functional nanomaterials for biomedical and bioanalysis applications. **2020**, *23*, 100184.

84. Lozhkomoev, A. S.; Pervikov, A. V.; Chumaevsky, A. V.; Dvilis, E. S.; Paygin, V. D.; Khasanov, O. L.; Lerner, M. I. Fabrication of Fe-Cu composites from electroexplosive bimetallic nanoparticles by spark plasma sintering. *Vacuum* **2019**, *170*, 108980.

85. Johnston, H.; Brown, D.; Kermanizadeh, A.; Gubbins, E.; Stone, V. Investigating the relationship between nanomaterial hazard and physicochemical properties: Informing the exploitation of nanomaterials within therapeutic and diagnostic applications. *J. Control. Release* **2012**, *164*, 307–313.

86. Siddique, S.; Chow, J. C. L. Application of nanomaterials in biomedical imaging and cancer therapy. **2020**, *10*, 1–41.

87. Yang, Y.; Wang, L.; Wan, B.; Gu, Y.; Li, X. Optically Active Nanomaterials for Bioimaging and Targeted Therapy. *Front. Bioeng. Biotechnol.* **2019**, *7*, 1–24.

88. Jacob, J.; Haponiuk, J. T.; Thomas, S.; Gopi, S. Biopolymer based nanomaterials in drug delivery systems: A review. *Mater. Today Chem.* **2018**, *9*, 43–55.

89. Murray, R. A.; Escobar, A.; Bastús, N. G.; Andreozzi, P.; Puntes, V.; Moya, S. E. Fluorescently labelled nanomaterials in nanosafety research: Practical advice to avoid artefacts and trace unbound dye. **2018**, *9*, 102–113.

90. Sharifi, S.; Zununi, S.; Ahmadian, E.; Maleki, S.; Eftekhari, A.; Khalilov, R.; Ahmadi, M.; Hamidi-asl, E.; Labib, M. Biosensors and Bioelectronics Detection of pathogenic bacteria via nanomaterials-modified aptasensors. *Biosens. Bioelectron.* **2020**, *150*, 111933.

91. Oliveira, O. N.; Iost, R. M.; Siqueira, J. R.; Crespilho, F. N.; Caseli, L.

Nanomaterials for diagnosis: Challenges and applications in smart devices based on molecular recognition. *ACS Appl. Mater. Interfaces* **2014**, *6*, 14745–14766.

92. Wang, Z.; Hu, T.; Liang, R.; Wei, M. Application of Zero-Dimensional Nanomaterials in Biosensing. *Front. Chem.* **2020**, *8*, 1–19.

93. Giacomazzo, G. E.; Palladino, P.; Gellini, C.; Salerno, G.; Baldoneschi, V.; Feis, A.; Scarano, S.; Minunni, M.; Richichi, B. A straightforward synthesis of phenyl boronic acid (PBA) containing BODIPY dyes: New functional and modular fluorescent tools for the tethering of the glycan domain of antibodies. *RSC Adv.* **2019**, *9*, 30773–30777.

94. Salerno, G.; Scarano, S.; Mamusa, M.; Consumi, M.; Giuntini, S.; Macagnano, A.; Nativi, S.; Fragai, M.; Minunni, M.; Berti, D.; Magnani, A.; Nativi, C.; Richichi, B. A small heterobifunctional ligand provides stable and water dispersible core-shell CdSe/ZnS quantum dots (QDs). *Nanoscale* **2018**, *10*, 19720–19732.

95. Xie, Y. P.; Shen, Y. L.; Duan, G. X.; Han, J.; Zhang, L. P.; Lu, X. Silver nanoclusters: synthesis, structures and photoluminescence. *Mater. Chem. Front.* **2020**, *4*, 2205–2222.

96. Sahu, D.; Mohapatra, P.; Swain, S. K. Highly orange fluorescence emission by water soluble gold nanoclusters for “turn off” sensing of Hg2+ ion. *J. Photochem. Photobiol. A Chem.* **2020**, *386*, 112098.

97. Vaid, P.; Raizada, P.; Saini, A. K.; Saini, R. V. Biogenic silver, gold and copper nanoparticles - A sustainable green chemistry approach for cancer therapy. *Sustain. Chem. Pharm.* **2020**, *16*, 100247.

98. Lai, W. F.; Wong, W. T.; Rogach, A. L. Development of Copper Nanoclusters for In Vitro and In Vivo Theranostic Applications. *Adv. Mater.* **2020**, *32*, 1–21.

99. Zhang, Q.; Yang, M.; Zhu, Y.; Mao, C. Metallic nanoclusters for cancer imaging and therapy. *Curr. Med. Chem.* **2017**, *24*, 1–1.

100. Zhou, M.; Tian, M.; Li, C. Copper-Based Nanomaterials for Cancer Imaging

and Therapy. *Bioconjug. Chem.* 2016, *27*, 1188–1199.

101. Benavides, J.; Quijada-Garrido, I.; García, O. The synthesis of switch-off fluorescent water-stable copper nanocluster Hg2+ sensors: Via a simple one-pot approach by an in situ metal reduction strategy in the presence of a thiolated polymer ligand template. *Nanoscale* **2020**, *12*, 944–955.
102. Prakash, K. T.; Singh, N.; Venkatesh, V. Synthesis of novel luminescent copper nanoclusters with substituent driven self-assembly and aggregation induced emission (AIE). *Chem. Commun.* **2019**, *55*, 322–325.
103. Kardar, Z. S.; Shemirani, F.; Zadmard, R. Determination of iron(II) and iron(III) via static quenching of the fluorescence of tryptophan-protected copper nanoclusters. *Microchim. Acta* **2020**, *187*, 1–9.
104. Lu, Y.; Chen, W. Sub-nanometre sized metal clusters: From synthetic challenges to the unique property discoveries. *Chem. Soc. Rev.* 2012, *41*, 3594–3623.
105. Zhao, M.; Sun, L.; Crooks, R. M. Preparation of Cu Nanoclusters within Dendrimer Templates. *J. Am. Chem. Soc.* **1998**, *120*, 4877–4878.
106. Balogh, L.; Tomalia, D. A. Nanocomposites . 1 . Synthesis of Zerovalent Copper Nanoclusters. *J. Am. Chem. Soc.* **1998**, *120*, 7355–7356.
107. Hu, X.; Liu, T.; Zhuang, Y.; Wang, W.; Li, Y.; Fan, W.; Huang, Y. Recent advances in the analytical applications of copper nanoclusters. *TrAC - Trends Anal. Chem.* 2016, *77*, 66–75.
108. Rotaru, A.; Dutta, S.; Jentzsch, E.; Gothelf, K.; Mokhir, A. Selective dsDNA-templated formation of copper nanoparticles in solution. *Angew. Chemie - Int. Ed.* **2010**, *49*, 5665–5667.
109. Nain, A.; Tseng, Y. T.; Wei, S. C.; Periasamy, A. P.; Huang, C. C.; Tseng, F. G.; Chang, H. T. Capping 1,3-propanedithiol to boost the antibacterial activity of protein-templated copper nanoclusters. *J. Hazard. Mater.* **2020**, *389*, 121821.
110. Huang, H.; Li, H.; Wang, A. J.; Zhong, S. X.; Fang, K. M.; Feng, J. J. Green synthesis of peptide-templated fluorescent copper nanoclusters for

temperature sensing and cellular imaging. *Analyst* **2014**, *139*, 6536–6541.

111. Yang, X.; Feng, Y.; Zhu, S.; Luo, Y.; Zhuo, Y.; Dou, Y. One-step synthesis and applications of fluorescent Cu nanoclusters stabilized by l-cysteine in aqueous solution. *Anal. Chim. Acta* **2014**, *847*, 49–54.

112. Chen, P. C.; Li, Y. C.; Ma, J. Y.; Huang, J. Y.; Chen, C. F.; Chang, H. T. Size-tunable copper nanocluster aggregates and their application in hydrogen sulfide sensing on paper-based devices. *Sci. Reports 2016 61* **2016**, *6*, 1–9.

113. Goswami, N.; Giri, A.; Bootharaju, M. S.; Xavier, P. L.; Pradeep, T.; Pal, S. K. Copper quantum clusters in protein matrix: Potential sensor of Pb 2+ ion. *Anal. Chem.* **2011**, *83*, 9676–9680.

114. Yang, K.; Wang, Y.; Lu, C.; Yang, X. Ovalbumin-directed synthesis of fluorescent copper nanoclusters for sensing both vitamin B1 and doxycycline. *J. Lumin.* **2018**, *196*, 181–186.

115. Cai, Z.; Li, H.; Wu, J.; Zhu, L.; Ma, X.; Zhang, C. Ascorbic acid stabilised copper nanoclusters as fluorescent sensors for detection of quercetin. *RSC Adv.* **2020**, *10*, 8989–8993.

116. Chen, S.; Wang, Y.; Feng, L. Specific detection and discrimination of dithiocarbamates using CTAB-encapsulated fluorescent copper nanoclusters. *Talanta* **2020**, *210*, 120627.

117. Yousefzadeh, A.; Hassanzadeh, J.; Mousavi, S. M. J.; Yousefzadeh, M. Surface molecular imprinting and powerfully enhanced chemiluminescence emission by Cu nanoclusters/MOF composite for detection of tramadol. *Sensors Actuators, B Chem.* **2019**, *286*, 154–162.

118. Aparna, R. S.; Anjali Devi, J. S.; Anjana, R. R.; Nebu, J.; George, S. Zn(II) ion modulated red emitting copper nanocluster probe for the fluorescence turn on sensing of RDX. *Sensors Actuators, B Chem.* **2019**, *291*, 298–305.

119. Wang, C.; Yao, Y.; Song, Q. Interfacial synthesis of polyethyleneimine-protected copper nanoclusters: Size-dependent tunable photoluminescence, pH sensor and bioimaging. *Colloids Surfaces B Biointerfaces* **2016**, *140*, 373–381.

120. Cai, Z.; Zhang, C.; Jia, K. l-Tyrosine protected Cu nanoclusters for reversible pH-sensors. *Chem. Pap.* **2020**, *74*, 1831–1838.

121. Zhang, G.; Xu, T.; Du, H.; Qiao, Y.; Guo, X.; Shi, L.; Zhang, Y.; Shuang, S.; Dong, C.; Ma, H. A reversible fluorescent pH-sensing system based on the one-pot synthesis of natural silk fibroin-capped copper nanoclusters. *J. Mater. Chem. C* **2016**, *4*, 3540–3545.

122. Cheng, Y.; Deng, S.; Sun, F.; Zhou, Y. H. Synthesis of luminescent Cu 9 S 5 nanoclusters from copper-2,5-dimercapto-1,3,4-thiadiazole coordination polymer as pH sensor. *J. Lumin.* **2019**, *210*, 38–46.

123. Ye, J.; Dong, X.; Jiang, H.; Wang, X. An intracellular temperature nanoprobe based on biosynthesized fluorescent copper nanoclusters. *J. Mater. Chem. B* **2017**, *5*, 691–696.

124. Bhamore, J. R.; Jha, S.; Mungara, A. K.; Singhal, R. K.; Sonkeshariya, D.; Kailasa, S. K. One-step green synthetic approach for the preparation of multicolor emitting copper nanoclusters and their applications in chemical species sensing and bioimaging. *Biosens. Bioelectron.* **2016**, *80*, 243–248.

125. Gao, X.; Zhuang, X.; Tian, C.; Liu, H.; Lai, W. F.; Wang, Z.; Yang, X.; Chen, L.; Rogach, A. L. A copper nanocluster incorporated nanogel: Confinement-assisted emission enhancement for zinc ion detection in living cells. *Sensors Actuators, B Chem.* **2020**, *307*, 127626.

126. Qing, T.; Zhang, K.; Qing, Z.; Wang, X.; Long, C.; Zhang, P.; Hu, H.; Feng, B. Recent progress in copper nanocluster-based fluorescent probing: a review. *Microchim. Acta* **2019**, *186.*

127. Pramanik, S.; Khamari, L.; Nandi, S.; Mukherjee, S. Discriminating Single Base Pair Mismatches in DNA Using Glutathione-Templated Copper Nanoclusters. *J. Phys. Chem. C* **2019**, *123*, 29047–29056.

128. Peng, X. S.; Chen, S. Y.; Ou, L. J.; Luo, F. W.; Qin, S. W.; Sun, A. M. Hairpin loop-enhanced fluorescent copper nanoclusters and application in S1 nuclease detection. *Analyst* **2018**, *143*, 415–419.

129. Mao, A.; Wei, C. Cytosine-rich ssDNA-templated fluorescent silver and

copper/silver nanoclusters: optical properties and sensitive detection for mercury(II). *Microchim. Acta* **2019**, *186*.

130. Wood, D. M.; Ashcroft, N. W. Quantum size effects in the optical properties of small metallic particles. *Phys. Rev. B* **1982**, *25*, 6255–6274.

131. Wang, Z.; Chen, B.; Rogach, A. L. Synthesis, optical properties and applications of light-emitting copper nanoclusters. **2017**, *2*, 135–146.

132. Pavliuk, M. V.; Gutiérrez Álvarez, S.; Hattori, Y.; Messing, M. E.; Czapla-Masztafiak, J.; Szlachetko, J.; Silva, J. L.; Araujo, C. M.; Fernandes, D. L.; Lu, L.; Kiely, C. J.; Abdellah, M.; Nordlander, P.; Sá, J. Hydrated Electron Generation by Excitation of Copper Localized Surface Plasmon Resonance. *J. Phys. Chem. Lett.* **2019**, *10*, 1743–1749.

133. Garrido, L. V. Q.; Gonçalves, J. M.; Rocha, J. C.; Bastos, E. L.; Toma, H. E.; Zamarion, V. M. Intriguing Plasmonic and Fluorescence Duality in Copper Nanoparticles. **2020**.

134. Ziashahabi, A.; Ghodselahi, T.; Heidari Saani, M. Localized Surface Plasmon Resonance properties of copper nano-clusters: A theoretical study of size dependence. *J. Phys. Chem. Solids* **2013**, *74*, 929–933.

135. Lu, Y. Z.; Wei, W. T.; Chen, W. Copper nanoclusters: Synthesis, characterization and properties. *Chinese Sci. Bull.* **2012**, *57*, 41–47.

136. Li, D.; Chen, Z.; Mei, X. Fluorescence enhancement for noble metal nanoclusters. *Adv. Colloid Interface Sci.* 2017, *250*, 25–39.

137. Vázquez-Vázquez, C.; Bañobre-López, M.; Mitra, A.; López-Quintela, M. A.; Rivas, J. Synthesis of small atomic copper clusters in microemulsions. **2009**, *25*, 8208–8216.

138. Luo, Z.; Yuan, X.; Yu, Y.; Zhang, Q.; Leong, D. T.; Lee, J. Y.; Xie, J. From aggregation-induced emission of Au(I)-thiolate complexes to ultrabright Au(0)@Au(I)-thiolate core-shell nanoclusters. *J. Am. Chem. Soc.* **2012**, *134*, 16662–16670.

139. Wu, Z.; Jin, R. On the ligand's role in the fluorescence of gold nanoclusters. *Nano Lett.* **2010**, *10*, 2568–2573.

140. Wang, Z.; Susha, A. S.; Chen, B.; Reckmeier, C.; Tomanec, O.; Zboril, R.; Zhong, H.; Rogach, A. L. Poly(vinylpyrrolidone) supported copper nanoclusters: Glutathione enhanced blue photoluminescence for application in phosphor converted light emitting devices. *Nanoscale* **2016**, *8*, 7197–7202.

141. Cui, M.; Song, G.; Wang, C.; Song, Q. Synthesis of cysteine-functionalized water-soluble luminescent copper nanoclusters and their application to the determination of chromium(VI). *Microchim. Acta* **2015**, *182*, 1371–1377.

142. Wang, C.; Huang, Y. Green route to prepare biocompatible and near infrared thiolate-protected copper nanoclusters for cellular imaging. *Nano* **2013**, *8*.

143. Rajamanikandan, R.; Ilanchelian, M. Red emitting human serum albumin templated copper nanoclusters as effective candidates for highly specific biosensing of bilirubin. *Mater. Sci. Eng. C* **2019**, *98*, 1064–1072.

144. Miao, Z.; Hou, W.; Liu, M.; Zhang, Y.; Yao, S. BSA capped bi-functional fluorescent Cu nanoclusters as pH sensor and selective detection of dopamine. *New J. Chem.* **2018**, *42*, 1446–1456.

145. Feng, J.; Chen, Y.; Han, Y.; Liu, J.; Ma, S.; Zhang, H.; Chen, X. pH-Regulated synthesis of trypsin-templated copper nanoclusters with blue and yellow fluorescent emission. *ACS Omega* **2017**, *2*, 9109–9117.

146. Wang, W.; Leng, F.; Zhan, L.; Chang, Y.; Yang, X. X.; Lan, J.; Huang, C. Z. One-step prepared fluorescent copper nanoclusters for reversible pH-sensing. *Analyst* **2014**, *139*, 2990–2993.

147. Wang, C.; Wang, C.; Xu, L.; Cheng, H.; Lin, Q.; Zhang, C. Protein-directed synthesis of pH-responsive red fluorescent copper nanoclusters and their applications in cellular imaging and catalysis. *Nanoscale* **2014**, *6*, 1775–1781.

148. Yuan, J.; Wang, L.; Wang, Y.; Hao, J. Stimuli-Responsive Fluorescent Nanoswitches: Solvent-Induced Emission Enhancement of Copper Nanoclusters. *Chem. – A Eur. J.* **2020**, *26*, 3545–3554.

149. Ling, Y.; Wu, J. J.; Gao, Z. F.; Li, N. B.; Luo, H. Q. Enhanced Emission of Polyethyleneimine-Coated Copper Nanoclusters and Their Solvent Effect. *J. Phys. Chem. C* **2015**, *119*, 27173–27177.

150. Han, A.; Xiong, L.; Hao, S.; Yang, Y.; Li, X.; Fang, G.; Liu, J.; Pei, Y.; Wang, S. Highly Bright Self-Assembled Copper Nanoclusters: A Novel Photoluminescent Probe for Sensitive Detection of Histamine. *Anal. Chem.* **2018**, *90*, 9060–9067.

151. Deng, H. H.; Li, K. L.; Zhuang, Q. Q.; Peng, H. P.; Zhuang, Q. Q.; Liu, A. L.; Xia, X. H.; Chen, W. An ammonia-based etchant for attaining copper nanoclusters with green fluorescence emission. *Nanoscale* **2018**, *10,* 6467–6473.

152. Das, N. K.; Mukherjee, S. Size-controlled atomically precise copper nanoclusters: Synthetic protocols, spectroscopic properties and applications. *Phys. Sci. Rev.* **2018**, *3,* 1–22.

153. Huseyinova, S.; Blanco, J.; Requejo, F. G.; Ramallo-López, J. M.; Blanco, M. C.; Buceta, D.; López-Quintela, M. A. Synthesis of Highly Stable Surfactant-free Cu5 Clusters in Water. *J. Phys. Chem. C* **2016**, *120*, 15902–15908.

154. Wang, C.; Cheng, H.; Sun, Y.; Lin, Q.; Zhang, C. Rapid Sonochemical Synthesis of Luminescent and Paramagnetic Copper Nanoclusters for Bimodal Bioimaging. **2015**, *1*, 27–31.

155. Gui, R.; Sun, J.; Cao, X.; Wang, Y.; Jin, H. Multidentate polymers stabilized water-dispersed copper nanoclusters: Facile photoreduction synthesis and selective fluorescence turn-on response. *RSC Adv.* **2014**, *4*, 29083–29088.

156. Rajamanikandan, R.; Ilanchelian, M. Protein-protected red emittive copper nanoclusters as a fluorometric probe for highly sensitive biosensing of creatinine. *Anal. Methods* **2018**, *10,* 3666–3674.

157. Zhang, D.; Fang, Y.; Miao, Z.; Ma, M.; Du, X.; Takahashi, S.; Anzai, J. I.; Chen, Q. Direct electrodeposion of reduced graphene oxide and dendritic copper nanoclusters on glassy carbon electrode for electrochemical detection of nitrite. *Electrochim. Acta* **2013**, *107,* 656–663.

158. Wang, C.; Cheng, H.; Huang, Y.; Xu, Z.; Lin, H.; Zhang, C. Facile sonochemical synthesis of pH-responsive copper nanoclusters for selective and sensitive detection of Pb2+ in living cells. *Analyst* **2015**, *140,* 5634–5639.

159. Chen, C. A.; Wang, C. C.; Jong, Y. J.; Wu, S. M. Label-Free Fluorescent Copper Nanoclusters for Genotyping of Deletion and Duplication of Duchenne Muscular Dystrophy. *Anal. Chem.* **2015**, *87*, 6228–6232.

160. Russo, N.; Toscano, M.; Grand, A. Gas-phase theoretical prediction of the metal affinity of copper(I) ion for DNA and RNA bases. *J. Mass Spectrom.* **2003**, *38*, 265–270.

161. Cao, Q.; Li, J.; Wang, E. Recent advances in the synthesis and application of copper nanomaterials based on various DNA scaffolds. *Biosens. Bioelectron.* **2019**, *132*, 333–342.

162. Wang, X.; Hu, P.; Wang, Z.; Liu, Q.; Xu, T.; Kou, M.; Huang, K.; Chen, P. A fluorescence strategy for silver ion assay via cation exchange reaction and formation of poly(thymine)-templated copper nanoclusters. *Anal. Sci.* **2019**, *35*, 917–922.

163. Bu, X.; Fu, Y.; Jiang, X.; Jin, H.; Gui, R. Self-assembly of DNA-templated copper nanoclusters and carbon dots for ratiometric fluorometric and visual determination of arginine and acetaminophen with a logic-gate operation. *Microchim. Acta* **2020**, *187*.

164. Han, B.; Xiang, R.; Hou, X.; Yu, M.; Peng, T.; Li, Y.; He, G. One-step rapid synthesis of single thymine-templated fluorescent copper nanoclusters for “turn on” detection of Mn2+. *Anal. Methods* **2017**, *9*, 2590–2595.

165. Zhao, H.; Dong, J.; Zhou, F.; Li, B. One facile fluorescence strategy for sensitive detection of endonuclease activity using DNA-templated copper nanoclusters as signal indicators. *Sensors Actuators, B Chem.* **2017**, *238*, 828–833.

166. Pang, J.; Lu, Y.; Gao, X.; He, L.; Sun, J.; Yang, F.; Hao, Z.; Liu, Y. DNA-templated copper nanoclusters as a fluorescent probe for fluoride by using aluminum ions as a bridge. *Microchim. Acta* **2019**, *186*, 1–9.

167. Li, X. G.; Zhang, F.; Gao, Y.; Zhou, Q. M.; Zhao, Y.; Li, Y.; Huo, J. Z.; Zhao, X. J. Facile synthesis of red emitting 3-aminophenylboronic acid functionalized copper nanoclusters for rapid, selective and highly sensitive

detection of glycoproteins. *Biosens. Bioelectron.* **2016**, *86*, 270–276.

168. Muñoz-Bustos, C.; Tirado-Guízar, A.; Paraguay-Delgado, F.; Pina-Luis, G. Copper nanoclusters-coated BSA as a novel fluorescence sensor for sensitive and selective detection of mangiferin. *Sensors Actuators, B Chem.* **2017**, *244*, 922–927.

169. Liu, G.; He, W.; Liu, C. Sensitive detection of uracil-DNA glycosylase (UDG) activity based on terminal deoxynucleotidyl transferase-assisted formation of fluorescent copper nanoclusters (CuNCs). *Talanta* **2019**, *195*, 320–326.

170. Cao, J.; Wang, W.; Bo, B.; Mao, X.; Wang, K.; Zhu, X. A dual-signal strategy for the solid detection of both small molecules and proteins based on magnetic separation and highly fluorescent copper nanoclusters. *Biosens. Bioelectron.* **2017**, *90*, 534–541.

171. Lisi, S.; Fiore, E.; Scarano, S.; Pascale, E.; Boehman, Y.; Ducongé, F.; Chierici, S.; Minunni, M.; Peyrin, E.; Ravelet, C. Non-SELEX isolation of DNA aptamers for the homogeneous-phase fluorescence anisotropy sensing of tau Proteins. *Anal. Chim. Acta* **2018**, *1038*, 173–181.

172. Tombelli, S.; Minunni, M.; Mascini, M. Analytical applications of aptamers. *Biosens. Bioelectron.* **2005**, *20*, 2424–2434.

173. Chen, C. A.; Wang, C. C.; Jong, Y. J.; Wu, S. M. Label-Free Fluorescent Copper Nanoclusters for Genotyping of Deletion and Duplication of Duchenne Muscular Dystrophy. *Anal. Chem.* **2015**, *87*, 6228–6232.

174. Lalic, T.; Vossen, R. H. A. M.; Coffa, J.; Schouten, J. P.; Guc-Scekic, M.; Radivojevic, D.; Djurisic, M.; Breuning, M. H.; White, S. J.; den Dunnen, J. T. Deletion and duplication screening in the DMD gene using MLPA. *Eur. J. Hum. Genet.* **2005**, *13*, 1231–1234.

175. Gao, F.; Cai, P.; Yang, W.; Xue, J.; Gao, L.; Liu, R.; Wang, Y.; Zhao, Y.; He, X.; Zhao, L.; Huang, G.; Wu, F.; Zhao, Y.; Chai, Z.; Gao, X. Ultrasmall [64Cu]Cu nanoclusters for targeting orthotopic lung tumors using accurate positron emission tomography imaging. *ACS Nano* **2015**, *9*, 4976–4986.

176. Yan, Z.; Niu, Q.; Mou, M.; Wu, Y.; Liu, X.; Liao, S. A novel colorimetric

method based on copper nanoclusters with intrinsic peroxidase-like for detecting xanthine in serum samples. *J. Nanoparticle Res.* **2017**, *19*.

177. Xiaoqing, L.; Ruiyia, L.; Zaijun, L. Ultra sensitive and wide-range pH sensor based on the BSA-capped Cu nanoclusters fabricated by fast synthesis through the use of hydrogen peroxide additive. *RSC Adv.* **2015**, *10*, 2–8.

178. Wang, C.; Wang, C.; Xu, L.; Cheng, H.; Lin, Q.; Zhang, C. Protein-directed synthesis of pH-responsive red fluorescent copper nanoclusters and their applications in cellular imaging and catalysis. *Nanoscale* **2014**, *6*, 1775–1781.

179. Chen, M.; Li, W.; Xiong, H.; Wen, W.; Zhang, X.; Wang, S. Discrimination and ultrasensitive detection of β 2-agonists using copper nanoclusters as a fluorescent probe. *Microchim. Acta* **2017**, *184*, 3317–3324.

180. Wang, H. B.; Chen, Y.; Li, N.; Liu, Y. M. A fluorescent glucose bioassay based on the hydrogen peroxide-induced decomposition of a quencher system composed of MnO2 nanosheets and copper nanoclusters. *Microchim. Acta* **2017**, *184*, 515–523.

181. Ghosh, S.; Das, N. K.; Anand, U.; Mukherjee, S. Photostable copper nanoclusters: Compatible Förster resonance energy-transfer assays and a nanothermometer. *J. Phys. Chem. Lett.* **2015**, *6*, 1293–1298.

182. Lettieri, M.; Palladino, P.; Scarano, S.; Minunni, M. Protein-templated copper nanoclusters for fluorimetric determination of human serum albumin. *Mikrochim. Acta* **2021**, *188*, 116.

183. Wang, C.; Shu, S.; Yao, Y.; Song, Q. A fluorescent biosensor of lysozyme-stabilized copper nanoclusters for the selective detection of glucose. *RSC Adv.* **2015**, *5*, 101599–101606.

184. Ghosh, R.; Sahoo, A. K.; Ghosh, S. S.; Paul, A.; Chattopadhyay, A. Blue-emitting copper nanoclusters synthesized in the presence of lysozyme as candidates for cell labeling. *ACS Appl. Mater. Interfaces* **2014**, *6*, 3822–3828.

185. Li, X.; Wu, X.; Zhang, F.; Zhao, B.; Li, Y. Label-free detection of folic acid using a sensitive fluorescent probe based on ovalbumin stabilized copper nanoclusters. *Talanta* **2019**, *195*, 372–380.

186. Miao, H.; Zhong, D.; Zhou, Z.; Yang, X. Papain-templated Cu nanoclusters: Assaying and exhibiting dramatic antibacterial activity cooperating with H2O2. *Nanoscale* **2015**, *7*, 19066–19072.

187. Tan, Q.; Qiao, J.; Zhang, R.; Qi, L. Copper nanoclusters-modified with papaya juice for fluorescence turn-on detection of serum L-histidine Today four files of proofs was sent to m.saksena@elsevier.com Please check the files. *Microchem. J.* **2020**, *153*, 2–7.

188. Zhao, T.; He, X. W.; Li, W. Y.; Zhang, Y. K. Transferrin-directed preparation of red-emitting copper nanoclusters for targeted imaging of transferrin receptor over-expressed cancer cells. *J. Mater. Chem. B* **2015**, *3*, 2388–2394.

189. Tang, T.; Ouyang, J.; Hu, L.; Guo, L.; Yang, M.; Chen, X. Synthesis of peptide templated copper nanoclusters for fluorometric determination of Fe(III) in human serum. *Microchim. Acta* **2016**, *183*, 2831–2836.

190. Wang, Y.; Cui, Y.; Liu, R.; Wei, Y.; Jiang, X.; Zhu, H.; Gao, L.; Zhao, Y.; Chai, Z.; Gao, X. Blue two-photon fluorescence metal cluster probe precisely marking cell nuclei of two cell lines. *Chem. Commun.* **2013**, *49*, 10724–10726.

191. Rodrigues, B.; Shende, P. Monodispersed metal-based dendrimeric nanoclusters for potentiation of anti-tuberculosis action. *J. Mol. Liq.* **2020**, *304*, 112731.

192. Li, T.; Wang, Z.; Jiang, D.; Wang, H.; Lai, W. F.; Lv, Y.; Zhai, Y. A FRET biosensor based on MnO2 nanosphere/copper nanocluster complex: From photoluminescence quenching to recovery and magnification. *Sensors Actuators, B Chem.* **2019**, *290*, 535–543.

193. Feng, J.; Ju, Y.; Liu, J.; Zhang, H.; Chen, X. Polyethyleneimine-templated copper nanoclusters via ascorbic acid reduction approach as ferric ion sensor. *Anal. Chim. Acta* **2015**, *854*, 153–160.

194. Wang, Z.; Xiong, Y.; Kershaw, S. V.; Chen, B.; Yang, X.; Goswami, N.; Lai, W. F.; Xie, J.; Rogach, A. L. In Situ Fabrication of Flexible, Thermally Stable, Large-Area, Strongly Luminescent Copper Nanocluster/Polymer Composite Films. *Chem. Mater.* **2017**, *29*, 10206–10211.

195. Gou, S.; Shi, Y. E.; Li, P.; Wang, H.; Li, T.; Zhuang, X.; Li, W.; Wang, Z. Stimuli-Responsive Luminescent Copper Nanoclusters in Alginate and Their Sensing Ability for Glucose. *ACS Appl. Mater. Interfaces* **2019**.

196. Patel, R.; Bothra, S.; Kumar, R.; Crisponi, G.; Sahoo, S. K. Pyridoxamine driven selective turn-off detection of picric acid using glutathione stabilized fluorescent copper nanoclusters and its applications with chemically modified cellulose strips. *Biosens. Bioelectron.* **2018**, *102*, 196–203.

197. Dutta, A.; Goswami, U.; Chattopadhyay, A. Probing Cancer Cells through Intracellular Aggregation-Induced Emission Kinetic Rate of Copper Nanoclusters. *ACS Appl. Mater. Interfaces* **2018**, *10*, 19459–19472.

198. Nerthigan, Y.; Sharma, A. K.; Pandey, S.; Wu, H. F. Cysteine capped copper/molybdenum bimetallic nanoclusters for fluorometric determination of methotrexate via the inner filter effect. *Microchim. Acta* **2019**, *186*.

199. Wang, H. B.; Tao, B. B.; Wu, N. N.; Zhang, H. D.; Liu, Y. M. Glutathione-stabilized copper nanoclusters mediated-inner filter effect for sensitive and selective determination of p-nitrophenol and alkaline phosphatase activity. *Spectrochim. Acta - Part A Mol. Biomol. Spectrosc.* **2022**, *271*, 120948.

200. Huang, Y.; Feng, H.; Liu, W.; Zhang, S.; Tang, C.; Chen, J.; Qian, Z. Cation-driven luminescent self-assembled dots of copper nanoclusters with aggregation-induced emission for β-galactosidase activity monitoring. *J. Mater. Chem. B* **2017**, *5*, 5120–5127.

201. Jalili, R.; Khataee, A. Aluminum(III) triggered aggregation-induced emission of glutathione-capped copper nanoclusters as a fluorescent probe for creatinine. *Microchim. Acta* **2019**, *186*.

202. Wang, Y.; Chen, T.; Zhang, Z.; Ni, Y. Cytidine-stabilized copper nanoclusters as a fluorescent probe for sensing of copper ions and hemin. *RSC Adv.* **2018**, *8*, 9057–9062.

203. Li, Z.; Guo, S.; Lu, C. A highly selective fluorescent probe for sulfide ions based on aggregation of Cu nanocluster induced emission enhancement. *Analyst* **2015**, *140*, 2719–2725.

204. Hu, Y.; He, Y.; Han, Y.; Ge, Y.; Song, G.; Zhou, J. Determination of the activity of alkaline phosphatase based on aggregation-induced quenching of the fluorescence of copper nanoclusters. *Microchim. Acta* **2019**, *186*.

205. Borghei, Y. S.; Hosseini, M.; Khoobi, M.; Ganjali, M. R. Novel Fluorometric Assay for Detection of Cysteine as a Reducing Agent and Template in Formation of Copper Nanoclusters. *J. Fluoresc.* **2017**, *27*, 529–536.

206. Wang, H. B.; Tao, B. B.; Mao, A. L.; Xiao, Z. L.; Liu, Y. M. Self-assembled copper nanoclusters structure-dependent fluorescent enhancement for sensitive determination of tetracyclines by the restriction intramolecular motion. *Sensors Actuators B Chem.* **2021**, *348*, 130729.

207. Farzin, L.; Shamsipur, M.; Samandari, L.; Sheibani, S. HIV biosensors for early diagnosis of infection: The intertwine of nanotechnology with sensing strategies. *Talanta* **2020**, *206*, 120201.

208. Li, J.; Zhang, S.; Yu, Y.; Wang, Y.; Zhang, L.; Lin, B.; Guo, M.; Cao, Y. A novel universal nanoplatform for ratiometric fluorescence biosensing based on silver nanoclusters beacon. *Chem. Eng. J.* **2019**, 123526.

209. Zhang, Y.; Zhang, C.; Xu, C.; Wang, X.; Liu, C.; Waterhouse, G. I. N.; Wang, Y.; Yin, H. Ultrasmall Au nanoclusters for biomedical and biosensing applications: A mini-review. *Talanta* 2019, *200*, 432–442.

210. Liu, Y.; Dong, P.; Jiang, Q.; Wang, F.; Pang, D. W.; Liu, X. Assembly-enhanced fluorescence from metal nanoclusters and quantum dots for highly sensitive biosensing. *Sensors Actuators, B Chem.* **2019**, *279*, 334–341.

211. Liu, Z.; Jing, X.; Zhang, S.; Tian, Y. A Copper Nanocluster-Based Fluorescent Probe for Real-Time Imaging and Ratiometric Biosensing of Calcium Ions in Neurons. *Anal. Chem.* **2019**, *91*, 2488–2497.

212. Brazaca, L. C.; Ribovski, L.; Janegitz, B. C.; Zucolotto, V. Nanostructured materials and nanoparticles for point of care (POC) medical biosensors. In *Medical Biosensors for Point of Care (POC) Applications*; Med. Biosens. Point Care Appl.; Elsevier Inc., 2017; pp. 229–254.

213. Quesada-González, D.; Merkoçi, A. Nanomaterial-based devices for point-of-

care diagnostic applications. *Chem. Soc. Rev.* 2018, *47*, 4697–4709.

214. Bezinge, L.; Suea-Ngam, A.; Demello, A. J.; Shih, C. J. Nanomaterials for molecular signal amplification in electrochemical nucleic acid biosensing: Recent advances and future prospects for point-of-care diagnostics. *Mol. Syst. Des. Eng.* **2020**, *5*, 49–66.
215. Baldoneschi, V.; Palladino, P.; Scarano, S.; Minunni, M. Polynorepinephrine: state-of-the-art and perspective applications in biosensing and molecular recognition. *Anal. Bioanal. Chem.* **2020**, 5945–5954.
216. Torrini, F.; Palladino, P.; Brittoli, A.; Baldoneschi, V.; Minunni, M.; Scarano, S. Characterization of troponin T binding aptamers for an innovative enzyme-linked oligonucleotide assay (ELONA). *Anal. Bioanal. Chem.* **2019**, *411*, 7709–7716.
217. Palladino, P.; Brittoli, A.; Pascale, E.; Minunni, M.; Scarano, S. Colorimetric determination of total protein content in serum based on the polydopamine/protein adsorption competition on microplates. *Talanta* **2019**, *198*, 15–22.
218. Lettieri, M.; Palladino, P.; Scarano, S.; Minunni, M. Copper nanoclusters and their application for innovative fluorescent detection strategies: An overview. **2022**, *4*, 100108.
219. Fanali, G.; Di Masi, A.; Trezza, V.; Marino, M.; Fasano, M.; Ascenzi, P. Human serum albumin: From bench to bedside. *Mol. Aspects Med.* **2012**, *33*, 209–290.
220. Gupta, D.; Lis, C. G. Pretreatment serum albumin as a predictor of cancer survival: A systematic review of the epidemiological literature. *Nutr. J.* **2010**, *9*, 1–16.
221. Carvalho, J. R.; Machado, M. V. New insights about albumin and liver disease. *Ann. Hepatol.* **2018**, *17*, 547–560.
222. Tsuji, H.; Hashimoto, M.; Harada, T.; Tanaka, M.; Ito, H.; Murakami, K.; Ohmura, K.; Fujii, T.; Mimori, T. Persistent anemia and hypoalbuminemia in rheumatoid arthritis patients with low serum triiodothyronine level. *Mod.*

Rheumatol. **2020**, *30*, 640–647.

223. Saleem, T.; Dahpy, M.; Ezzat, G.; Abdelrahman, G.; Abdel-Aziz, E.; Farghaly, R. The Profile of Plasma Free Amino Acids in Type 2 Diabetes Mellitus with Insulin Resistance: Association with Microalbuminuria and Macroalbuminuria. *Appl. Biochem. Biotechnol.* **2019**, *188*, 854–867.

224. Dallatu, M. K.; Kaoje, A. M.; Adoke, A. U.; Kehinde, J. A.; Bunza, J. M. Microalbuminuria in Women with Risk Factors for Gestational Diabetes Mellitus in Some Selected Hospitals in Sokoto, Nigeria. *Asian J. Res. Med. Pharm. Sci.* **2019**, *6*, 1–8.

225. Gounden, V.; Vashisht, R.; Jialal, I. *Hypoalbuminemia*; StatPearls Publishing, 2020.

226. Heerspink, H. J. L.; Greene, T.; Tighiouart, H.; Gansevoort, R. T.; Coresh, J.; Simon, A. L.; Chan, T. M.; Hou, F. F.; Lewis, J. B.; Locatelli, F.; Praga, M.; Schena, F. P.; Levey, A. S.; Inker, L. A.; Sevillano, A.; Kamper, A. L.; van Zuilen, A. D.; Brenner, B. M.; Maes, B.; Ihle, B. U.; Barret, B.; Leung, C. B.; Szeto, C. C.; Fitzner, C.; Wanner, C.; Pozzi, C.; Montagnino, C. P.; Xie, D.; de Zeeuw, D.; Lewis, E.; Verde, E.; Gutierrez, E.; Imai, E.; Caravaca, F.; Fervenza, F. C.; Kobayashi, F.; Moroni, G.; Becker, G. J.; Beck, G. J.; Appel, G. B.; Frisch, G.; van Essen, G. G.; Maschio, G.; Remuzzi, G.; Montogrino, G.; Parving, H. H.; Heerspink, H. J. L.; Makino, H.; Jehan, I.; Wetzels, J. F. M.; Donadio, J.; Dwyer, J.; van den Brand, J.; Kusek, J.; Lachin, J. M.; Luño, J.; Lewis, J. B.; Floege, J.; Abebe, K. Z.; Chow, K. M.; Hunsicker, L. G.; del Vecchio, L.; Carlo, M.; Goicoechea, M.; von Eynatten, M.; Poulter, N.; Chaturvedi, N.; Passerini, P.; de Jong, P. E.; Blankestijn, P. J.; Li, P.; Ruggenenti, P.; Zucchelli, P.; Kincaid-Smith, P. S.; Hilgers, R. D.; Estacio, R. O.; Rohde, R. D.; Katafuchi, R.; Toto, R. D.; Schrier, R. W.; Rodby, R. A.; Perrone, R. D.; Ito, S.; Klahr, S.; Andrulli, S.; Strandgaard, S.; Hannedouche, T. P.; Rauen, T.; Verdalles, U.; Perkovic, V.; Keane, W. Change in albuminuria as a surrogate endpoint for progression of kidney disease: a meta-analysis of treatment effects in randomised clinical trials. *Lancet Diabetes*

Endocrinol. **2019**, *7*, 128–139.

227. Watts, G. F.; Bennett, J. E.; Rowe, D. J.; Morris, R. W.; Gatling, W.; Shaw, K. M.; Polak, A. Assessment of immunochemical methods for determining low concentrations of albumin in urine. *Clin. Chem.* **1986**, *32*, 1544–1548.
228. Aitekenov, S.; Gaipov, A.; Bukasov, R. Review: Detection and quantification of proteins in human urine. *Talanta* **2020**, 121718.
229. Xu, J. F.; Yang, Y. S.; Jiang, A. Q.; Zhu, H. L. Detection Methods and Research Progress of Human Serum Albumin. *Crit. Rev. Anal. Chem.* **2020**.
230. Regeniter, A.; Siede, W. H. Peaks and tails: Evaluation of irregularities in capillary serum protein electrophoresis. *Clin. Biochem.* **2018**, *51*, 48–55.
231. Marre, M.; Claudel, J. P.; Ciret, P.; Luis, N.; Suarez, L.; Passa, P. Laser immunonephelometry for routine quantification of urinary albumin excretion. *Clin. Chem.* **1987**, *33*, 209–213.
232. Lloyd, D. R.; Hindle, E. J.; Marples, J.; Gatt, J. A. Urinary albumin measurement by immunoturbidimetry. *Ann. Clin. Biochem.* **1987**, *24*, 209–210.
233. Shahsavari, S.; Hadian-Ghazvini, S.; Hooriabad Saboor, F.; Menbari Oskouie, I.; Hasany, M.; Simchi, A.; Rogach, A. L. Ligand functionalized copper nanoclusters for versatile applications in catalysis, sensing, bioimaging, and optoelectronics. *Mater. Chem. Front.* **2019**, *3*, 2326–2356.
234. An, Y.; Ren, Y.; Bick, M.; Dudek, A.; Hong-Wang Waworuntu, E.; Tang, J.; Chen, J.; Chang, B. Highly fluorescent copper nanoclusters for sensing and bioimaging. *Biosens. Bioelectron.* **2020**, *154*.
235. Chen, M.; Xiang, X.; Wu, K.; He, H.; Chen, H.; Ma, C. A novel detection method of human serum albumin based on the poly(Thymine)-templated copper nanoparticles. **2017**, *17*.
236. Jayasree, M.; Aparna, R. S.; Anjana, R. R.; Anjali Devi, J. S.; John, N.; Abha, K.; Manikandan, A.; George, S. Fluorescence turn on detection of bilirubin using Fe (III) modulated BSA stabilized copper nanocluster; A mechanistic perception. *Anal. Chim. Acta* **2018**, *1031*, 152–160.

237. Yang, K.; Wang, Y.; Lu, C.; Yang, X. Ovalbumin-directed synthesis of fluorescent copper nanoclusters for sensing both vitamin B1 and doxycycline. *J. Lumin.* **2018**, *196*, 181–186.

238. Xie, J.; Zheng, Y.; Ying, J. Y. Protein-directed synthesis of highly fluorescent gold nanoclusters. *J. Am. Chem. Soc.* **2009**, *131*, 888–889.

239. Lawaetz, A. J.; Stedmon, C. A. Fluorescence intensity calibration using the Raman scatter peak of water. *Appl. Spectrosc.* **2009**, *63*, 936–940.

240. Zhao, M.; Chen, A. Y.; Huang, D.; Zhuo, Y.; Chai, Y. Q.; Yuan, R. Cu nanoclusters: Novel electrochemiluminescence emitters for bioanalysis. *Anal. Chem.* **2016**, *88*, 11527–11532.

241. Gao, Z.; Su, R.; Qi, W.; Wang, L.; He, Z. Copper nanocluster-based fluorescent sensors for sensitive and selective detection of kojic acid in food stuff. *Sensors Actuators, B Chem.* **2014**, *195*, 359–364.

242. Andersson, C.; Lönnroth, C.; Moldawer, L. L.; Ternell, M.; Lundholm, K. Increased degradation of albumin in cancer is not due to conformational or chemical modifications in the albumin molecule. *J. Surg. Res.* **1990**, *49*, 23–29.

243. Boonpipattanapong, T.; Chewatanakornkul, S. Preoperative carcinoembryonic antigen and albumin in predicting survival in patients with colon and rectal carcinomas. *J. Clin. Gastroenterol.* **2006**, *40*, 592–595.

244. Siddiqui, A.; Heinzerling, J.; Livingston, E. H.; Huerta, S. Predictors of early mortality in veteran patients with pancreatic cancer. *Am. J. Surg.* **2007**, *194*, 362–366.

245. Brinkman, J. W.; Bakker, S. J. L.; Gansevoort, R. T.; Hillege, H. L.; Kema, I. P.; Gans, R. O. B.; De Jong, P. E.; De Zeeuw, D. Which method for quantifying urinary albumin excretion gives what outcome? A comparison of immunonephelometry with HPLC. *Kidney Int. Suppl.* **2004**, *66*, S69–S75.

246. Shaikh, A.; Seegmiller, J. C.; Borland, T. M.; Burns, B. E.; Ladwig, P. M.; Singh, R. J.; Kumar, R.; Larson, T. S.; Lieske, J. C. Comparison between immunoturbidimetry, size-exclusion chromatography, and LC-MS to quantify

urinary albumin. *Clin. Chem.* **2008**, *54*, 1504–1510.

247. Huang, Z.; Wang, H.; Yang, W. Gold nanoparticle-based facile detection of human serum albumin and its application as an INHIBIT logic gate. *ACS Appl. Mater. Interfaces* **2015**, *7*, 8990–8998.

248. Lin, Z. H.; Chen, I. C.; Chang, H. T. Detection of human serum albumin through surface-enhanced Raman scattering using gold “pearl necklace” nanomaterials as substrates. *Chem. Commun.* **2011**, *47*, 7116–7118.

249. Scaglione, F.; Alladio, E.; Damin, A.; Turci, F.; Baggiani, C.; Giovannoli, C.; Bordiga, S.; Battezzati, L.; Rizzi, P. Functionalized nanoporous gold as a new biosensor platform for ultra-low quantitative detection of human serum albumin. *Sensors Actuators, B Chem.* **2019**, *288*, 460–468.

250. Jean, R. Der; Larsson, M.; Cheng, W. Da; Hsu, Y. Y.; Bow, J. S.; Liu, D. M. Design and optimization of a nanoprobe comprising amphiphilic chitosan colloids and Au-nanorods: Sensitive detection of human serum albumin in simulated urine. *Appl. Surf. Sci.* **2016**, *390*, 675–680.

251. Wang, T.; Chen, M.; Niu, C.; Liu, N.; Wang, L.; Sun, B.; Hua, W.; Ouyang, J. Flow-injection with enhanced evaporative light scattering detector detection and quantification of human serum albumin using gold nanoparticles. *Anal. Methods* **2015**, *7*, 3185–3192.

252. Lai, T.; Hou, Q.; Yang, H.; Luo, X.; Xi, M. Clinical application of a novel sliver nanoparticles biosensor based on localized surface plasmon resonance for detecting the microalbuminuria. *Acta Biochim. Biophys. Sin. (Shanghai).* **2010**, *42*, 787–792.

253. Sieroń, A.; Sieroń-Stołtny, K.; Kawczyk-Krupka, A.; Latos, W.; Kwiatek, S.; Straszak, D.; Bugaj, A. M. The role of fluorescence diagnosis in clinical practice. *Onco. Targets. Ther.* **2013**, *6*, 977.

254. Chowdhury, S.; Rooj, B.; Dutta, A.; Mandal, U. Review on Recent Advances in Metal Ions Sensing Using Different Fluorescent Probes. *J. Fluoresc. 2018 284* **2018**, *28*, 999–1021.

255. Liu, Z. M.; Feng, L.; Hou, J.; Lv, X.; Ning, J.; Ge, G. B.; Wang, K. W.; Cui,

J. N.; Yang, L. A ratiometric fluorescent sensor for highly selective detection of human carboxylesterase 2 and its application in living cells. *Sensors Actuators B Chem.* **2014**, *205*, 151–157.

256. Hu, G.; Jia, H.; Zhao, L.; Cho, D. H.; Fang, J. Small molecule fluorescent probes of protein vicinal dithiols. *Chinese Chem. Lett.* **2019**, *30*, 1704–1716.

257. Tian, M.; Ma, Y.; Lin, W. Fluorescent Probes for the Visualization of Cell Viability. *Acc. Chem. Res.* **2019**, *52*, 2147–2157.

258. Mohammad-Zadeh, L. F.; Moses, L.; Gwaltney-Brant, S. M. Serotonin: a review. *J. Vet. Pharmacol. Ther.* **2008**, *31*, 187–199.

259. Jeon, K.; Andoy, N. M. O.; Schmitt, C. W.; Xue, Y.; Barner, L.; Sullan, R. M. A. Size-controlled synthesis of bioinspired polyserotonin nanoparticles with free radical scavenging activity. *J. Mater. Chem. B* **2021**, *9*, 634–637.

260. Nakatsuka, N.; Hasani-Sadrabadi, M. M.; Cheung, K. M.; Young, T. D.; Bahlakeh, G.; Moshaverinia, A.; Weiss, P. S.; Andrews, A. M. Polyserotonin Nanoparticles as Multifunctional Materials for Biomedical Applications. *ACS Nano* **2018**, *12*, 4761–4774.

261. Ishino, K.; Nishitani, S.; Man, Y.; Saito, A.; Sakata, T. Surface Characteristics and Formation of Polyserotonin Thin Films for Bioelectrical and Biocompatible Interfaces. *ACS Appl. Mater. Interfaces* **2022**.

262. Kiratitanavit, W.; Bruno, F. F.; Xia, Z.; Yu, S.; Kumar, J.; Nagarajan, R. Biocatalytic synthesis of fluorescent conjugated polyserotonin. *J. Renew. Mater.* **2019**, *7*, 205–214.

263. Farahmand Nejad, M. A.; Ghasemi, F.; Hormozi-Nezhad, M. R. A wide-color-varying ratiometric nanoprobe for detection of norepinephrine in urine samples. *Anal. Chim. Acta* **2018**, *1039*, 124–131.

264. Koh, D. Y.; Kook, J. K.; Lee, S. W. Highly fluorescent oligodopamine (F-ODA) for accurate and sensitive detection of the neurotransmitter dopamine. *Anal. Biochem.* **2020**, *591*, 113571.

265. Maung, M. T.; Carlson, A.; Olea-Flores, M.; Elkhadragy, L.; Schachtschneider, K. M.; Navarro-Tito, N.; Padilla-Benavides, T. The

molecular and cellular basis of copper dysregulation and its relationship with human pathologies. *FASEB J.* **2021**, *35*, 1–50.

266. Tsang, T.; Davis, C. I.; Brady, D. C. Copper biology. *Curr. Biol.* **2021**, *31*, R421–R427.

267. Zuily, L.; Lahrach, N.; Fassler, R.; Genest, O.; Faller, P.; Sénèque, O.; Denis, Y.; Castanié-Cornet, M. P.; Genevaux, P.; Jakob, U.; Reichmann, D.; Giudici-Orticoni, M. T.; Ilbert, M. Copper Induces Protein Aggregation, a Toxic Process Compensated by Molecular Chaperones. *MBio* **2022**, *13*.

268. Donnelly, P. S.; Xiao, Z.; Wedd, A. G. Copper and Alzheimer's disease. *Curr. Opin. Chem. Biol.* **2007**, *11*, 128–133.

269. Davies, K. M.; Mercer, J. F. B.; Chen, N.; Double, K. L. Copper dyshomoeostasis in Parkinson's disease: Implications for pathogenesis and indications for novel therapeutics. *Clin. Sci.* **2016**, *130*, 565–574.

270. Ni, M.; You, Y.; Chen, J.; Zhang, L. Copper in depressive disorder: A systematic review and meta-analysis of observational studies. *Psychiatry Res.* **2018**, *267*, 506–515.

271. Moini, M.; To, U.; Schilsky, M. L. Recent advances in Wilson disease. *Transl. Gastroenterol. Hepatol.* **2021**, *6*, 21–21.

272. Brewer, G. J.; Gow, P. J.; Smallwood, R. A.; Angus, P. W.; Sewell, R. B.; Smith, A. L.; Wall, A. J. Diagnosis of Wilson's disease: An experience over three decades. *Gut* **2002**, *50*, 136.

273. Walshe, J. M. The pattern of urinary copper excretion and its responseto treatment in patients with Wilson's disease. **2011**, *104*, 775–778.

274. Gray, L. W.; Peng, F.; Molloy, S. A.; Pendyala, V. S.; Muchenditsi, A.; Muzik, O.; Lee, J.; Kaplan, J. H.; Lutsenko, S. Urinary Copper Elevation in a Mouse Model of Wilson's Disease Is a Regulated Process to Specifically Decrease the Hepatic Copper Load. *PLoS One* **2012**, *7*, e38327.

275. Woimant, F.; Djebrani-Oussedik, N.; Poujois, A. New tools for Wilson's disease diagnosis: exchangeable copper fraction. *Ann. Transl. Med.* **2019**, *7*, S70–S70.

276. Robson, A. F.; Lockett, P.; Tetlow, L.; Chaloner, C. Evaluation of 24-h urine containers for urine copper measurement by inductively coupled plasma mass spectrometry. *Ann. Clin. Biochem.* **2020**, *57*, 246–248.

277. Lakowicz, J. R. Principles of fluorescence spectroscopy. *Princ. Fluoresc. Spectrosc.* **2006**, 1–954.

278. Heuther, G.; Reimer, A.; Schmidt, F.; Schuff-Werner, P.; Brudny, M. M. Oxidation of the indole nucleus of 5-hydroxytryptamine and formation of dimers in the presence of peroxidase and H2O2. *J. Neural Transm. Suppl.* **1990**, *32*, 249–257.

279. Dai, Z.; Chauhan, S.; Green, T. K. Synthesis and enantioseparation of atropisomers of serotonin dimer. *Tetrahedron Lett.* **2015**, *56*, 4022–4024.

280. Wrona, M. Z.; Dryhurst, G. Electrochemical oxidation of 5-hydroxytryptamine in aqueous solution at physiological pH. *Bioorg. Chem.* **1990**, *18*, 291–317.

281. Wrona, M. Z.; Dryhurst, G. Oxidation Chemistry of 5-Hydroxytryptamine. 1. Mechanism and Products Formed at Micromolar Concentrations. *J. Org. Chem.* **1987**, *52*, 2817–2825.

282. Jones, C. E.; Underwood, C. K.; Coulson, E. J.; Taylor, P. J. Copper induced oxidation of serotonin: analysis of products and toxicity. *J. Neurochem.* **2007**, *102*, 1035–1043.

283. Strambini, G. B.; Gabellieri, E. Quenching of indole luminescence by copper ions: A distance dependence study. *J. Phys. Chem.* **1991**, *95*, 4347–4352.

284. Bu, J.; Duan, H.; Wang, X. Fluorescence sensors for Cu2+ based on conjugated indole Schiff base. *Res. Chem. Intermed.* **2014**, *40*, 3119–3126.

285. Lin, J. H.; Yu, C. J.; Yang, Y. C.; Tseng, W. L. Formation of fluorescent polydopamine dots from hydroxyl radical-induced degradation of polydopamine nanoparticles. *Phys. Chem. Chem. Phys.* **2015**, *17*, 15124–15130.

286. An, T.; Lee, N.; Cho, H. J.; Kim, S.; Shin, D. S.; Lee, S. M. Ultra-selective detection of Fe2+ ion by redox mechanism based on fluorescent polymerized

dopamine derivatives. *RSC Adv.* **2017**, *7*, 30582–30587.

287. García-Moreno, E.; Tomás, A.; Atrián-Blasco, E.; Gascón, S.; Romanos, E.; Rodriguez-Yoldi, J. M.; Cerrada, E.; Laguna, M. In vitro and in vivo evaluation of organometallic gold(I) derivatives as anticancer agents. *Dalt. Trans.* **2016**, *45*, 2462–2475.

288. Zhou, Q.; Guo, W.; Jia, Y.; Xu, J. Comparison of chromium and iron distribution in serum and urine among healthy people and prediabetes and diabetes patients. *Biomed Res. Int.* **2019**, *2019*.

289. Neslihan Sarigul, F. K. & İ. K. A New Artificial Urine Protocol to Better Imitate Human Urine. *Sci. Rep.* **2019**, *9*, 1–11.

290. Huang, L. K.; Chao, S. P.; Hu, C. J. Clinical trials of new drugs for Alzheimer disease. *J. Biomed. Sci.* **2020**, *27*, 1–13.

291. Höllein, L.; Kaale, E.; Mwalwisi, Y. H.; Schulze, M. H.; Holzgrabe, U. Routine quality control of medicines in developing countries: Analytical challenges, regulatory infrastructures and the prevalence of counterfeit medicines in Tanzania. *TrAC - Trends Anal. Chem.* **2016**, *76*, 60–70.

292. Substandard and falsified medical products. Available online: https://www.who.int/news-room/fact-sheets/detail/substandard-and-falsified-medical-products (accessed on 11 Aug 2022).

293. Fernandez, F. M.; Green, M. D.; Newton, P. N. Prevalence and detection of counterfeit pharmaceuticals: A mini review. *Ind. Eng. Chem. Res.* **2008**, *47*, 582–590.

294. European Pharmacopoeia, Supplement 4.1 to the 4th Edition (April 2002 edition) | Open Library. Available online: https://openlibrary.org/books/OL12948556M/European_Pharmacopoeia_Supplement_4.1_to_the_4th_Edition (accessed on 15 Jan 2023).

295. The United States Pharmacopeia : USP 28 : the National Formulary : NF 23 : by authority of the United States Pharmacopeial Convention, Inc., meeting at Washington, D.C., April 12-16, 2000 : United States Pharmacopeial Convention : Free Download, Borrow, a. Available online:

https://archive.org/details/unitedstatesphar00unit (accessed on 26 Aug 2022).

296. Görög, S. The sacred cow: the questionable role of assay methods in characterising the quality of bulk pharmaceuticals. *J. Pharm. Biomed. Anal.* **2005**, *36*, 931–937.

297. European Pharmacopoeia (Ph. Eur.) 11th Edition - European Directorate for the Quality of Medicines & HealthCare. Available online: https://www.edqm.eu/en/european-pharmacopoeia-ph.-eur.-11th-edition (accessed on 15 Jan 2023).

298. Japanese Pharmacopoeia 18th Edition | Pharmaceuticals and Medical Devices Agency. Available online: https://www.pmda.go.jp/english/rs-sb-std/standards-development/jp/0029.html (accessed on 15 Jan 2023).

299. US Pharmacopeia (USP). Available online: https://www.usp.org/ (accessed on 15 Jan 2023).

300. Görög, S. *Ultraviolet-visible spectrophotometry in pharmaceutical analysis*; Ultraviolet-Visible Spectrophotometry Pharm. Anal.; CRC Press, 2018.

301. Karpińska, J. Derivative spectrophotometry—recent applications and directions of developments. *Talanta* **2004**, *64*, 801–822.

302. Haque, M. S. Review on Quantification of Some Selected Cardiovascular Drugs and Their Metabolites in Pharmaceuticals. *Der Pharma Chem.* **2017**, *9*, 100–108.

303. Saleh, M. S.; Youssef, A. K.; Hashem, E. Y.; Abdel-Kader, D. A. A Novel Spectrophotometric Method for Determination of Gabapentin in Pharmaceutical Formulations Using 2,5-Dihydroxybenzaldehyde. *Comput. Chem.* **2014**, *02*, 22–30.

304. Blaih, S. M.; Abdine, H. H.; El-yazbi, F. A.; Shaalan, R. A. Spectrophotometric determination of enalapril maleate and ramipril in dosage forms. *Spectrosc. Lett.* **2000**, *33*, 91–102.

305. Çekiç, S. D.; Filik, H.; Apak, R. Simultaneous Spectrophotometric Determination of Paracetamol and p-Aminophenol in Pharmaceutical Products with Tiron Using Dissolved Oxygen as Oxidant. *J. Anal. Chem. 2005 6011*

2005, *60*, 1019–1023.

306. Raza, A.; Zia-ul-Haq, M. Application of Certain π-Acceptors for the Spectrophotometric Determination of Alendronate Sodium in Pharmaceutical Bulk and Dosage Forms. *Int. J. Anal. Chem.* **2011**, *2011*, 1–6.

307. Toker, S. E.; Önal, A. Spectrophotometric determination of antidepressant drug duloxetine in pharmaceutical preparations using π-Acceptors. *E-Journal Chem.* **2012**, *9*, 323–329.

308. Helmy, A.; Abdel-Gawad, F. M.; Mohamed, E. F. *Spectrophotometric Study on Determination of Aripiprazole in Tablets by Charge-Transfer and Ion-Pair Complexation Reactions with Some Acceptors*; Asian J. Pharm. Anal.; 2012.

309. Omar, M. A.; Abdelmageed, O. H.; Abdelgaber, A. A.; Saleh, S. F.; Omar, M. A.; Abdelmageed, O. H.; Abdelgaber, A. A.; Saleh, S. F. Spectrophotometric determination of some calcium channel blockers using Sulfochlorophenol-S, Bromopyrogallol red, Eriochromecyanine-R and Pyrocatechoil violet. *Nat. Sci.* **2013**, *5*, 514–525.

310. Bali, A.; Gaur, P. A novel method for spectrophotometric determination of pregabalin in pure form and in capsules. *Chem. Cent. J.* **2011**, *5*, 1–7.

311. Rahman, N.; Singh, M.; Hoda, M. N. Optimized and validated spectrophotometric methods for the determination of lisinopril in pharmaceutical formulations using ninhydrin and ascorbic acid. *J. Braz. Chem. Soc.* **2005**, *16*, 1001–1009.

312. Gandhimathi, M.; Kochupappy Ravi, T. Use of Folin-Ciocalteu phenol reagent and 3-methyl-2-benzothiazolinone hydrazine hydrochloride in the determination of oxcarbazepine in pharmaceuticals. *Acta Pharm* **2008**, *58*, 111–118.

313. Ahmad, A. S.; Rahman, N.; Islam, F. Spectrophotometric Determination of Ampicillin, Amoxycillin, and Carbenicillin Using Folin-Ciocalteu Phenol Reagent. *J. Anal. Chem. 2004 592* **2004**, *59*, 119–123.

314. Kramancheva, I.; Dobrev, I.; Brakalov, L.; Andreeva, A. Spectrophotometric determination of diclofenac sodium in gel-ointment. **1997**, *30*, 2235–2249.

315. Rahman, N.; Azmi, S. N. H. Spectrophotometric determination of diltiazem hydrochloride with sodium metavanadate. *Microchem. J.* **2000**, *65*, 39–43.

316. Chennaiah, M.; Veeraiah, T.; Singh, T. C.; Venkateshwarlu, G. Extractive spectrophotometric methods for determination of rasagiline mesylate in pharmaceutical formulations using acidic triphenylmethane dyes. *J. Chil. Chem. Soc.* **2011**, *56*, 926–929.

317. Spectrophotometric determination of carbinoxamine maleate in pharmaceutical formulations by ternary complex formation with Cu(II) and eosin. | DrugBank Online. Available online: https://go.drugbank.com/articles/A5556 (accessed on 26 Aug 2022).

318. Rahman, N.; Rahman, H.; Azmi, S. N. H. Validated Kinetic Spectrophotometric Method for the Determination of Metoprolol Tartrate in Pharmaceutical Formulations. *Chem. Pharm. Bull.* **2005**, *53*, 942–948.

319. Vinay Revenasiddappa, K. H. Spectrophotometric determination of quetiapine fumarate in pharmaceuticals and human urine by two charge-transfer complexation reactions. *Chem. Ind. Chem. Eng. Q.* **2012**, *18*, 263–272.

320. Lampadius, W. A. Ueber die Verfälschung der Kobaltsaflore (Zaffer) und deren technisch-chemische Prüfung. *J. für Prakt. Chemie* **1838**, *13*, 385–397.

321. Beer Bestimmung der Absorption des rothen Lichts in farbigen Flüssigkeiten. *Ann. Phys.* **1852**, *162*, 78–88.

322. Willard, H. H. From Buret and Balance to Spectrometer and Titrimeter (Fisher Award Address). *Anal. Chem.* **1951**, *23*, 1726–1729.

323. Tomberg, V. Über eine neue Methode der Messung sehr kleiner Mengen von CO in Luft, Blut und Lunge. *Experientia* **1954**, *10*, 388–389.

324. MÜller, E. Über eine einfache colorimetrische Methode zur Bestimmung von Serumspeudocholinesterase. *Fresenius' Zeitschrift für Anal. Chemie 1960 1763* **1960**, *176*, 240–240.

325. Noburo Ohta, A. R. R. *Colorimetry Fundamentals and Applications*; 2005.

326. Yang, J.; Wang, K.; Xu, H.; Yan, W.; Jin, Q.; Cui, D. Detection platforms for point-of-care testing based on colorimetric, luminescent and magnetic assays:

A review. *Talanta* **2019**, *202*, 96–110.

327. Umapathi, R.; Sonwal, S.; Lee, M. J.; Mohana Rani, G.; Lee, E. S.; Jeon, T. J.; Kang, S. M.; Oh, M. H.; Huh, Y. S. Colorimetric based on-site sensing strategies for the rapid detection of pesticides in agricultural foods: New horizons, perspectives, and challenges. *Coord. Chem. Rev.* **2021**, *446*, 214061.

328. Liu, D. M.; Xu, B.; Dong, C. Recent advances in colorimetric strategies for acetylcholinesterase assay and their applications. *TrAC Trends Anal. Chem.* **2021**, *142*, 116320.

329. Stephens, I. O.; Thomas, E. M. New Colorimetric Assay of Apurinic/Apyrimidinic (Abasic) Sites of Deoxyribonucleic Acid (DNA) Nucleotides Using Bicinchoninic Assay: A Bioanalytical Chemistry Experiment for the Undergraduate Curriculum. *J. Chem. Educ.* **2022**, *99*, 1454–1459.

330. Green, M. D.; Hostetler, D. M.; Nettey, H.; Swamidoss, I.; Ranieri, N.; Newton, P. N. Integration of Novel Low-Cost Colorimetric, Laser Photometric, and Visual Fluorescent Techniques for Rapid Identification of Falsified Medicines in Resource-Poor Areas: Application to Artemether–Lumefantrine. *Am. J. Trop. Med. Hyg.* **2015**, *92*, 8–16.

331. Jähnke, R. W. O.; Küsters, G.; Fleischer, K. Low-Cost Quality Assurance of Medicines Using the Gphf-Minilab®. *Drug Inf. J. DIJ / Drug Inf. Assoc. 2001 353* **2001**, *35*, 941–945.

332. Weaver, A. A.; Lieberman, M. Paper test cards for presumptive testing of very low quality antimalarial medications. *Am. J. Trop. Med. Hyg.* **2015**, *92*, 17–23.

333. Görög, S.; Horváth, P. Analysis of steroids. Part XXXI. Mechanism of the tetrazolium reaction of corticosteroids. *Analyst* **1978**, *103*, 346–353.

334. Freeman, H. S. Aromatic amines: Use in azo dye chemistry. *Front. Biosci.* **2013**, *18*, 145–164.

335. Bisaglia, M.; Filograna, R.; Beltramini, M.; Bubacco, L. Are dopamine derivatives implicated in the pathogenesis of Parkinson's disease? *Ageing Res.*

Rev. **2014**, *13*, 107–114.

336. Jeitner, T. M.; Kalogiannis, M.; Krasnikov, B. F.; Gomlin, I.; Peltier, M. R.; Moran, G. R. Linking Inflammation and Parkinson Disease: Hypochlorous Acid Generates Parkinsonian Poisons. *Toxicol. Sci.* **2016**, *151*, 388–402.

337. Palladino, P.; Torrini, F.; Scarano, S.; Minunni, M. Colorimetric analysis of the early oxidation of dopamine by hypochlorous acid as preliminary screening tool for chemical determinants of neuronal oxidative stress. *J. Pharm. Biomed. Anal.* **2020**, *179*, 113016.

338. Leong, S. L.; Cappai, R.; Barnham, K. J.; Pham, C. L. L. Modulation of α-synuclein aggregation by dopamine: A review. *Neurochem. Res.* **2009**, *34*, 1838–1846.

339. Connolly, B. S.; Lang, A. E. Pharmacological Treatment of Parkinson Disease: A Review. **2014**, *311*, 1670–1683.

340. Oertel, W. H.; Hallett, M.; Lewitt, P. Recent advances in treating Parkinson’s disease. *F1000Research 2017 6260* **2017**, *6*, 260.

341. Wollmer, E.; Klein, S. Development and Validation of a Robust and Efficient HPLC Method for the Simultaneous Quantification of Levodopa, Carbidopa, Benserazide and Entacapone in Complex Matrices. *J. Pharm. Pharm. Sci.* **2017**, *20*, 258–269.

342. Fanali, S.; Pucci, V.; Sabbioni, C.; Raggi, M. A. Quality control of benserazide-levodopa and carbidopa-levodopa tablets by capillary zone electrophoresis. **2000**, *12*, 2432–7.

343. Wang, J.; Zhou, Y.; Liang, J.; He, P. G.; Fang, Y. Z. Determination of Levodopa and Benserazide Hydrochloride in Pharmaceutical Formulations by CZE with Amperometric Detection. *Chromatographia* **2005**, *61*, 265–270.

344. Maia Quintino, M. S.; Yamashita, M.; Angnes, L. Voltammetric Studies and Determination of Levodopa and Carbidopa in Pharmaceutical Products. *Electroanalysis* **2006**, *18*, 655–661.

345. Saini, A. S.; Kumar, J.; Melo, J. S. Microplate based optical biosensor for l-Dopa using tyrosinase from Amorphophallus campanulatus. *Anal. Chim. Acta*

2014, *849*, 50–56.

346. Hassib, S. T.; El-Khateeb, S. Z. Sepectrometric Determination of Madopar Capsules. *Pharm. Anal.* **2006**, *23*, 255–271.

347. Coello, J.; Maspoch, S.; Villegas, N. Simultaneous kinetic-spectrophotometric determination of levodopa and benserazide by bi- and three-way partial least squares calibration. *Talanta* **2000**, *53*, 627–637.

348. Nagaraja, P.; Vasantha, R. A.; Sunitha, K. R. A sensitive and selective spectrophotometric estimation of catechol derivatives in pharmaceutical preparations. *Talanta* **2001**, *55*, 1039–1046.

349. Uslu, B.; Özkan, S. A. Determination of binary mixtures of levodopa and benserazide in pharmaceuticals by ratio-spectra derivative spectrophotometry. *J Pharm Biomed Anal* **2007**, *35*, 303–314.

350. Damiani, P. C.; Moschetti, A. C.; Rovetto, A. J.; Benavente, F.; Olivieri, A. C. Design and optimization of a chemometrics-assisted spectrophotometric method for the simultaneous determination of levodopa and carbidopa in pharmaceutical products. *Anal. Chim. Acta* **2005**, *543*, 192–198.

351. Chamsaz, M.; Safavi, A.; Fadaee, J. Simultaneous kinetic-spectrophotometric determination of carbidopa, levodopa and methyldopa in the presence of citrate with the aid of multivariate calibration and artificial neural networks. *Anal. Chim. Acta* **2007**, *603*, 140–146.

352. Chou, Y. C.; Shih, C. I.; Chiang, C. C.; Hsu, C. H.; Yeh, Y. C. Reagent-free DOPA-dioxygenase colorimetric biosensor for selective detection of L-DOPA. *Sensors Actuators B Chem.* **2019**, *297*, 126717.

353. Baron, R.; Zayats, M.; Willner, I. Dopamine-, L-DOPA-, adrenaline-, and noradrenaline-induced growth of Au nanoparticles: Assays for the detection of neurotransmitters and of tyrosinase activity. *Anal. Chem.* **2005**, *77*, 1566–1571.

354. Khanmohammadi, M.; Mobedi, E.; Garmarudi, A. B.; Mobedi, H.; Kargosha, K. Simultaneous Determination of Levodopa and Carbidopa in Levodopa-Carbidopa Tablets by ATR-FTIR Spectrometry. *Pharm. Dev. Technol.* **2008**,

12, 573–580.

355. Talebpour, Z.; Haghgoo, S.; Shamsipur, M. 1H nuclear magnetic resonance spectroscopy analysis for simultaneous determination of levodopa, carbidopa and methyldopa in human serum and pharmaceutical formulations. *Anal. Chim. Acta* **2004**, *506*, 97–104.

356. Ong, J. J.; Pollard, T. D.; Goyanes, A.; Gaisford, S.; Elbadawi, M.; Basit, A. W. Optical biosensors - Illuminating the path to personalized drug dosing. *Biosens. Bioelectron.* **2021**, *188*, 113331.

357. Vachtenheim, J.; Duchoň, J.; Matouš, B. A spectrophotometric assay for mammalian tyrosinase utilizing the formation of melanochrome from l-dopa. *Anal. Biochem.* **1985**, *146*, 405–410.

358. Palladino, P.; Minunni, M.; Scarano, S. Cardiac Troponin T capture and detection in real-time via epitope-imprinted polymer and optical biosensing. *Biosens. Bioelectron.* **2018**, *106*, 93–98.

359. Scarano, S.; Pascale, E.; Palladino, P.; Fratini, E.; Minunni, M. Determination of fermentable sugars in beer wort by gold nanoparticles@polydopamine: A layer-by-layer approach for Localized Surface Plasmon Resonance measurements at fixed wavelength. *Talanta* **2018**, *183*, 24–32.

360. Scarano, S.; Palladino, P.; Pascale, E.; Brittoli, A.; Minunni, M. Colorimetric determination of p-nitrophenol by using ELISA microwells modified with an adhesive polydopamine nanofilm containing catalytically active gold nanoparticles. *Microchim. Acta* **2019**, *186*, 1–7.

361. Palladino, P.; Bettazzi, F.; Scarano, S. Polydopamine: surface coating, molecular imprinting, and electrochemistry—successful applications and future perspectives in (bio)analysis. *Anal. Bioanal. Chem.* **2019**, *411*, 4327–4338.

362. Baldoneschi, V.; Palladino, P.; Banchini, M.; Minunni, M.; Scarano, S. Norepinephrine as new functional monomer for molecular imprinting: An applicative study for the optical sensing of cardiac biomarkers. *Biosens. Bioelectron.* **2020**, *157*, 112161.

363. Torrini, F.; Palladino, P.; Baldoneschi, V.; Scarano, S.; Minunni, M. Sensitive ‘two-steps’ competitive assay for gonadotropin-releasing hormone detection via SPR biosensing and polynorepinephrine-based molecularly imprinted polymer. *Anal. Chim. Acta* **2021**, *1161*, 338481.

364. Palladino, P.; Brittoli, A.; Pascale, E.; Minunni, M.; Scarano, S. Colorimetric determination of total protein content in serum based on the polydopamine/protein adsorption competition on microplates. *Talanta* **2019**, *198*, 15–22.

365. Torrini, F.; Scarano, S.; Palladino, P.; Minunni, M. Polydopamine-based quantitation of albuminuria for the assessment of kidney damage. *Anal. Bioanal. Chem.* **2021**, *413*, 2217–2224.

366. Tan, X.; Gao, P.; Li, Y.; Qi, P.; Liu, J.; Shen, R.; Wang, L.; Huang, N.; Xiong, K.; Tian, W.; Tu, Q. Poly-dopamine, poly-levodopa, and poly-norepinephrine coatings: Comparison of physico-chemical and biological properties with focus on the application for blood-contacting devices. *Bioact. Mater.* **2021**, *6*, 285–296.

367. Ruiz-Valdepeñas Montiel, V.; Pellicanò, A.; Campuzano, S.; Torrente-Rodríguez, R. M.; Reviejo, Á. J.; Cosio, M. S.; Pingarrón, J. M. Electrochemical detection of peanuts at trace levels in foods using a magnetoimmunosensor for the allergenic protein Ara h 2. *Sensors Actuators, B Chem.* **2016**, *236*, 825–833.

368. Fatibello-Filho, O.; Da Cruz Vieira, I. Flow Injection Spectrophotometric Determination of L-Dopa andCarbidopa in Pharmaceutical Formulations Using a Crude Extract of SweetPotato Root [Ipomoea batatas (L.) Lam.] as EnzymaticSource. *Analyst* **1997**, *122*, 345–350.

369. Mason, H. S.; Peterson, E. W. Melanoproteins. I. Reactions between enzyme-generated quinones and amino acids. *Biochim. Biophys. Acta* **1965**, *111*, 134–146.

370. Napolitano, A.; Corradini, M. G.; Prota, G. A reinvestigation of the structure of melanochrome. *Tetrahedron Lett.* **1985**, *26*, 2805–2808.

371. Pezzella, A.; Panzella, L.; Crescenzi, O.; Napolitano, A.; Navaratman, S.; Edge, R.; Land, E. J.; Barone, V.; D'Ischia, M. Short-lived quinonoid species from 5,6-dihydroxyindole dimers en route to eumelanin polymers: Integrated chemical, pulse radiolytic, and quantum mechanical investigation. *J. Am. Chem. Soc.* **2006**, *128*, 15490–15498.

372. Micillo, R.; Panzella, L.; Iacomino, M.; Prampolini, G.; Cacelli, I.; Ferretti, A.; Crescenzi, O.; Koike, K.; Napolitano, A.; D'Ischia, M. Eumelanin broadband absorption develops from aggregation-modulated chromophore interactions under structural and redox control. *Sci. Reports 2017 71* **2017**, *7*, 1–12.

373. Fu, Y.; Liu, L.; Wang, Y. M.; Li, J. N.; Yu, T. Q.; Guo, Q. X. Quantum-chemical predictions of redox potentials of organic anions in dimethyl sulfoxide and reevaluation of bond dissociation enthalpies measured by the electrochemical methods. *J. Phys. Chem. A* **2006**, *110*, 5874–5886.

374. Zhu, X. Q.; Wang, C. H.; Liang, H. Scales of oxidation potentials, p K a, and BDE of various hydroquinones and catechols in DMSO. *J. Org. Chem.* **2010**, *75*, 7240–7257.

375. Rossini, E.; Bochevarov, A. D.; Knapp, E. W. Empirical Conversion of pKa Values between Different Solvents and Interpretation of the Parameters: Application to Water, Acetonitrile, Dimethyl Sulfoxide, and Methanol. *ACS Omega* **2018**, *3*, 1653–1662.

376. Answers, F.; Lives, C.; Parkinson, B. Lessons from the 2011 Sinemet Shortage. **2011**.

377. Go, C. L.; Rosales, R. L.; Schmidt, P.; Lyons, K. E.; Pahwa, R.; Okun, M. S. Generic versus branded pharmacotherapy in Parkinson's disease: Does it matter? A review. *Parkinsonism Relat. Disord.* **2011**, *17*, 308–312.

378. Kish, S. J.; Shannak, K.; Hornykiewicz, O. Uneven Pattern of Dopamine Loss in the Striatum of Patients with Idiopathic Parkinson's Disease. *N. Engl. J. Med.* **1988**, *318*, 876–880.

379. Connolly, B. S.; Lang, A. E. Pharmacological treatment of Parkinson disease:

a review. **2014**, *311*, 1670–1683.

380. Oertel, W. H.; Hallett, M.; Lewitt, P. Recent advances in treating Parkinson's disease. *F1000Research 2017 6260* **2017**, *6*, 260.

381. Lettieri, M.; Emanuele, R.; Scarano, S.; Palladino, P.; Minunni, M. Melanochrome-based colorimetric assay for quantitative detection of levodopa in co-presence of carbidopa and its application to relevant anti-Parkinson drugs. *Anal. Bioanal. Chem.* **2022**, *414*, 1713–1722.

382. Mason, H. S.; Peterson, E. W. Melanoproteins. I. Reactions between enzyme-generated quinones and amino acids. *Biochim. Biophys. Acta* **1965**, *111*, 134–146.

383. Vachtenheim, J.; Duchoň, J.; Matouš, B. A spectrophotometric assay for mammalian tyrosinase utilizing the formation of melanochrome from l-dopa. *Anal. Biochem.* **1985**, *146*, 405–410.

384. Beer, R. J. S.; Broadhurst, T.; Robertson, A. The chemistry of the melanins. Part V. The autoxidation of 5 : 6-dihydroxyindoles. **1954**, 1947–1953.

385. Napolitano, A.; Pezzella, A.; D'Ischia, M.; Prota, G. The first characterisation of a transient 5,6-indolequinone. *Tetrahedron Lett.* **1996**, *37*, 4241–4242.

386. Napolitano, A.; Palumbo, A.; D'Ischia, M.; Prota, G. Mechanism of selective incorporation of the melanoma seeker 2-thiouracil into growing melanin. *J. Med. Chem.* **1996**, *39*, 5192–5201.

387. D'Ischia, M.; Napolitano, A.; Pezzella, A.; Land, E. J.; Ramsden, C. A.; Riley, P. A. 5,6-Dihydroxyindoles and indole-5,6-diones. *Adv. Heterocycl. Chem.* **2005**, *89*, 1–63.

388. Pezzella, A.; Crescenzi, O.; Natangelo, A.; Panzella, L.; Napolitano, A.; Navaratnam, S.; Edge, R.; Land, E. J.; Barone, V.; D'Ischia, M. Chemical, pulse radiolysis and density functional studies of a new, labile 5,6-indolequinone and its semiquinone. *J. Org. Chem.* **2007**, *72*, 1595–1603.

389. Shariatgorji, M.; Nilsson, A.; Fridjonsdottir, E.; Vallianatou, T.; Källback, P.; Katan, L.; Sävmarker, J.; Mantas, I.; Zhang, X.; Bezard, E.; Svenningsson, P.; Odell, L. R.; Andrén, P. E. Comprehensive mapping of neurotransmitter

networks by MALDI–MS imaging. *Nat. Methods 2019 1610* **2019**, *16*, 1021–1028.

390. Okuda, H.; Wakamatsu, K.; Ito, S.; Sota, T. Possible oxidative polymerization mechanism of 5,6-dihydroxyindole from ab initio calculations. *J. Phys. Chem. A* **2008**, *112*, 11213–11222.

391. Antidormi, A.; Melis, C.; Canadell, E.; Colombo, L. Assessing the Performance of Eumelanin/Si Interface for Photovoltaic Applications. *J. Phys. Chem. C* **2017**, *121*, 11576–11584.

392. Alves, G. G. B.; Lavarda, F. C.; Graeff, C. F. O.; Batagin-Neto, A. Reactivity of eumelanin building blocks: A DFT study of monomers and dimers. *J. Mol. Graph. Model.* **2020**, *98*.

393. Manini, P.; Panzella, L.; Napolitano, A.; D'Ischia, M. Oxidation chemistry of norepinephrine: partitioning of the O-quinone between competing cyclization and chain breakdown pathways and their roles in melanin formation. *Chem. Res. Toxicol.* **2007**, *20*, 1549–1555.

394. Sugumaran, M. Reactivities of Quinone Methides versus o-Quinones in Catecholamine Metabolism and Eumelanin Biosynthesis. *Int. J. Mol. Sci.* **2016**, *17*.

395. Ajith, A.; Sthanikam, Y.; Banerjee, S. Chemical analysis of the human brain by imaging mass spectrometry. *Analyst* **2021**, *146*, 5451–5473.

396. Dutton, J.; Copeland, L. G.; Playfer, J. R.; Roberts, N. B. Measuring L-dopa in plasma and urine to monitor therapy of elderly patients with Parkinson disease treated with L-dopa and a dopa decarboxylase inhibitor. *Clin. Chem.* **1993**, *39*, 629–634.

397. Tuomainen, P.; Männistö, P. T. Optimization of the Hydrolysis of Conjugated L-DOPA, Dopamine and Dihydroxyphenylacetic Acid in Human Urine for Assay by High-Performance Liquid Chromatography with Electrochemical Detection. *Clin. Chem. Lab. Med.* **1997**, *35*, 229–236.

398. Baranowska, I.; Płonka, J. Determination of levodopa and biogenic amines in urine samples using high-performance liquid chromatography. *J. Chromatogr.*

Sci. **2008**, *46*, 30–34.

399. Davidson, D. F.; Grosset, K.; Grosset, D. Parkinson’s disease: the effect of L-dopa therapy on urinary free catecholamines and metabolites. *Ann. Clin. Biochem.* **2007**, *44,* 364–368.

400. Wollmer, E.; Klein, S. Development and Validation of a Robust and Efficient HPLC Method for the Simultaneous Quantification of Levodopa, Carbidopa, Benserazide and Entacapone in Complex Matrices. *J. Pharm. Pharm. Sci.* **2017**, *20*, 258–269.

401. Khanmohammadi, M.; Mobedi, E.; Garmarudi, A. B.; Mobedi, H.; Kargosha, K. Simultaneous Determination of Levodopa and Carbidopa in Levodopa-Carbidopa Tablets by ATR-FTIR Spectrometry. **2008**, *12*, 573–580.

402. Brenner, K. P.; Rose-Pehrsson, S. L. *Performance Evaluation of a Colorimetric Hydrazine Dosimeter*; 1994.

403. Rani, A.; Kumar, M.; Tuli, H. S.; Abbas, Z.; Prakash, V. Synthesis and spectral studies of 4,4′-(Hydrazine-1,2-diylidenedimethylylidene)-bis-(2-methoxyphenol) and its transition metal complexes with promising biological activities. *Asian J. Chem.* **2020**, *32*, 1768–1772.

404. Rüger, N.; Fassauer, G. M.; Bock, C.; Emmrich, T.; Bodtke, A.; Link, A. Substituted tetrazoles as multipurpose screening compounds. *Mol. Divers.* **2017**, *21*, 9–27.

405. Vickers, S.; Stuart, E. K. Spectrofluorometric determination of carbidopa [l-(-)-α-hydrazino-3,4-dihydroxy-α-methylhydrocinnamic acid] in plasma. *J. Pharm. Sci.* **1973**, *62*, 1550–1551.

406. González, C. G.; Mustafa, N. R.; Wilson, E. G.; Verpoorte, R.; Choi, Y. H. Application of natural deep eutectic solvents for the “green”extraction of vanillin from vanilla pods. *Flavour Fragr. J.* **2018**, *33*, 91–96.

407. Weerawatanakorn, M.; Wu, J. C.; Pan, M. H.; Ho, C. T. Reactivity and stability of selected flavor compounds. *J. Food Drug Anal.* **2015**, *23*, 176–190.

408. Watt, G. W.; Chrisp, J. D. A Spectrophotometric Method for the Determination of Hydrazine. *Anal. Chem.* **1952**, *24*, 2006–2008.

409. Malone, H. E. *The Determination of Hydrazino-Hydrazide Groups Chapter 3 – Colorimetric and Spectrophotometric methods*; Pergamon Press. Head. Hill Hall, Oxford; Pergamon, 1970.

410. Baymak, M. S.; Zuman, P. Equilibria of formation and dehydration of the carbinolamine intermediate in the reaction of benzaldehyde with hydrazine. *Tetrahedron* **2007**, *63*, 5450–5454.

411. González-Baró, A. C.; Pis-Diez, R.; Parajón-Costa, B. S.; Rey, N. A. Spectroscopic and theoretical study of the o-vanillin hydrazone of the mycobactericidal drug isoniazid. *J. Mol. Struct.* **2012**, *1007*, 95–101.

412. Wang, L.; Su, Q.; Wu, Q.; Gao, W.; Mu, Y. Synthesis of new substituted benzaldazine derivatives, hydrogen bonding-induced supramolecular structures and luminescent properties. *Comptes Rendus Chim.* **2012**, *15*, 463–470.

413. Chourasiya, S. S.; Kathuria, D.; Wani, A. A.; Bharatam, P. V. Azines: synthesis, structure, electronic structure and their applications. *Org. Biomol. Chem.* **2019**, *17*, 8486–8521.

414. Walash, M. I.; Abou Ouf, A.; Salem, F. B. Colorimetric Determination of Sympathomimetic Amines Methyldopa and Noradrenaline. *J. AOAC Int.* **1985**, *68*, 91–95.

415. Salem, F. B. Colorimetric Determination of Certain Sympathominetic Amines. *Anal. Lett.* **1985**.

416. Dose, K. Catalytic Decarboxylation of α-Amino-Acids. *Nat. 1957 1794562* **1957**, *179*, 734–735.

417. Vickers, S.; Stuart, E. K.; Hucker, H. B.; Vandenheuvel, W. J. A. Further Studies on the Metabolism of Carbidopa, (-)-L-α-Hydrazino-3,4-dihydroxy-α-methylbenzenepropanoic Acid Monohydrate, in the Human, Rhesus Monkey, Dog, and Rat. *J. Med. Chem.* **1975**, *18*, 134–138.

418. Tolosa, E.; Martí, M. J.; Valldeoriola, F.; Molinuevo, J. L. History of levodopa and dopamine agonists in Parkinson's disease treatment. *Neurology* **1998**, *50*, S2–S10.

419. Marras, C.; Beck, J. C.; Bower, J. H.; Roberts, E.; Ritz, B.; Ross, G. W.; Abbott, R. D.; Savica, R.; Van Den Eeden, S. K.; Willis, A. W.; Tanner, C. Prevalence of Parkinson’s disease across North America. *npj Park. Dis.* **2018**, *4*.

Acknowledgement

Il ringraziamento più grande va alle persone che hanno camminato insieme a me in questo percorso. Ai miei supervisori, Prof.ssa Minunni, Prof.ssa Scarano, Dott. Palladino, che mi hanno seguito e accompagnato in questo percorso formando la persona che sono ora. Le cose che ho imparato in questi anni sono il regalo più prezioso che i miei supervisori potessero donarmi. Ai miei colleghi, colleghi che sono diventati una vera e propria famiglia. La famiglia che qui non ho potuto avere accanto. Alla mia amica, quella che non avrei mai pensato di incontrare e quella che c'è sempre stata. Ai miei genitori, a mio fratello, ai miei nonni, alla mia famiglia i quali mi hanno sostenuto in ogni mia scelta. A mia madre, la mia forza, la mia speranza, la mia roccia. E' stato un lungo cammino e ringrazio tutte le persone che ho incontrato in questo percorso e che hanno contribuito a formare ogni pezzetto di me.

Ringrazio il Dott. Giovanni Ferraro del CSGI (Center for Colloid and Surface Science) del Dipartimento di Chimica "Ugo Schiff" dell'Università di Firenze per gli esperimenti SEM.

Grazie

Microchimica Acta (2021) 188:116
https://doi.org/10.1007/s00604-021-04764-7

ORIGINAL PAPER

Protein-templated copper nanoclusters for fluorimetric determination of human serum albumin

Mariagrazia Lettieri[1] · **Pasquale Palladino**[1] · **Simona Scarano**[1] · **Maria Minunni**[1]

Received: 17 December 2020 / Accepted: 16 February 2021

Abstract

Copper nanoclusters (CuNCs) are attractive for their unique optical properties, providing sensitive fluorescent detection of several kinds of targets even in complex matrices. Their ability in growing on suitable protein and nucleic acid templates make CuNCs efficient optical reporters to be exploited in bioanalysis. In this work, we report the specific and sensitive determination of human serum albumin (HSA) in human serum (HS) and urine via CuNCs fluorescence. HSA is the most abundant protein in plasma, and plays a key role in the early diagnosis of serious pathological conditions such as albuminuria and albuminemia. Recently, HSA has become clinically central also as a biomarker to assess severity, progression, and prognosis of various cancers. We report the controlled and reproducible growth of CuNCs directly on the target analyte, HSA, which results in a fine dose-dependent fluorescent emission at 405 nm. The protocol is optimized in water, and then applied to serum and urine specimens, without matrix pretreatment. The method linearly responds within the whole concentration of clinical interest, with a sensitivity of $1.8 \pm 0.1 \times 10^{-3}$ g L^{-1} and $0.62 \pm 0.03 \times 10^{-3}$ g L^{-1} in serum and urine, respectively, and excellent reproducibility (CV_{av}% ca. 3% for both). The assay is designed to have a single protocol working for both matrices, with recovery of 95% (HS) and 96% (urine). The stability of the fluorescence after CuNCs formation was tested over 3 days, displaying good results (yet higher in urine than in serum).

Keywords Copper nanoclusters · Human serum albumin · Fluorescence · Label-free assay

Introduction

Human serum albumin (HSA), the most abundant protein in human blood (35–50 g L^{-1}), is a multi-domain protein able to bind different endogenous and exogenous macromolecules. Therefore, the key role of HSA consists in carrying many biomolecules and, consequently, in modulating oncotic blood pressure [1]. In addition, HSA is a notable biomarker of many diseases such as cancer [2], liver disorders [3] (i.e., cirrhosis or hepatitis), rheumatoid arthritis [4], diabetes, hypertension, kidney disease, and cardiovascular diseases [5, 6]. In particular, low HSA concentration in human serum and high HSA values in urine denote two important pathological states known, respectively, as albuminemia and albuminuria [7, 8]. As a whole, the accurate determination of HSA in different biological specimens plays a critical role both from a diagnostic and a prognostic point of view. In the past, precipitation-based methods were commonly applied to detect albumin [9]. Presently, a large number of analytical methods (i.e., immunochemical, dye-binding, chromatographic, spectroscopic, and electrophoresis-based methods) are reported in literature for the accurate estimation of HSA [10–12]. For HSA detection in blood, electrophoretic technique represents the first choice [13], whereas immunonephelometry and immunoturbidimetry are preferred for HSA determination in urine samples [14, 15]. There is a lack, therefore, of a method allowing HSA determination in these two specimens through the same procedure, i.e., in a matrix-independent manner. Moreover, most of the analytical methods proposed so far, taken together, suffer from some disadvantages because are often expensive, time-consuming, and laborious, requiring in some cases (e.g., electrophoretic investigations) many pre-analytical steps and the use of synthetic dyes. In this framework, here we present a low cost and rapid method for the accurate and selective determination of HSA, both in human

✉ Simona Scarano
simona.scarano@unifi.it

[1] Department of Chemistry “Ugo Schiff”, University of Florence, 50019 Sesto Fiorentino, FI, Italy

serum and urine, without the need for any sample pretreatment (except dilution for human serum). The outstanding properties of copper nanoclusters (CuNCs) [16] were exploited to develop an assay able to directly detect albumin-templated CuNCs by fluorescence. As far as we know, this is the first report on the use of CuNCs for the selective albumin detection for clinical diagnostics. Differently from metallic nanoparticles, widely employed in bioanalytics, metallic nanoclusters are still poorly explored for such applications. However, in recent years, the unique fluorescent properties of CuNCs, such as high quantum yield, photostability, and large Stokes shifts, enabled their frequent use in numerous bioanalytical assays [17, 18]. In addition, remarkable features as low toxicity and good biocompatibility allow the use of CuNCs as fluorophores for biolabeling and bioimaging [19], representing an alternative to the quantum dots and organic dyes. However, two works referred about CuNCs and HSA [20, 21]. In the first, bilirubin is quantified in urine and human blood samples by the quenching induced by the analyte upon its interaction with red fluorescent CuNCs synthesized by using HSA as a template [20]. In the second, Chen et al. quantified HSA in plasma by following the reduction of fluorescence of poly(thymine)-templated copper nanoparticles (CuNPs) due to HSA that inhibits the CuNPs formation [21]. Differently from above reported turn-off fluorescence strategies, here we report for the first time that HSA-templated CuNCs are able to directly detect and quantify HSA itself by a turn-on strategy that exploits the selective growth of CuNCs on the albumin template. The optimized experimental conditions only require the addition of Cu(II) and NaOH aliquots to the serum/urine sample, followed by 1–3 h of incubation at 55 °C. The blue-emitting HSA-templated CuNCs allow to detect HSA with high sensitivity, selectivity, and reproducibility in serum and urine specimens without any pretreatment, except for a 1:300 dilution of serum in water. Serum dilution allowed to process serum and urine within the same calibration range but could be tailored on the basis of specific testing requirements. The excellent analytical performances of the developed assay represent a valid alternative to current screening techniques, paving the route toward an effective and innovative method for HSA detection in clinical diagnostics.

Materials and methods

Chemicals and reagents

Copper sulfate ($CuSO_4$) and sodium hydroxide (NaOH) were from Thermo Fisher Scientific (Parma, Italy). Human serum albumin (HSA), human serum from male AB (HS), and human IgG were purchased from Merck (Milan, Italy). Artificial urine (AU) was from LCTech GmbH (Obertaufkirchen, Germany). High Select™ HSA/Immunoglobulins (IgG, IgA, IgM, IgD, and IgE) Depletion Mini Spin Columns used for selectivity studies were from Thermo Fisher Scientific (Rodano, MI). The columns were used by following the manufacturer’s instructions.

Instrumentation and optical measurements

HSA-CuNCs were synthesized in water, serum, or urine samples, by incubation at 55 °C (Thermomixer comfort, Eppendorf, VWR International, Milan). Fluorescence experiments were performed with Spectrofluorometer FP-6500 (Jasco, Easton, PA, USA), and absorbance measurements were recorded by using Thermo Scientific™ Evolution™ 201/220 UV-Visible Spectrophotometer (Rodano, MI). Data management was performed by using OriginLab (Origin Pro 8.5.1) software. In order to define the proper excitation wavelength, λ_{ex} were scanned from 325 to 450 nm, by using an interval of 10 nm. Experimental conditions: 1.5 g L^{-1} HSA-CuNCs, wavelength range 200–650 nm, integration time 60 s, spectral bandwidth 1 nm, scan speed 100 nm min^{-1}. This step allowed us to establish the best conditions for fluorescence measurements, i.e., $\lambda_{ex} = 325$ nm and $\lambda_{em} = 405$ nm (emission bandwidth 5 nm, excitation bandwidth 5 nm, data pitch 1 nm, scanning speed 100 nm min^{-1}, sensitivity low). The same operative conditions were used for water, serum, and urine samples.

Assay protocol for HSA determination

HSA-templated CuNCs were synthesized starting from the protocol proposed by Goswami et al. [22], with some modifications, as reported in the Electronic Supporting Material (ESM), Scheme SI 1. The fluorescent HSA-templated CuNCs do not require any purification step. All the measurements were performed at 25 °C in triplicates, at least. The same protocol is used for water, serum, and urine samples, except for 1:300 serum dilution in water, which permits it to work within the same calibration range for both the matrices. The linear trend of the assay in HS was first evaluated by the standard addition method, since it naturally contains physiological HSA (ca. 35–50 g L^{-1}). To this aim, a series of equal HS aliquots were prepared, adding to each a different concentration of HSA (standard in water, concentration range 0–0.50 g L^{-1}). Subsequently, the protocol proceeded as described in ESM. The fluorescence emission intensity of the samples was measured in triplicate both just after the reaction ended (intraday variation) and for the three consecutive days (inter-day standard deviation), by subjecting the samples to a daily freeze/thaw cycle before fluorescence measurement.

Results and discussions

CuNCs synthesis and optical behavior

The experimental procedure optimized to synthesize HSA-CuNCs gave highly photoluminescent nanoclusters in an easy, quick, and cheap manner (Fig. 1 and Scheme SI 1). Advantageously, this protocol does not require purification steps or the use of reducing agents nor toxic substances as reported by other procedures [23, 24]. This simplifies the detection of compounds of interest in complex biological matrices, such as urine, human serum, and human blood. The mechanism of nanoclusters formation involves principally amine, thiol, and carboxyl groups of HSA that act as template and trigger the formation and stabilization of the nanoclusters by using $-NH_2$ and $–COOH$ groups for the coordination of Cu(II), while the –SH groups allow the reduction mediated by alkaline pH of copper ions to metallic Cu atoms, which aggregate in stable nanoclusters.

The absorption spectra of HSA-CuNCs obtained in water show a main peak at 280 nm, due to aromatic amino acids, and a second peak, weaker, at 325 nm, characteristic of copper nanoclusters, as previously reported [22] (ESM, Fig. SI 1). The absence of the characteristic localized surface plasmon resonance (LSPR) band of copper nanoparticles between 500 and 600 nm [25] confirms the effective formation of nanoclusters while avoiding the presence of bigger nanoparticles. The maximum intensity of fluorescence emission (Fig. SI 2A) was obtained by using $\lambda_{ex} = 325$ nm, with the emission peak centered at 405 nm, as reported elsewhere [22]. Accordingly, when the fluorescence at 405 nm was examined, the excitation spectrum of HSA-CuNCs exhibited a sharp peak at 325 nm, and both show a clear dose-response trend as a function of HSA concentration in solution (Fig. SI 2B). For this reason, all fluorescence measurements were performed employing $\lambda_{ex} = 325$ nm and $\lambda_{em=}$ 405 nm. The smaller shoulder at about 375 nm, particularly evident at low analyte concentrations, is due to the Raman scatter peak, which depends on solvent and excitation wavelength [26].

Optimization of parameters for HSA detection

The photoluminescent properties of CuNCs strongly depend on the medium pH and, in particular, an alkaline pH is necessary for their formation. At pH 7.0, Cu(II) is reduced to Cu(I), which binds the protein structure to form the metalloprotein complex. Subsequently, when the pH is raised close to 12.0, copper ions are further reduced to metallic copper (Cu(0)) that leads to the initiation of the nucleation and growth of the clusters [22].To optimize the CuNCs formation, the pH influence was carefully evaluated by preparing several aqueous HSA-CuNCs solutions at pH ranging from 9.0 to 13.0. The maximum luminescence signal was reached at pH 11.5 (see Fig. SI 3), presumably due to the enhancement of the reducing properties of albumin thiol groups, which promote the effective formation of copper nanoclusters. This pH value was thus kept for all the following experiments. We also investigated the ability of the method in giving valuable responses in the shortest possible time with the aim to improve the current protocols in diagnosing and monitoring hypoalbuminemic and microalbuminueric patients. At this purpose, the Cu(II)/HSA mixtures were incubated from 1 to 7 h at 55 °C, monitoring the fluorescence signal evolution. As shown in Fig. SI 4, the highest fluorescent emission was obtained after 3 h, reaching a plateau stage for a longer incubation time, followed by a decrease of the signal around 7 h. Therefore, 3 h was

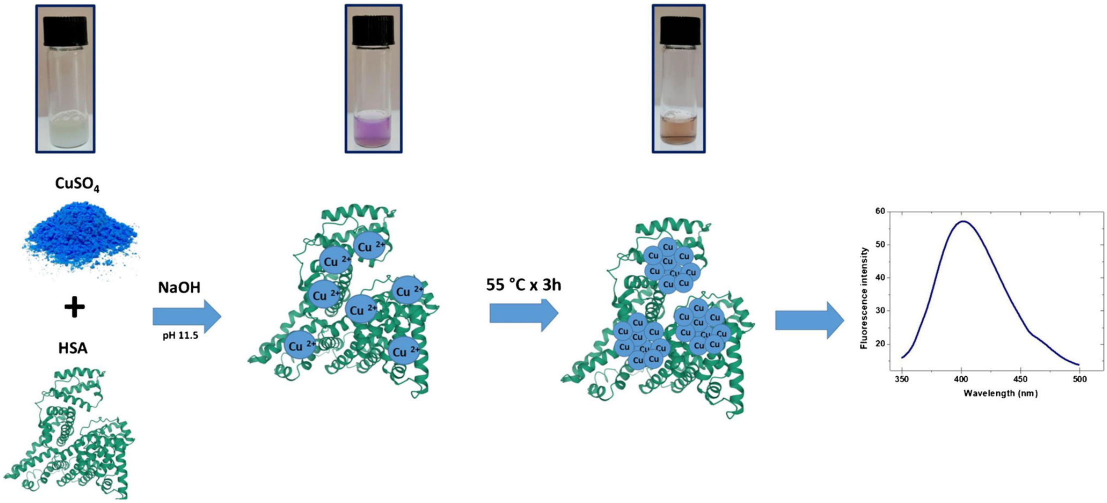

Fig. 1 Schematic illustration of the experimental steps involved in HSA-CuNCs synthesis

chosen as the best incubation time for CuNCs formation, which is shorter than reaction times from 5 to 8 h previously reported for HSA-CuNCs formation [27, 28]. However, these results may foresee the possibility of shortening the incubation time to ca. 1 h, reinforcing the real applicability of the method in clinical settings. We also explored the possible influence of the stirring speed (200, 500, 1000, and 1400 rpm (rpm)) during the formation of the clusters, finding that this parameter does not affect the final CuNCs fluorescence intensity (data not shown). The CuNCs obtained with the optimized protocol show excellent fluorescence stability up to 4 months of storage at room temperature and/or after multiple freezing/thawing steps (data not shown).

Sensitive detection of human serum albumin

HSA detection in water solution

Preliminary studies were carried out in Milli-Q water in order to study the calibrator in ideal conditions. To this aim, the fluorescence spectra of HSA-CuNCs formed in solution at different concentrations of HSA were recorded (Fig. 2a), showing a clear dose-response. The intensity of the fluorescence signal, i.e., the peak centered at 405 nm (with a minor shoulder at 460 nm), was considered to construct the standard HSA calibration within the range 0.03–1.50 g L^{-1} (Fig. 2b). It shows a very well-correlated ($R^2 = 0.994$) linear response ($y = 96.6$ x-1.4) up to 0.5 g L^{-1} (Fig. 2b), with a slight deviation at higher concentrations of HSA (data not shown). The limit of detection (LOD) obtained was $2.48 \pm 0.07 \times 10^{-3}$ g L^{-1} (LOD = 3*SD_{blank}/slope), with an average coefficient of variability (CV_{av}%) of 5%. The inter-day stability of HSA-CuNCs in water was also investigated. After CuNCs formation, the samples were stored at −20 °C, and then subjected to a 3-day freeze/thaw cycles, giving the fluorescence data reported in Fig. SI 5A. The overall variability, expressed as CV_{av}% over all the data collected over the 3 days (7 concentration points for each calibration, each point in triplicate, see Fig. SI 5B), resulted in 9%, confirming the good reproducibility of the measurements despite the freeze/thaw cycles the samples were subjected to. The overall recovery of fluorescence intensity at the second and the third day resulted in 92% and 70%, respectively, compared to the intraday results.

HSA detection in human serum

The blue emitting HSA-CuNCs were successfully applied to albumin quantification in untreated human serum (except 1:300 water dilution), where HSA values lower than 35 g L^{-1} define a pathological state known as hypoalbuminemia [7]. The patients suffering from analbuminemia, in which the HSA level is less than 1 g L^{-1}, are rare [7]. However, both hypoalbuminemia and analbuminemia may be signs of severe liver, kidney, or gastrointestinal diseases, as well as cancer evolution [29–31], and all require the accurate determination of albumin. Albumin is the most abundant protein in human serum with physiological concentrations generally between 35 and 50 g L^{-1} [7]. Therefore, to obtain its absolute estimation, we first applied the standard addition method to assess the linear dose-response trend in the matrix. Due to the high albumin concentration in human serum with respect to our calibration range, a 1:300 dilution of the serum sample is preliminary performed. Then, known increasing concentrations of standard HSA were spiked (0.03–0.50 g L^{-1} final concentration range) to six aliquots of the same serum sample. CuNCs formation was finally carried out simultaneously on all the aliquots following the protocol optimized in water, and the fluorescence responses were recorded (Fig. 3). Also, in this case, we confirmed the presence of a well-defined peak centered at 405 nm (with a minor

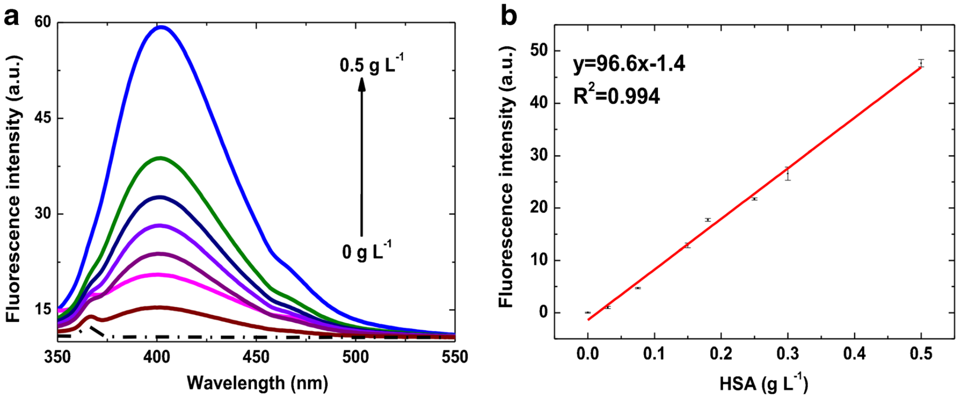

Fig. 2 HSA-CuNCs fluorescence in water: (**a**) Emission spectra at different HSA concentrations. Dashed line is the blank sample (H_2O). (**b**) Calibration plot of CuNCs fluorescence intensity at 405 nm versus HSA concentration after blank subtraction. The error bars represent the triplicate measurements (intraday standard deviation)

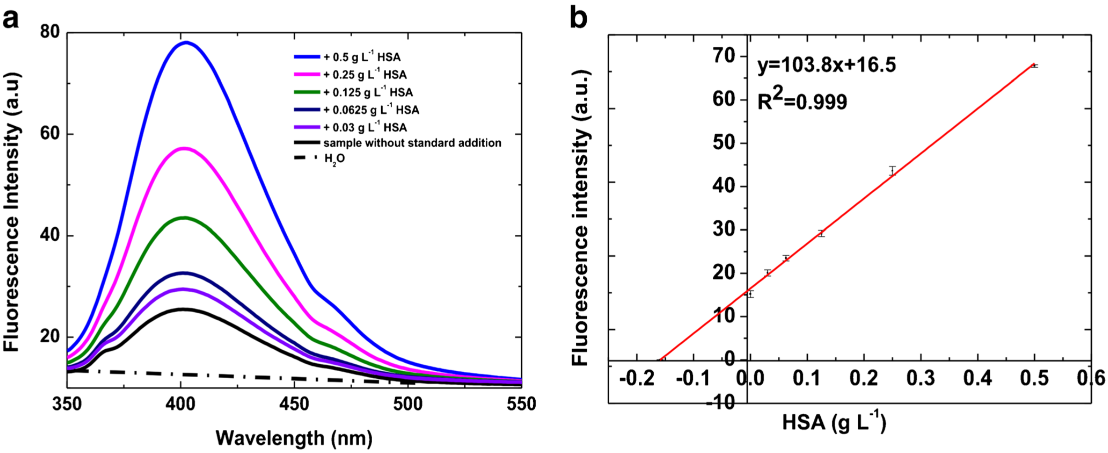

Fig. 3 HSA-CuNCs in human serum: (**a**) Emission spectra at different HSA concentrations. Dashed line is the blank sample (HSA-depleted serum). (**b**) Calibration plot corresponding to the quantitative determination of HSA by using the standard addition method. Fluorescence intensity values, in the calibration plot, were obtained by the subtraction of blank fluorescence signal (HSA-depleted serum). The error bars represent the intraday standard deviation calculated on three replicates

shoulder at 460 nm). As evidenced in water, the overall optical response is thus related to the endogenous HSA in the sample plus the contribution of the spiked standard HSA. An excellent linear correlation ($R^2 = 0.999$) allowed us to fit the data and extrapolate the concentration of serum HSA, which resulted in 48.0 ± 1.8 g L^{-1}. The CV$_{av}$% resulted in 3%, highlighting the excellent reproducibility of the proposed assay.

The inter-day variability of the method was estimated over 3 days, as previously performed in water, to assess the possibility of storing the processed serum samples until the analysis (Fig. SI 6A). In this case, the overall CV$_{av}$% averaged on all the collected data resulted significantly higher than that obtained in water (19%), although the most marked effect of signal decrease was observed between the first and second day. Due to the complexity of the matrix, the observed progressive decrease could be reasonably ascribed to some serum components that interfere with fluorescence stability over time. However, data up to 0.25 g L^{-1} of the second and the third day show recovery values on all the concentrations of 80% and 73%, respectively. This could indicate a stabilization of the fluorescence after the first 24 h and/or the first freeze/thaw cycle that should be investigated for longer times. The selectivity of the CuNCs-based fluorescent assay was first tested by considering that the protein portion of human serum other than albumin is predominantly composed by immunoglobulins. Therefore, we reproduced the assay on immunoglobulin solutions to assess the absence of their contribution in the final fluorescent signal. Fig. SI 7A shows that the fluorescent spectra recorded in the IgG solutions are comparable to a blank solution. Moreover, we have excluded possible interferences due to other matrix components by using separation columns to remove HSA and immunoglobulins from samples. Also, such depleted samples have given negligible response (see Fig. SI 7B), confirming the selectivity of the method.

HSA detection in urine

Albuminuria consists in release of a large quantity of albumin in urine as a consequence of kidney damage. The mild form of albuminuria is known as microalbuminuria and is characterized by low HSA values in urine, i.e., 0.02–0.2 g L^{-1}, whereas higher values are associated with the severe condition called macroalbuminuria [5]. Cardiovascular and kidney diseases, such as hypertension and diabetes mellitus, are closely related to micro and macroalbuminuria [5, 6]. To demonstrate the applicability of the method also to urine matrix, artificial urine samples were added with increasing standard HSA concentrations, and the CuNCs growth was conducted as above for water and serum. Differently from serum, urine does not contain physiological HSA; therefore, a classical dose-response calibration was carried out by testing urine samples fortified with HSA in the range 0.01–0.50 g L^{-1} (Fig. 4). Figure 4 a displays the intensity evolution of CuNCs fluorescence upon HSA increase. Differently from water and serum, spectra recorded in urine show two minor peaks at wavelengths higher than the main emission peak (Fig. 4a). Moreover, the latter appears red-shifted to ca. 425 nm, likely due to the fact that in this case the matrix is not subjected to dilution in water as above reported for serum. The calibration curve, described by the equation $y = 100.2x + 3.9$, correlates with a R^2 value of 0.984 giving a LOD of 0.62 ± 0.03 × 10^{-3} g L^{-1} and a CV$_{av}$% = 3%. The best linear correlation was obtained up to

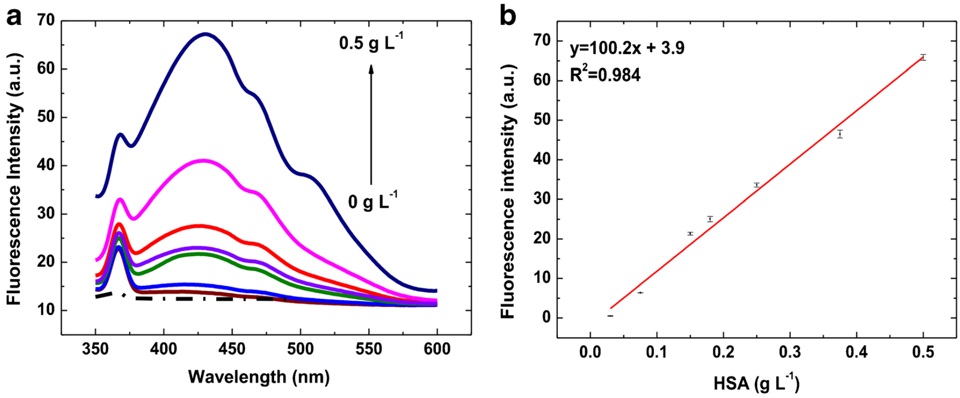

Fig. 4 HSA-CuNCs in artificial urine: (**a**) Emission spectra at different HSA concentrations. Dashed line is the blank sample (unspiked urine). (**b**) Calibration plot of standard HSA in artificial urine. Fluorescence intensity values were obtained by the subtraction of the blank (unspiked urine). The error bars represent the triplicate measurements (intra-day standard deviation)

0.50 g L^{-1}, and after that, a loss of linearity is clearly visible (data not shown). Considering the clinical range of interest, the assay showed its ability in detecting with high precision and accuracy even microalbuminuria condition. The inter-day standard deviations display an averaged calibration curve with a very similar trend and a $CV_{av}\%$ of 10% (Fig. SI 8). The recovery efficiency, inferred by comparing the fluorescence responses obtained over the 3 days, resulted in 98% and 90% for the second and the third day, respectively.

Performance of the assay in serum and urine

To reinforce the validity of the developed method, we compared the dose-response curves obtained in both the matrices by testing a serial dilution of serum and urine containing the same HSA content (serum and urine absorbance and fluorescence spectra are reported in Fig. SI 9). In the case of HS, we diluted a sample of known HSA concentration to 0.50 g L^{-1}; to directly compare the responses, an undiluted aliquot of urine was spiked with the same HSA concentration, and the same serial dilutions were performed and tested for both the matrices. As reported in Fig. 5, a very good overlapping of the dynamic ranges over the tested conditions is found within the whole range of concentration. In these conditions, the limit of detection in serum can be also directly extrapolated, resulting in $1.8 \pm 0.1 \times 10^{-3}$ g L^{-1}, with a $CV_{av}\% =$ 3%. This result enables HSA detection at concentrations lower than those achieved by reference techniques [32, 33]. In addition, recovery has been calculated for all the urine and human serum spiked samples by comparison with the calibration curve of HSA in Milli-Q water. A recovery value of 95% for human serum and of 96% for urine was obtained.

Assay performances compared to other nanomaterials-based methods

The CuNCs-based assay here developed was finally compared to other nanomaterial-based methods reported in literature for HSA detection (Table 1). Despite the declared LODs referred to standard solutions display better performances in all the cases, no information about the performances obtained in human serum and urine is reported (except for Huang et al. [34]),

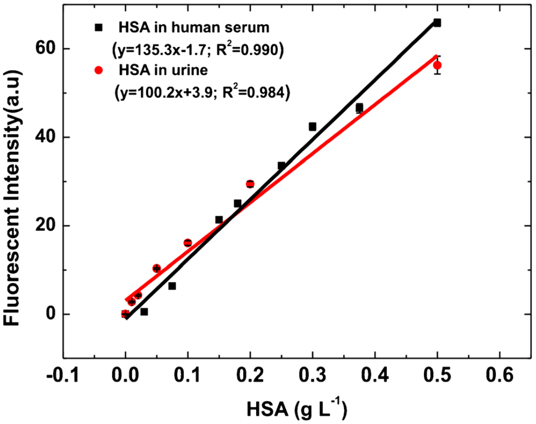

Fig. 5 Analytical performance of HSA detection assay in human serum (black line) and urine (red line). The respective blanks (HSA-depleted serum for HS, and unspiked urine for urine samples) were subtracted to the fluorescence signals. Fluorescence values are reported as the mean value ± intraday standard deviation) calculated on three replicates

Table 1 Nanomaterial-based methods for the determination of HSA

Probe	*Method*	*LOD*	*Specificity*	*Matrix*	*References*
HSA-templated copper nanoclusters (CuNCs)	Spectrofluorimetry	$2.48 \pm 0.07 \times 10^{-3}$ g L^{-1} (in H_2O); $1.8 \pm 0.1 \times 10^{-3}$ g L^{-1} (in human serum) $0.62 \pm 0.03 \times 10^{-3}$ g L^{-1} (in urine)	Yes	Artificial urine Human serum	This work
Poly(thymine)-templated copper nanoparticles (CuNPs)	Spectrofluorimetry	8.2×10^{-11} g L^{-1} (in buffer solution)	Yes	Human serum	[21]
Gold nanoparticles (AuNPs)	Colorimetry	9.3×10^{-5} g L^{-1} (in urine)	Yes	Artificial urine	[34]
Gold “pearl necklace” (Au PNNs)	Surface-enhanced Raman scattering (SERS)	4.6×10^{-6} g L^{-1} (in buffer solution)	Yes	Artificial urine	[35]
Nanoporous gold (NPG)	SERS	0.1×10^{-9} g L^{-1} (in buffer solution)	–	–	[36]
Gold nanorods (AuNR)	Surface plasmon resonance (SPR)	–	–	Artificial urine	[37]
AuNPs	Evaporative light scattering detection (ELSD)	21.0 ng (in buffer solution)	–	Human serum	[38]
Silver nanoparticles (AgNPs)	Localized surface plasmon resonance (LSPR)	1.0×10^{-6} g L^{-1} (in buffer solution)	Yes	Urine	[39]

and none of them shows the possibility of applying the assay to both the matrices by the same protocol. Since from a clinical point of view the lowest concentration of interest for HSA in urine (in serum the interest goes to the relative variation of physiological levels) is around 0.02 g L^{-1}, the reported LODs play a marginal role in the evaluation of a realistic application of the method for clinical purposes. Moreover, some detection methods, such as SERS and ELSD, are far from being considered simple since they require multiple synthesis steps for the nanomaterials involved in the protocol and expensive instrumentation. Finally, a CuNCs-based platform is cheaper than gold- and silver-based nanomaterials, since Cu(II) salts are less expensive than the relative Au(III) and Ag(I) ones. In this framework, the assay here developed allows to achieve a step forward in its application in clinical settings.

Conclusions

A novel CuNCs-based assay for the fluorescent detection of HSA in urine and human serum is reported. Both the matrices are successfully analyzed by the same protocol, without significant pretreatment (except for a 1:300 dilution of serum in water), and high selectivity. The whole protocol is performed within 3 h, but it could be further reduced down to 1 h, in line with clinical requirements. The sensitivity of the CuNCs-based assay resulted higher than other diagnostic methods, i.e., 0.03–1.00 g L^{-1} in serum, and 0.01–0.75 g L^{-1} in urine, with excellent intraday variability (3%). Despite at this development stage, we demonstrated its applicability to reinforced matrices, and we foresee that the method could be further validated for its application in clinical diagnostics with improved accuracy, shorter times, and very low costs with respect to current available assays. To the best of our knowledge, this is the first example of an assay for HSA able to work in serum and urine without the need of a matrix-dependent protocol and very similar analytical performances.

Supplementary Information The online version contains supplementary material available at https://doi.org/10.1007/s00604-021-04764-7.

Funding Open access funding provided by Università degli Studi di Firenze within the CRUI-CARE Agreement. The authors thank the Italian Ministry of Health for the project “Development of optical biosensors for the detection of peptide hormones through molecularly imprinted polymers” within the 2018 call “Research and training/information program on drugs, medical substances and practices that can be used for doping purposes and for health protection in sporting activities”; EC Horizon 2020, ERA-NET - PhotonicSensing Transnational Call 2016, for the project PLABAN “advanced PLAsmonic Biosensors ANalysis of nucleic acids”; and Ministry of Education, University and Research (MIUR), for the project “Dipartimenti di Eccellenza 2018-2022”.

Compliance with ethical standards

Conflict of interest The authors declare that they have no competing interests.

References

1. Fanali G, Di Masi A, Trezza V et al (2012) Human serum albumin: from bench to bedside. Mol Asp Med 33:209–290. https://doi.org/10.1016/j.mam.2011.12.002
2. Gupta D, Lis CG (2010) Pretreatment serum albumin as a predictor of cancer survival: a systematic review of the epidemiological literature. Nutr J 9:1–16. https://doi.org/10.1186/1475-2891-9-69
3. Carvalho JR, Machado MV (2018) New insights about albumin and liver disease. Ann Hepatol 17:547–560. https://doi.org/10.5604/01.3001.0012.0916
4. Tsuji H, Hashimoto M, Harada T, Tanaka M, Ito H, Murakami K, Ohmura K, Fujii T, Mimori T (2020) Persistent anemia and hypoalbuminemia in rheumatoid arthritis patients with low serum triiodothyronine level. Mod Rheumatol 30:640–647. https://doi.org/10.1080/14397595.2019.1649109
5. Saleem T, Dahpy M, Ezzat G, Abdelrahman G, Abdel-Aziz E, Farghaly R (2019) The profile of plasma free amino acids in type 2 diabetes mellitus with insulin resistance: association with microalbuminuria and macroalbuminuria. Appl Biochem Biotechnol 188:854–867. https://doi.org/10.1007/s12010-019-02956-9
6. Dallatu MK, Kaoje AM, Adoke AU, Kehinde JA, Bunza JM (2019) Microalbuminuria in women with risk factors for gestational diabetes mellitus in some selected hospitals in Sokoto, Nigeria. Asian J Res Med Pharm Sci 6:1–8. https://doi.org/10.9734/ajrimps/2019/v6i230097
7. Gounden V, Vashisht R, Jialal I (2020) Hypoalbuminemia. StatPearls Publishing
8. Heerspink HJL, Greene T, Tighiouart H, Gansevoort RT, Coresh J, Simon AL, Chan TM, Hou FF, Lewis JB, Locatelli F, Praga M, Schena FP, Levey AS, Inker LA, Sevillano A, Kamper AL, van Zuilen AD, Brenner BM, Maes B, Ihle BU, Barret B, Leung CB, Szeto CC, Fitzner C, Wanner C, Pozzi C, Montagnino CP, Xie D, de Zeeuw D, Lewis E, Verde E, Gutierrez E, Imai E, Hou FF, Caravaca F, Fervenza FC, Locatelli F, Schena FP, Kobayashi F, Moroni G, Becker GJ, Beck GJ, Appel GB, Frisch G, van Essen G, Maschio G, Remuzzi G, Montogrino G, Parving HH, Heerspink HJL, Makino H, Jehan I, Wetzels JFM, Donadio J, Dwyer J, van den Brand J, Kusek J, Lachin JM, Luño J, Lewis JB, Floege J, Abebe KZ, Chow KM, Hunsicker LG, del Vecchio L, Carlo M, Praga M, Goicoechea M, von Eynatten M, Poulter N, Chaturvedi N, Passerini P, de Jong PE, Blankestijn PJ, Li P, Ruggenenti P, Zucchelli P, Kincaid-Smith PS, Hilgers RD, Estacio RO, Rohde RD, Katafuchi R, Toto RD, Schrier RW, Rodby RA, Perrone RD, Ito S, Klahr S, Andrulli S, Strandgaard S, Chan TM, Hannedouche TP, Rauen T, Greene T, Verdalles U, Perkovic V, Keane W (2019) Change in albuminuria as a surrogate endpoint for progression of kidney disease: a meta-analysis of treatment effects in randomised clinical trials. Lancet Diabetes Endocrinol 7:128–139. https://doi.org/10.1016/S2213-8587(18)30314-0
9. Watts GF, Bennett JE, Rowe DJ, Morris RW, Gatling W, Shaw KM, Polak A (1986) Assessment of immunochemical methods for determining low concentrations of albumin in urine. Clin Chem 32:1544–1548. https://doi.org/10.1093/clinchem/32.8.1544
10. Palladino P, Brittoli A, Pascale E, Minunni M, Scarano S (2019) Colorimetric determination of total protein content in serum based on the polydopamine/protein adsorption competition on microplates. Talanta 198:15–22. https://doi.org/10.1016/j.talanta.2019.01.095
11. Aitekenov S, Gaipov A, Bukasov R (2020) Review: detection and quantification of proteins in human urine. Talanta 121718:121718. https://doi.org/10.1016/j.talanta.2020.121718
12. Xu JF, Yang YS, Jiang AQ, Zhu HL (2020) Detection methods and research Progress of human serum albumin. Crit Rev Anal Chem 1–21. https://doi.org/10.1080/10408347.2020.1789835
13. Regeniter A, Siede WH (2018) Peaks and tails: evaluation of irregularities in capillary serum protein electrophoresis. Clin Biochem 51:48–55. https://doi.org/10.1016/j.clinbiochem.2017.09.017
14. Marre M, Claudel JP, Ciret P, Luis N, Suarez L, Passa P (1987) Laser immunonephelometry for routine quantification of urinary albumin excretion. Clin Chem 33:209–213. https://doi.org/10.1093/clinchem/33.2.209
15. Lloyd DR, Hindle EJ, Marples J, Gatt JA (1987) Urinary albumin measurement by immunoturbidimetry. Ann Clin Biochem 24:209–210. https://doi.org/10.1177/000456328702400218
16. Tang T, Ouyang J, Hu L, Guo L, Yang M, Chen X (2016) Synthesis of peptide templated copper nanoclusters for fluorometric determination of Fe(III) in human serum. Microchim Acta 183:2831–2836. https://doi.org/10.1007/s00604-016-1935-z
17. Qing T, Zhang K, Qing Z, Wang X, Long C, Zhang P, Hu H, Feng B (2019) Recent progress in copper nanocluster-based fluorescent probing: a review. Microchim Acta 186. https://doi.org/10.1007/s00604-019-3747-4
18. Shahsavari S, Hadian-Ghazvini S, Hooriabad Saboor F, Menbari Oskouie I, Hasany M, Simchi A, Rogach AL (2019) Ligand functionalized copper nanoclusters for versatile applications in catalysis, sensing, bioimaging, and optoelectronics. Mater Chem Front 3:2326–2356. https://doi.org/10.1039/c9qm00492k
19. An Y, Ren Y, Bick M, Dudek A, Hong-Wang Waworuntu E, Tang J, Chen J, Chang B (2020) Highly fluorescent copper nanoclusters for sensing and bioimaging. Biosens Bioelectron 154:112078. https://doi.org/10.1016/j.bios.2020.112078
20. Rajamanikandan R, Ilanchelian M (2019) Red emitting human serum albumin templated copper nanoclusters as effective candidates for highly specific biosensing of bilirubin. Mater Sci Eng C 98:1064–1072. https://doi.org/10.1016/j.msec.2019.01.048
21. Chen M, Xiang X, Wu K et al (2017) A novel detection method of human serum albumin based on the poly(thymine)-templated copper nanoparticles. Sensors (Switzerland) 17. https://doi.org/10.3390/s17112684
22. Goswami N, Giri A, Bootharaju MS, Xavier PL, Pradeep T, Pal SK (2011) Copper quantum clusters in protein matrix: potential sensor of Pb 2+ ion. Anal Chem 83:9676–9680. https://doi.org/10.1021/ac202610e
23. Jayasree M, Aparna RS, Anjana RR, Anjali Devi JS, John N, Abha K, Manikandan A, George S (2018) Fluorescence turn on detection of bilirubin using Fe (III) modulated BSA stabilized copper nanocluster; a mechanistic perception. Anal Chim Acta 1031:152–160. https://doi.org/10.1016/j.aca.2018.05.026
24. Yang K, Wang Y, Lu C, Yang X (2018) Ovalbumin-directed synthesis of fluorescent copper nanoclusters for sensing both vitamin B1 and doxycycline. J Lumin 196:181–186. https://doi.org/10.1016/j.jlumin.2017.12.038
25. Xie J, Zheng Y, Ying JY (2009) Protein-directed synthesis of highly fluorescent gold nanoclusters. J Am Chem Soc 131:888–889. https://doi.org/10.1021/ja806804u
26. Lawaetz AJ, Stedmon CA (2009) Fluorescence intensity calibration using the Raman scatter peak of water. Appl Spectrosc 63:936–940. https://doi.org/10.1366/000370209788964548
27. Zhao M, Chen AY, Huang D, Zhuo Y, Chai YQ, Yuan R (2016) Cu nanoclusters: novel electrochemiluminescence emitters for bioanalysis. Anal Chem 88:11527–11532. https://doi.org/10.1021/acs.analchem.6b02770

28. Gao Z, Su R, Qi W, Wang L, He Z (2014) Copper nanocluster-based fluorescent sensors for sensitive and selective detection of kojic acid in food stuff. Sensors Actuators B Chem 195:359–364. https://doi.org/10.1016/j.snb.2014.01.051
29. Andersson C, Lönnroth C, Moldawer LL, Ternell M, Lundholm K (1990) Increased degradation of albumin in cancer is not due to conformational or chemical modifications in the albumin molecule. J Surg Res 49:23–29. https://doi.org/10.1016/0022-4804(90)90105-B
30. Boonpipattanapong T, Chewatanakornkul S (2006) Preoperative carcinoembryonic antigen and albumin in predicting survival in patients with colon and rectal carcinomas. J Clin Gastroenterol 40:592–595. https://doi.org/10.1097/00004836-200608000-00006
31. Siddiqui A, Heinzerling J, Livingston EH, Huerta S (2007) Predictors of early mortality in veteran patients with pancreatic cancer. Am J Surg 194:362–366. https://doi.org/10.1016/j.amjsurg.2007.02.007
32. Brinkman JW, Bakker SJL, Gansevoort RT, Hillege HL, Kema IP, Gans ROB, de Jong PE, de Zeeuw D (2004) Which method for quantifying urinary albumin excretion gives what outcome? A comparison of immunonephelometry with HPLC. Kidney Int Suppl 66:S69–S75. https://doi.org/10.1111/j.1523-1755.2004.09219.x
33. Shaikh A, Seegmiller JC, Borland TM, Burns BE, Ladwig PM, Singh RJ, Kumar R, Larson TS, Lieske JC (2008) Comparison between immunoturbidimetry, size-exclusion chromatography, and LC-MS to quantify urinary albumin. Clin Chem 54:1504–1510. https://doi.org/10.1373/clinchem.2008.107508
34. Huang Z, Wang H, Yang W (2015) Gold nanoparticle-based facile detection of human serum albumin and its application as an INHIBIT logic gate. ACS Appl Mater Interfaces 7:8990–8998. https://doi.org/10.1021/acsami.5b01552
35. Lin ZH, Chen IC, Chang HT (2011) Detection of human serum albumin through surface-enhanced Raman scattering using gold “pearl necklace” nanomaterials as substrates. Chem Commun 47:7116–7118. https://doi.org/10.1039/c1cc11818h
36. Scaglione F, Alladio E, Damin A, Turci F, Baggiani C, Giovannoli C, Bordiga S, Battezzati L, Rizzi P (2019) Functionalized nanoporous gold as a new biosensor platform for ultra-low quantitative detection of human serum albumin. Sensors Actuators B Chem 288:460–468. https://doi.org/10.1016/j.snb.2019.03.005
37. Der Jean R, Larsson M, Da Cheng W et al (2016) Design and optimization of a nanoprobe comprising amphiphilic chitosan colloids and Au-nanorods: sensitive detection of human serum albumin in simulated urine. Appl Surf Sci 390:675–680. https://doi.org/10.1016/j.apsusc.2016.08.143
38. Wang T, Chen M, Niu C, Liu N, Wang L, Sun B, Hua W, Ouyang J (2015) Flow-injection with enhanced evaporative light scattering detector detection and quantification of human serum albumin using gold nanoparticles. Anal Methods 7:3185–3192. https://doi.org/10.1039/c4ay02918f
39. Lai T, Hou Q, Yang H, Luo X, Xi M (2010) Clinical application of a novel sliver nanoparticles biosensor based on localized surface plasmon resonance for detecting the microalbuminuria. Acta Biochim Biophys Sin Shanghai 42:787–792. https://doi.org/10.1093/abbs/gmq085

Sensors and Actuators Reports 4 (2022) 100108

Contents lists available at ScienceDirect

Sensors and Actuators Reports

journal homepage: www.sciencedirect.com/journal/sensors-and-actuators-reports

Copper nanoclusters and their application for innovative fluorescent detection strategies: An overview

Mariagrazia Lettieri, Pasquale Palladino, Simona Scarano, Maria Minunni *

Department of Chemistry "Ugo Schiff", University of Florence, Sesto Fiorentino, FI 50019, Italy

ARTICLE INFO

Keywords:
Copper nanocluster
CuNCs synthetic approach
CuNCs-based assays
Fluorescence detection strategies

ABSTRACT

Nanomaterials have revolutionized the design of the detection strategies, and nowadays nanoparticles are extensively employed in innovative assays for the selective and sensitive detection of a large variety of analytes. Recently, a new nanomaterials category, namely nanoclusters (NCs), is rapidly emerging. These nanostructures offer great advantages in terms of stability and ease of fabrication. The increasing interest in NCs applications, well represented by the wide bibliography reporting on gold and silver NCs, opens new perspectives for copper nanoclusters (CuNCs). Compared to noble metals, CuNCs not only are more easily available and inexpensive, but also display unique photoluminescent properties with large Stokes shifts, low toxicity, and high biocompatibility, providing high sensitivity even in complex biological matrices. In this review, we present some relevant aspects in the application of CuNCs to various detection strategies, reporting the main features that define the most interesting CuNCs properties, focusing on CuNCs as a promising functional nanomaterial for the development of innovative fluorescent-based platforms.

1. Introduction

There is a need in bioanalytical chemistry of simple, easy, sensitive, and inexpensive assays. In the last years, nanomaterials have been used to improve bioassays' analytical performances, mainly in terms of detection limits. Metal or carbon nanostructures have been applied to Surface Plasmon Resonance (SPR) coupled to nucleic acids or protein based biosensing [1,2] or used in fluorescent-based measurements such as quantum dots (QDs). Recently, a new category of nanomaterials, namely nanoclusters (NCs), is rapidly attracting the interest of bioanalytical chemists for the important fluorescence features applied to the development of bioassays.

Metal nanoclusters (MNCs) are exciting and versatile nanomaterials with intermediate properties between isolated metal atoms and metal nanoparticles (MNPs). To date, the majority of the sensing strategies based on MNCs exploit noble metals, *e.g.,* silver (AgNCs) [3] and gold (AuNCs) [4].

Thanks to their low toxicity and high biocompatibility, in the last decade, copper nanoclusters (CuNCs) were successful used in biomedical and biological fields for *in vitro* and *in vivo* applications [5–8], including molecular diagnostics, nanotheranostic, and environmental analysis. Furthermore, copper is less expensive and more accessible on earth than noble metals, positively impacting on NCs-based systems development. CuNCs appear as excellent substitutes of QDs and organic dyes, thanks to high quantum yield (QY), photostability [9], and large Stokes shifts [10]. The outstanding fluorescence and catalysis features of CuNCs are size-dependent [11], limited by definition to few-to-tens atoms, and diameters within 1 nm, leading to a quantum-like behavior with discrete HOMO-LUMO electronic transitions [12].

The first reports on the formation of fluorescent CuNCs nanoclusters were proposed in 1998 by Zaho et al. [13,14]. They used a class of monodisperse polymeric macromolecular compounds (dendrimers) as templates triggering metal ion reduction which stabilize formed metal clusters, avoiding their aggregation [15]. Other useful templates are nucleic acids [16], proteins [17], peptides [18], and small molecules [19], which reduce copper ions and inhibit the formation of aggregates by steric hindrance [20]. CuNCs were used as sensing probes (enhancing or quenching their fluorescence) to achieve the high-sensitive determination of small and macromolecules even in complex real matrices. First studies reported the Pb^{2+} ions detection by using BSA as template for copper clustering and CuNCs fluorescence quenching to reveal Pb^{2+} presence in solution [21]. Since then, CuNCs were used for quali-quantitative molecular targets' analysis [22–26], pH determination [27–30], or biological imaging [31–33]. The coupling of CuNCs

---

* Corresponding author.
E-mail address: maria.minunni@unifi.it (M. Minunni).

https://doi.org/10.1016/j.snr.2022.100108
Received 23 March 2022; Received in revised form 13 May 2022; Accepted 21 May 2022
Available online 6 June 2022

with a biological recognition element, enabled the development of fluorescence-based platforms characterized by good detection range and detection limit, great stability, and selectivity, which are of great importance in bioanalysis to develop simple and ultrasensitive strategies for biomolecular targets. In this framework, the use of peptides, proteins [34], single (ssDNA), double stranded (dsDNA) [35], and hairpins DNA [36], has been reported [37].

This review firstly describes the general synthetic strategies of CuNCs, then it summarizes the CuNCs-based platform focusing on nucleotides-based CuNCs applied to sensing strategies [38,39] in a framework of easy-to-use, portable, and low-cost devices. Differently from interesting published reviews [38–43], we will distinguish between homogeneous (in solution) and heterogeneous (*e.g.*, lateral flow strips) assays, preserving the definition of sensors and biosensors to devices where a transducer is coupled to a biological receptor immobilized on the surface, including electrodes, planar waveguides, optic fibers, quartz crystals, for electrochemical, optical, and gravimetric based sensing.

2. Synthesis and features of CuNCs

2.1. Experimental parameters that influence fluorescence of CuNCs

The fluorescent properties of CuNCs depend on their nanometric dimensions (Fig. 1) and, similarly to NPs, can be tuned by playing on the synthesis conditions (metal and template concentration/type, reducing agent, solvent, pH, temperature, growth time, etc.), generating atomically precise entities [44]. The emission energy (E_g) of CuNCs depends on Fermi energy of the bulk metal (E_{fermi}) and the number of atoms in single clusters (n), according to equation $E_g=E_{fermi}/n^{1/3}$ [44,45], with the emission wavelengths (λ) spanning from the visible to the near-infrared (NIR) region. Consequently, NCs represent a link between optical properties of a single atom, with discrete electronic transitions between the occupied *d* bands and the Fermi level, and those of nanoparticles, exhibiting localized surface plasmon resonance (LSPR) [46–50]. The core size is directly proportional to the quantity of the reducing agent used during the synthesis but inversely proportional to fluorescence intensity. In particular, fluorescence is limited to NCs with less than ten copper atoms that can be obtained using very low percentages of reducing agent with respect to stoichiometric amount of copper ($\alpha < 0.1$) [51].

Coordination of ligands to the metal core [52] and pH influence both the photoluminescence (PL) of the CuNCs. In particular, electron-rich or electron donor groups, like -SH, –COOH, -NH_2 and –OH, increase the emission intensity and fluorescence lifetime of CuNCs [53,54]. Moreover, pH changes lead to CuNCs emission and excitation peaks shifts due to protonation/deprotonation mechanisms [55], inducing aggregation, emission enhancement, and impacting on CuNCs growth [56]. For example, alkaline pH favors disulfide bonds breaking within the protein scaffold, stabilizing CuNCs by thiol groups coordination [57]. Thanks to the CuNCs pH sensibility, pH sensors are reported [58–61] in the range from 2.0 to 13.2.

Solvents also influence CuCNs PL spectra, due to interactions among the ground state, the excited state, and solvent molecules [62,63]. In particular, CuNCs fluorescence spectra show lower number of peaks and greater Stokes shift in solvents with higher polarity [64], but the fluorescent emission intensity is higher when CuNCs are dispersed in solvents with lower polarity [65].

2.2. Synthetic strategies of copper nanoclusters

Top-down and bottom-up approaches are leading strategies to obtain photoluminescent CuNCs (Fig. 2). Top-down synthesis is based on CuNPs resizing to obtain smaller CuNCs; this approach is very laborious [66,67] while the bottom-up one, simple and mostly used, involves the reduction of metal atoms, followed by their aggregation into clusters, often in presence of a stabilizing agent. Different procedures including electrochemical [68], sonochemical [69], photo-reduction [70], microwave-assisted [32], and template-based synthesis [71] are used in the bottom-up approach. In electrochemical methods, an anode is used as the metal ions source that are reduced at the cathodic surface to metal atoms forming aggregates or nanoclusters stabilized by using surfactants [72]. The sonochemical method is a green and easy synthetic method, exploiting ultrasounds derived from acoustic cavitation [73]. Its limitation is the low quantity of metal atoms obtained, which impairs the following nanoclusters' growth. In photo-reduction synthesis, the production of NCs is induced directly by UV radiation [70]. The microwave-assisted method produces rapid CuNCs crystallization due to homogenous and fast heating [72]. The most used approach is the template-assisted one, allowing a facile, fast, cheap, and green synthesis of nanoclusters by using a template to control the kinetics of copper ions reduction, tuning CuCNs size and shape, and preventing their aggregation [74]. Micro and macromolecules like polymers, oligonucleotides, proteins, peptides, and small molecules have been adopted as scaffolds to induce the controlled nucleation of copper nanoclusters as detailed in the following paragraphs.

2.2.1. Nucleotide sequences as templates

Copper ions interact with nucleotide bases through the coordination of the negatively charged phosphodiester backbone [75]. The length and

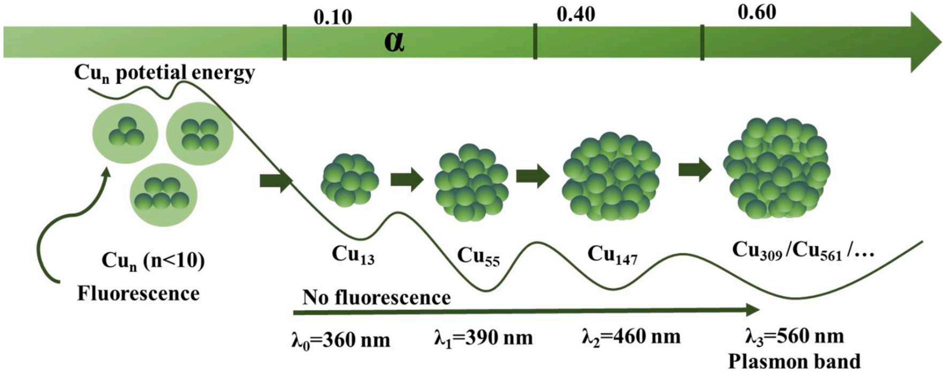

Fig. 1. The influence of the reducing agent-to-copper ratio (α) on CuNCs size (n) and absorption band (λ). Size changes proportionally with α values, whereas photoluminescence is observed when the number of atoms (n) is smaller than 10. The estimated wavelengths (λ) for each cluster and the trend of potential energy are reported [51].

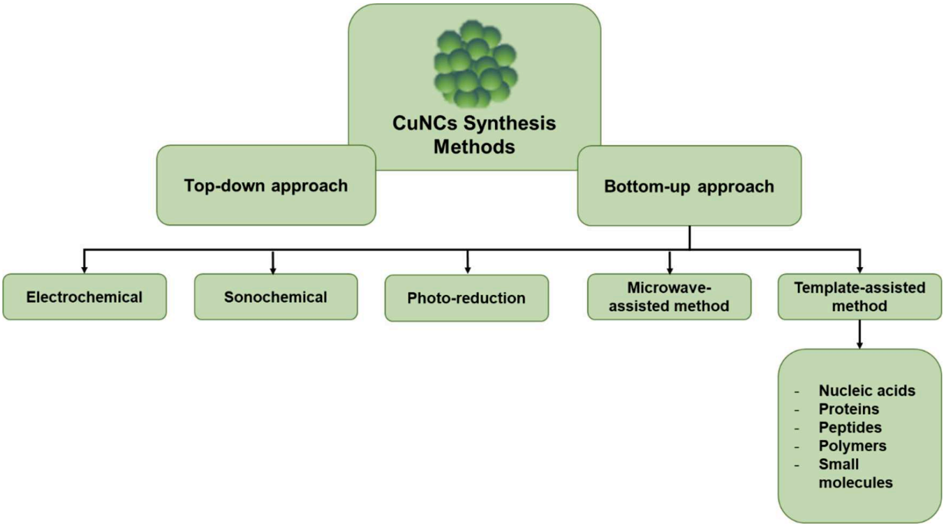

Fig. 2. Synthetic strategies of copper nanoclusters.

the nucleic acid sequence of the dsDNA template strongly influence the CuNCs synthesis and photoluminescence properties [41]. Firstly, random dsDNA was initially exploited for the CuNCs synthesis. Subsequently, it was noticed that a remarkable fluorescent signal improvement was obtained by using polyT ssDNA or poly(AT-TA) dsDNA, where adenine and thymine represent the nucleation site for reduction of Cu(II) to Cu(0) and its clustering to CuNCs. This mechanism is impaired by adopting cytosine and guanine rich sequences likely due to strong copper complexation that could limit copper reduction. Summarizing, ssDNA containing poly(thymine) sequences [76–78], dsDNA with AT-rich domains, as well as long oligonucleotide sequences [79,80], in presence of a reducing agent (usually ascorbic acid), favor the formation of high fluorescent CuNCs with an excitation wavelength at 340 nm and an emission peak around at 600 nm. Beside the stabilizing effect and its influence on the CuNCs photoluminescent properties, nucleotide sequences may also possess specific molecular recognition ability, that can be exploited in solution assays to selectively bind different analytes [81, 82], like for the aptamers that are nucleic acid sequences (DNA or RNA) able to bind a target molecule [83,84]. They are obtained *in vitro* after a selection process by exponential enrichment (SELEX) or non-SELEX approaches [85,86]. DNA is a privileged scaffold for the synthesis of CuNCs also because it can be used for a rapid detection of genetic alteration [87], differently from classic genetic tests that usually require long analysis time [88].

2.2.2. *Proteins and peptides as templates*

Proteins and peptides are often used as templates for building stable and biocompatible CuNCs, requiring mild conditions for the synthesis [89,90]. They contain several functional groups, like amine-, thiol- and carboxyl groups, which initiate the complexation through electrostatic forces. Amine- and carboxyl groups coordinate copper ions while thiol groups contribute to the reduction and stabilization of CuNCs. Thus, the diversity of the amino acid sequence affects the final CuNCs properties. A conventional protein-CuNCs synthesis implies the use of various additives that alter the protein structure by breaking the disulfide bonds, like dithiothreitol (DTT) [91], H_2O_2 [92], hydrazine hydrate [93], and NaOH [94]. So far, different protein templates have been explored to synthesize luminescent CuNCs. For instance, bovine serum albumin (BSA) leads to high QY fluorescent CuNCs [81,82,95]. Bustos et al. produced blue emitting CuNCs (610 nm) with high photostability with a decrease of only 15% in emission signal after 50 min [82]. Other proteins, such as human serum albumin (HSA) [96,97], lysozyme [98,99], ovalbumin [100], papain [101,102], transferrin [103] and trypsin [60] have been also applied as templates for CuNCs production. Although proteins are preferred as templates for the presence of multiple active sites that favor the reduction and the accumulation of copper ions promoting the CuNCs growth, few studies report the use of peptides as template [104,105]. For example, Tang and co-workers prepared stable and well water-dispersed CuNCs by reducing copper chloride with ascorbic acid in the presence of a short peptide template Cys-Cys-Cys-Asp-Leu, highlighting the importance of $CuCl_2$-to-peptide molar ratio (1:4) in the formation of CuNCs [104].

2.2.3. *Polymers as templates*

Dendrimers, *i.e.*, highly ordered branched polymers with different size and the chemical structure, are the most exploited templates to produce very stable CuNCs [13,106]. Polyvinyl pyrrolidone (PVP)-CuNCs were applied to develop a FRET-based assay in solution (named sensor) for the micromolar detection of glutathione (GSH) in human serum with performances comparable to HPLC [107]. Polyethyleneimine (PEI) was also used as scaffold for facile one-pot synthesis of water soluble CuNCs applied to Fe^{2+} detection in tap, river water, and urine, with very good analytical performances, *i.e.*, micromolar level concentration and 100% recovery [108]. Furthemore, CuNCs were incorporated into composite polymer films by reduction of copper ions in a hydrogel network with 30% QY, opening to possible applications in heterogeneous phase assays/sensors [109].

2.2.4. *Small molecules as templates*

Small molecules, containing thiolates and carboxylates groups, like glutathione (GSH) and cysteine, act as reducing, protecting, and capping agents to stabilize CuNCs through to a facile one-step green synthetic approach [110–114]. Glutathione was exploited also for its ability to coordinate metal cations like aluminum ions that guide the self-assembly of nanoclusters resulting in the formation of CuNCs with controllable size and retained bright luminescence in neutral conditions [115,116]. Many authors took advantage of the easy and cheap synthesis of copper nanoclusters by using small molecules as template [117–120]. Additional small molecules like 4-methylthiophenol and 4-chlorothiophenol were also applied to synthesize CuNCs able to sensitively detect different kinds of target molecules like tetracycline (LOD 40 nM) [121].

3. CuNCs-based detection strategies

CuNCs were exploited as sensing probes in solution since they are able to detect different types of targets, from ions to macromolecules (*i. e.*, proteins, DNA, enzyme, etc.) [122]. Numerous publications are related to the integration of noble metal nanomaterials in bioanalytical assays development [123–126], leading to remarkable improvement in bio-detection processes.

Generally, an efficient detection system should be characterized by the following properties: stability, selectivity towards the analyte, reproducibility, desired sensitivity, a null or minimal sample pre-treatment. Moreover, to ensure the development of a potential commercial device, the assay should be simple, cheap, and able to perform rapid analysis making it suitable as a point-of-care (POC) test [127–129].

Copper nanoclusters employed as signal transducers in “sensors” design lead great advantages in the assay performance, such as high selectivity, sensitivity, low detection limits, and wide detection range. Typically, when the bioreceptor is associated with CuNCs, the binding event leads to a fluorescence signal variation depending on analyte concentration [130–132].

In the following sections, different types of detection strategies combined with CuNCs are reported, with the focus on oligonucleotide sequences as bioreceptors both in solution and in heterogeneous assays. Nucleic acids are employed for CuNCs growth and may hybridize or not the complementary DNA sequences. Alternatively, NAs act as synthetic biomimetic receptors *i.e.*, aptamers, binding different analytes (both small and macromolecules), leading to several detecting strategies. The nucleic acids-, proteins-, and immuno-based approaches will be

Table 1
DNA-based detection strategies for CuNCs-based assays.

Template	Target	Technique	Read out	Sample	Linear range	LOD	QY	Refs.
dsDNA	miRNAs	*340/608 nm	Turn-on	-	1.0 pM–10.0 nM	1 pm	-	[134]
polyT DNA	miRNA21	*340/605 nm	Turn-on	Cancer cells	50 pM – 1 nM	18.7 pM	-	[135]
hp-DNA	miRNA155	*400/510	Turn-on	Human serum, saliva, plasma, MCF-7, fibroblast	5.0 pM –10.0 nM	2.2 pM	-	[136]
AT-rich dsDNA	miRNAs	*340/580 nm	Turn-on	Urine	-	500 fM	-	[137]
dsDNA	T4 PNKP	*340/570 nm	Turn-off	HeLa cells	0.07–15.0 U mL	60 U L	3.4 %	[155]
AT-rich dsDNA	MNase	*340/570 nm	Turn-off	-	1.0–50 U L	1.0 U L	-	[142]
dsDNA	ExoIII	*345/610 nm	Turn-off	-	-	-	-	[168]
hpDNA	S1 nuclease	*490/660 nm	Turn-on	-	5.0–8.0 U L	3.0 U L	-	[36]
AT-rich dsDNA	EcoRI	*340/575 nm	Turn-off	-	2.0 –100 U mL	0.87 U mL	-	[79]
polyT DNA	UDG	*345/650 nm	Turn-on	HeLa Cells	0.05–2.0 U L^{-1}	0.002 U L^{-1}	-	[143]
polyT DNA	UDG	*340/602 nm	Turn-on	HeLa Cells	0.1–10 U L	0.05 U L^{-1}	-	[144]
AT-rich dsDNA	UDG	*340/570 nm	Turn-off	HeLa Cells	1.0 – 100 U L	0.5 U L^{-1}	0.039	[145]
AT-rich dsDNA	Dam MTase	*340/590 nm	Turn-off	Human Serum	0.5–10.0 U mL	0.5 U mL	-	[146]
AT-rich dsDNA	TdT	*340/570 nm	Turn-on	Leukemia cells	0.7–14.0 U mL	60.0 mU L^{-1}	0.112	[147]
dsDNA	SNP	*344/593 nm	Turn-on	-	-	-	-	[138]
polyT DNA	SMN1	*340/500 nm	Turn-on	Clinical samples	-	-	-	[139]
dsDNA	Abasic sites	*340/585 nm	Turn-off	Linear plasmid, onion and HeLa Cells	-	-	-	[140]
Nucleosides	Nucleosides	*300/380 nm	Turn-on	-	-	-	0.27–1.34%	[141]
Nanowire-DNA	TdT and BamH1	Electrochemical	Turn-on	Human serum and urine	0.5 –160 U mL^{-1} (TdT); 2×10^{-2} –30 U mL^{-1} (BamH1)	100 U L^{-1} (TdT); 4 U L^{-1} (BamH1)	-	[156]
AT-rich dsDNA	miRNA21	ECL	Turn-on	Human breast cancer cells (MCF-7) and human cervical cancer cells (Hela)	100 aM–100 pM	16.05 aM	-	[157]
AT-rich dsDNA	miRNA155	ECL	Turn-on	Human serum	100 aM– 100 pM	36aM	-	[158]
polyT-DNA	miRNA155	Colorimetric	Turn-off	Human plasma	1.0 pM to 10.0 nM	0.6 pM	-	[159]
dsDNA	HBV DNA	Colorimetric	Turn-on	Human serum	12×10^{9}–12×10^{13} DNA molecules	12×10^{9} DNA molecules	-	[160]
polyT-DNA	DNA	SPR	Turn-on	-	-	3.21 fM	-	[163]

[*] Fluorescence ($\lambda_{ex}/\lambda_{em}$)

discussed with the focus in real matrices detection, when available in the literature.

The CuNCs-based solution assays/sensors are reported in three tables and three paragraphs to differentiate DNA- (Table 1, paragraph 3.1), aptamer- (Table 2, paragraph 3.3), and immuno-based (Table 3, paragraph 3.3) detection strategies, *i.e.*, defining the probe used for the biorecognition of the target molecule. Within each table and detection strategy, the assays are classified according to the template used for copper reduction and CuCNs generation, the target molecule, the analytical technique used for signal transduction, the turn-on/turn-off read out, the kind of sample, and the analytical parameters, *i.e.*, the linear range for the detection of the analyte, the limit of detection (LOD), and the QY for fluorescent probes only.

3.1. DNA-based detection strategies

3.1.1. Fluorescent detection of oligonucleotides

One of the most used biorecognition elements in sensing strategies are nucleic acids, in particular, single stranded DNA [133]. In the case of CuNCs, DNA sequences have a dual role. They act as template and molecular probe at the same time, stabilizing NCs and selectively binding the analyte. The recognition mechanism involves affinity interaction, hybridization between the probe and complementary sequences or, as in the case of aptamers, Van der Waals, hydrogen bonding, and electrostatic interactions, without hybridization. The crucial role of miRNAs in the regulation of gene expression and, consequently, their association with several diseases, prompted the development of CuNCs-based assays. The pioneering work from Ye's group reported the miRNA detection via an isothermal enzymatic reaction [134], using an amplified template to generate a dsDNA as scaffold for the synthesis of fluorescent CuNCs, showing a detection range from 1 pM to 10 nM (Fig. 3A). Subsequently, similar assays were proposed [134–137]. In particular, miRNA21 was determined in cancer cells by using a duplex-specific nuclease (DSN). When miRNA binds the DNA probe, the DSN digests the DNA sequence, releasing an oligonucleotide that forms a long polyT acting as scaffold for the synthesis of high fluorescent CuNCs [135] (Fig. 3B). DNA-CuNCs are also employed to identify single nucleotide polymorphisms (SNPs) [138], or nucleotide variants [139–141], linked to diseases and drug responses. For example, Chen and coworkers [139] used luminescent polyT (DNA)-CuNCs to identify the Survival Motor Neuron genes SMN1 involved in spinal muscular atrophy, observing fluorescence in 65 DNA clinical samples containing the SMN1 gene. This approach could be exported to other SNPs or nucleotide variants by designing suitable sensing probes (Fig. 3C).

3.1.2. Fluorescent detection of enzymes and small molecules

DNA-CuNCs based assays are also applied to detect enzymes and their activity. Recently, Zhang and coworkers designed a fluorimetric method to detect the activity of the T4 polynucleotide kinase phosphatase (PNKP) by using a short phosphorylated DNA (pDNA) strand, and a long-dephosphorylated DNA (dsDNA) as complementary probes [119]. When PNKP is present, pDNA undergoes dephosphorylation and the dsDNA thus operates as template for CuNCs growth (Fig. 3D). Several research groups adopted similar strategies to develop different DNA-based bioassays for micrococcal nuclease [142], exonuclease III [141], S1 nuclease [36], endonuclease EcoRI [79], Uracil-DNA Glycosylase (UDG) [143–145] and transferase [146,147]. Details relative to LODs and detection ranges of the cited assays are reported in Table 1.

Finally, DNA is also employed as an indirect probe to detect ions [80, 148], or small molecules [149–154]. In these cases, the fluorescent signal could be the result of:

- Interaction between copper ions and small molecules;
- Electron transfer effect between copper ions and the detected target;
- Oxidation of CuNCs;
- Binding between the small molecule and the DNA template, resulting in CuNCs formation;
- Binding between the small molecule and the DNA template which leads to DNA destruction, avoiding CuNCs growth.

3.1.3. Electrochemical and electro-chemiluminescence detection strategies

Most CuNCs-based detection strategies exploit their PL properties for direct analyte detection. However, alternative analytical electrochemical and electrochemiluminescent (ECL) methods have been proposed [156–160] also because of low fabrication costs, simple and low-cost experimental setup, as well as high sensitivity and selectivity. ECL is a kind of luminescence produced by an electrochemically generated intermediates, and the absence of a light source dramatically reduces the background signal from scattered light and luminescent impurities [161]. In this context, Hu et al. reported a CuNCs DNA-based electrochemical sensor to determine the enzymatic activity of terminal deoxynucleotidyl transferase (TdT) that catalyzes the growth of long T-rich DNA nanowires, here used as CuNCs template, further attached to a graphene oxide (GO)-modified electrode where occurs the H_2O_2 reduction, with an electrochemical signal proportional to the TdT amount (LOD = 0.1 U mL^{-1}, detection range: 0.5–160 U mL^{-1}) [156]. The same strategy has been applied to test BamH1 activity, an site-specific endonuclease employed to detect hepatitis C virus (LOD = 0.004 U mL^{-1}, detection range: 0.02–30 U mL^{-1} [156]).

Different sensing mechanisms based on ECL were designed [157, 158]. For example, miRNA21 was detected within an excellent concetration range 100 aM - 100 pM, with the ultrasensitive detection limit of 19 aM [157]. The same range and a LOD of 36 aM was obtained for microRNA-155 detection by using an innovative DNA probe (DNA nanocranes) stabilized by an AT-rich domain [158] (Fig. 4A).

3.1.4. Colorimetric detection strategies

Simple colorimetric assays for NA detection are also reported,

Table 2
Aptamer-based detection strategies for CuNCs-based assays.

Template	Target	Technique	Read out	Sample	Linear range	LOD	QY	Refs.
DNA	ATP and ADA	*460/580 nm	Turn-on (ATP), Turn-off (ADA)	Fetal bovine serum	2–18 mM (ATP); 5–50 U L^{-1} (ADA)	7.0 µM (ATP); 5 U L^{-1} (ADA)	-	[170]
dsDNA	MC-LR	*34/575 nm	Turn-off	Water	0.01–1000 mg L^{-1}	4.8 ng L^{-1}	-	[174]
polyT-DNA	VEGF165	*332/393 *463/524 nm	Turn-on	Human serum	10–800 pM	12 pM	0.082	[175]
PDANS	PKA	*390/492 nm	Turn-off	HepG2 cell lysates	0.05–4.5 U mL^{-1}	0.021 U mL^{-1}	1.24%	[172]
dsDNA	PKA	*345/595 nm	Turn-off	HepG2 cell lysates	0.1–5.0 U mL^{-1}	0.039 U mL^{-1}.	-	[177]
dsDNA	ATP	*340/598 nm	Turn-on	-	0.01 nM - 100 nM	5 pM	-	[171]
Y-DNA	miRNA21	Electrochemical	Turn-on	Human blood	0 pM-0.1fM	10 aM	-	[176]

* Fluorescence ($\lambda_{ex}/\lambda_{em}$).

Table 3
Immunoassay-based detection strategies for CuNCs-based assays.

Template	Target	Technique	Read out	Sample	Linear range	LOD	QY	Refs.
-	HIV-1 p24	*394/598 nm	Turn-on	Human plasma	27–1000 ng L^{-1}	23.8 ng L^{-1}	-	[178]
BSA	PKA	Electrochemical	Turn-on	Human serum	0.5 ng L- 100 ug L	146 pg L	-	[179]
-	LSR	PEC-Colorimetric	Turn-off	Human serum	1 pg L^{-1}–10 ug L^{-1}	1 pg L^{-1}	-	[180]
dsDNA	ALP	*340/575 nm	Turn-on	Human serum	0.04–100 U L^{-1}	7.0 ng L^{-1}	-	[181]
DNA	PSA	PEC	Turn-off	Human serum	0.02–100 ug L^{-1}	5.0 ng L^{-1}	-	[182]
DNA	MM-7	Potentiometric	Turn-on	Human serum	0.02–100 ug L^{-1}	5.3 ng L^{-1}	-	[184]
-	hc-TnT	PEC	Turn-off	Human serum	0.1 to 2 ng L	0.03 ng L	-	[183]

* Fluorescence ($\lambda_{ex}/\lambda_{em}$).

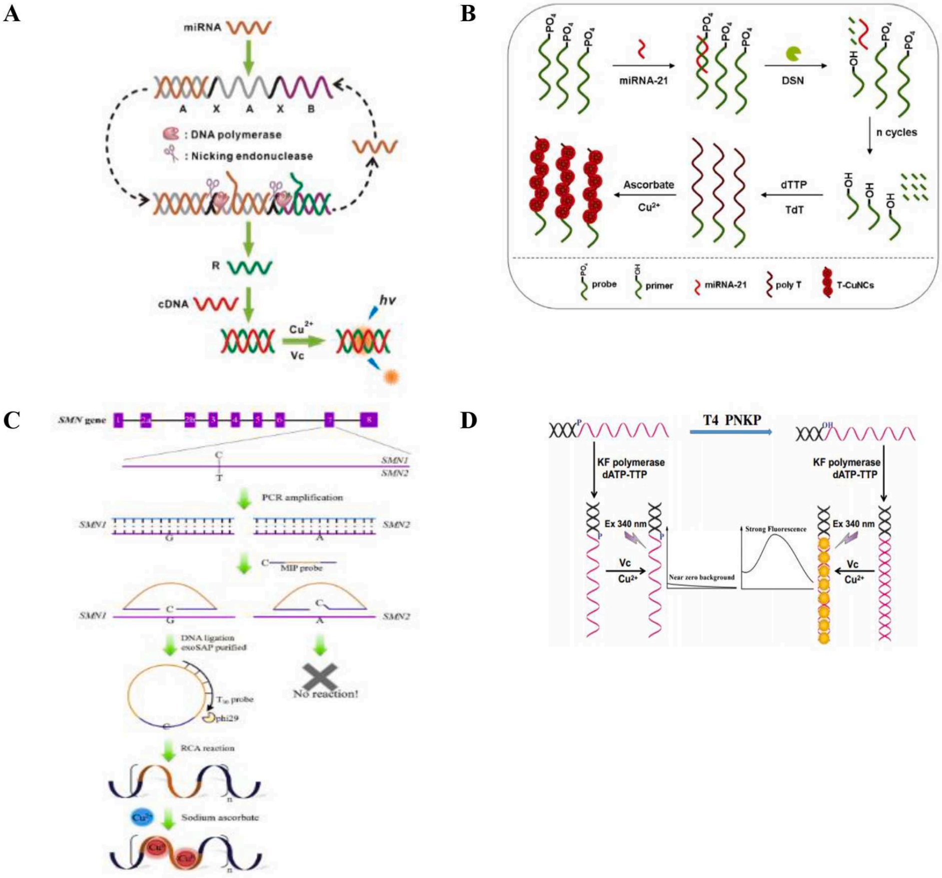

Fig. 3. Schematic illustration of CuNCs DNA-based assays for: (A) miRNA detection according to the assay strategy proposed by Ye's group, reprinted from Ref. [134] with permission of Royal Society of Chemistry; (B) miRNA detection according to the assay strategy proposed by Li's group, reprinted from Ref. [135] with permission of Elsevier B.V.; (C) enzymes detection according to the assay strategy proposed by Zhang and co-workers, reprinted from Ref. [155] with permission of Springer Nature; (D) nucleotide variants detection according to the assay strategy proposed by Chen and co-workers, reprinted from Ref. [139] with permission of Elsevier B.V.

employing CuNCs DNA platforms [91,160,162,163]. Borghei and co-workers developed a colorimetric assay based on methylene blue (MB) to detect a cancer biomarker miRNA-155 in solution. In detail, polyT-DNA was used for CuNCs synthesis, exhibiting an enzyme-like peroxidase activity (Fig. 4B). After miRNA-155 incubation, the complementary sequence on DNA-CuNCs hybridizes miRNA sequences and CuNCs catalyze the oxidation of the methylene blue [159]. Increasing the miRNA concentration, the absorbance of MB decreases with a dynamic range from 1.0 pM to 10.0 nM with a LOD equal to 0.6 pM. Application to the detection in human blood plasma resulted in excellent recovery (99%). This offers an interesting application in clinical diagnostics since miRNA-155 amount can be related to cancer stage and expression, increasing with advancing cancer stage. The use of MB is not new in DNA sensing, since it has been widely and successfully reported coupled to electrochemical transduction [164], but reinforces the CuNCs applicability to companion diagnostics.

Virus detection has also been successfully achieved by an inexpensive colorimetric heterogeneous assay to identify Hepatitis B virus

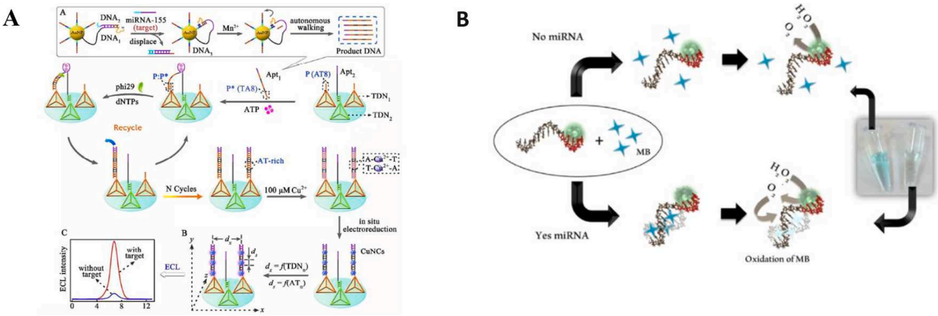

Fig. 4. Schematic illustration of CuNCs DNA-based (A) electrochemiluminescence (ECL) platform according to the assay strategy proposed by Zhou et al. reprinted from Ref. [158] with permission of American Chemical Society (C) colorimetric platform according to the assay strategy proposed by Borghei et al. reprinted from Ref. [159] with permission of Elsevier B.V.

(HBV) by naked eye [160], with possible use in remote areas. In this strategy, a ssDNA probe is immobilized on the surface of a 96-well plate, hybridizing the complementary HBV NA, if present. The resulting dsDNA acts as a CuNCs template. To reveal the hybridization by naked eye, a chromogen is necessary. Thus, simple and cheap reagents leading to ox-red reactions, with final color development, are further added to the mixture:

(1) creatinine with the consequent formation of a copper-creatinine complex
(2) Azino-bis(3-ethylbenzothiazoline-6-sulfonic acid) diammonium salt (ABTS used as substrate)
(3) H_2O_2

The copper-creatinine complex shows peroxidase-like enzyme properties converting H_2O_2 into H_2O and ABTS into its oxidized form [160]. Different concentrations of HBV DNA led to different degrees of ABTS oxidation reaction and, consequently, different green color gradations. This assay was applied also to explore single nucleotide polymorphism (SNP) analysis, in which, in case of SNP presence, decreased color intensity *versus* wild type DNA, can be observed. The possibility to analyze the presence of the target sequence, wild type or mismatched (SNP), in the sample by naked eye and using very simple chemistry, represents an important possibility for bioanalytical applications *in situ*, in remote and/or disadvantaged places of the planet.

3.1.5. Surface Plasmon resonance (SPR)

SPR spectroscopy was explored in combination with CuCNs [163] to achieve ultrasensitive NA detection in real samples [165–167] (*i.e.*, human blood), including SNP detection. An interesting approach is reported by Yuan et al. dealing with the CuCNs synthesis on dsDNA formed at the SPR gold chip surface, followed by target NA extension by terminal deoxynucleotidyl transferase. Here, TdT-mediated prolongation reaction was activated onto the dsDNA modified gold chip, originating an origami scaffold for CuCNs synthesis and precipitation by addition of ascorbic acid, leading to an ultrasensitive determination of femtomolar-level nucleic acid [163].

3.2. Aptamer-based detection strategies

3.2.1. Fluorescence detection

Another important class of oligonucleotide-based sensing strategy exploits aptamers as a biorecognition element, where the aptamers are short ssDNA or ssRNA sequences able to recognize a specific target [169]. The aptamer-target recognition is independent from both the detection principle and signal transduction that can be optical (*e.g.*, fluorometric, colorimetric, plasmonic, etc.), electrochemical, or piezoelectric. Conventional fluorescent aptamer-based platforms (not employing CuNCs) use a fluorophore and a quencher label to produce a Förster resonance energy transfer (FRET) event in which a fluorophore (the donor), in an excited state, transfers its energy to a neighboring molecule (the acceptor) by nonradiative dipole-dipole interaction. Although not necessary, in most cases the acceptor is also a fluorescent dye. In biological applications, this technique has become popular to qualitatively map protein-protein interactions.

In aptamer-based assays, the presence of the target triggers a change in the aptamer conformation, corresponding to a distancing between fluorophore and quencher and, in turn, a fluorescent response. FRET technique has been extensively investigated, however presents some limitations such as low fluorescent signal, due to an overlap between donor emission and acceptor excitation spectra, leading to low quantum yield and low sensitivity, high background due to an incomplete quenching phenomenon, and high cost of the labeled aptamer. These drawbacks encourage the design of new aptamer-based platforms, where CuNCs are exploited as fluorescent probes and the DNA aptamer acts both as template and bioreceptor. Currently, Zhang and Wei developed a ‘turn-on’ fluorescent method based on DNA-templated copper/silver nanoclusters (DNA-Cu/Ag NCs) for the detection of ATP (adenosine triphosphate) and the enzyme ADA (adenosine deaminase) [170], involved in the purine metabolism, playing a central role in the differentiation and maturation of the lymphoid system. The aptamer sequence is inserted in the middle of the DNA template (Fig. 5A). When the aptamer binds ATP or ADA, it changes its conformation, and, consequently, DNA-Cu/Ag NCs get closer, becoming bright emitters. This approach, in standard solutions, showed a linear range of 2–18 mM and of 5 to 50 U L^{-1} with 7.0 μM and 5 U L^{-1}as LOD, respectively for ATP and ADA. Furthermore, the approach succeeded also in detecting ATP and ADA in a complex matrix, *i.e.*, fetal bovine serum, opening new perspective for a real applicability of this strategy. This aptamer-based “turn-on” fluorescent assay combined with Cu and Ag and nanoclusters is the only example found so far, including silver.

ATP detection has been achieved also by a fluorescent aptasensor, where the structural switch induced by the affinity ATP binding leads to the aptamer harpin open conformation. This results in a primer hybridization which drives a target-cycling strand displacement amplification (TCSDA). As a result, a large quantity of dsDNA is produced, acting as template for CuNCs growth with high fluorescent signal [171]. Relatively to enzymatic activity testing a FRET-based assay for Protein Kinase (PKA) is also reported. In this case, an aptamer-based “in solution” assay/sensor utilizing CuNCs and polydopamine nanospheres (PDANS) was employed [172]. The ATP- CuNCs aptamer (apt-CuNCs) was adsorbed onto PDANS surface. The ox/red event regulates the signal generation. Here the donor apt-CuNCs is in close proximity to the acceptor polydopamine (PDANS), leading to apt-CuNCs fluorescence

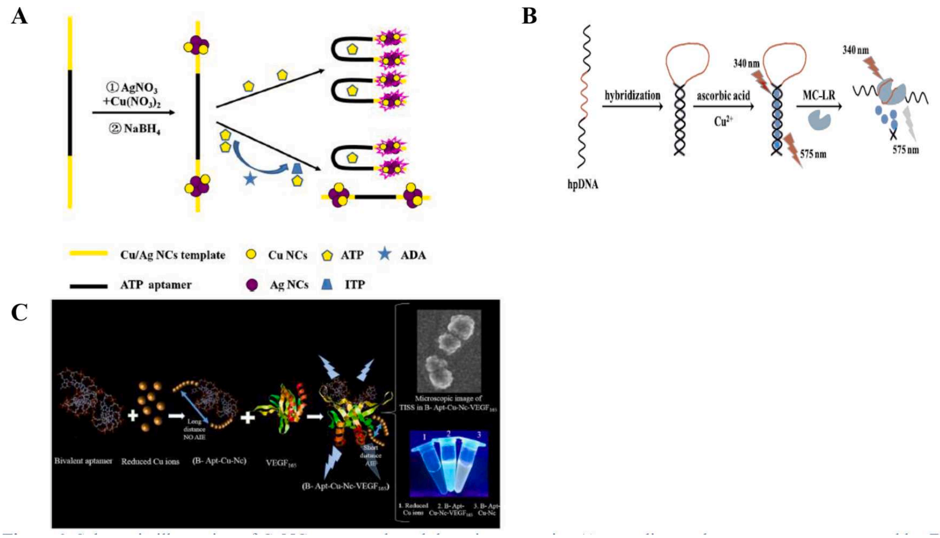

Fig. 5. Schematic illustration of CuNCs-aptamer based detection strategies (A) according to the assay strategy proposed by Zhang and Wei, reprinted from Ref. [170] with permission of Springer Nature. (B) according to the assay strategy proposed by Yanli Zhang's group, reprinted from Ref. [174] with permission of Elsevier B.V. (C) according to the assay strategy proposed by Moghadam's group, reprinted from Ref. [175] with permission of Elsevier B.V.

quenching.

In the case of toxic molecules analysis, an assay targeting microcystins is reported. Microcystins are toxins produced by cyanobacteria with microcystin-leucine arginine (MC-LR) [173]. Zhang et al. designed an aptamer-CuCNs assay selective for MC-LR. The aptamer is also designed to hybridize the complementary DNA sequence (cDNA) which acts as template for CuCNs growth (dsDNA-CuNCs) (Fig. 5B) [174]. After MC-LR addition, the affinity interaction aptamer-target leads to aptamer conformational changes resulting in DNA hybrid (dsDNA/-CuNCs) opening, with CuCNs fluorescence quenching. MC-LR detection in 0.01 to 1000 mg L^{-1} concentration level, with 4.8 ng L^{-1} as LOD in real water samples is reported.

Relatively to protein detection, Vascular Endothelial Growth Factor (VEGF) was quantified via a "signal-on" fluorescent method, based on bivalent aptamer-CuNCs (Fig. 5C) [165]. A multimerized VEGF aptamer works as template for CuCNs growth. VEGF detection is successfully achieved in the 10–800 pM linear range with a LOD of 12 pM. The selectivity and specificity assessment displayed high discriminant capability in serum samples. This strategy is based on a previous work conducted by the same research group, in which graphene dioxide and dsDNA were employed [167].

3.2.2. *Electrochemical detection*

miRNA21 detection has been reported also with electrochemical techniques [176]. Here NA sequences are immobilized on a gold electrode (GE), and the analysis is performed by differential pulse stripping voltammetry (DPSV) [176], by detecting the Cu^{2+} ion of dissolved and stripped CuNCs. miRNA21, as already underlined, is a very interesting

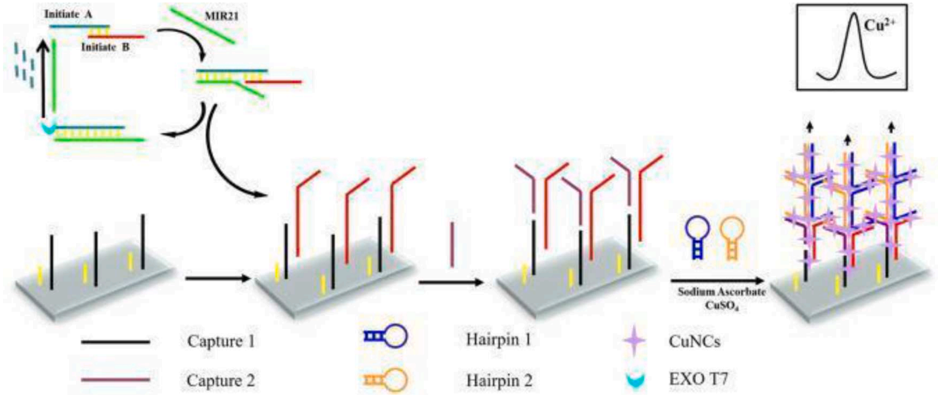

Fig. 6. Schematic illustration of CuNCs aptamer-based electrochemical platform according to the assay strategy proposed by Yijia Wang's research group. This reported detection strategy consists in a multi-steps assay. First, sequence A and B are mixed together to form a duplex DNA. Thus, in this first step A and B are hybridized. Then, it was added MIR21 that lead a displacement between A and B. At this point, EXO T7 degrades A and the fragment binds MIR21 forming a hybrid sequence. Instead, sequence B contributes to the Y-shaped DNA with capture 1 and capture 2 on the electrode. Once obtained the final arrangement of the detection strategy, the Y-shaped branched DNA was used as template for CuNCs synthesis to finally detect MIR21 through oxidation peak current of copper by using DPSV techniques. From Ref. [176], with permission of Elsevier B.V.

target, upregulated in many pathological conditions including cancer and cardiovascular diseases. The approach proposes the fast (in 3 min) and precise *in situ* growth of CuNCs on tree-like overlapping and branching Y shaped dsDNA on the electrode surface [176], with the advantage of being time-saving and allowing controlled dimension of CuNCs (with diameter around 2.5 nm). A simplified scheme is reported in Fig. 6. The assay results a bit cumbersome, requiring several experimental steps: immobilization of NA probes, efficient enzyme with nuclease activity (exonuclease T7 for triggered targets recycling) to cleave only one strand of dsDNA, and the hybridization chain reaction (HCR) amplification for more signal molecules loading on Y-shaped dsDNA [176]. To obtain the Y-shaped branching DNA template, aptamers and hairpin sequences are adsorbed on the gold electrode surface. Subsequently, miRNA21 is added to form the overlapping Y-shaped branching ds-DNA template. This latter was exploited as a template to grow CuNCs. Then, the electrode was immersed in a HNO_3 solution which oxidized Cu (0) to Cu (II) that is thus released in solution. In conclusion, miRNA21 is determined by the oxidation peak current of copper obtained by applying differential pulse stripping voltammetry (DPSV) analysis. The aptasensor shows a linear range within 10 pM and 0.1 fM and 10 aM as LOD. This LOD is competitive with the ones recorded with fluorescence and ECL detection respectively in the order of pM [135] and aM [157] as displayed in Table 1. Moreover, this electrochemical platform was tested in blood samples, with around 100% recovery in human blood spiked with miRNA21 down to 0.1 fM, demonstrating an excellent ability to operate in real samples.

3.3. *Immuno-based CuNCs assays*

Over the past decades, considerable advances have interested the design of immunoassays thanks to the introduction of photoluminescent metal nanomaterials that improved the detection efficiency of biomolecules. However, the combination of CuNCs with immuno-based strategies is still poorly applied and only few studies are reported in the literature. Among these, detection strategies involving the growth of CuNCs on glutathione (GSH) and the subsequent coupling to streptavidin have been reported for detection of HIV-1 p24 biomarker in AIDS tests [178]. In particular, a secondary biotinylated antibody interacts with a CuNCs-conjugate streptavidin, emitting a fluorescence signal HIV-1 p24 concentration dependent (Fig. 7A). A dynamic range of 27–1000 pg mL^{-1} is achieved with a LOD of 23.8 pg mL^{-1} standard solution. Reliable results were obtained also in plasma samples spiked with known concentrations of p24 antigen. Moving to tumor markers analysis, prostate specific antigen (PSA) detection was achieved by electrochemical detection, where Square Wave Voltammetry (SWV)-based immunosensing was coupled CuNCs growth [179] (Fig. 7B). The capturing Ab (Ab1) is immobilized on a glassy carbon electrode modified with Au nanoparticles (AuNPs), to bind PSA; the secondary Ab (Ab2) binds PSA on a different epitope of the Ab1. The novelty of the work is the use of BSA-templated CuNCs carried on platinum NPs and modified with Ab2. Thus, after the immunocomplex formation (Ab1-PSA-Ab2), catalytic signal amplification occurs, mediated by presence of Pt and Cu nanostructures. The recorded current is due to Cu^{2+} reduction at the electrode. The proposed immunosensor works in a wide linear range from 0.5 pg mL^{-1} to 100 ng mL^{-1} displaying a LOD of 145.69 fg mL^{-1} ($S/N = 3$). In addition, the assay demonstrated good response in clinical serum samples; compared to reference ELISA assays the two methods displayed from %RSD of 5.0% and 5.5%, respectively, thus good accuracy and an acceptable reliability for PSA analysis in real practice.

The detection of stimulated lipoprotein receptor (LSR), a biomarker closely related to ovarian cancer, deals with a photoelectrochemical (PEC)–colorimetric immunoassay [180]. Basically, the PEC response is reduced when the Antigen-Antibody reaction takes place. At the same time, color variations in Leuco-MB functionalized colorimetric poly (vinyl alcohol) (PVA) film occurs, providing a dual mechanism and independent signal transduction. The immunoassay is in a simple direct format, *i.e.*, the Ab, immobilized on the transducer surface, directly binds the Ag, added in solution. In detail, the immunoreaction takes place on the CuNCs, grown on several layers of TiO_2 (mixed TiO_2 mesocrystals junction (MMMJ)). CuNCs improve photoelectrochemical colorimetric properties and the catalytic activity of hydrogen peroxide (H_2O_2) that catalyzes Leuco-MB conversion from colorless to blue. When the antibody and the target antigen are captured onto the MMMJ, PEC properties and catalytic activities are inhibited. Spiked human serum samples with LSR, at sub ng/ml concentration level, provided excellent recovery (in the range from 98.4% to 100.7%). The assay analytical parameters are listed in Table 3.

Behind biosensing-based approaches, disposable platforms can be combined with CuNCs use, to improve test analytical performances, in ELISA-like assays. The sandwich immunoassay format is quite common for protein detection. In particular, Immunoglobulins (Ig) and cancer biomarkers like prostate-specific antigen (PSA), matrix metalloproteinase-7 (MMP7) detection has been addressed, by fluorescent, photoelectrochemical (PEC) and electrochemical *i.e.*, potentiometric analysis respectively. A fluorescent ELISA platform for IgG analysis with a new strategy for *in-situ i.e.*, in solution synthesis of CuNCs, is reported. A sandwich assay format is used, where Alkaline Phosphatase (ALP) is bound to the secondary Ab and catalyzes the hydrolysis of ascorbic acid 2-phosphate (AAP) leading to ascorbic acid, that, in presence of Cu^{2+} and the DNA template, allows the *in situ* growth of CuNCs [181] with fluorescence emission. A LOD of 7 pg mL^{-1} is achieved in IgG standard solutions. This novel, easy-to-use and cost-effective fluorescent ELISA platform, led to improved performances with respect to the common commercial ELISA kit and can be transferred to other analytes, if validity in real matrices is further explored.

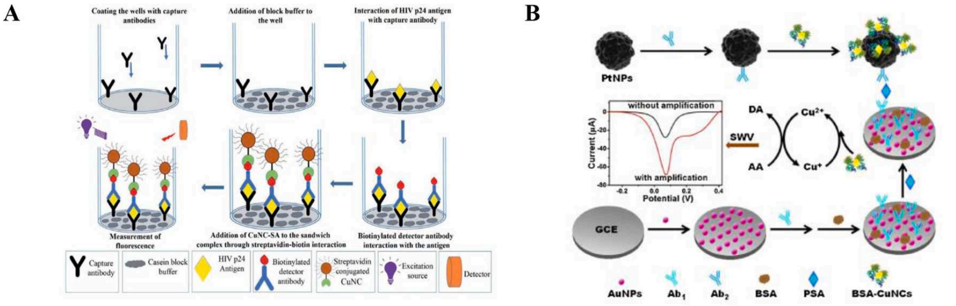

Fig. 7. Schematic illustration of CuNCs immunoassay-based detection strategies (A) according to the assay strategy proposed by Kurdekar's et al. reprinted from Ref. [178]., with permission of Royal Society of Chemistry; (B) according to the assay strategy proposed by Lihua Zhao and Zhanfang Ma, reprinted from Ref. [179], with permission of Elsevier B.V.

PSA is detected by a PEC-CuNCs-based immunoassay employing a Carbon Dots/g-C_3N_4 [182], while MMP7, involved in cancer progression, was quantitatively detected by potentiometric immunoassay using copper ion-selective electrode (Cu-ISE) with a portable detector [183]. Cu^{2+}, under acidic conditions, was released from CuCNs formed at the immunocomplex, where the secondary Ab was linked to a short nucleic acid sequence, acting as probe for further hybridization reaction cycles forming dsDNA structures, promoting CuCNs growth. A dynamic linear range of 0.01–100 ng mL^{-1} with a detection limit of 5.3 pg mL^{-1} MMP7 was achieved in human serum samples.

Behind the cancer biomarker MMP7, the quantitative analysis of cardiac troponin T (cTnT), an important marker of Acute Myocardial Infarction (AMI) is reported by a PEC approach [183]. Here CuCNs were synthesized on BSA, eventually encapsulated in liposomes for further labeling of antibodies to their external surface. After the sandwich immunocomplexing, the confined liposomal labels were lysed to release the CuNCs and numerous Cu^{2+} ions, free to interact with the ITO electrode modified with quantum dots (QD) modifying the photocurrent [183]. The photocurrent signal decreased linearly with the increasing cTnT concentrations from 0.1 to 2 pg mL^{-1}, with a LOD of 0.03 pg mL^{-1} in standard solutions. The details relative to the CuNCs immunoassay-based detection strategies are reported in Table 3. Finally, considering the CuCNs growth on some proteins, carrying suitable characteristics, one may think of simple and direct antibody-free assays. We very recently reported on sensitive and selective Human Serum Albumin (HSA) fluorimetric detection in body fluids, *i.e.*, urine with interest in kidney related diseases. HSA in different matrices was detected, obtaining excellent limits of detection: 2.48 ± 0.07 mg L^{-1} (in H_2O), 1.8 ± 0.1 mg L^{-1} (in human serum) and 0.62 ± 0.03 mg L^{-1} (in urine). This confirms the potentialities of these very powerful nanostructures [97].

3.4. *Ratiometric fluorescent sensing based on CuNCs*

Recently, ratiometric fluorescent methods have attracted growing research interest [185]. Generally, this emerging fluorescent technique exploits double tunable emission characteristics of two fluorescence species [186].

In order to design a ratiometric sensor, a suitable reference probe should be choice [187]. Emerging nanomaterial used for the development of ratiometric fluorescent probe are CuNCs [188]. Generally, the CuNCs-based ratiometric methods take advantage of the combination of CuNCs PL properties with additionally fluorescent species (*e.g.*. dye, QDs, NMs etc.) [189]. The fabrication of ratiometric fluorescent probes usually exploits several photophysical properties including internal charge transfer (ICT), fluorescence resonance energy transfer (FRET), monomer–excimer formation, and excited-state intramolecular proton transfer (ESIPT) [190]. Despite the gain in terms of method accuracy, the reports of ratiometric fluorescent sensor based on CuNCs, are limited. This is probably due to the lack of effective means to tune emission wavelength of the synthesized Cu NCs [191] . However, we report an interesting study on ratiometric fluorescence sensing platform developed by Wang and its collaborators [192]. This work was based on the sensing platform developed in which GSH-CuNCs and o-phenylenediamine was integrated into same device. This label-free fluorescent ratiometric assay allowed very sensitively and simultaneously detection of Cu^{2+} and kojic acid. This method paved the way for future application in real sample analysis closely concerned with human health [192].

4. Biological application of CuNCs

The biocompatibility and the low toxicity of CuNCs enable their application as fluorophores for *in vitro* and *in vivo* biological imaging by using different kinds of templates for the preparation of CuNCs. Numerous works reported blue emitting CuNCs for the labeling of various kinds of cell lines, including human and cancerous cells, as well as microorganism cells [193–195]. In order to verify the compatibility of CuNCs in biological systems, diverse tests were performed in biological samples like blood or serum [99,196]. An interesting study was conducted by Mukherjee's group in which Glutathione (GSH)-CuNCs were employed to perform cell viability and uptake assays on three cancerous cell lines, HeLa (malignant immortal cell line derived from cervical cancer), A549 (human lung carcinoma) and MDAMB-231 (human breast adenocarcinoma) [197]. They demonstrated the low toxicity of CuNCs localizing the nanoclusters close to the nucleus by laser scanning confocal microscopy. The same procedure was followed on *Bacillus subtilis* cells by Kailasa's group for *in vitro* imaging tests [32]. In the last years, great advances in the application of CuNCs combined with *in vivo* imaging strategies, have been reached (Table 4). One of the most innovative research is represented by the synthesis of radioactive BSA-CuNCs conjugated with the Luteinizing Hormone Releasing Hormone (LHRH) whose receptor is overexpressed in some cancer cells such as breast, ovarian, prostate, lung, and hepatic ones. The 64CuNCs@BSA-LHRH structure was thought to be used as a contrast agent for *in vivo* PET imaging and the uptake by tumor cells in a primary lung cancer model [90]. Theranostic applications based on the use of CuNCs are instead more common [6,43]. For example, a hydrogel-based anticancer carrier containing CuNCs and Cisplatin were exploited for mammalian cell uptake monitoring [198]. Moreover, CuNCs was used as a biological dye to stain proteins or oligonucleotides in gel electrophoresis [199] and cells in flow cytometry [200]. Copper, like other noble metals, is known also for its antibacterial properties; therefore, CuNCs were used for their antimicrobial action [201].

5. Conclusions and future perspectives

In this review, we focused on the remarkable progress in the synthesis and use of fluorescent copper nanoclusters combined with different detection strategies. We first evaluated diverse aspects that influence the photoluminescent properties of CuNCs, in particular size, surface ligands, and reaction environment. The synthesis of CuNCs can be effectively controlled by using a template-assisted approach. Nucleic acids, proteins, polymers, peptides, and small molecules are usually employed to reduce copper ions, stabilize and protect the growth of nanoclusters. In particular, nucleic acids, beside being excellent templates, are powerful biological recognition elements for bioanalytical assay development. Here, we discussed the combination of oligonucleotide sequences, as capture probes, and copper nanoclusters in CuNCs DNA-based detection strategies. We at first reported the CuNCs-based assays classified according to the capture probe used (*i.e.*, DNA, aptamer, antibody) and, consequently, we discussed the CuNCs-based assays diversified depending on the transduction element (*i.e.*, electrochemical, photoelectrochemical, colorimetric). Then we analyzed the biological application of copper nanoclusters. Despite the numerous advantages in terms of excellent fluorescent properties, cost effectiveness, selectivity, sensitivity, rapidity in the response, versatility and environmental-benign, the use of CuNCs for analytical applications is mostly unexplored, with a low number of publications about immuno-based or electrochemical-based assays involving CuNCs in the detection strategy. Consequently, this research area offers considerable margins of improvement and new investigations. Firstly, large scale synthesis does not allow to obtain CuNCs with uniform size distribution. This mainly occurs in DNA-CuNCs synthesis where it is necessary to pay more attention to the experimental condition to guarantee a long-term stability of DNA-templated CuNCs. Secondly, the CuNCs formation mechanism on nucleotides template is still unknown. In addition, CuNCs signal can be quenched by many biomolecules and this could influence the system selectivity. Finally, more studies are expected for practical applications. For example, the development of CuNCs-based disposable devices, *i.e.*, paper-based assay systems, as well as the combination of CuNCs with antibody-free biomimetic receptors, such as molecularly imprinted polymers (MIP), could lead to a great advantage in the fast and cost-effective target analyte detection.

Table 4
Biological application of CuNCs.

Application	Template	Target	$\lambda_{ex}/\lambda_{em}$	Sample	Linear range	LOD	Q.Y.	Refs.
In vitro Bioimaging	Lysozyme	–	375/450 nm	HeLa cells, Human blood	–	–	14%	[99]
In vitro Bioimaging	Tannic acid	Fe^{3+}	360/480 nm	Serum and living cell (A549)	10 nM-10 μM	10nM	18%	[196]
In vitro Bioimaging	GSH	Fe^{3+}	340/430 nm	HeLa, A549, MDAMB-231 human cells	10 nM-50 μM	25 nM	6%	[197]
In vitro Bioimaging	Egg white	Thiram and paraquat	340/600 nm	Food samples and *Bacillus subtilis*	0.5- 1000 μM (thiram), 0.2–1000 μM (paraquat)	70 nM (thiram) 49 nM (paraquat)	6.7%	[32]
In vivo Bioimaging	BSA	Orthopedic lung tumor	488/640 nm	Mice, MRC-5 and A549 cells	–	–	–	[90]
Theranostic	PVP	Cisplatin	365/650 nm	HeLa cells	1.5–8.4 mg L^{-1}	–	7.2%	[198]
Biological dye	DNA	DNA	343/584 nm	–	–	–	–	[199]
Flow cytometry	L-cysteine (NCs1) and GSH (NCs2)	Tetracycline	368/493 nm (NCs1) 373/595 nm (NCs2)	HeLa cells	–	5.6 μM (NCs1), 8.4 μM (NCs2)	5.8%–3.6%	[200]
Antimicrobial action	GSH	–	588/488 nm	*E. coli*, DH5α	–	–	1.3×10^{-4}	[201]

Declaration of Competing Interest

The authors declare that they have no known competing financial interests or personal relationships that could have appeared to influence the work reported in this paper.

References

[1] G.E. Giacomazzo, P. Palladino, C. Gellini, G. Salerno, V. Baldoneschi, A. Feis, S. Scarano, M. Minunni, B. Richichi, A straightforward synthesis of phenyl boronic acid (PBA) containing BODIPY dyes: new functional and modular fluorescent tools for the tethering of the glycan domain of antibodies, RSC Adv. 9 (2019) 30773–30777, https://doi.org/10.1039/c9ra07608e.

[2] G. Salerno, S. Scarano, M. Mamusa, M. Consumi, S. Giuntini, A. Macagnano, S. Nativi, M. Fragai, M. Minunni, D. Berti, A. Magnani, C. Nativi, B. Richichi, A small heterobifunctional ligand provides stable and water dispersible core-shell CdSe/ZnS quantum dots (QDs), Nanoscale 10 (2018) 19720–19732, https://doi.org/10.1039/c8nr05566a.

[3] S. Hong, Y.A. Kuo, T.D. Nguyen, Y.I. Chen, Y.L. Liu, P.B. Shankar, H.C. Yeh, D. Fixler, S. Wachsmann-Hogiu, E.M. Goldys, Array-based differential sensing of cancer cells using DNA-templated silver nanoclusters. Nanoscale Imaging, Sensing, and Actuation for Biomedical Applications XVII, SPIE, 2020, p. 34, https://doi.org/10.1117/12.2540132.

[4] D. Sahu, P. Mohapatra, S.K. Swain, Highly orange fluorescence emission by water soluble gold nanoclusters for "turn off" sensing of Hg^{2+} ion, J. Photochem. Photobiol. A Chem. 386 (2020), 112098, https://doi.org/10.1016/j.jphotochem.2019.112098.

[5] P. Vaid, P. Raizada, A.K. Saini, R.V. Saini, Biogenic silver, gold and copper nanoparticles - a sustainable green chemistry approach for cancer therapy, Sustain. Chem. Pharm. 16 (2020), 100247, https://doi.org/10.1016/j.scp.2020.100247.

[6] W.F. Lai, W.T. Wong, A.L. Rogach, Development of copper nanoclusters for *in vitro* and *in vivo* theranostic applications, Adv. Mater. 32 (2020) 1–21, https://doi.org/10.1002/adma.201906872.

[7] Q. Zhang, M. Yang, Y. Zhu, C. Mao, Metallic nanoclusters for cancer imaging and therapy, Curr. Med. Chem. 24 (2017), https://doi.org/10.2174/0929867324666170331122757, 1–1.

[8] M. Zhou, M. Tian, C. Li, Copper-based nanomaterials for cancer imaging and therapy, Bioconjug. Chem. 27 (2016) 1188–1199, https://doi.org/10.1021/acs.bioconjchem.6b00156.

[9] J. Benavides, I. Quijada-Garrido, O. García, The synthesis of switch-off fluorescent water-stable copper nanocluster Hg^{2+} sensors: via a simple one-pot approach by an *in situ* metal reduction strategy in the presence of a thiolated polymer ligand template, Nanoscale 12 (2020) 944–955, https://doi.org/10.1039/c9nr08439h.

[10] K.T. Prakash, N. Singh, V. Venkatesh, Synthesis of novel luminescent copper nanoclusters with substituent driven self-assembly and aggregation induced emission (AIE), Chem. Commun. 55 (2019) 322–325, https://doi.org/10.1039/c8cc09109a.

[11] Z.S. Kardar, F. Shemirani, R. Zadmard, Determination of iron(II) and iron(III) via static quenching of the fluorescence of tryptophan-protected copper nanoclusters, Microchim. Acta 187 (2020) 1–9, https://doi.org/10.1007/s00604-019-4067-4.

[12] Y. Lu, W. Chen, Sub-nanometre sized metal clusters: from synthetic challenges to the unique property discoveries, Chem. Soc. Rev. 41 (2012) 3594–3623, https://doi.org/10.1039/c2cs15325d.

[13] M. Zhao, L. Sun, R.M. Crooks, Preparation of Cu nanoclusters within dendrimer templates, J. Am. Chem. Soc. 120 (1998) 4877–4878, https://doi.org/10.1021/ja980438n.

[14] L. Balogh, D.A. Tomalia, Nanocomposites . 1. Synthesis of zerovalent copper nanoclusters, J. Am. Chem. Soc. 120 (1998) 7355–7356.

[15] X. Hu, T. Liu, Y. Zhuang, W. Wang, Y. Li, W. Fan, Y. Huang, Recent advances in the analytical applications of copper nanoclusters, TrAC Trends Anal. Chem. 77 (2016) 66–75, https://doi.org/10.1016/j.trac.2015.12.013.

[16] A. Rotaru, S. Dutta, E. Jentzsch, K. Gothelf, A. Mokhir, Selective dsDNA-templated formation of copper nanoparticles in solution, Angew. Chem. Int. Ed. 49 (2010) 5665–5667, https://doi.org/10.1002/anie.200907256.

[17] A. Nain, Y.T. Tseng, S.C. Wei, A.P. Periasamy, C.C. Huang, F.G. Tseng, H. T. Chang, Capping 1,3-propanedithiol to boost the antibacterial activity of protein-templated copper nanoclusters, J. Hazard. Mater. 389 (2020), 121821, https://doi.org/10.1016/j.jhazmat.2019.121821.

[18] H. Huang, H. Li, A.J. Wang, S.X. Zhong, K.M. Fang, J.J. Feng, Green synthesis of peptide-templated fluorescent copper nanoclusters for temperature sensing and cellular imaging, Analyst 139 (2014) 6536–6541, https://doi.org/10.1039/c4an01757a.

[19] X. Yang, Y. Feng, S. Zhu, Y. Luo, Y. Zhuo, Y. Dou, One-step synthesis and applications of fluorescent Cu nanoclusters stabilized by L-cysteine in aqueous solution, Anal. Chim. Acta 847 (2014) 49–54, https://doi.org/10.1016/j.aca.2014.07.019.

[20] S. Kolay, D. Bain, S. Maity, A. Devi, A. Patra, R. Antoine, Self-assembled metal nanoclusters: driving forces and structural correlation with optical properties, (2022).

[21] N. Goswami, A. Giri, M.S. Bootharaju, P.L. Xavier, T. Pradeep, S.K. Pal, Copper quantum clusters in protein matrix: potential sensor of Pb^{2+} ion, Anal. Chem. 83 (2011) 9676–9680, https://doi.org/10.1021/ac202610e.

[22] K. Yang, Y. Wang, C. Lu, X. Yang, Ovalbumin-directed synthesis of fluorescent copper nanoclusters for sensing both vitamin B1 and doxycycline, J. Lumin. 196 (2018) 181–186, https://doi.org/10.1016/j.jlumin.2017.12.038.

[23] Z. Cai, H. Li, J. Wu, L. Zhu, X. Ma, C. Zhang, Ascorbic acid stabilised copper nanoclusters as fluorescent sensors for detection of quercetin, RSC Adv. 10 (2020) 8989–8993, https://doi.org/10.1039/d0ra01265c.

[24] S. Chen, Y. Wang, L. Feng, Specific detection and discrimination of dithiocarbamates using CTAB-encapsulated fluorescent copper nanoclusters, Talanta 210 (2020), 120627, https://doi.org/10.1016/j.talanta.2019.120627.

[25] A. Yousefzadeh, J. Hassanzadeh, S.M.J. Mousavi, M. Yousefzadeh, Surface molecular imprinting and powerfully enhanced chemiluminescence emission by Cu nanoclusters/MOF composite for detection of tramadol, Sens. Actuators B Chem. 286 (2019) 154–162, https://doi.org/10.1016/j.snb.2019.01.155.

[26] R.S. Aparna, J.S. Anjali Devi, R.R. Anjana, J. Nebu, S. George, Zn(II) ion modulated red emitting copper nanocluster probe for the fluorescence turn on sensing of RDX, Sens. Actuators B Chem. 291 (2019) 298–305, https://doi.org/10.1016/j.snb.2019.04.051.

[27] C. Wang, Y. Yao, Q. Song, Interfacial synthesis of polyethyleneimine-protected copper nanoclusters: size-dependent tunable photoluminescence, pH sensor and bioimaging, Colloids Surf. B Biointerfaces 140 (2016) 373–381, https://doi.org/10.1016/j.colsurfb.2016.01.001.

[28] Z. Cai, C. Zhang, K. Jia, L-tyrosine protected Cu nanoclusters for reversible pH-sensors, Chem. Pap. 74 (2020) 1831–1838, https://doi.org/10.1007/s11696-019-01027-x.

[29] G. Zhang, T. Xu, H. Du, Y. Qiao, X. Guo, L. Shi, Y. Zhang, S. Shuang, C. Dong, H. Ma, A reversible fluorescent pH-sensing system based on the one-pot synthesis of natural silk fibroin-capped copper nanoclusters, J. Mater. Chem. C 4 (2016) 3540–3545, https://doi.org/10.1039/c6tc00314a.

[30] Y. Cheng, S. Deng, F. Sun, Y.H. Zhou, Synthesis of luminescent Cu 9 S 5 nanoclusters from copper-2,5-dimercapto-1,3,4-thiadiazole coordination polymer as pH sensor, J. Lumin. 210 (2019) 38–46, https://doi.org/10.1016/j.jlumin.2019.02.014.

[31] J. Ye, X. Dong, H. Jiang, X. Wang, An intracellular temperature nanoprobe based on biosynthesized fluorescent copper nanoclusters, J. Mater. Chem. B 5 (2017) 691–696, https://doi.org/10.1039/c6tb02751b.

[32] J.R. Bhamore, S. Jha, A.K. Mungara, R.K. Singhal, D. Sonkeshariya, S.K. Kailasa, One-step green synthetic approach for the preparation of multicolor emitting copper nanoclusters and their applications in chemical species sensing and bioimaging, Biosens. Bioelectron. 80 (2016) 243–248, https://doi.org/10.1016/j.bios.2016.01.066.

[33] X. Gao, X. Zhuang, C. Tian, H. Liu, W.F. Lai, Z. Wang, X. Yang, L. Chen, A. L. Rogach, A copper nanocluster incorporated nanogel: confinement-assisted emission enhancement for zinc ion detection in living cells, Sens. Actuators B Chem. 307 (2020), 127626, https://doi.org/10.1016/j.snb.2019.127626.

[34] T. Qing, K. Zhang, Z. Qing, X. Wang, C. Long, P. Zhang, H. Hu, B. Feng, Recent progress in copper nanocluster-based fluorescent probing: a review, Microchim. Acta (2019) 186, https://doi.org/10.1007/s00604-019-3747-4.

[35] S. Pramanik, L. Khamari, S. Nandi, S. Mukherjee, Discriminating single base pair mismatches in DNA using glutathione-templated copper nanoclusters, J. Phys. Chem. C 123 (2019) 29047–29056, https://doi.org/10.1021/acs.jpcc.9b10069.

[36] X.S. Peng, S.Y. Chen, L.J. Ou, F.W. Luo, S.W. Qin, A.M. Sun, Hairpin loop-enhanced fluorescent copper nanoclusters and application in S1 nuclease detection, Analyst 143 (2018) 415–419, https://doi.org/10.1039/c7an01725a.

[37] A. Mao, C. Wei, Cytosine-rich ssDNA-templated fluorescent silver and copper/silver nanoclusters: optical properties and sensitive detection for mercury(II), Microchim. Acta (2019) 186, https://doi.org/10.1007/s00604-019-3658-4.

[38] Y. An, Y. Ren, M. Bick, A. Dudek, E. Hong-Wang Waworuntu, J. Tang, J. Chen, B. Chang, Highly fluorescent copper nanoclusters for sensing and bioimaging, Biosens. Bioelectron. (2020) 154, https://doi.org/10.1016/j.bios.2020.112078.

[39] S. Shahsavari, S. Hadian-Ghazvini, F. Hooriabad Saboor, I. Menbari Oskouie, M. Hasany, A. Simchi, A.L. Rogach, Ligand functionalized copper nanoclusters for versatile applications in catalysis, sensing, bioimaging, and optoelectronics, Mater. Chem. Front. 3 (2019) 2326–2356, https://doi.org/10.1039/c9qm00492k.

[40] L. Farzin, M. Shamsipur, L. Samandari, S. Sadjadi, S. Sheibani, Biosensing strategies based on organic-scaffolded metal nanoclusters for ultrasensitive detection of tumor markers, Talanta 214 (2020), 120886, https://doi.org/10.1016/j.talanta.2020.120886.

[41] Q. Cao, J. Li, E. Wang, Recent advances in the synthesis and application of copper nanomaterials based on various DNA scaffolds, Biosens. Bioelectron. 132 (2019) 333–342, https://doi.org/10.1016/j.bios.2019.01.046.

[42] R. Gui, H. Jin, X. Bu, Y. Fu, Z. Wang, Q. Liu, Recent advances in dual-emission ratiometric fluorescence probes for chemo/biosensing and bioimaging of biomarkers, Coord. Chem. Rev. 383 (2019) 82–103, https://doi.org/10.1016/j.ccr.2019.01.004.

[43] K.B. Busi, M. Palanivel, K.K. Ghosh, W.B. Ball, B. Gulyás, P. Padmanabhan, S. Chakrabortty, The multifarious applications of copper nanoclusters in biosensing and bioimaging and their translational role in early disease detection, Nanomaterials (2022) 12, https://doi.org/10.3390/nano12030301.

[44] D.M. Wood, N.W. Ashcroft, Quantum size effects in the optical properties of small metallic particles, Phys. Rev. B 25 (1982) 6255–6274, https://doi.org/10.1103/PhysRevB.25.6255.

[45] Z. Wang, B. Chen, A.L. Rogach, Synthesis, optical properties and applications of light-emitting copper nanoclusters, Nanoscale Horiz. 2 (2017) 135–146, https://doi.org/10.1039/c7nh00013h.

[46] M.V. Pavliuk, S. Gutiérrez Álvarez, Y. Hattori, M.E. Messing, J. Czapla-Masztafiak, J. Szlachetko, J.L. Silva, C.M. Araujo, D.L. Fernandes, L. Lu, C. J. Kiely, M. Abdellah, P. Nordlander, J. Sá, Hydrated electron generation by excitation of copper localized surface plasmon resonance, J. Phys. Chem. Lett. 10 (2019) 1743–1749, https://doi.org/10.1021/acs.jpclett.9b00792.

[47] L.V.Q. Garrido, J.M. Gonçalves, J.C. Rocha, E.L. Bastos, H.E. Toma, V. M. Zamarion, Intriguing plasmonic and fluorescence duality in copper nanoparticles, Plasmonics (2020), https://doi.org/10.1007/s11468-020-01143-5.

[48] A. Ziashahabi, T. Ghodselahi, M.H. Saani, Localized surface plasmon resonance properties of copper nano-clusters: a theoretical study of size dependence, J. Phys. Chem. Solids 74 (2013) 929–933, https://doi.org/10.1016/j.jpcs.2013.02.009.

[49] Y.Z. Lu, W.T. Wei, W. Chen, Copper nanoclusters: synthesis, characterization and properties, Chinese Sci. Bull. 57 (2012) 41–47, https://doi.org/10.1007/s11434-011-4896-y.

[50] D. Li, Z. Chen, X. Mei, Fluorescence enhancement for noble metal nanoclusters, Adv. Colloid Interface Sci. 250 (2017) 25–39, https://doi.org/10.1016/j.cis.2017.11.001.

[51] C. Vázquez-Vázquez, M. Bañobre-López, A. Mitra, M.A. López-Quintela, J. Rivas, Synthesis of small atomic copper clusters in microemulsions, Langmuir 25 (2009) 8208–8216, https://doi.org/10.1021/la900100w.

[52] Z. Luo, X. Yuan, Y. Yu, Q. Zhang, D.T. Leong, J.Y. Lee, J. Xie, From aggregation-induced emission of Au(I)-thiolate complexes to ultrabright Au(0)@Au(I)-thiolate core-shell nanoclusters, J. Am. Chem. Soc. 134 (2012) 16662–16670, https://doi.org/10.1021/ja306199p.

[53] Z. Wu, R. Jin, On the ligand's role in the fluorescence of gold nanoclusters, Nano Lett. 10 (2010) 2568–2573, https://doi.org/10.1021/nl101225f.

[54] Z. Wang, A.S. Susha, B. Chen, C. Reckmeier, O. Tomanec, R. Zboril, H. Zhong, A. L. Rogach, Poly(vinylpyrrolidone) supported copper nanoclusters: glutathione enhanced blue photoluminescence for application in phosphor converted light emitting devices, Nanoscale 8 (2016) 7197–7202, https://doi.org/10.1039/c6nr00806b.

[55] M. Cui, G. Song, C. Wang, Q. Song, Synthesis of cysteine-functionalized water-soluble luminescent copper nanoclusters and their application to the determination of chromium(VI), Microchim. Acta 182 (2015) 1371–1377, https://doi.org/10.1007/s00604-015-1458-z.

[56] C. Wang, Y. Huang, Green route to prepare biocompatible and near infrared thiolate-protected copper nanoclusters for cellular imaging, Nano 8 (2013), https://doi.org/10.1142/S1793292013500549.

[57] R. Rajamanikandan, M. Ilanchelian, Red emitting human serum albumin templated copper nanoclusters as effective candidates for highly specific biosensing of bilirubin, Mater. Sci. Eng. C 98 (2019) 1064–1072, https://doi.org/10.1016/j.msec.2019.01.048.

[58] Z. Miao, W. Hou, M. Liu, Y. Zhang, S. Yao, BSA capped bi-functional fluorescent Cu nanoclusters as pH sensor and selective detection of dopamine, New J. Chem. 42 (2018) 1446–1456, https://doi.org/10.1039/c7nj03524a.

[59] J. Feng, Y. Chen, Y. Han, J. Liu, S. Ma, H. Zhang, X. Chen, PH-Regulated synthesis of trypsin-templated copper nanoclusters with blue and yellow fluorescent emission, ACS Omega 2 (2017) 9109–9117, https://doi.org/10.1021/acsomega.7b01052.

[60] W. Wang, F. Leng, L. Zhan, Y. Chang, X.X. Yang, J. Lan, C.Z. Huang, One-step prepared fluorescent copper nanoclusters for reversible pH-sensing, Analyst 139 (2014) 2990–2993, https://doi.org/10.1039/c4an00113c.

[61] C. Wang, C. Wang, L. Xu, H. Cheng, Q. Lin, C. Zhang, Protein-directed synthesis of pH-responsive red fluorescent copper nanoclusters and their applications in cellular imaging and catalysis, Nanoscale 6 (2014) 1775–1781, https://doi.org/10.1039/c3nr04835g.

[62] J. Yuan, L. Wang, Y. Wang, J. Hao, Stimuli-responsive fluorescent nanoswitches: solvent-induced emission enhancement of copper nanoclusters, Chem. A Eur. J. 26 (2020) 3545–3554, https://doi.org/10.1002/chem.201905094.

[63] Y. Ling, J.J. Wu, Z.F. Gao, N.B. Li, H.Q. Luo, Enhanced emission of polyethyleneimine-coated copper nanoclusters and their solvent effect, J. Phys. Chem. C 119 (2015) 27173–27177, https://doi.org/10.1021/acs.jpcc.5b09488.

[64] N. Vilar-Vidal, M.C. Blanco, M.A. López-Quintela, J. Rivas, C. Serra, Electrochemical synthesis of very stable photoluminescent copper clusters, J. Phys. Chem. C (2010) 15924–15930, https://doi.org/10.1021/jp911380s. American Chemical Society.

[65] A. Han, L. Xiong, S. Hao, Y. Yang, X. Li, G. Fang, J. Liu, Y. Pei, S. Wang, Highly bright self-assembled copper nanoclusters: a novel photoluminescent probe for sensitive detection of histamine, Anal. Chem. 90 (2018) 9060–9067, https://doi.org/10.1021/acs.analchem.8b01384.

[66] H.H. Deng, K.L. Li, Q.Q. Zhuang, H.P. Peng, Q.Q. Zhuang, A.L. Liu, X.H. Xia, W. Chen, An ammonia-based etchant for attaining copper nanoclusters with green fluorescence emission, Nanoscale 10 (2018) 6467–6473, https://doi.org/10.1039/c7nr09449c.

[67] N.K. Das, S. Mukherjee, Size-controlled atomically precise copper nanoclusters: synthetic protocols, spectroscopic properties and applications, Phys. Sci. Rev. 3 (2018) 1–22, https://doi.org/10.1515/psr-2017-0081.

[68] S. Huseyinova, J. Blanco, F.G. Requejo, J.M. Ramallo-López, M.C. Blanco, D. Buceta, M.A. López-Quintela, Synthesis of highly stable surfactant-free Cu5 clusters in water, J. Phys. Chem. C 120 (2016) 15902–15908, https://doi.org/10.1021/acs.jpcc.5b12227.

[69] C. Wang, H. Cheng, Y. Sun, Q. Lin, C. Zhang, Rapid sonochemical synthesis of luminescent and paramagnetic copper nanoclusters for bimodal bioimaging, ChemNanoMat 1 (2015) 27–31, https://doi.org/10.1002/cnma.201500004.

[70] R. Gui, J. Sun, X. Cao, Y. Wang, H. Jin, Multidentate polymers stabilized water-dispersed copper nanoclusters: facile photoreduction synthesis and selective fluorescence turn-on response, RSC Adv. 4 (2014) 29083–29088, https://doi.org/10.1039/c4ra03606a.

[71] R. Rajamanikandan, M. Ilanchelian, Protein-protected red emittive copper nanoclusters as a fluorometric probe for highly sensitive biosensing of creatinine, Anal. Methods 10 (2018) 3666–3674, https://doi.org/10.1039/c8ay00827b.

[72] D. Zhang, Y. Fang, Z. Miao, M. Ma, X. Du, S. Takahashi, J.I. Anzai, Q. Chen, Direct electrodeposition of reduced graphene oxide and dendritic copper nanoclusters on glassy carbon electrode for electrochemical detection of nitrite, Electrochim. Acta 107 (2013) 656–663, https://doi.org/10.1016/j.electacta.2013.06.015.

[73] C. Wang, H. Cheng, Y. Huang, Z. Xu, H. Lin, C. Zhang, Facile sonochemical synthesis of pH-responsive copper nanoclusters for selective and sensitive detection of Pb^{2+} in living cells, Analyst 140 (2015) 5634–5639, https://doi.org/10.1039/c5an00741k.

[74] C.A. Chen, C.C. Wang, Y.J. Jong, S.M. Wu, Label-free fluorescent copper nanoclusters for genotyping of deletion and duplication of duchenne muscular dystrophy, Anal. Chem. 87 (2015) 6228–6232, https://doi.org/10.1021/acs.analchem.5b00918.

[75] N. Russo, M. Toscano, A. Grand, Gas-phase theoretical prediction of the metal affinity of copper(I) ion for DNA and RNA bases, J. Mass Spectrom. 38 (2003) 265–270, https://doi.org/10.1002/jms.436.

[76] X. Wang, P. Hu, Z. Wang, Q. Liu, T. Xu, M. Kou, K. Huang, P. Chen, A fluorescence strategy for silver ion assay via cation exchange reaction and formation of poly

(thymine)-templated copper nanoclusters, Anal. Sci. 35 (2019) 917–922, https://doi.org/10.2116/analsci.19P036.

[77] X. Bu, Y. Fu, X. Jiang, H. Jin, R. Gui, Self-assembly of DNA-templated copper nanoclusters and carbon dots for ratiometric fluorometric and visual determination of arginine and acetaminophen with a logic-gate operation, Microchim. Acta (2020) 187, https://doi.org/10.1007/s00604-020-4146-6.

[78] B. Han, R. Xiang, X. Hou, M. Yu, T. Peng, Y. Li, G. He, One-step rapid synthesis of single thymine-templated fluorescent copper nanoclusters for "turn on" detection of Mn^{2+}, Anal. Methods 9 (2017) 2590–2595, https://doi.org/10.1039/c7ay00625j.

[79] H. Zhao, J. Dong, F. Zhou, B. Li, One facile fluorescence strategy for sensitive detection of endonuclease activity using DNA-templated copper nanoclusters as signal indicators, Sens. Actuators B Chem. 238 (2017) 828–833, https://doi.org/10.1016/j.snb.2016.07.083.

[80] J. Pang, Y. Lu, X. Gao, L. He, J. Sun, F. Yang, Z. Hao, Y. Liu, DNA-templated copper nanoclusters as a fluorescent probe for fluoride by using aluminum ions as a bridge, Microchim. Acta 186 (2019) 1–9, https://doi.org/10.1007/s00604-019-3468-8.

[81] X.G. Li, F. Zhang, Y. Gao, Q.M. Zhou, Y. Zhao, Y. Li, J.Z. Huo, X.J. Zhao, Facile synthesis of red emitting 3-aminophenylboronic acid functionalized copper nanoclusters for rapid, selective and highly sensitive detection of glycoproteins, Biosens. Bioelectron. 86 (2016) 270–276, https://doi.org/10.1016/j.bios.2016.06.054.

[82] C. Muñoz-Bustos, A. Tirado-Guízar, F. Paraguay-Delgado, G. Pina-Luis, Copper nanoclusters-coated BSA as a novel fluorescence sensor for sensitive and selective detection of mangiferin, Sens. Actuators B Chem. 244 (2017) 922–927, https://doi.org/10.1016/j.snb.2017.01.071.

[83] G. Liu, W. He, C. Liu, Sensitive detection of uracil-DNA glycosylase (UDG) activity based on terminal deoxynucleotidyl transferase-assisted formation of fluorescent copper nanoclusters (CuNCs), Talanta 195 (2019) 320–326, https://doi.org/10.1016/j.talanta.2018.11.083.

[84] J. Cao, W. Wang, B. Bo, X. Mao, K. Wang, X. Zhu, A dual-signal strategy for the solid detection of both small molecules and proteins based on magnetic separation and highly fluorescent copper nanoclusters, Biosens. Bioelectron. 90 (2017) 534–541, https://doi.org/10.1016/j.bios.2016.10.021.

[85] S. Lisi, E. Fiore, S. Scarano, E. Pascale, Y. Boehman, F. Ducongé, S. Chierici, M. Minunni, E. Peyrin, C. Ravelet, Non-SELEX isolation of DNA aptamers for the homogeneous-phase fluorescence anisotropy sensing of tau proteins, Anal. Chim. Acta 1038 (2018) 173–181, https://doi.org/10.1016/j.aca.2018.07.029.

[86] S. Tombelli, M. Minunni, M. Mascini, Analytical applications of aptamers, Biosens. Bioelectron. 20 (2005) 2424–2434, https://doi.org/10.1016/J.BIOS.2004.11.006.

[87] C.A. Chen, C.C. Wang, Y.J. Jong, S.M. Wu, Label-free fluorescent copper nanoclusters for genotyping of deletion and duplication of Duchenne muscular dystrophy, Anal. Chem. 87 (2015) 6228–6232, https://doi.org/10.1021/acs.analchem.5b00918.

[88] T. Lalic, R.H.A.M. Vossen, J. Coffa, J.P. Schouten, M. Guc-Scekic, D. Radivojevic, M. Djurisic, M.H. Breuning, S.J. White, J.T. den Dunnen, Deletion and duplication screening in the DMD gene using MLPA, Eur. J. Hum. Genet. 13 (2005) 1231–1234, https://doi.org/10.1038/sj.ejhg.5201465.

[89] Y.L. Ankur Choksi, X. Zhang, G. Seong Heo, H. Luehmanna, Synthesis of temozolomide loaded copper nanoclusters for glioblastoma multiforme theranostics, (n.d.). http://jnm.snmjournals.org/content/59/supplement_1/1122.short (accessed August 5, 2020).

[90] F. Gao, P. Cai, W. Yang, J. Xue, L. Gao, R. Liu, Y. Wang, Y. Zhao, X. He, L. Zhao, G. Huang, F. Wu, Y. Zhao, Z. Chai, X. Gao, Ultrasmall [64Cu]Cu nanoclusters for targeting orthotopic lung tumors using accurate positron emission tomography imaging, ACS Nano 9 (2015) 4976–4986, https://doi.org/10.1021/nn507130k.

[91] Z. Yan, Q. Niu, M. Mou, Y. Wu, X. Liu, S. Liao, A novel colorimetric method based on copper nanoclusters with intrinsic peroxidase-like for detecting xanthine in serum samples, J. Nanoparticle Res. (2017) 19, https://doi.org/10.1007/s11051-017-3904-9.

[92] L. Xiaoqing, L. Ruiyia, L. Zaijun, Ultra sensitive and wide-range pH sensor based on the BSA-capped Cu nanoclusters fabricated by fast synthesis through the use of hydrogen peroxide additive, RSC Adv. 10 (2015) 2–8.

[93] C. Wang, C. Wang, L. Xu, H. Cheng, Q. Lin, C. Zhang, Protein-directed synthesis of pH-responsive red fluorescent copper nanoclusters and their applications in cellular imaging and catalysis, Nanoscale 6 (2014) 1775–1781, https://doi.org/10.1039/c3nr04835g.

[94] M. Chen, W. Li, H. Xiong, W. Wen, X. Zhang, S. Wang, Discrimination and ultrasensitive detection of β 2-agonists using copper nanoclusters as a fluorescent probe, Microchim. Acta 184 (2017) 3317–3324, https://doi.org/10.1007/s00604-017-2357-2.

[95] H.B. Wang, Y. Chen, N. Li, Y.M. Liu, A fluorescent glucose bioassay based on the hydrogen peroxide-induced decomposition of a quencher system composed of MnO2 nanosheets and copper nanoclusters, Microchim. Acta 184 (2017) 515–523, https://doi.org/10.1007/s00604-016-2045-7.

[96] S. Ghosh, N.K. Das, U. Anand, S. Mukherjee, Photostable copper nanoclusters: compatible Förster resonance energy-transfer assays and a nanothermometer, J. Phys. Chem. Lett. 6 (2015) 1293–1298, https://doi.org/10.1021/acs.jpclett.5b00378.

[97] M. Lettieri, P. Palladino, S. Scarano, M. Minunni, Protein-templated copper nanoclusters for fluorimetric determination of human serum albumin, Mikrochim. Acta 188 (2021) 116, https://doi.org/10.1007/s00604-021-04764-7.

[98] C. Wang, S. Shu, Y. Yao, Q. Song, A fluorescent biosensor of lysozyme-stabilized copper nanoclusters for the selective detection of glucose, RSC Adv. 5 (2015) 101599–101606, https://doi.org/10.1039/c5ra19421k.

[99] R. Ghosh, A.K. Sahoo, S.S. Ghosh, A. Paul, A. Chattopadhyay, Blue-emitting copper nanoclusters synthesized in the presence of lysozyme as candidates for cell labeling, ACS Appl. Mater. Interfaces 6 (2014) 3822–3828, https://doi.org/10.1021/am500040t.

[100] X. Li, X. Wu, F. Zhang, B. Zhao, Y. Li, Label-free detection of folic acid using a sensitive fluorescent probe based on ovalbumin stabilized copper nanoclusters, Talanta 195 (2019) 372–380, https://doi.org/10.1016/j.talanta.2018.11.067.

[101] H. Miao, D. Zhong, Z. Zhou, X. Yang, Papain-templated Cu nanoclusters: assaying and exhibiting dramatic antibacterial activity cooperating with H_2O_2, Nanoscale 7 (2015) 19066–19072, https://doi.org/10.1039/c5nr05362e.

[102] Q. Tan, J. Qiao, R. Zhang, L. Qi, Copper nanoclusters-modified with papaya juice for fluorescence turn-on detection of serum L-histidine today four files of proofs was sent to m.saksena@elsevier.com Please check the files, Microchem. J. 153 (2020) 2–7, https://doi.org/10.1016/j.microc.2019.104333.

[103] T. Zhao, X.W. He, W.Y. Li, Y.K. Zhang, Transferrin-directed preparation of red-emitting copper nanoclusters for targeted imaging of transferrin receptor over-expressed cancer cells, J. Mater. Chem. B 3 (2015) 2388–2394, https://doi.org/10.1039/c4tb02130d.

[104] T. Tang, J. Ouyang, L. Hu, L. Guo, M. Yang, X. Chen, Synthesis of peptide templated copper nanoclusters for fluorometric determination of Fe(III) in human serum, Microchim. Acta 183 (2016) 2831–2836, https://doi.org/10.1007/s00604-016-1935-z.

[105] Y. Wang, Y. Cui, R. Liu, Y. Wei, X. Jiang, H. Zhu, L. Gao, Y. Zhao, Z. Chai, X. Gao, Blue two-photon fluorescence metal cluster probe precisely marking cell nuclei of two cell lines, Chem. Commun. 49 (2013) 10724–10726, https://doi.org/10.1039/c3cc46690f.

[106] B. Rodrigues, P. Shende, Monodispersed metal-based dendrimeric nanoclusters for potentiation of anti-tuberculosis action, J. Mol. Liq. 304 (2020), 112731, https://doi.org/10.1016/j.molliq.2020.112731.

[107] T. Li, Z. Wang, D. Jiang, H. Wang, W.F. Lai, Y. Lv, Y. Zhai, A FRET biosensor based on MnO_2 nanosphere/copper nanocluster complex: from photoluminescence quenching to recovery and magnification, Sens. Actuators B Chem. 290 (2019) 535–543, https://doi.org/10.1016/j.snb.2019.04.033.

[108] J. Feng, Y. Ju, J. Liu, H. Zhang, X. Chen, Polyethyleneimine-templated copper nanoclusters via ascorbic acid reduction approach as ferric ion sensor, Anal. Chim. Acta 854 (2015) 153–160, https://doi.org/10.1016/j.aca.2014.11.024.

[109] Z. Wang, Y. Xiong, S.V. Kershaw, B. Chen, X. Yang, N. Goswami, W.F. Lai, J. Xie, A.L. Rogach, *In situ* fabrication of flexible, thermally stable, large-area, strongly luminescent copper nanocluster/polymer composite films, Chem. Mater. 29 (2017) 10206–10211, https://doi.org/10.1021/acs.chemmater.7b04239.

[110] S. Gou, Y.E. Shi, P. Li, H. Wang, T. Li, X. Zhuang, W. Li, Z. Wang, Stimuli-responsive luminescent copper nanoclusters in alginate and their sensing ability for glucose, ACS Appl. Mater. Interfaces (2019), https://doi.org/10.1021/acsami.8b20835.

[111] R. Patel, S. Bothra, R. Kumar, G. Crisponi, S.K. Sahoo, Pyridoxamine driven selective turn-off detection of picric acid using glutathione stabilized fluorescent copper nanoclusters and its applications with chemically modified cellulose strips, Biosens. Bioelectron. 102 (2018) 196–203, https://doi.org/10.1016/j.bios.2017.11.031.

[112] A. Dutta, U. Goswami, A. Chattopadhyay, Probing cancer cells through intracellular aggregation-induced emission kinetic rate of copper nanoclusters, ACS Appl. Mater. Interfaces 10 (2018) 19459–19472, https://doi.org/10.1021/acsami.8b05160.

[113] Y. Nerthigan, A.K. Sharma, S. Pandey, H.F. Wu, Cysteine capped copper/molybdenum bimetallic nanoclusters for fluorometric determination of methotrexate via the inner filter effect, Microchim. Acta (2019) 186, https://doi.org/10.1007/s00604-019-3230-2.

[114] H.B. Wang, B.B. Tao, N.N. Wu, H.D. Zhang, Y.M. Liu, Glutathione-stabilized copper nanoclusters mediated-inner filter effect for sensitive and selective determination of p-nitrophenol and alkaline phosphatase activity, Spectrochim. Acta Part A Mol. Biomol. Spectrosc. 271 (2022), 120948, https://doi.org/10.1016/j.saa.2022.120948.

[115] Y. Huang, H. Feng, W. Liu, S. Zhang, C. Tang, J. Chen, Z. Qian, Cation-driven luminescent self-assembled dots of copper nanoclusters with aggregation-induced emission for β-galactosidase activity monitoring, J. Mater. Chem. B 5 (2017) 5120–5127, https://doi.org/10.1039/c7tb00901a.

[116] R. Jalili, A. Khataee, Aluminum(III) triggered aggregation-induced emission of glutathione-capped copper nanoclusters as a fluorescent probe for creatinine, Microchim. Acta (2019) 186, https://doi.org/10.1007/s00604-018-3111-0.

[117] Y. Wang, T. Chen, Z. Zhang, Y. Ni, Cytidine-stabilized copper nanoclusters as a fluorescent probe for sensing of copper ions and hemin, RSC Adv. 8 (2018) 9057–9062, https://doi.org/10.1039/c7ra11383h.

[118] Z. Li, S. Guo, C. Lu, A highly selective fluorescent probe for sulfide ions based on aggregation of Cu nanocluster induced emission enhancement, Analyst 140 (2015) 2719–2725, https://doi.org/10.1039/c5an00017c.

[119] Y. Hu, Y. He, Y. Han, Y. Ge, G. Song, J. Zhou, Determination of the activity of alkaline phosphatase based on aggregation-induced quenching of the fluorescence of copper nanoclusters, Microchim. Acta (2019) 186, https://doi.org/10.1007/s00604-018-3122-x.

[120] Y.S. Borghei, M. Hosseini, M. Khoobi, M.R. Ganjali, Novel fluorometric assay for detection of cysteine as a reducing agent and template in formation of copper nanoclusters, J. Fluoresc. 27 (2017) 529–536, https://doi.org/10.1007/s10895-016-1980-3.

[121] H.B. Wang, B.B. Tao, A.L. Mao, Z.L. Xiao, Y.M. Liu, Self-assembled copper nanoclusters structure-dependent fluorescent enhancement for sensitive determination of tetracyclines by the restriction intramolecular motion, Sens. Actuators B Chem. 348 (2021), 130729, https://doi.org/10.1016/j.snb.2021.130729.

[122] L. Farzin, M. Shamsipur, L. Samandari, S. Sheibani, HIV biosensors for early diagnosis of infection: the intertwine of nanotechnology with sensing strategies, Talanta 206 (2020), 120201, https://doi.org/10.1016/j.talanta.2019.120201.

[123] J. Li, S. Zhang, Y. Yu, Y. Wang, L. Zhang, B. Lin, M. Guo, Y. Cao, A novel universal nanoplatform for ratiometric fluorescence biosensing based on silver nanoclusters beacon, Chem. Eng. J. (2019), 123526, https://doi.org/10.1016/j.cej.2019.123526.

[124] Y. Zhang, C. Zhang, C. Xu, X. Wang, C. Liu, G.I.N. Waterhouse, Y. Wang, H. Yin, Ultrasmall Au nanoclusters for biomedical and biosensing applications: a mini-review, Talanta 200 (2019) 432–442, https://doi.org/10.1016/j.talanta.2019.03.068.

[125] Y. Liu, P. Dong, Q. Jiang, F. Wang, D.W. Pang, X. Liu, Assembly-enhanced fluorescence from metal nanoclusters and quantum dots for highly sensitive biosensing, Sens. Actuators B Chem. 279 (2019) 334–341, https://doi.org/10.1016/j.snb.2018.10.016.

[126] Z. Liu, X. Jing, S. Zhang, Y. Tian, A copper nanocluster-based fluorescent probe for real-time imaging and ratiometric biosensing of calcium ions in neurons, Anal. Chem. 91 (2019) 2488–2497, https://doi.org/10.1021/acs.analchem.8b05360.

[127] L.C. Brazaca, L. Ribovski, B.C. Janegitz, V. Zucolotto, Nanostructured materials and nanoparticles for point of care (POC) medical biosensors, Med. Biosens. Point Care Appl. (2017) 229–254, https://doi.org/10.1016/B978-0-08-100072-4.00010-1.

[128] D. Quesada-González, A. Merkoçi, Nanomaterial-based devices for point-of-care diagnostic applications, Chem. Soc. Rev. 47 (2018) 4697–4709, https://doi.org/10.1039/c7cs00837f.

[129] L. Bezinge, A. Suea-Ngam, A.J. Demello, C.J. Shih, Nanomaterials for molecular signal amplification in electrochemical nucleic acid biosensing: recent advances and future prospects for point-of-care diagnostics, Mol. Syst. Des. Eng. 5 (2020) 49–66, https://doi.org/10.1039/c9me00135b.

[130] V. Baldoneschi, P. Palladino, S. Scarano, M. Minunni, Polynorepinephrine: state-of-the-art and perspective applications in biosensing and molecular recognition, Anal. Bioanal. Chem. (2020) 5945–5954, https://doi.org/10.1007/s00216-020-02578-9.

[131] F. Torrini, P. Palladino, A. Brittoli, V. Baldoneschi, M. Minunni, S. Scarano, Characterization of troponin T binding aptamers for an innovative enzyme-linked oligonucleotide assay (ELONA), Anal. Bioanal. Chem. 411 (2019) 7709–7716, https://doi.org/10.1007/s00216-019-02014-7.

[132] P. Palladino, A. Brittoli, E. Pascale, M. Minunni, S. Scarano, Colorimetric determination of total protein content in serum based on the polydopamine/protein adsorption competition on microplates, Talanta 198 (2019) 15–22, https://doi.org/10.1016/j.talanta.2019.01.095.

[133] R. Liu, C. Wang, J. Hu, Y. Su, Y. Lv, DNA-templated copper nanoparticles: versatile platform for label-free bioassays, TrAC Trends Anal. Chem. 105 (2018) 436–452, https://doi.org/10.1016/j.trac.2018.06.003.

[134] X.P. Wang, B.C. Yin, B.C. Ye, A novel fluorescence probe of dsDNA-templated copper nanoclusters for quantitative detection of microRNAs, RSC Adv. 3 (2013) 8633–8636, https://doi.org/10.1039/c3ra23296d.

[135] Y. Li, D. Tang, L. Zhu, J. Cai, C. Chu, J. Wang, M. Xia, Z. Cao, H. Zhu, Label-free detection of miRNA cancer markers based on terminal deoxynucleotidyl transferase-induced copper nanoclusters, Anal. Biochem. 585 (2019), 113346, https://doi.org/10.1016/j.ab.2019.113346.

[136] Y.S. Borghei, M. Hosseini, M.R. Ganjali, S. Hosseinkhani, Label-free fluorescent detection of microRNA-155 based on synthesis of hairpin DNA-templated copper nanoclusters by etching (top-down approach), Sens. Actuators B Chem. 248 (2017) 133–139, https://doi.org/10.1016/j.snb.2017.03.148.

[137] K.M. Koo, L.G. Carrascosa, M. Trau, DNA-directed assembly of copper nanoblocks with inbuilt fluorescent and electrochemical properties: application in simultaneous amplification-free analysis of multiple RNA species, Nano Res. 11 (2018) 940–952, https://doi.org/10.1007/s12274-017-1706-0.

[138] X. Jia, J. Li, L. Han, J. Ren, X. Yang, E. Wang, DNA-hosted copper nanoclusters for fluorescent identification of single nucleotide polymorphisms, ACS Nano 6 (2012) 3311–3317, https://doi.org/10.1021/nn3002455.

[139] C. Chen, C. Wang, H. Kou, S. Wu, Molecular inversion probe-rolling circle amplification with single-strand poly-T luminescent copper nanoclusters for fluorescent detection of single-nucleotide variant of SMN gene in diagnosis of spinal muscular atrophy, Anal. Chim. Acta (2020), https://doi.org/10.1016/j.aca.2020.04.026.

[140] S. Singh, M.K. Singh, P. Das, Biosensing of solitary and clustered abasic site DNA damage lesions with copper nanoclusters and carbon dots, Sens. Actuators B Chem. 255 (2018) 763–774, https://doi.org/10.1016/j.snb.2017.08.100.

[141] Y. Wang, T. Chen, Q. Zhuang, Y. Ni, One-pot aqueous synthesis of nucleoside-templated fluorescent copper nanoclusters and their application for discrimination of nucleosides, ACS Appl. Mater. Interfaces 9 (2017) 32135–32141, https://doi.org/10.1021/acsami.7b09768.

[142] T. Qing, C. Long, X. Wang, K. Zhang, P. Zhang, B. Feng, Detection of micrococcal nuclease for identifying Staphylococcus aureus based on DNA templated fluorescent copper nanoclusters, Microchim. Acta (2019) 186, https://doi.org/10.1007/s00604-019-3363-3.

[143] G. Liu, W. He, C. Liu, Sensitive detection of uracil-DNA glycosylase (UDG) activity based on terminal deoxynucleotidyl transferase-assisted formation of fluorescent copper nanoclusters (CuNCs), Talanta 195 (2019) 320–326, https://doi.org/10.1016/j.talanta.2018.11.083.

[144] Y. Ling, J. Zhou, X.F. Zhang, X.H. Wang, N.B. Li, H.Q. Luo, A ratiometric fluorescent sensor for sensitive detection of UDG using poly(thymine)-templated copper nanoclusters and DAPI with exonuclease III assisted amplification, Sens. Actuators B Chem. 286 (2019) 46–51, https://doi.org/10.1016/j.snb.2019.01.108.

[145] M. Cao, Y. Jin, B. Li, Simple and sensitive detection of uracil-DNA glycosylase activity using dsDNA-templated copper nanoclusters as fluorescent probes, Anal. Methods 8 (2016) 4319–4323, https://doi.org/10.1039/c6ay00900j.

[146] D. Gao, H. Zhang, Y. Xu, Y. Liu, H. Xu, J. Cui, Fluorescent copper nanoclusters as a nano-dye for DNA methyltransferase activity analysis and inhibitor screening, Anal. Biochem. 559 (2018) 5–10, https://doi.org/10.1016/j.ab.2018.08.011.

[147] F. Zhou, X. Cui, A. Shang, J. Lian, L. Yang, Y. Jin, B. Li, Fluorometric determination of the activity and inhibition of terminal deoxynucleotidyl transferase via *in-situ* formation of copper nanoclusters using enzymatically generated DNA as template, Microchim. Acta 184 (2017) 773–779, https://doi.org/10.1007/s00604-016-2065-3.

[148] H. Zhang, Y. Guan, X. Li, L. Lian, X. Wang, W. Gao, B. Zhu, X. Liu, D. Lou, Ultrasensitive biosensor for detection of mercury(II) ions based on DNA-Cu nanoclusters and exonuclease III-assisted signal amplification, Anal. Sci. 34 (2018) 1155–1161, https://doi.org/10.2116/analsci.18P124.

[149] Z. Gu, Z. Cao, Molecular switch-modulated fluorescent copper nanoclusters for selective and sensitive detection of histidine and cysteine, Anal. Bioanal. Chem. 410 (2018) 4991–4999, https://doi.org/10.1007/s00216-018-1149-9.

[150] H. Li, J. Chang, T. Hou, L. Ge, F. Li, A facile, sensitive, and highly specific trinitrophenol assay based on target-induced synergetic effects of acid induction and electron transfer towards DNA-templated copper nanoclusters, Talanta 160 (2016) 475–480, https://doi.org/10.1016/j.talanta.2016.07.030.

[151] C. Ma, M. Chen, H. Liu, K. Wu, H. He, K. Wang, A rapid method for the detection of humic acid based on the poly(thymine)-templated copper nanoparticles, Chin. Chem. Lett. 29 (2018) 136–138, https://doi.org/10.1016/j.cclet.2017.09.012.

[152] H.B. Wang, Y. Li, H.Y. Bai, Y.M. Liu, Fluorescent determination of dopamine using polythymine-templated copper nanoclusters, Anal. Lett. 51 (2018) 2868–2877, https://doi.org/10.1080/00032719.2018.1454457.

[153] X. Wang, C. Long, Z. Jiang, T. Qing, K. Zhang, P. Zhang, B. Feng, *In situ* synthesis of fluorescent copper nanoclusters for rapid detection of ascorbic acid in biological samples, Anal. Methods 11 (2019) 4580–4585, https://doi.org/10.1039/c9ay01627a.

[154] Y. Xiong, B. Gao, K. Wu, Y. Wu, Y. Chai, X. Huang, Y. Xiong, Fluorescence immunoassay based on the enzyme cleaving ss-DNA to regulate the synthesis of histone-ds-poly(AT) templated copper nanoparticles, Nanoscale 10 (2018) 19890–19897, https://doi.org/10.1039/c8nr06175k.

[155] X. Zhang, Q. Liu, Y. Jin, B. Li, Determination of the activity of T4 polynucleotide kinase phosphatase by exploiting the sequence-dependent fluorescence of DNA-templated copper nanoclusters, Microchim. Acta 186 (2019) 1–9, https://doi.org/10.1007/s00604-018-3102-1.

[156] Y. Hu, Q. Zhang, L. Xu, J. Wang, J. Rao, Z. Guo, S. Wang, Signal-on electrochemical assay for label-free detection of TdT and BamHI activity based on grown DNA nanowire-templated copper nanoclusters, Anal. Bioanal. Chem. 409 (2017) 6677–6688, https://doi.org/10.1007/s00216-017-0623-0.

[157] H. Liao, Y. Zhou, Y. Chai, R. Yuan, An ultrasensitive electrochemiluminescence biosensor for detection of MicroRNA by *in-situ* electrochemically generated copper nanoclusters as luminophore and TiO_2 as coreaction accelerator, Biosens. Bioelectron. 114 (2018) 10–14, https://doi.org/10.1016/j.bios.2018.05.011.

[158] Y. Zhou, H. Wang, H. Zhang, Y. Chai, R. Yuan, Programmable modulation of copper nanoclusters electrochemiluminescence via DNA nanocranes for ultrasensitive detection of microRNA, Anal. Chem. 90 (2018) 3543–3549, https://doi.org/10.1021/acs.analchem.7b05402.

[159] Y.S. Borghei, M. Hosseini, M.R. Ganjali, Visual detection of miRNA using peroxidase-like catalytic activity of DNA-CuNCs and methylene blue as indicator, Clin. Chim. Acta 483 (2018) 119–125, https://doi.org/10.1016/j.cca.2018.04.031.

[160] X. Mao, S. Liu, C. Yang, F. Liu, K. Wang, G. Chen, Colorimetric detection of hepatitis B virus (HBV) DNA based on DNA-templated copper nanoclusters, Anal. Chim. Acta 909 (2016) 101–108, https://doi.org/10.1016/j.aca.2016.01.009.

[161] M. Chen, Z. Ning, K. Chen, Y. Zhang, Y. Shen, Recent advances of electrochemiluminescent system in bioassay, J. Anal. Test. 4 (2020) 57–75, https://doi.org/10.1007/s41664-020-00136-x.

[162] R.S. Aparna, J.S. Anjali Devi, P. Sachidanandan, S. George, Polyethylene imine capped copper nanoclusters- fluorescent and colorimetric onsite sensor for the trace level detection of TNT, Sens. Actuators B Chem. 254 (2018) 811–819, https://doi.org/10.1016/j.snb.2017.07.097.

[163] P.X. Yuan, S.Y. Deng, C.Y. Zheng, S. Cosnier, D. Shan, *In situ* formed copper nanoparticles templated by TdT-mediated DNA for enhanced SPR sensor-based DNA assay, Biosens. Bioelectron. 97 (2017) 1–7, https://doi.org/10.1016/j.bios.2017.05.033.

[164] C.G. Pheeney, J.K. Barton, DNA electrochemistry with tethered methylene blue, Langmuir 28 (2012) 7063–7070, https://doi.org/10.1021/la300566x.

[165] S. Mariani, S. Scarano, J. Spadavecchia, M. Minunni, A reusable optical biosensor for the ultrasensitive and selective detection of unamplified human genomic DNA with gold nanostars, Biosens. Bioelectron. 74 (2015) 981–988, https://doi.org/10.1016/j.bios.2015.07.071.

[166] S. Mariani, S. Scarano, M.L. Ermini, M. Bonini, M. Minunni, Investigating nanoparticle properties in plasmonic nanoarchitectures with DNA by surface

plasmon resonance imaging, Chem. Commun. 51 (2015) 6587–6590, https://doi.org/10.1039/c4cc09889g.
[167] M. Calcagno, R. D'Agata, G. Breveglieri, M. Borgatti, N. Bellassai, R. Gambari, G. Spoto, Nanoparticle-enhanced surface plasmon resonance imaging enables the ultrasensitive detection of non-amplified cell-free fetal DNA for non-invasive prenatal testing, Anal. Chem. 94 (2022) 1118–1125, https://doi.org/10.1021/acs.analchem.1c04196.
[168] C. Lee, J. Gang, Label-free rapid and simple detection of exonuclease III activity with DNA-templated copper nanoclusters, J. Microbiol. Biotechnol. 28 (2018) 1467–1472.
[169] Y. Seok Kim, N.H. Ahmad Raston, M. Bock Gu, Aptamer-based nanobiosensors, Biosens. Bioelectron. 76 (2016) 2–19, https://doi.org/10.1016/j.bios.2015.06.040.
[170] B. Zhang, C. Wei, The sensitive detection of ATP and ADA based on turn-on fluorescent copper/silver nanoclusters, Anal. Bioanal. Chem. (2020) 2529–2536, https://doi.org/10.1007/s00216-020-02476-0.
[171] Y.M. Wang, J.W. Liu, L.Y. Duan, S.J. Liu, J.H. Jiang, Aptamer-based fluorometric determination of ATP by using target-cycling strand displacement amplification and copper nanoclusters, Microchim. Acta 184 (2017) 4183–4188, https://doi.org/10.1007/s00604-017-2337-6.
[172] M. Wang, S. Wang, D. Su, X. Su, Copper nanoclusters/polydopamine nanospheres based fluorescence aptasensor for protein kinase activity determination, Anal. Chim. Acta 1035 (2018) 184–191, https://doi.org/10.1016/j.aca.2018.06.043.
[173] H.Y. Dar, Y. Lone, R.K. Koiri, P.K. Mishra, R.K. Srivastava, Microcystin-leucine arginine (MC-LR) induces bone loss and impairs bone micro-architecture by modulating host immunity in mice: implications for bone health, Environ. Pollut. 238 (2018) 792–802, https://doi.org/10.1016/J.ENVPOL.2018.03.059.
[174] Y. Zhang, Z. Zhu, X. Teng, Y. Lai, S. Pu, P. Pang, H. Wang, C. Yang, C.J. Barrow, W. Yang, Enzyme-free fluorescent detection of microcystin-LR using hairpin DNA-templated copper nanoclusters as signal indicator, Talanta 202 (2019) 279–284, https://doi.org/10.1016/j.talanta.2019.05.013.
[175] F.M. Moghadam, M. Rahaie, A signal-on nanobiosensor for VEGF 165 detection based on supraparticle copper nanoclusters formed on bivalent aptamer, Biosens. Bioelectron. 132 (2019) 186–195, https://doi.org/10.1016/j.bios.2019.02.046.
[176] Y. Wang, X. Zhang, L. Zhao, T. Bao, W. Wen, X. Zhang, S. Wang, Integrated amplified aptasensor with *in-situ* precise preparation of copper nanoclusters for ultrasensitive electrochemical detection of microRNA 21, Biosens. Bioelectron. 98 (2017) 386–391, https://doi.org/10.1016/j.bios.2017.07.009.
[177] M. Wang, Z. Lin, Q. Liu, S. Jiang, H. Liu, X. Su, DNA-hosted copper nanoclusters/graphene oxide based fluorescent biosensor for protein kinase activity detection, Anal. Chim. Acta 1012 (2018) 66–73, https://doi.org/10.1016/j.aca.2018.01.029.
[178] A.D. Kurdekar, C. Sai Manohar, L.A.A. Chunduri, M.K. Haleyurgirisetty, I. K. Hewlett, V. Kamisetti, Computational design and clinical demonstration of a copper nanocluster based universal immunosensor for sensitive diagnostics, Nanoscale Adv. 2 (2020) 304–314, https://doi.org/10.1039/c9na00503j.
[179] L. Zhao, Z. Ma, New immunoprobes based on bovine serum albumin-stabilized copper nanoclusters with triple signal amplification for ultrasensitive electrochemical immunosensing for tumor marker, Sens. Actuators B Chem. 241 (2017) 849–854, https://doi.org/10.1016/j.snb.2016.11.012.
[180] Y. Chen, S. Zhang, H. Dai, Z. Hong, Y. Lin, A multiple mixed TiO_2 mesocrystal junction based PEC-colorimetric immunoassay for specific recognition of lipolysis stimulated lipoprotein receptor, Biosens. Bioelectron. 148 (2020), 111809, https://doi.org/10.1016/j.bios.2019.111809.
[181] R. Li, Q. Liu, Y. Jin, B. Li, Fluorescent enzyme-linked immunoassay strategy based on enzyme-triggered *in-situ* synthesis of fluorescent copper nanoclusters, Sens. Actuators B Chem. 281 (2019) 28–33, https://doi.org/10.1016/j.snb.2018.09.128.
[182] S. Lv, Y. Li, K. Zhang, Z. Lin, D. Tang, Carbon Dots/g-C3N4 nanoheterostructures-based signal-generation tags for photoelectrochemical immunoassay of cancer biomarkers coupling with copper nanoclusters, ACS Appl. Mater. Interfaces 9 (2017) 38336–38343, https://doi.org/10.1021/acsami.7b13272.
[183] L.P. Mei, X.Y. Jiang, X.D. Yu, Z. Wei-Wei, J.J. Xu, C. Hong-Yuan, Cu nanoclusters-encapsulated liposomes : toward sensitive liposomal photoelectrochemical immunoassay, Anal. Chem. 90 (2018) 2749–2755, https://doi.org/10.1021/acs.analchem.7b04789.
[184] W. Zhuang, Y. Li, J. Chen, W. Liu, H. Huang, Copper nanocluster-labeled hybridization chain reaction for potentiometric immunoassay of matrix metalloproteinase-7 in acute kidney injury and renal cancer, Anal. Methods 11 (2019) 2597–2604, https://doi.org/10.1039/c9ay00681h.
[185] Y. Zhao, X. Wang, J. Mi, Y. Jiang, C. Wang, Metal nanoclusters–based ratiometric fluorescent probes from design to sensing applications, Part. Part. Syst. Charact. 36 (2019), 1900298, https://doi.org/10.1002/PPSC.201900298.
[186] S. Garima, S. Jindal, S. Garg, I. Matai, G. Packirisamy, A. Sachdev, Dual-emission copper nanoclusters–based ratiometric fluorescent probe for intracellular detection of hydroxyl and superoxide anion species, Microchim. Acta (2021) 188, https://doi.org/10.1007/s00604-020-04683-z.
[187] Y. Shi, W. Li, X. Feng, L. Lin, P. Nie, J. Shi, X. Zou, Y. He, Sensing of mercury ions in Porphyra by Copper @ Gold nanoclusters based ratiometric fluorescent aptasensor, Food Chem. 344 (2021), 128694, https://doi.org/10.1016/J.FOODCHEM.2020.128694.
[188] W. Li, X. Hu, Q. Li, Y. Shi, X. Zhai, Y. Xu, Z. Li, X. Huang, X. Wang, J. Shi, X. Zou, S. Kang, Copper nanoclusters @ nitrogen-doped carbon quantum dots-based ratiometric fluorescence probe for lead (II) ions detection in porphyra, Food Chem. 320 (2020), 126623, https://doi.org/10.1016/J.FOODCHEM.2020.126623.
[189] C. Ma, P. Li, L. Xia, F. Qu, R.M. Kong, Z.L. Song, A novel ratiometric fluorescence nanoprobe for sensitive determination of uric acid based on CD@ZIF-CuNC nanocomposites, Microchim. Acta (2021) 188, https://doi.org/10.1007/s00604-021-04914-x.
[190] S.H. Park, N. Kwon, J.H. Lee, J. Yoon, I. Shin, Synthetic ratiometric fluorescent probes for detection of ions, Chem. Soc. Rev. 49 (2020) 143–179, https://doi.org/10.1039/C9CS00243J.
[191] X. Hu, H. Cao, W. Dong, J. Tang, Ratiometric fluorescent sensing of ethanol based on copper nanoclusters with tunable dual emission, Talanta 233 (2021), 122480, https://doi.org/10.1016/J.TALANTA.2021.122480.
[192] B.B. Tao, N.N. Wu, H.D. Zhang, H.B. Wang, Blocking the Cu (II) ions mediated catalytical ability for construction of ratiometric fluorescence sensing platform based on glutathione-stabilized copper nanoclusters, J. Electrochem. Soc. 169 (2022), 037529, https://doi.org/10.1149/1945-7111/AC5F1E.
[193] P.S. Zangabad, S. Mirkiani, S. Shahsavari, B. Masoudi, M. Masroor, H. Hamed, Z. Jafari, Y.D. Taghipour, H. Hashemi, M. Karimi, M.R. Hamblin, Stimulus-responsive liposomes as smart nanoplatforms for drug delivery applications, Nanotechnol. Rev. 7 (2018) 95–122, https://doi.org/10.1515/ntrev-2017-0154.
[194] M. Karimi, P. Sahandi Zangabad, A. Ghasemi, M. Amiri, M. Bahrami, H. Malekzad, H. Ghahramanzadeh Asl, Z. Mahdieh, M. Bozorgomid, A. Ghasemi, M.R. Rahmani Taji Boyuk, M.R. Hamblin, Temperature-responsive smart nanocarriers for delivery of therapeutic agents: applications and recent advances, ACS Appl. Mater. Interfaces 8 (2016) 21107–21133, https://doi.org/10.1021/acsami.6b00371.
[195] S. Shahsavari, Cellular functions analyses based on nanorobotics, J. Nanomedicine Res. 5 (2017) 34–35, https://doi.org/10.15406/jnmr.2017.05.00101.
[196] H. Cao, Z. Chen, H. Zheng, Y. Huang, Copper nanoclusters as a highly sensitive and selective fluorescence sensor for ferric ions in serum and living cells by imaging, Biosens. Bioelectron. 62 (2014) 189–195, https://doi.org/10.1016/j.bios.2014.06.049.
[197] N.K. Das, S. Ghosh, A. Priya, S. Datta, S. Mukherjee, Luminescent copper nanoclusters as a specific cell-imaging probe and a selective metal ion sensor, J. Phys. Chem. C 119 (2015) 24657–24664, https://doi.org/10.1021/acs.jpcc.5b08123.
[198] R. Ghosh, U. Goswami, S.S. Ghosh, A. Paul, A. Chattopadhyay, Synergistic anticancer activity of fluorescent copper nanoclusters and cisplatin delivered through a hydrogel nanocarrier, ACS Appl. Mater. Interfaces 7 (2015) 209–222, https://doi.org/10.1021/am505799q.
[199] X. Zhu, H. Shi, Y. Shen, B. Zhang, J. Zhao, G. Li, A green method of staining DNA in polyacrylamide gel electrophoresis based on fluorescent copper nanoclusters synthesized *in situ*, Nano Res. 8 (2015) 2714–2720, https://doi.org/10.1007/s12274-015-0778-y.
[200] Z. Wang, C.C. Zhang, J. Gao, Q. Wang, Copper clusters-based luminescence assay for tetracycline and cellular imaging studies, J. Lumin. 190 (2017) 115–122, https://doi.org/10.1016/j.jlumin.2017.05.038.
[201] A. Baghdasaryan, R. Grillo, S.R. Bhattacharya, M. Sharma, E. Reginato, H. Theraulaz, I. Dolamic, M. Dadras, S. Rudaz, E. Varesio, T. Burgi, Facile synthesis, size-separation, characterization, and antimicrobial properties of thiolated copper clusters, ACS Appl. Nano Mater. 1 (2018) 4258–4267, https://doi.org/10.1021/acsanm.8b01049.

Analytical and Bioanalytical Chemistry
https://doi.org/10.1007/s00216-021-03804-8

RESEARCH PAPER

Melanochrome-based colorimetric assay for quantitative detection of levodopa in co-presence of carbidopa and its application to relevant anti-Parkinson drugs

Mariagrazia Lettieri[1] · **Roberta Emanuele**[1] · **Simona Scarano**[1] · **Pasquale Palladino**[1] · **Maria Minunni**[1]

Received: 8 September 2021 / Revised: 16 November 2021 / Accepted: 24 November 2021

Abstract

In this paper is reported the selective detection and quantification of levodopa in co-presence of carbidopa. The method took advantage of the spontaneous oxidation and color development of levodopa at basic pH here driven by alkaline earth cations and co-solvent in solution. We have shown for the first time the generation and stabilization of the purple melanochrome from levodopa, by using magnesium acetate and dimethyl sulfoxide, which was here exploited for the development of a quantitative colorimetric assay for the active principle ingredient in commercial drugs for the treatment of Parkinson's disease. The calibration curves of levodopa in the two tablet formulations, containing carbidopa as decarboxylase inhibitor, showed a common linear trend between 10 mg L^{-1} and 40 mg L^{-1} with levodopa alone or in combination with carbidopa in standard solutions, with very good reproducibility (CV_{av}%, 3.3% for both brand and generic drug) and very good sensitivity, with limit of quantification about 0.6 mg L^{-1} in any case. The colorimetric method here developed is very simple and effective, appearing as a rapid and low-cost alternative to other methodologies, involving large and expensive instrumentations, for drug estimation and quality control of pharmaceutical formulations.

Keywords Carbidopa · Colorimetry · Drug analysis · Levodopa · Melanochrome · Parkinson

Introduction

Parkinson's disease (PD), like many human neurodegenerative disorders, is related to dopaminergic neuron disruption upon pH-dependent oxidative conversion of neurotransmitters like dopamine (DA) into cytotoxic molecules [1–3] and protein misfolding and aggregation, eventually causing neuronal death [4]. Unfortunately, there is no cure for PD, but several medications, dependent on the stage and the age at disease onset, may improve the quality of life of patients, starting from the pharmacological treatment of motor symptoms, i.e., rigidity, bradykinesia, and tremor [5]. Particularly effective, although fluctuating and transitory, appears the administration of levodopa (LD) as molecular precursor of DA that, being unable to cross the blood-brain barrier, cannot be directly taken as a medicine. However, to avoid LD metabolization prior to reach the brain, anti-Parkinson drugs always contain a decarboxylase and/or catechol-O-methyltransferase inhibitor like carbidopa (CD), benserazide (BZ), or entacapone, which also reduces side effects associated to LD therapy [6]. In this framework, several methods were developed for LD determination in presence of adjuvants and impurities in such drugs by means of chromatography [7], electrochemistry and electrophoresis [8–10], spectrophotometry [10–21], and NMR [22]. Literature about colorimetric determination of LD in pharmaceutical formulations is not very vast although representing an advantageous alternative, for easiness, rapidity, and low-cost, to the other methodologies requiring large instrumentation. These visible spectroscopy researches were based on LD chemical or enzymatic oxidation, for example, by using KIO_4 or tyrosinase to form the aminochrome (λ_{max}= 480 nm) [10, 12], or 4,5-dioxygenase to form betaxanthin pigment (λ_{max} = 430 nm) [20], or Au^{3+} to form gold nanoparticles (λ_{max} = 520 nm) [18]; other strategies were based on LD derivatization with a dye to form a colored adduct, for example, by using 4-aminoantipyrine (4-AAP) (λ_{max} = 454 nm) [19].

✉ Pasquale Palladino
pasquale.palladino@unifi.it

[1] Department of Chemistry 'Ugo Schiff', University of Florence, Via della Lastruccia 3-13, 50019 Sesto Fiorentino, Italy

Simple colorimetric quantitative assays are thus welcome for fast, simple, and low-cost drug estimation with several potential applications including quality control of pharmaceutical formulations, illicit drug testing, and monitoring in advanced drug delivery systems and personalized drug dosing [23].

Here, we obtained for the first time the generation and stabilization of the elusive purple melanochrome [24] from levodopa and dopamine (λ_{max} about 585 nm) without the use of chemical oxidant, enzyme, transition metal ions, or dye conjugation. This achievement inspired the analytical study of the O_2/pH-driven oxidation of some fundamental neurotransmitters (LD, DA, NE), and two synthetic analogues (CD, BZ) either one found in combination with LD in pharmaceutical formulations for the treatment of Parkinson's disease (Fig. 1), reporting the modulation of the color development, corresponding to different stages of molecular oxidation prior to self-polymerization, in dependence of alkaline earth cation and co-solvent concentration. We found the generation of the purple color only from levodopa and dopamine, instead obtaining yellow solutions for norepinephrine and benserazide, and uncolored solutions for carbidopa in the same conditions. Therefore, we focused our investigations on the selective detection and quantification of LD in some anti-Parkinson tablet formulations (see "Materials ad Methods") where levodopa is in co-presence of carbidopa at a mass ratio of 4:1 (LD 200 mg + CD 50 mg), together with numerous excipients. We optimized the solvent composition and experimental conditions for the selective detection and quantification of LD also in pharmaceutical formulations, after tablet dissolution, by using for the first time the purple stage of catecholamine oxidation here obtained as a colorimetric probe. The modulation of purple color intensity upon oxidation was explored up to 1 g L^{-1} for LD, following a dose-response trend, with a superimposable, selective, and linear colorimetric response for levodopa alone, after proper dilution between 10 mg L^{-1} and 40 mg L^{-1}, and in combination with carbidopa as for some anti-Parkinson drugs with a very good data reproducibility and sensitivity, appearing a valuable tool for rapid and low-cost point-of-care testing of LD content in such formulations.

Experimental section

Materials and chemicals

Sodium acetate trihydrate (NaOAc, $(CH_3COO)Na \cdot 3H_2O$), magnesium acetate tetrahydrate ($Mg(OAc)_2$, $(CH_3COO)_2Mg \cdot 4H_2O$), calcium acetate monohydrate ($Ca(OAc)_2$, $(CH_3COO)_2Ca \cdot H_2O$), barium acetate ($Ba(OAc)_2$, $(CH_3COO)_2Ba$), ammonium chloride (NH_4Cl), hydrochloric acid (HCl), dimethyl sulfoxide (DMSO, C_2H_6OS), methanol (MeOH, CH_3OH), acetonitrile (MeCN, CH_3CN), levodopa (LD, $C_9H_{11}NO_4$), dopamine hydrochloride (DA, $C_8H_{11}NO_2 \bullet HCl$), norepinephrine (NE, $C_8H_{11}NO_3$), carbidopa

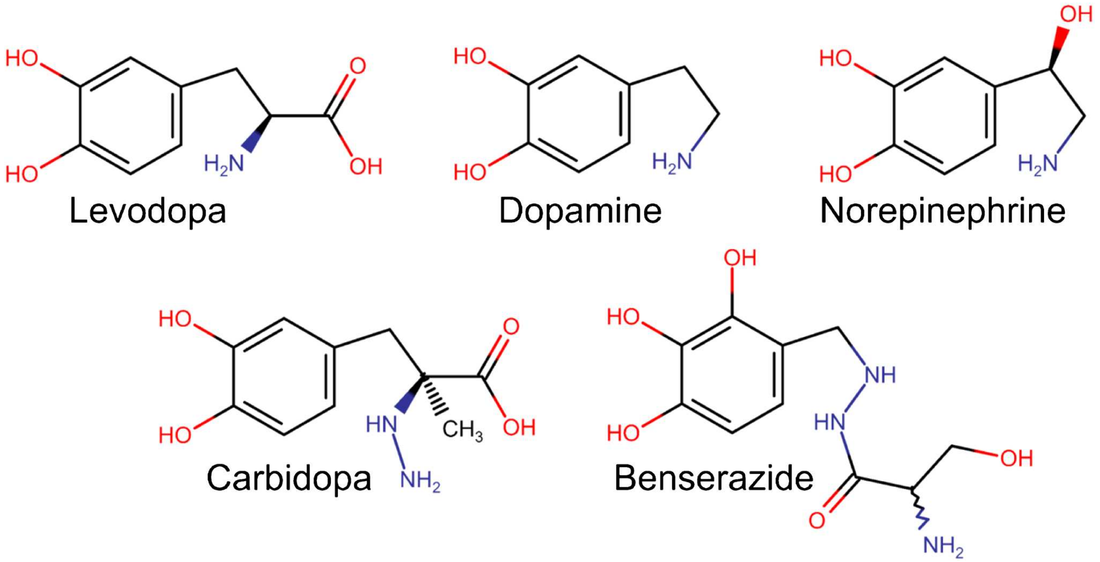

Fig. 1 Structural representation of some natural catecholamines levodopa (LD), dopamine (DA), norepinephrine (NE), and their synthetic analogues carbidopa (CD) and benserazide (BZ)

(CD, $C_{10}H_{14}N_2O_4$), and benserazide hydrochloride (BZ, $C_{10}H_{15}N_3O_5 \bullet HCl$) were purchased from Sigma-Aldrich (Milan, Italy). Brand drug Sinemet (200 mg levodopa, 50 mg carbidopa, 35 mg excipients) was obtained from MSD (Rome, Italy) and its pharmaceutical alternative (generic drug) Hexal (200 mg levodopa, 50 mg carbidopa, 194 mg excipients) was produced by Sandoz (Basel, Switzerland). All chemicals were of analytical reagent grade and used as received without any further purification. All solutions were prepared using water obtained from Milli-Q Water Purification System (resistivity ≥ 18 MΩcm) (Germany, www.merckmillipore.com).

Methods and instrumentation

Levodopa, dopamine, norepinephrine, carbidopa, and benserazide were dissolved in HCl 1 M to obtain 100 g L^{-1} stock solutions. Stock solutions of a brand drug and the generic drug containing 5 g L^{-1} of levodopa were prepared by stirring for 10 min one tablet (200 mg LD, 50 mg CD) in 4 mL of 1 M HCl, then adding 36 mL of DMSO and continuing stirring at 37 °C. The brand drug dissolved in 20 min giving a transparent orange solution, whereas the generic drug required 50 min, resulting in yellow suspension. The working solutions in DMSO, H_2O, and salts were prepared within 24 h from tablet dissolution, as further detailed in the "Results and discussion" section. Preliminary analysis was carried out in disposable polystyrene 96-well microtest plates (Sarstedt, Milan, Italy) by using iMark™ microplate visible absorbance reader with optical filters (Bio-Rad, Milan, Italy). Further absorbance measurements were performed in 1.0 cm cell at 20 °C by using a UV-Visible Spectrophotometer Evolution™ 201/220 from Thermo Scientific™ (Rodano, Milan, Italy).

Results and discussion

Assay principle

The O_2/pH-induced non-enzymatic oxidation and self-polymerization of catecholamines was recently exploited to generate biocompatible nanometric films with several applications ranging from (bio)analytical chemistry to materials science [25–33], using for example dopamine [26, 27], norepinephrine [30, 31], and levodopa [34], as functional monomers. Typically, catecholamine spontaneous oxidation is achieved at basic pH, which gives a black/brown polymer with a broad absorbance spectrum, including the visible region, with thickness and, consequently, absorbance intensity also depending on temperature, buffer concentration, and starting amount of catecholamine monomer [32, 33]. Exploring unusual conditions for the growth of a polydopamine film, we noticed the different oxidation behaviors of catecholamines in dependence of alkaline earth cations in solution at a high millimolar range, leading to distinct colors corresponding to different stages of monomer oxidation, cyclization, and rearrangement, naturally occurring prior to polymerization. For levodopa (LD) and dopamine (DA), we obtained purple/blue color solutions ascribable to melanochrome formation, an elusive intermediate stage of catecholamine polymerization isolated by enzymatic oxidation [24, 35], and tentatively identified as the dimer of indolequinone (Fig. 2) [36–39]. Consequently, we explored the chemical determinants of color development for some fundamental neurotransmitters (LD, DA, NE), and two synthetic analogues (CD, BZ) (Fig. 1), by changing cation, pH, ionic strength, and co-solvent concentration as detailed in the following sections, focusing the study on the detection of LD in combination with CD that, like BZ, is found in pharmaceutical formulations for the treatment of Parkinson's

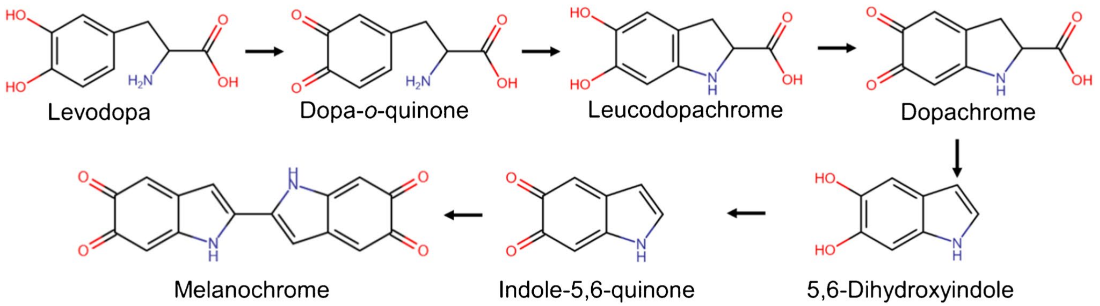

Fig. 2 Schematic representation of melanochrome synthetic pathway analogue to Raper-Mason pathway for the biosynthesis of melanin [35–37]. The oxidation of levodopa produces dopa-*o*-quinone, which gives leucodopachrome upon cyclization. The subsequent oxidation leads to dopachrome that rearranges to 5,6-dihydroxyindole, before to be oxidized to indole-5,6-quinone that dimerizes forming melanochrome

disease, whereas the other catecholamines here investigated (DA and NE) are not included in such drugs.

Influence of pH and Mg^{2+} concentration on color development by levodopa

Preliminary experiments on 96-well microplates were devoted to determining the influence of pH and magnesium salt concentration on melanochrome formation by oxidation of levodopa solution in H_2O/DMSO (1:1). Data were acquired by using a filter-based plate reader, reporting the absorbance at 595 nm (Fig. 3), i.e., the best available optical filter for melanochrome detection. Absorbance values of levodopa solutions in 150 mM Mg^{2+} increased with pH (Fig. 3a), as expected for metal coordination by catechol moiety. However, the best condition was achieved at pH 9.4, due to high absorbance, lowest CV% (2.2%), and the absence of any precipitation that instead occurred at higher pH, where the solutions turned cloudy and orange (data not shown). Analogously, we observed that the absorbance values of levodopa solutions at pH 9.4 increased with Mg^{2+} concentration up to 150 mM (Fig. 3b), representing the best condition also in terms of CV% (1.9%). Accordingly, pH 9.4 and 150 mM Mg^{2+} were identified as the optimal conditions for any further experimental investigation.

Influence of cation and solvent on color development by natural catecholamine

Here, we investigated the O_2/pH-induced oxidation [28] of levodopa (LD), dopamine (DA), and norepinephrine (NE) at fixed final concentration of 0.20 g L^{-1} in water or water/co-solvent in presence of 150 mM Na^+, Mg^{2+}, Ca^{2+}, or Ba^{2+} acetate salt and 150 mM NH_4Cl at pH 9.4.

We showed the main role of cations and solvent in regulation of catecholamine oxidation. Remarkably, dopamine and levodopa solutions in DMSO/H_2O (1:1) containing magnesium salt stood out for the appearance of a purple/blue color (λ_{max} = 580–590 nm) at 20 °C, reaching the maximum absorbance after 15 min. It is worth to note that the similarity of levodopa and dopamine spectra and color here described was a consequence of their common synthetic pathway reported in Fig. 2, sharing the stages of the generation of 5,6-dihydroxyindole, and the oxidation to indole-5,6-quinone that dimerizes virtually forming the same melanochrome. DMSO could act as further oxidant; nevertheless, the purple color here ascribed to melanochrome formation [24, 35–39] were also obtained by using methanol/water (1:1) as solvent for levodopa (Fig. S1A) and dopamine (Fig. S1B) solutions, or acetonitrile/water (1:1) for dopamine only (Fig. S1B), likely underling the main influence of these solvents on pK_as and on the oxidation potentials of catecholamines and their derivatives [40–42]. However, the complete characterization and description of chemical reactions and the role of co-solvent in catecholamine oxidation and color development was beyond the scope of this paper. Finally, DMSO was selected as the only co-solvent since it is non-flammable, less harmful, and less volatile among the tested ones.

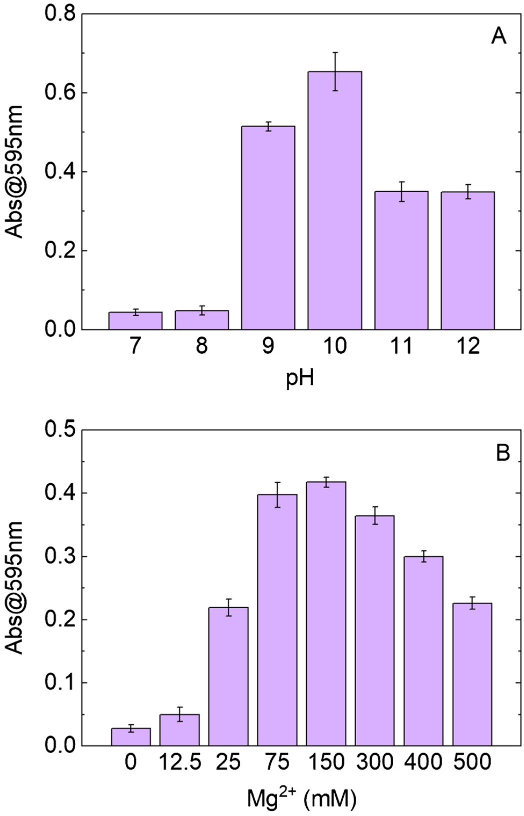

Fig. 3 Levodopa color development in dependence of pH and concentration of $Mg(OAc)_2$ in NH_4Cl at 20 °C on 96-well microplates. LD was solubilized at fixed final concentration of 0.20 g L^{-1} in H_2O/DMSO (1:1) **a** in presence of 150 mM Mg^{2+} acetate salt and 150 mM NH_4Cl at several pH values, or **b** in presence of Mg^{2+} acetate salt and NH_4Cl up to 500 mM at pH 9.4. The absorbance values at 595 nm were acquired 15 min after mixing by using a filter-based microplate reader. Each bar represents the mean ± SD of 4 replicates

Differently from levodopa and dopamine, norepinephrine solution resulted yellow (λ_{max} = 410 nm) in the same conditions, likely due to the additional hydroxyl group in the ethyl chain when compared with dopamine and levodopa (Fig. 1 and Fig. S1C), which confers peculiar properties to this catecholamine and its polymers as reported elsewhere [30, 34]. Figure 4 displays the colored solutions and the corresponding absorption spectra for natural catecholamines

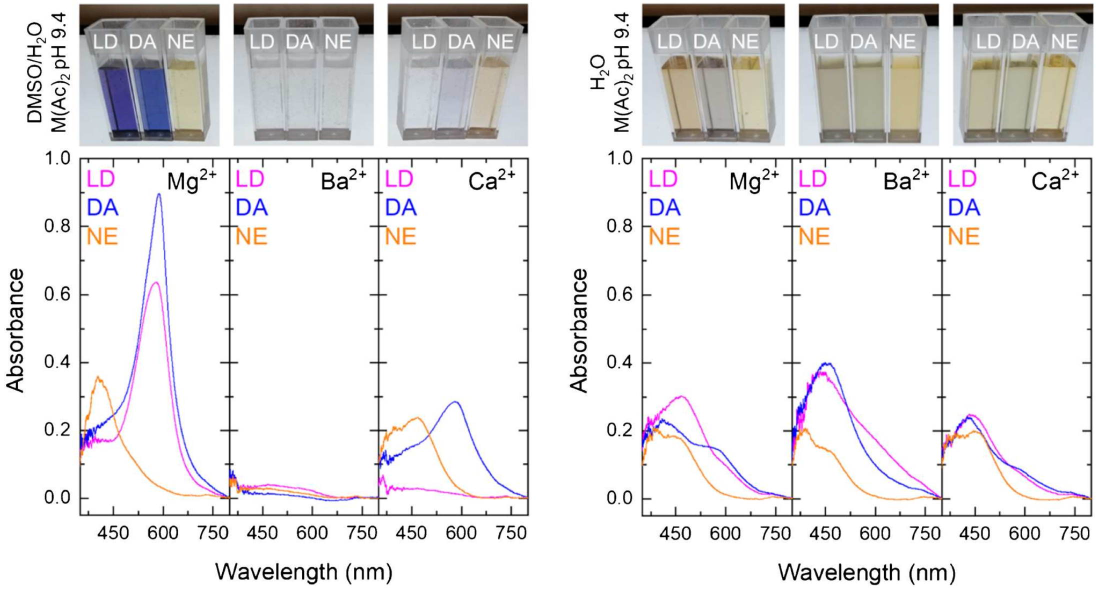

Fig. 4 Natural catecholamines color development in dependence of Mg^{2+}, Ba^{2+}, and Ca^{2+} at basic pH and fixed solvent composition. Levodopa (LD), dopamine (DA), and norepinephrine (NE) were solubilized at fixed final concentration of 0.20 g L^{-1} in H_2O/DMSO (1:1) (left panels), or H_2O (right panels), in presence of 150 mM Na^+, Mg^{2+}, Ca^{2+}, or Ba^{2+} acetate salt and 150 mM NH_4Cl at pH 9.4. Images and spectra were acquired at 20 °C, 15 min after mixing

upon addition of 150 mM alkaline earth cations in water and water/DMSO mixture at pH 9.4. In the absence of the co-solvent, for any cation and catecholamine explored, the main absorption peak was around 440–470 nm due to formation of dopa-, dopamine-, and norepinephrine-chrome, corresponding to yellow-orange solutions (Fig. 4 right panels, and Fig S1). Differently, water/DMSO mixtures in presence of 150 mM Mg^{2+} (to a minor extent with 150 mM Ca^{2+}, and without any color development with 150 mM Ba^{2+}) generated brilliant purple/blue colors for LD and DA, with a maximum absorbance around 580–590 nm (melanochrome), and yellow-orange solutions for NE (Fig. 4 left panels). Moreover, increasing concentration of DMSO up to 50%v/v, in presence of 150 mM Mg^{2+}, led to red shift for LD and DA solutions due to conversion of yellow dopa- and dopamine-chrome to deeper blue/purple color of melanochrome according to the scheme reported in Fig. 2, whereas the NE solutions stayed yellow (Fig. 5) due to different reactivity. These colors were formed in 15 min, but solutions became darker with time, up to formation of black precipitate after 3 days (Figs. S2 and S3). No color development and no precipitation was observed during 3 days for water/DMSO mixtures of any catecholamine in presence of 150 mM Na^+ at pH 9.4 (Fig. S4, lower panels), whereas the same solutions became darker in absence of DMSO (Fig. S4, upper panels), underling the capability of DMSO to slow down the kinetics of oxidation of these neurotransmitters here followed by using the absorbance at 415 nm in Fig. S5, elsewhere reported as characteristic of catecholamine polymerization [32].

Influence of Mg^{2+} and DMSO on color development by synthetic catecholamine analogues

On the base of the results reported above, aiming to finally selectively detect and quantify levodopa directly in pharmaceutical formulations, we evaluated the colorimetric behavior of two levodopa-decarboxylase inhibitors, carbidopa (CD) and benserazide (BZ), as possible interferents, taken singularly; CD and BZ are structurally related to endogenous catecholamines (Fig. 1), largely, but never together, present in levodopa tablets for the treatment of Parkinson's disease, whereas the other catecholamines here investigated, i.e., dopamine and norepinephrine, are not included in such pharmaceutical formulations and, therefore, cannot interfere with the assay. We thus analyzed DMSO/water 1:1 (v/v), solutions of CD or BZ at constant concentration of Mg^{2+} (150 mM $Mg(OAc)_2$ solutions at pH 9.4) (Fig. 6); this was the selected condition to obtain the purple color development in presence of levodopa and thus used to explore the behavior of its analogues, eventually co-present in formulations. First, we analyzed CD and BZ solution alone to evaluate the

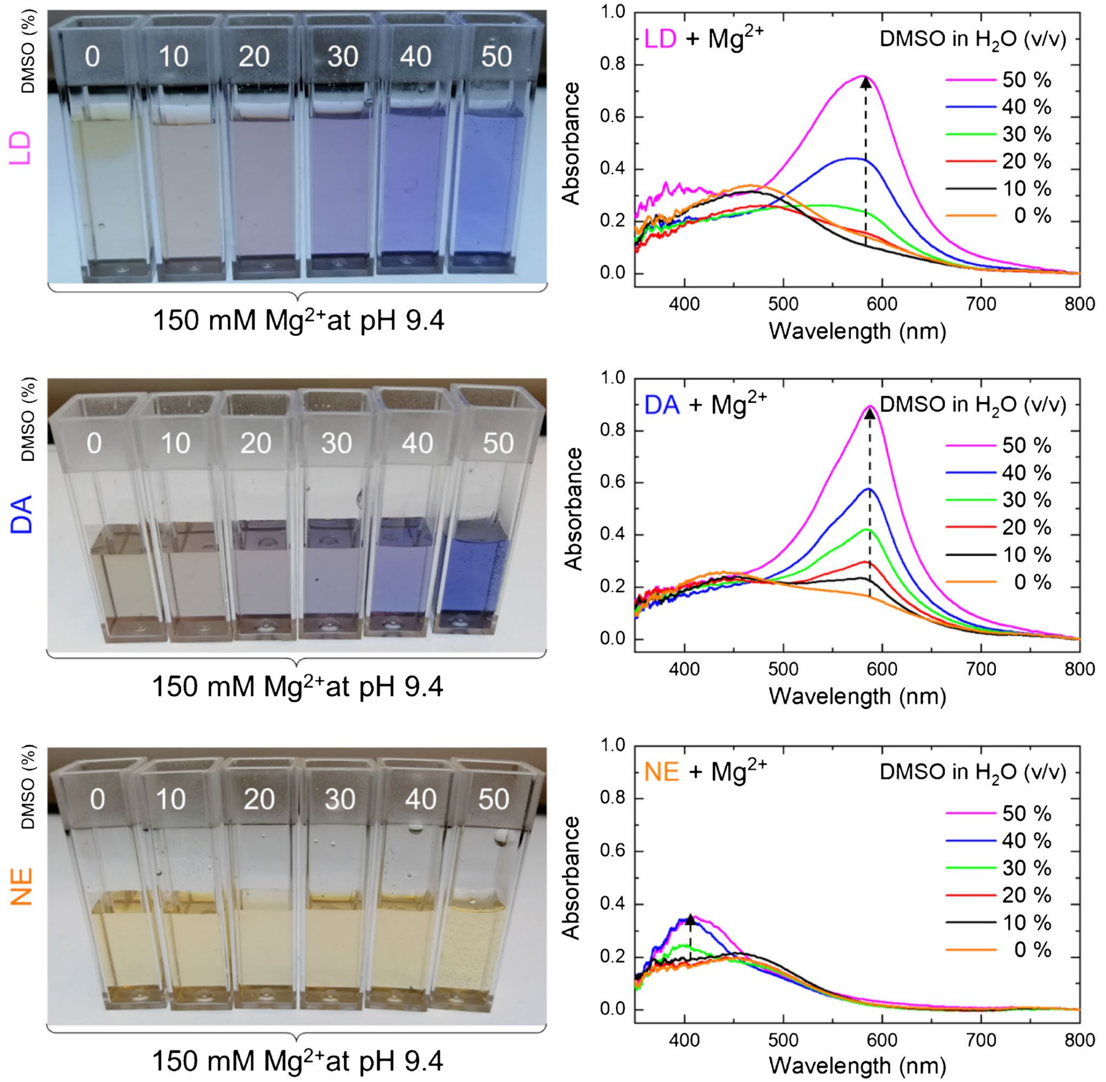

Fig. 5 Natural catecholamines color development in dependence of DMSO at basic pH and at fixed magnesium salt concentration. Levodopa (LD), dopamine (DA), and norepinephrine (NE) were solubilized at 0.4 g L^{-1} in DMSO HCl 10 mM, or H_2O, and mixed with $Mg(OAc)_2$ in NH_4Cl at pH 9.4 to obtain a final concentration of 0.20 g L^{-1} with different percentage in volume of DMSO in H_2O from zero to 50% as indicated by the arrow. Images and spectra were acquired at 20 °C, 15 min after mixing

assay applicability to binary solutions of LD and CD or BZ. In the case of BZ, a yellow solution ($\lambda_{max} = 430–450$ nm) was produced at any percentage of DMSO tested, becoming darker at 50% DMSO. Accordingly, BZ was no further studied in this paper, requiring additional selectivity investigations and improvement for the application of such method to drugs containing both LD and BZ. Differently, CD solutions showed an orange/pink color ($\lambda_{max} = 400$ and 480 nm) decreasing in intensity with increasing amount of co-solvent, becoming uncolored ($\lambda_{max} = 360$ nm) at 50% DMSO. Such peculiar behavior for CD among all the natural and synthetic molecules here studied, i.e., the absence of any color development at high DMSO concentration, encouraged to test the approach here described in solutions containing both LD and CD as preliminary step for quantifying LD in pharmaceutical formulations also containing CD (see after).

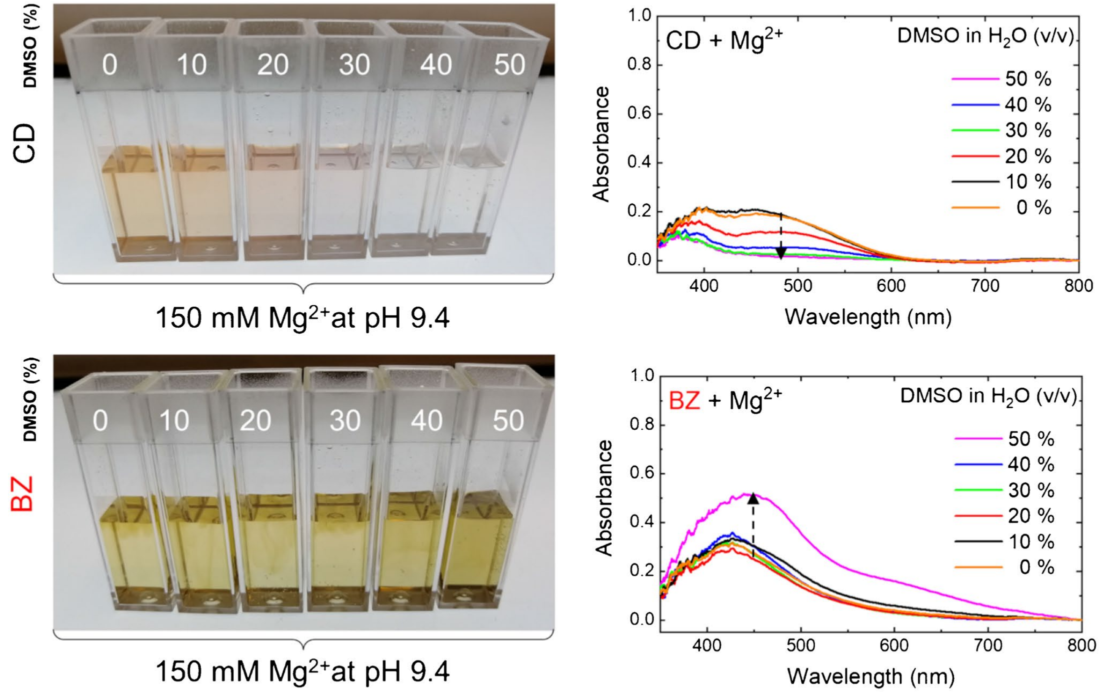

Fig. 6 Synthetic catecholamine analogues color development in dependence of DMSO at basic pH at fixed magnesium salt concentration. Carbidopa (CD) (upper panels) and Benserazide (BZ) (lower panels) were solubilized at 0.4 g L^{-1} in DMSO HCl 10 mM, or H_2O, and mixed with $Mg(OAc)_2$ in NH_4Cl at pH 9.4 to obtain a final concentration of 0.20 g L^{-1} with different percentage in volume of DMSO in H_2O from zero to 50% as indicated by the arrow. Images and spectra were acquired at 20 °C, 15 min after mixing

Colorimetric quantification of levodopa in tablets by using melanochrome as molecular probe

The best conditions here determined for color development from LD solutions, i.e., 150 mM $MgAc_2$ in presence of 150 mM NH_4Cl at pH 9.4 in water/dimethyl sulfoxide 1:1 (v/v), were also applied to CD and LD+CD binary solutions with mass ratio of 4:1 as indicated in pharmaceutical formulations here used. The spectrophotometric analysis of LD and CD standard solutions showed (Fig. 7) a very clear concentration-dependent signal at 585 nm only for LD (black circles), giving the largest absorbance increase up to 40 mg L^{-1}, considered as the limit of linearity for the LD curve in Fig. 7 (left panel), and reaching a plateau at higher concentration. CD solutions (white circles), instead, did not show any absorption at this visible wavelength over the entire concentration range, as expected from uncolored solution already observed at high (50%) DMSO concentrations as reported in Fig. 6. Therefore, the developed colorimetric assay was applied to the binary mixture (LD+CD 4:1), as simplified model, and validated by using commercially available levodopa/carbidopa tablets (the real samples) containing 200 mg of levodopa and 50 mg of carbidopa (from the package leaflet of tablets) as the large number of generic formulations appeared during the worldwide shortage of brand drug in 2010–2011 [43, 44]. Figure 7 (right panel) shows the superposition of calibration curves for the standard solutions of LD alone (black circle), LD+CD 4:1 mixtures (black and white circles), and both the brand drug (blue circles) and the generic drug (red circles). All data were fitted according to the linear equation A @ 585nm = $m \times C$, (1), where m represents the slope of the melanochrome absorbance at 585 nm. The excellent test performances were also highlighted by the fitting parameters reported in Table 1, indicating very limited, if any, matrix effect despite to numerous excipients (see "Experimental section"), also excluding any interference of CD with the assay in such conditions. The assay reproducibility between 10 mg L^{-1} and 40 mg L^{-1}, expressed as CV_{av}%, was 3.7% for LD, and 3.3% for LD+CD 4:1 mixture, brand drug, and generic drug. Other fitting parameters are reported in Table 1, including the limit of quantification found to be about 0.6 mg L^{-1} (3 μM) even in target matrices represented by tablets.

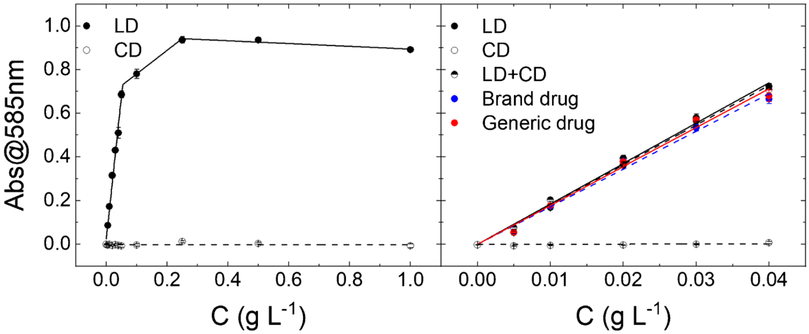

Fig. 7 Levodopa quantification curves up to 1 g L^{-1} (left) or 40 mg L^{-1} (right). Levodopa (LD, black circles), carbidopa (CD, white circles), LD+CD 4:1 mixture (black and white circles), brand drug (blue circles), and generic drug (red circles) were solubilized separately in DMSO/H_2O 1:1 (v/v) with 150 mM $Mg(OAc)_2$ and 150 mM NH_4Cl pH 9.4. Absorbance at 585 nm was acquired at 20 °C after 15 min of solution mixing. Each point represents the mean ± SD of 4 replicates. Absorbance data in right panel were fitted according to linear equation 1

Table 1 Linear fitting parameters for levodopa quantification

Sample	m (L g^{-1})	LOD (mg L^{-1})	LOQ (mg L^{-1})	R^2	CV$_{av}$ (%)*
LD	18.19 ± 0.35	0.184 ± 0.036	0.615 ± 0.119	0.996	3.7
LD+CD	18.49 ± 0.42	0.181 ± 0.041	0.605 ± 0.138	0.993	3.3
Brand drug	17.24 ± 0.44	0.195 ± 0.051	0.649 ± 0.167	0.992	3.3
Generic drug	17.81 ± 0.51	0.188 ± 0.054	0.628 ± 0.182	0.990	3.3

*Calculated between 10 mg L^{-1} and 40 mg L^{-1}

Conclusion

The main discovery behind the focus of this paper was the synergistic capability of dimethyl sulfoxide and magnesium cation to trigger and stabilize the purple melanochrome formation for natural catecholamines levodopa and dopamine only, likely modulating the pK$_a$s and the oxidation potentials of these natural neurotransmitters. In the same conditions, instead, norepinephrine and benserazide displayed yellow solutions, and the synthetic analogue carbidopa appeared uncolored. These results inspired the subsequent application of the optimized protocol to some pharmaceutical formulations for the treatment of patients with the Parkinson's disease, which contain levodopa in presence of carbidopa at fixed ratio 4:1. The analytic colorimetric method here developed allowed the selective detection and quantification of the active substance, levodopa, in co-presence of a decarboxylase inhibitor, carbidopa, achieving a superimposable matrix- and carbidopa-independent colorimetric response with a common linear dynamic trend with high reproducibility in target matrices (CV$_{av}$%, 3.3% for brand drug and the generic drug) and very good sensitivity, with limit of quantification found to be 0.6 mg L^{-1}. Accordingly, this simple colorimetric method requiring just proper dissolution and dilution of pharmaceutical formulations could be used for rapid (15 min) and low-cost point-of-care testing of the LD content of drug tablets, resulting potentially useful for high-throughput analysis of brand and generic levodopa drugs. Finally, the results here reported could pave the way for future investigations of levodopa and its metabolites in specimens from patients with Parkinson's disease treated with such drugs in clinical practice, representing a first step for a fast and non-invasive therapeutic drug monitoring.

Supplementary Information The online version contains supplementary material available at https://doi.org/10.1007/s00216-021-03804-8.

Funding The authors received support from the Ministry of Education, University and Research (MIUR), through the project "Dipartimenti di Eccellenza 2018-2022," and Horizon 2020, ERA-NET – Photonic Sensing Transnational Call 2016, through the project PLABAN "advanced PLAsmonic Biosensors ANalysis of nucleic acids."

Declarations

Conflict of interest The authors declare no competing interests.

References

1. Bisaglia M, Filograna R, Beltramini M, Bubacco L. Are dopamine derivatives implicated in the pathogenesis of Parkinson's disease? Ageing Res Rev. 2014. https://doi.org/10.1016/j.arr.2013.12.009.
2. Jeitner TM, Kalogiannis M, Krasnikov BF, Gomlin I, Peltier MR, Moran GR. Linking inflammation and Parkinson disease: hypochlorous acid generates parkinsonian poisons. Toxicol Sci. 2016. https://doi.org/10.1093/toxsci/kfw052.
3. Palladino P, Torrini F, Scarano S, Minunni M. Colorimetric analysis of the early oxidation of dopamine by hypochlorous acid as preliminary screening tool for chemical determinants of neuronal oxidative stress. J Pharm Biomed Anal. 2020. https://doi.org/10.1016/j.jpba.2019.113016.
4. Leong SL, Cappai R, Barnham KJ, Pham CL. Modulation of alpha-synuclein aggregation by dopamine: a review. Neurochem Res. 2009. https://doi.org/10.1007/s11064-009-9986-8.
5. Connolly BS, Lang AE. Pharmacological treatment of Parkinson disease: a review. JAMA. 2014:1670–83. https://doi.org/10.1001/jama.2014.3654.
6. Oertel WH. Recent advances in treating Parkinson's disease. F1000Research. 2017. https://doi.org/10.12688/f1000research.10100.1.
7. Wollmer E, Klein S. Development and validation of a robust and efficient HPLC method for the simultaneous quantification of levodopa, carbidopa, benserazide and entacapone in complex matrices. J Pharm Pharm Sci. 2017. https://doi.org/10.18433/J3K923.
8. Fanali S, Pucci V, Sabbioni C, Raggi MA. Quality control of benserazide levodopa and carbidopa-levodopa tablets by capillary zone electrophoresis. Electrophoresis. 2000. https://doi.org/10.1002/1522-2683(20000701)21:12<2432::AID-ELPS2432>3.0.CO;2-E.
9. Wang J, Zhou Y, Liang J, He PG, Fang YZ. Determination of levodopa and benserazide hydrochloride in pharmaceutical formulations by CZE with amperometric detection. Chromatographia. 2005. https://doi.org/10.1365/s10337-005-0515-x2005.
10. Quintino M, Yamashita M, Angnes L. Voltammetric studies and determination of levodopa and carbidopa in pharmaceutical products. Electroanalysis. 2006. https://doi.org/10.1002/elan.200503445.
11. Saini AS, Kumar J, Melo JS. Microplate based optical biosensor for L-dopa using tyrosinase from Amorphophallus campanulatus. Anal Chim Acta. 2014. https://doi.org/10.1016/j.aca.2014.08.016.
12. Hassib ST, El-Khateeb SZ. Spectrometric determination of madopar capsules. Anal Lett. 1990. https://doi.org/10.1080/00032719008052442.
13. Coello J, Maspoch S, Villegas N. Simultaneous kinetic-spectrophotometric determination of levodopa and benserazide by bi-and three-way partial least squares calibration. Talanta. 2000. https://doi.org/10.1016/S0039-9140(00)00539-7.
14. Nagaraja P, Vasantha RA, Sunitha KR. A sensitive and selective spectrophotometric estimation of catechol derivatives in pharmaceutical preparations. Talanta. 2001. https://doi.org/10.1016/S0039-9140(01)00438-6.
15. Uslu B, Özkan SA. Determination of binary mixtures of levodopa and benserazide in pharmaceuticals by ratio-spectra derivative spectrophotometry. Anal Lett. 2002. https://doi.org/10.1081/AL-120002531.
16. Damiani PC, Moschetti AC, Rovetto AJ, Benavente F, Olivieri AC. Design and optimization of a chemometrics assisted spectrophotometric methods for the simultaneous determination of levodopa and carbidopa in pharmaceutical products. Anal Chim Acta. 2005. https://doi.org/10.1016/j.aca.2005.04.065.
17. Chamsaz M, Safavi A, Fadaee J. Simultaneous kinetic spectrophotometric determination of carbidopa, levodopa and methyldopa in the presence of citrate with the aid of multivariate calibration and artificial neural networks. Anal Chim Acta. . https://doi.org/10.1016/j.aca.2007.09.006.
18. Chou YC, Shih CI, Chiang CC, Hsu CH, Yeh YC. Reagent-free dopa-dioxygenase colorimetric biosensor for selective detection of L-dopa. Sens Actuat B: Chemical. 2019. https://doi.org/10.1016/j.snb.2019.126717.
19. Baron R, Zayats M, Willner I. Dopamine-, L-DOPA-, adrenaline-, and noradrenaline-induced growth of Au nanoparticles: assays for the detection of neurotransmitters and of tyrosinase activity. Anal Chem. 2005. https://doi.org/10.1021/ac048691v.
20. Mohamed G, Nour-El-Dien F, El-Nahas R. Spectrophotometric and standard addition methods for quantitative determination of dopamine hydrochloride and levodopa in tablets and ampoules. Afinidad. 2009; https://raco.cat/index.php/afinidad/article/view/277273.
21. Khanmohammadi M, Mobedi E, Garmarudi AB, Mobedi H, Kargosha K. Simultaneous determination of levodopa and carbidopa in levodopa-carbidopa tablets by ATR-FTIR spectrometry. Pharm Dev Technol. 2007. https://doi.org/10.1080/10837450701481249.
22. Talebpour Z, Haghgoo S, Shamsipur M. 1H nuclear magnetic resonance spectroscopy analysis for simultaneous determination of levodopa, carbidopa and methyldopa in human serum and pharmaceutical formulations. Anal Chim Acta. 2004. https://doi.org/10.1016/j.aca.2003.10.081.
23. Ong JJ, Pollard TD, Goyanes A, Gaisford S, Elbadawi M, Basit AW. Optical biosensors-illuminating the path to personalized drug dosing. Biosens Bioelectron. 2021. https://doi.org/10.1016/j.bios.2021.113331.
24. Vachtenheim J, Duchoň J, Matouš B. A spectrophotometric assay for mammalian tyrosinase utilizing the formation of melanochrome from L-dopa. Anal Biochem. 1985. https://doi.org/10.1016/0003-2697(85)90559-7.
25. Palladino P, Minunni M, Scarano S. Cardiac Troponin T capture and detection in real-time via epitope-imprinted polymer and optical biosensing. Biosens Bioelectron. 2018. https://doi.org/10.1016/j.bios.2018.01.068.
26. Scarano S, Pascale E, Palladino P, Fratini E, Minunni M. Determination of fermentable sugars in beer wort by gold nanoparticles@polydopamine: a layer-by-layer approach for Localized Surface Plasmon Resonance measurements at fixed wavelength. Talanta. 2018. https://doi.org/10.1016/j.talanta.2018.02.044.
27. Scarano S, Palladino P, Pascale E, Brittoli A, Minunni M. Colorimetric determination of p-nitrophenol by using ELISA microwells modified with an adhesive polydopamine nanofilm containing catalytically active gold nanoparticles. Microchim Acta. 2019. https://doi.org/10.1007/s00604-019-3259-2.
28. Palladino P, Bettazzi F, Scarano S. Polydopamine: surface coating, molecular imprinting, and electrochemistry d successful applications and future perspectives in (bio)analysis. Anal Bioanal Chem. 2019. https://doi.org/10.1007/s00216-019-01665-w.
29. Baldoneschi V, Palladino P, Scarano S, Minunni M. Polynorepinephrine: state-of-the-art and perspective applications in biosensing and molecular recognition. Anal Bioanal Chem. 2020. https://doi.org/10.1007/s00216-020-02578-9.
30. Baldoneschi V, Palladino P, Banchini M, Minunni M, Scarano S. Norepinephrine as new functional monomer for molecular imprinting: an applicative study for the optical sensing of cardiac biomarkers. Biosens Bioelectron. 2020. https://doi.org/10.1016/j.bios.2020.112161.
31. Torrini F, Palladino P, Baldoneschi V, Scarano S, Minunni M. Sensitive 'two-steps' competitive assay for gonadotropin-releasing hormone detection via SPR biosensing and

polynorepinephrine-based molecularly imprinted polymer. Anal Chim Acta. 2021. https://doi.org/10.1016/j.aca.2021.338481.
32. Palladino P, Brittoli A, Pascale E, Minunni M, Scarano S. Colorimetric determination of total protein content in serum based on the polydopamine/protein adsorption competition on microplates. Talanta. 2019. https://doi.org/10.1016/j.talanta.2019.01.095.
33. Torrini F, Scarano S, Palladino P, Minunni M. Polydopamine-based quantification of albuminuria for the assessment of kidney damage. Anal Bioanal Chem. 2021. https://doi.org/10.1007/s00216-021-03192-z.
34. Tan X, Gao P, Li Y, Qi P, Liu J, Shen R, Wang L, Huang N, Xiong K, Tian W, Tu Q. Poly-dopamine, poly-levodopa, and poly-norepinephrine coatings: comparison of physico-chemical and biological properties with focus on the application for blood-contacting devices. Bioact Mater. 2021. https://doi.org/10.1016/j.bioactmat.2020.06.024.
35. Fatibello-Filho O, da Cruz VI. Flow injection spectrophotometric determination of L-Dopa and carbidopa in pharmaceutical formulations using a crude extract of sweet potato root [Ipomoea batatas (L.) Lam.] as enzymatic source. Analyst. 1997; https://doi.org/10.1039/A606852I.
36. Mason HS, Peterson EW, Melanoproteins I. Reactions between enzyme-generated quinones and amino acids. Biochim Biophys Acta. 1965:10.1016/0304-4165(65)90479-4.
37. Napolitano A, Corradini MG, Prota G. A reinvestigation of the structure of melanochrome. Tetrahedron Lett. 1985. https://doi.org/10.1016/S0040-4039(00)94917-7.
38. Pezzella A, Panzella L, Crescenzi O, Napolitano A, Navaratman S, Edge R, Land EJ, Barone V, d'Ischia M. Short-lived quinonoid species from 5,6-dihydroxyindole dimers en route to eumelanin polymers: integrated chemical, pulse radiolytic, and quantum mechanical investigation. J Am Chem Soc. 2006. https://doi.org/10.1021/ja0650246.
39. Micillo R, Panzella L, Iacomino M, Prampolini G, Cacelli I, Ferretti A, Crescenzi O, Koike K, Napolitano A, d'Ischia M. Eumelanin broadband absorption develops from aggregation-modulated chromophore interactions under structural and redox control. Sci Rep. 2017. https://doi.org/10.1038/srep41532.
40. Fu Y, Liu L, Wang YM, Li JN, Yu TQ, Guo QX. Quantum-chemical predictions of redox potentials of organic anions in dimethyl sulfoxide and reevaluation of bond dissociation enthalpies measured by the electrochemical methods. J Phys Chem A. 2006. https://doi.org/10.1021/jp055682x.
41. Zhu XQ, Wang CH, Liang H. Scales of oxidation potentials, pKa, and BDE of various hydroquinones and catechols in DMSO. J Organic Chem. 2010. https://doi.org/10.1021/jo101455m.
42. Rossini E, Bochevarov AD, Knapp EW. Empirical Conversion of pKa Values between different solvents and interpretation of the parameters: application to water, acetonitrile, dimethyl sulfoxide, and methanol. ACS Omega. 2018. https://doi.org/10.1021/acsomega.7b01895.
43. Go CL, Rosales RL, Schmidt P, Lyons KE, Pahwa R, Okun MS. Generic versus branded pharmacotherapy in Parkinson's disease: does it matter? A review. Parkinsonism Relat Disord. 2011. https://doi.org/10.1016/j.parkreldis.2011.02.005.
44. The National Parkinson Foundation's Helpline Speaks: Lessons from the 2011 Sinemet Shortage 2012. http://comitatoparkinson.it/wp-content/uploads/2019/05/anpfreport_sinimetshortage201.pdf. Accessed 08 Sept 2021.

Analytical and Bioanalytical Chemistry
https://doi.org/10.1007/s00216-022-04256-4

RESEARCH PAPER

Colorimetric determination of carbidopa in anti-Parkinson drugs based on 4-hydroxy-3-methoxybenzaldazine formation by reaction with vanillin

Mariagrazia Lettieri[1] · **Simona Scarano**[1] · **Pasquale Palladino**[1] · **Maria Minunni**[1]

Received: 31 May 2022 / Revised: 28 June 2022 / Accepted: 27 July 2022

Abstract

In this paper is reported the selective colorimetric detection and quantification of carbidopa, an inhibitor of aromatic amino acid decarboxylase, in the co-presence of levodopa as dopamine precursor in pharmaceutical formulations for the treatment of Parkinson's disease. The method is based on the selective condensation reaction between the hydrazine group from carbidopa and the formyl functional group of vanillin, a natural flavoring agent, in acidified alcoholic solution. The yellow color development (λ_{max} ~ 420 nm) due to the formation of 4-hydroxy-3-methoxybenzaldazine (HMOB) was observed for carbidopa only, whereas levodopa, lacking the hydrazine group, did not color the solution, as expected. The calibration curves for two tablet formulations of levodopa in combination with carbidopa (4:1) were superimposable with levodopa/carbidopa (4:1), as well as carbidopa alone, in standard solution, i.e., the excipients and additives did not interfere with carbidopa determination, corresponding to a mean recovery about 105%. The linear dynamic range was between 5.00 and 50.0 mg L^{-1} with very good reproducibility within this range (CV_{av}% about 3–4%) and very good sensitivity, with limits of quantification of about 1 mg L^{-1}. The colorimetric method developed here is very simple, inexpensive, and effective for drug estimation and quality control of pharmaceutical formulations.

Keywords Anti-Parkinson drugs · Vanillin · Benzaldazine · Levodopa · Carbidopa · Colorimetry

Introduction

The Parkinson's disease (PD) is associated with abnormal dopaminergic neuron disruption and neurotransmitters loss and conversion into cytotoxic molecules, affecting 10 million people worldwide [1–4]. At the present time, there is no cure for PD, but the administration of some medications to restore the dopamine (DA) concentration in the brain may improve, although variably and transiently, the quality of life of patients [5, 6]. Unfortunately, DA cannot be directly taken as a medicine because it is unable to reach the brain. Accordingly, the pharmacological treatment of PD is based on levodopa (LD), which is the molecular precursor of DA, together with carbidopa (CD), which works as peripheral inhibitor of aromatic amino acid decarboxylase, avoiding the conversion of LD in DA prior to crossing the blood–brain barrier, thus largely reducing the dose, and the resulting side effects, of levodopa to be administered. Several methods were developed for CD determination in presence of LD in such drugs by means of chromatography [7], electrochemistry and electrophoresis [8, 9], spectrophotometry [10–12], and NMR [13]. Recently, we have reported the selective detection and quantification of levodopa in co-presence of carbidopa in these commercial drugs for the treatment of PD. The method was based on the generation and stabilization of the purple melanochrome (λ_{max} ~ 585 nm) from levodopa by using magnesium acetate and dimethyl sulfoxide [14]. Here, instead, we report the detection and quantification of carbidopa for the same tablet formulations, exploiting the well-known and selective reactivity of hydrazine group of carbidopa with an (aromatic) aldehyde. At the same time, the levodopa, lacking the hydrazine group, forms only an imine and leaves the solution not colored at acidic pH. We decided to use vanillin (4-hydroxy-3-methoxybenzaldehyde), observing the yellow color development (λ_{max} ~ 420 nm) due to formation

✉ Pasquale Palladino
pasquale.palladino@unifi.it

[1] Department of Chemistry 'Ugo Schiff',
University of Florence, Via della Lastruccia 3-13,
50019 Sesto Fiorentino, Italy

of 4-hydroxy-3-methoxybenzaldazine by reaction with carbidopa (Fig. 1). The same azine was previously obtained by the condensation of free hydrazine molecule with vanillin: (a) as a probe to develop a colorimetric hydrazine dosimeter [15]; (b) as a Schiff base ligand to generate biologically active transition metal complexes [16]; (c) as side-products [17]. Moreover, an analogous azine was obtained by reaction of carbidopa with p-dimethylaminobenzaldehyde (DMAB) for spectrofluorometric determination of carbidopa in monkey plasma [18]. However, being vanillin a well-known water-soluble and naturally occurring flavoring agent used in food industries [19, 20], although adverse effect can occur due to chemical reactivity, it appears a safer and convenient alternative to the synthetic and low water-soluble DMAB. Based on this, we decided to develop a colorimetric quantitative assay for CD estimation, offering a simple, fast, and low-cost alternative to the other methodologies requiring large instrumentation, for control of pharmaceutical formulations also in advanced drug delivery systems [21]. We explored the chemical determinants of color development for CD by changing vanillin concentration, solvent composition and pH, heating temperature and time, as detailed in the following sections, focusing the study on the detection of CD in combination with LD as found in some pharmaceutical formulations (Sinemet and Hexal) for the treatment of parkinsonism. Major efforts were devoted to obtaining large, selective, and reproducible color development from CD solutions, avoiding at the same time both the possible interference from the pharmaceutical additives and the spontaneous oxidation and polymerization of LD, typical of catecholamines, which gives rise to a black/brown polymer with a broad absorbance spectrum, including the visible region, therefore potentially affecting the colorimetric assay [22–26]. We found the generation of the yellow color from carbidopa and uncolored solutions for levodopa in the same buffer conditions, irrespective of the notable redox properties of LD [14]. Therefore, we focused our investigations on the selective detection and quantification of CD in some anti-Parkinson tablet formulations at a mass ratio of 4:1 (LD 200 mg + CD 50 mg), together with numerous excipients. The modulation of yellow color intensity upon vanillin reaction was explored up to 200 mg L^{-1} LD and 50.0 mg L^{-1} CD. The calibration

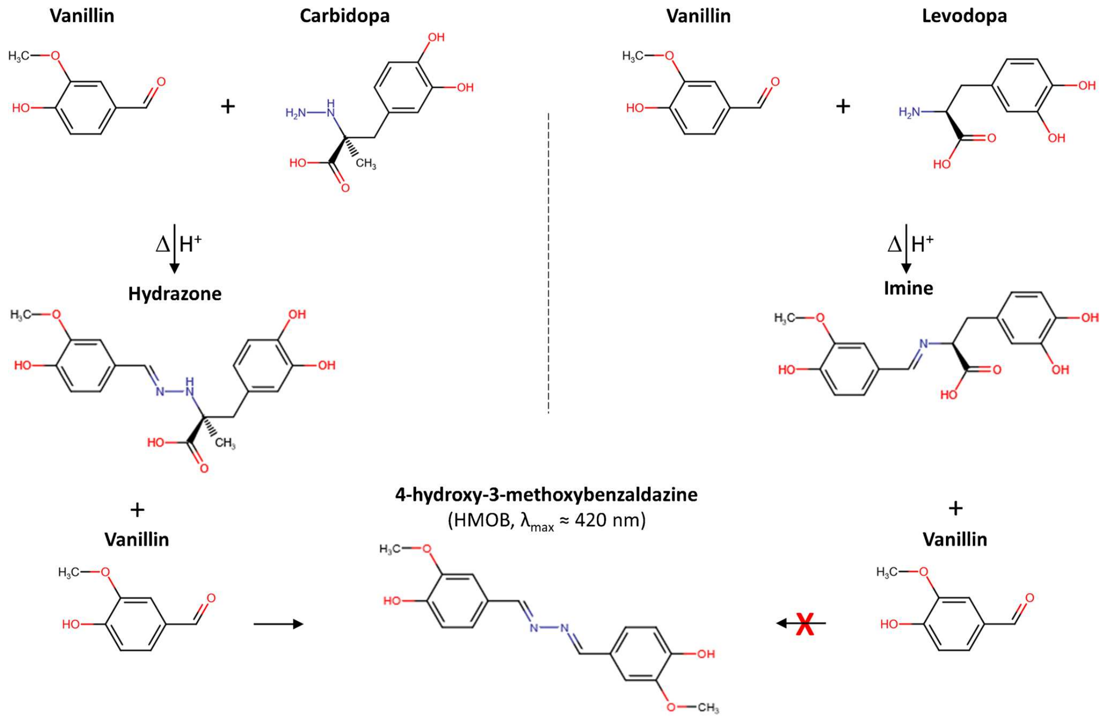

Fig. 1 Scheme of condensation reactions of vanillin with carbidopa and levodopa. Carbidopa hydrazide functional group produces a hydrazone that further reacts with an excess of vanillin to form the 4-hydroxy-3-methoxybenzaldazine (HMOB), with a maximum visible absorbance about 420 nm (yellow). Levodopa amine group produces an imine that cannot generate the azine, leaving the solution uncolored at acidic pH

curves for two tablet formulations were superimposable to levodopa/carbidopa (4:1), as well as to CD alone, showing a linear dynamic range between 50.0 and 5.00 mg L^{-1} of CD with very good reproducibility within this range and a good mean recovery of CD for both drugs. Data were acquired by using a common microplate reader, underlining the affordability of the method for drug estimation and quality control of pharmaceutical formulations. Furthermore, based on the very good sensitivity, for brand and generic drugs, this assay could pave the way for future research into therapeutic monitoring area for carbidopa-based medications.

Materials and methods

Chemicals

Carbidopa (CD, (2S)-3-(3,4-dihydroxyphenyl)-2-hydrazinyl-2-methylpropanoic acid), levodopa (LD, (2S)-2-amino-3-(3,4-dihydroxyphenyl)propanoic acid), vanillin (4-hydroxy-3-methoxybenzaldehyde), acetonitrile (MeCN), ethanol (EtOH), dimethyl sulfoxide (DMSO, methylsulfinylmethane), methanol (MeOH), and hydrogen chloride (HCl) were purchased from Sigma-Aldrich (Milan, Italy). Brand drug Sinemet (200 mg levodopa, 50 mg carbidopa, 35 mg excipients) was obtained from MSD (Rome, Italy), and its pharmaceutical alternative (generic drug) Hexal (200 mg levodopa, 50 mg carbidopa, 194 mg excipients) was produced by Sandoz (Basel, Switzerland). All chemicals were of analytical reagent grade and used as received without any further purification. All solutions were prepared using water obtained from Milli-Q Water Purification System (resistivity ≥ 18 MΩcm) (Germany, www.merckmillipore.com).

Methods and instrumentation

Carbidopa and levodopa were dissolved in HCl 1.00 M to obtain 100 g L^{-1} stock solutions. Stock solutions of a brand drug and the generic drug containing 5.00 g L^{-1} of levodopa were prepared by stirring for 10 min one tablet (200 mg LD, 50 mg CD) in 40.0 mL of 1.00 M HCl. The working solutions were prepared within 24 h from tablet dissolution. The samples were heated by using thermomixer to control time and temperature of the reaction. All the solutions in different solvents (acetonitrile, methanol, ethanol, water, dimethyl sulfoxide, and EtOH:H_2O mixtures) contained 50.0 mg L^{-1} (0.221 mM) of CD and 10.0 mM vanillin. The same CD and vanillin concentrations were used for EtOH:H_2O (1:1) solutions containing HCl 5 mM, 50 mM, or 500 mM. In all these cases the absorbance spectra were acquired after 4 h at 70 °C. The condition of CD 50.0 mg L^{-1} in EtOH/H_2O 1:1 with HCl 0.500 M at 70 °C was applied also to different vanillin concentrations (0.00, 1.25, 2.50, 5.00, 10.0, 20.0 mM) for 4 h: vanillin 10.0 mM at 30 °C, 40 °C, 50 °C, 60 °C, 70 °C, 80 °C for 4 h; vanillin 10.0 mM at 70 °C for 15, 30, 60, 120, 240 min. For calibration curves, each concentration of CD, LD + CD 4:1, or pharmaceutical formulations was in HCl 1.00 M, and added then to vanillin 20.0 mM in ethanol, obtaining the final sample solutions in EtOH:H_2O 1:1, HCl 0.500 mM and vanillin 10.0 mM. The limit of detection (LOD) and the limit of quantification (LOQ) were calculated based on the standard deviation (SD) of the mean of the blank values, as $3 \times SD/m$ and $10 \times SD/m$, respectively, where m indicates the slope of the calibration curve. The assay reproducibility is reported as (mean) coefficient of variation (CV_{av}). Absorbance spectra were acquired in disposable polystyrene 96-well microtest plates (Sarstedt, Milan, Italy) by using iMark™ microplate visible absorbance reader with optical filters (Bio- Rad, Milan, Italy), as well as in 1.0 cm cell by using a UV–Visible Spectrophotometer Evolution™ 201/220 from Thermo Scientific™ (Rodano, Milan, Italy).

Assay principle

Pioneering works described the reaction between hydrazine and an acidified alcoholic solution of p-dimethylaminobenzaldehyde (DMAB), resulting in the development of a characteristic yellow color that was used for the quantitative determination of hydrazine and hydrazide derivatives [18, 27–29]. More in general, the reactivity of the hydrazine, or hydrazide group, allows the formation of hydrazone by 1:1 by condensation with an aldehyde [15, 30, 31]. The hydrazone can further react with an aldehyde to form an azine [16–18, 32, 33] with several applications, ranging from material chemistry to medicinal chemistry [33]. When the aldehyde is aromatic, like a benzaldehyde derivative, the product of condensation resulted colored and fluorescent, depending on several factors, including the ring substitutions and solvent polarity [18, 32]. Levodopa, instead, can give an aldimine (Schiff base) by amine/aldehyde condensation reaction, but cannot lead to azine formation, lacking the hydrazine group and therefore leaving the solution not colored at acidic pH, whereas at basic pH, LD, as other catecholamines (dopamine, norepinephrine, methyldopa), can form yellow unstable aminochrome derivatives [3, 14, 34, 35]. Grounded on this, we decided to develop a colorimetric assay for carbidopa quantification based on the reaction of an excess of vanillin (4-hydroxy-3-methoxybenzaldehyde) with the hydrazide group of carbidopa at acidic pH to generate the yellow 4-hydroxy-3-methoxybenzaldazine (HMOB, $\lambda_{max} \sim 420$ nm in ethanol/water solution) and 3,4-dihydroxyphenylacetone in Fig. 1 [36, 37].

Results and discussion

Influence of solvent composition and pH on color development

Several experimental parameters of HMOB formation were tested here by using a spectrophotometer or a microplate reader for visible absorbance detection. Firstly, the role of solvent composition and pH on carbidopa/vanillin reaction at 70 °C for 4 h was evaluated for 50.0 mg L^{-1} (0.221 mM) of CD in presence of a large excess of vanillin (10.0 mM) by using absorbance spectra acquired in quartz cuvettes. Figure 2A shows that the absorbance of the solution decreased with the polarity of the solvent, reaching the largest values for acetonitrile or methanol, and the lowest values for H_2O or DMSO. Pure ethanol appeared as a good compromise between sensitivity and health risk. Accordingly, we decided to continue the method development based on ethanol:water solutions. Figure 2B reports the results of the same reaction for different compositions of EtOH:H_2O as solvent system. The color development was proportional to ethanol content, as expected from Fig. 2B. Interestingly, absorbance spectra for EtOH:H_2O 3:7 and 1:1 appeared almost superimposable, and this aspect resulted very useful to develop a robust assay with a minimal dependence on possible variation of solvent composition. Therefore, we focused on EtOH:H_2O (1:1) solvent system, exploring the dependence of the reaction on the acidity of the solution. Figure 2C shows the large intensity increase obtained incrementing the HCl content from 5 to 500 mM, with a λ_{max} about 420 nm.

Influence of vanillin concentration, temperature, and heating time on color development

Subsequent measurements were performed by using iMark™ Microplate Absorbance Reader determining the absorbance values for 0.200 mL solutions in disposable polystyrene 96-well microtest plates at 415 nm, i.e., the available optical filter closest to the absorbance λ_{max} about 420 nm. Figure 3 shows the results of the experiments for CD 50.0 mg L^{-1} dissolved in EtOH /H_2O 1:1 with HCl 0.500 M. Figure 3A shows the effect of vanillin concentration (0.00, 0.50, 2.5, 4.4, 10.0, 20.0 mM) on color development after 4 h at 70 °C. The color change was almost undetectable by vanillin addition up to 5.00 mM; a large absorbance increase occurred for vanillin between 5.00 and 10.0 mM, and further increase for vanillin at 20 mM. Considering that carbidopa is fixed at 50.0 mg L^{-1} (0.221 mM), this results underlining the need of a large excess of vanillin to obtain the condensation reaction described in Fig. 1, which is responsible for HMOB formation and color development. Vanillin at 10 mM appears as the best concentration in terms of data reproducibility (CV% 1.1). Figure 3B shows that the absorbance recorded at 415 nm increases with the temperature, reaching the maximum at 70 °C, and then falling at 80 °C. Although the reproducibility is very good at any temperature, 70 °C appeared the best choice (CV% 2.9). Finally, Fig. 3C reports the absorbance of the CD solutions that increased with the heating time up to 2 h, and then decreased up to 4 h in these

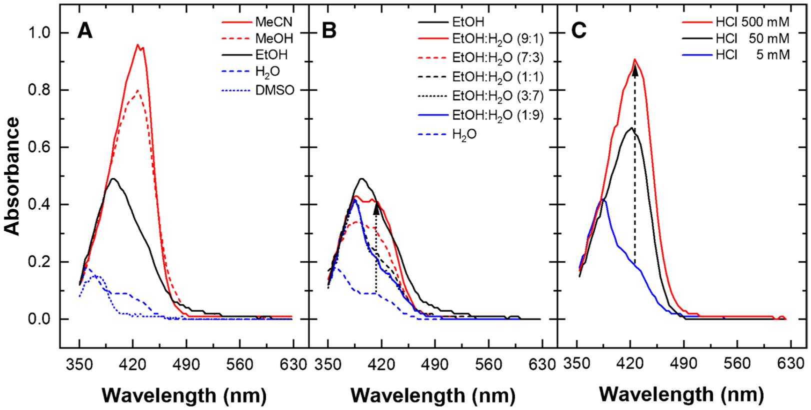

Fig. 2 Influence of solvent composition and pH on color development. All the solutions contain 50.0 mg L^{-1} (0.221 mM) of CD and 10.0 mM vanillin reacted for 4 h at 70 °C. (**A**) Absorbance spectra in acetonitrile (MeCN, red line), methanol (MeOH, red dashes), ethanol (EtOH, black line), water (H_2O, blue dashes), dimethyl sulfoxide (DMSO, blue dots). (**B**) Absorbance spectra for different EtOH:H_2O compositions, from neat water (H_2O, blue dashes) to neat ethanol (EtOH, black line). (**C**) Absorbance spectra in EtOH:H_2O (1:1), containing HCl 5 mM (blue line), 50 mM (black line), or 500 mM (red line)

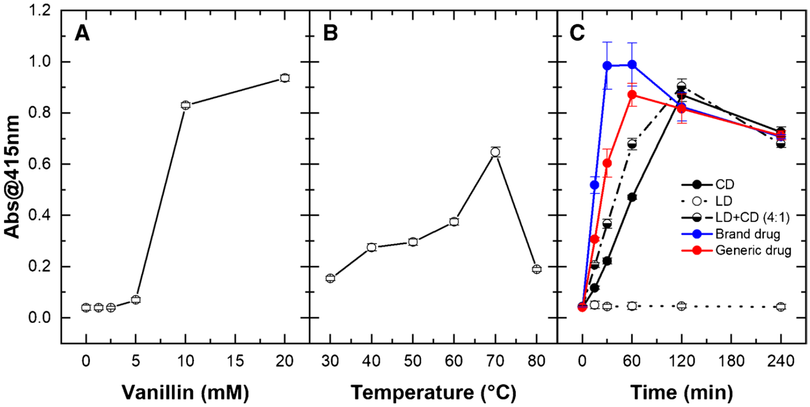

Fig. 3 Influence of vanillin concentration, temperature, and heating time on color development. Absorbance at 415 nm for CD 50.0 mg L^{-1} samples dissolved in EtOH/H_2O 1:1 with HCl 0.500 M. (**A**) Vanillin 0.00, 1.25, 2.50, 5.00, 10.0, 20.0 mM after 4 h at 70 °C. (**B**) Vanillin 10.0 mM at 20 °C, 30 °C, 40 °C, 50 °C, 60 °C, 70 °C after 4 h. (**C**) Vanillin 10.0 mM at 70 °C after 15, 30, 60, 120, 240 min in presence of carbidopa (CD, black circles), levodopa (LD, white circles), LD + CD 4:1 (half black circles), brand drug (blue circles), and generic drug (red circles). Each point represents the mean ± SD of 4 replicates

conditions. Data reproducibility was very good for carbidopa at any reaction time. However, the advantage to use 4 h for color development was clear when we applied the same procedure to levodopa/carbidopa as mixed standards or in real drugs (Fig. 3C). In detail, apart from LD alone that gave no color development, as expected, all mixtures containing CD gave rise to yellow solutions but with a much worse reproducibility and faster kinetics with respect to carbidopa alone. Such discrepancy among the absorbance values decreased at 2 h, reaching a minimum after 4 h, as evident from the data superposition in Fig. 3C for CD, LD + CD, brand drug, and generic drug, indicating this reaction time as the best option to build a calibration curve to estimate the carbidopa concentration in pharmaceutical formulation, as detailed below.

Colorimetric quantification of carbidopa in tablets by using of HMOB as molecular probe

The best experimental parameters for HMOB formation and the concomitant color development from CD solutions in terms of sensitivity and reproducibility were identified here as 10.0 mM vanillin in presence of 0.500 M HCl in EtOH/H_2O 1:1 (v/v) at 70 °C for 4 h. Accordingly, these parameters were fixed to selectively detect CD in co-presence of LD, as for the pharmaceutical formulations for the treatment of parkinsonism. Figure 4 reports the calibration curves for CD (black circle), LD (white circles), the binary mixture of pure components (LD + CD 4:1) (black and white circles), brand drug (blue circles), and the generic drug (red circles). In detail, LD standard solutions did not show any absorption at 415 nm over the entire concentration range here explored,

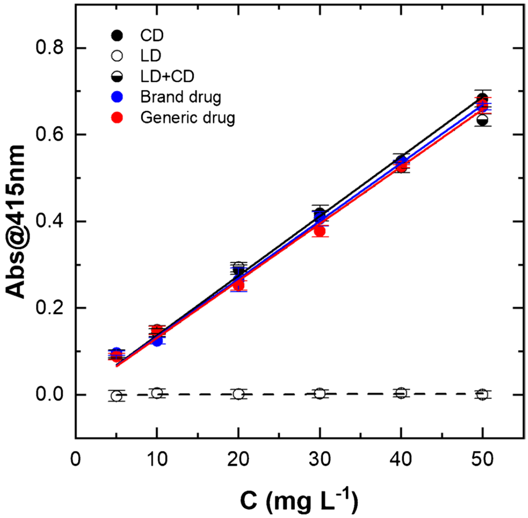

Fig. 4 Colorimetric calibration plots. Absorbance values at 415 nm for sample solutions in EtOH/H_2O 1:1 with HCl 0.500 M and vanillin 10.0 mM after 4 h. Carbidopa (CD, black circles), levodopa (LD, white circles), LD + CD 4:1 (half black circles), brand drug (blue circles), and generic drug (red circles). The explored concentration range was between 5.00 and 50.0 mg L^{-1} for CD, and between 20.0 and 200 mg L^{-1} for LD alone or in combination with CD. Each point represents the mean ± SD of 4 replicates. Data were fitted according to linear Eq. 1

Table 1 Linear fitting parameters for carbidopa quantification at 415 nm (Fig. 4)

Sample	[1] m (L g^{-1})	[2]LOD (mg L^{-1})	[3]LOQ (mg L^{-1})	R^2	[4]CV_{av} (%)
CD	13.7 ± 0.2	0.399 ± 0.005	1.330 ± 0.018	0.996	4.2
LD + CD	13.2 ± 0.3	0.184 ± 0.005	0.615 ± 0.015	0.987	3.5
Brand drug	13.4 ± 0.2	0.215 ± 0.003	0.778 ± 0.010	0.996	3.7
Generic drug	13.2 ± 0.2	0.342 ± 0.006	1.140 ± 0.019	0.995	3.4

[1] *m*, slope of the calibration curve. [2]*LOD*, limit of detection. [3]*LOQ*, limit of quantification. [4]CV_{av}, mean coefficient of variation calculated between 0.005 and 0.050 g L^{-1}

as expected due to the absence of the hydrazine group, preventing the synthesis of the HMOB (Fig. 1). Differently, the LD + CD 4:1 mixture, which represents a simplified model of commercial drugs, and the levodopa/carbidopa tablets, which represent the real samples, containing 200 mg of levodopa and 50 mg of carbidopa, together with the excipients (see "Materials and methods"), all gave colored solutions, as for CD standard solutions. After blank subtraction, data corresponding to CD between and 50.0 mg L^{-1} were fitted according to the linear equation

$$\text{Abs@415nm} = m \times C, \tag{1}$$

where *m* indicates the slope of the HMOB absorbance at 415 nm. The excellent performances of the assay are well highlighted by the superposition of the curves, due to the almost identical slope values reported in Table 1. Moreover, the analytical parameters from data fitting underline the absence of the matrix effect, due to the different formulations of such drugs, as well as the absence of interference from LD in such conditions, leading to a very good assay reproducibility and promising sensitivity (CV_{av}% 3.7 and 3.4; LOD 0.215 ± 0.003 mg L^{-1} and 0.342 ± 0.006 mg L^{-1} for carbidopa in brand and generic drugs, respectively). Finally, Table S1 (see Electronic Supplementary Material) reports the recovery estimated by using the absorbance values for carbidopa alone with respect to pharmaceutical formulations at the corresponding nominal concentration of CD, obtaining a mean recovery value of 104.6% and 105.3% for brand and generic drugs, respectively, over the entire range of calibration.

Conclusion

Carbidopa was added to levodopa and commercialized under the name of Sinemet since 1975, which represents the gold standard for the care of parkinsonism and generating, together with several other levodopa/carbidopa formulations, millions of prescriptions per year [4, 38]. Here, we reported the development of a colorimetric assay for the detection and quantification of carbidopa in such medications. The method is based on selective condensation reaction between carbidopa and vanillin, observing the yellow color development due to formation of HMOB, irrespective of levodopa content. The modulation of yellow color intensity upon vanillin reaction was explored up to 200.0 mg L^{-1} LD and 50.0 mg L^{-1} CD. The calibration curves for two tablet formulations were superimposable to levodopa/carbidopa (4:1), as well as to CD alone, showing a linear dynamic range between 50.0 mg L^{-1} and 5.00 mg L^{-1} of CD with very good reproducibility within this range (CV_{av}%, 3–4%) and good mean recovery (105%). Data were acquired by using a common microplate reader, underlining the affordability of the method, appearing as an effective tool for drug estimation and quality control of pharmaceutical formulations. Moreover, considering that about 30% of carbidopa excreted in urine from patients that received an oral dose of such substance is not metabolized [36], the very good sensitivity of the assay, with limit of quantification about 1 mg L^{-1} for commercial drugs, stimulates a perspective study on non-invasive therapeutic monitoring of carbidopa-based medications in human excretion.

Supplementary Information The online version contains supplementary material available at https://doi.org/10.1007/s00216-022-04256-4.

Funding Open access funding provided by Università degli Studi di Firenze within the CRUI-CARE Agreement. This work received financial support from the Ministry of University and Research (MUR), for the project "Dipartimenti di Eccellenza 2018–2022".

Declarations

Conflict of interest The authors declare no competing interests.

References

1. Bisaglia M, Filograna R, Beltramini M, Bubacco L. Are dopamine derivatives implicated in the pathogenesis of Parkinson's disease? Ageing Res Rev. 2014. https://doi.org/10.1016/j.arr.2013.12.009.
2. Jeitner TM, Kalogiannis M, Krasnikov BF, Gomlin I, Peltier MR, Moran GR. Linking inflammation and Parkinson disease: hypochlorous acid generates parkinsonian poisons. Toxicol Sci. 2016. https://doi.org/10.1093/toxsci/kfw052.
3. Palladino P, Torrini F, Scarano S, Minunni M. Colorimetric analysis of the early oxidation of dopamine by hypochlorous acid as preliminary screening tool for chemical determinants of neuronal oxidative stress. J Pharm Biomed Anal. 2020. https://doi.org/10.1016/j.jpba.2019.113016.
4. https://www.parkinson.org/Understanding-Parkinsons/Statistics Accessed 31 May 2022.
5. Connolly BS, Lang AE. Pharmacological treatment of Parkinson disease: a review. JAMA. 2014;1670–83. https://doi.org/10.1001/jama.2014.3654.
6. Oertel WH. Recent advances in treating Parkinson's disease. F1000Research. 2017. https://doi.org/10.12688/f1000research.10100.1.
7. Wollmer E, Klein S. Development and validation of a robust and efficient HPLC method for the simultaneous quantification of levodopa, carbidopa, benserazide and entacapone in complex matrices. J Pharm Pharm Sci. 2017. https://doi.org/10.18433/J3K923.
8. Fanali S, Pucci V, Sabbioni C, Raggi MA. Quality control of benserazide levodopa and carbidopa-levodopa tablets by capillary zone electrophoresis. Electrophoresis. 2000. https://doi.org/10.1002/1522-2683(20000701)21:12%3c2432::AID-ELPS2432%3e3.0.CO;2-E.
9. Quintino M, Yamashita M, Angnes L. Voltammetric studies and determination of levodopa and carbidopa in pharmaceutical products. Electroanalysis. 2006. https://doi.org/10.1002/elan.200503445.
10. Damiani PC, Moschetti AC, Rovetto AJ, Benavente F, Olivieri AC. Design and optimization of a chemometrics assisted spectrophotometric methods for the simultaneous determination of levodopa and carbidopa in pharmaceutical products. Anal Chim Acta. 2005. https://doi.org/10.1016/j.aca.2005.04.065.
11. Chamsaz M, Safavi A, Fadaee J. Simultaneous kinetic spectrophotometric determination of carbidopa, levodopa and methyldopa in the presence of citrate with the aid of multivariate calibration and artificial neural networks. Anal Chim Acta. 2007. https://doi.org/10.1016/j.aca.2007.09.006.
12. Khanmohammadi M, Mobedi E, Garmarudi AB, Mobedi H, Kargosha K. Simultaneous determination of levodopa and carbidopa in levodopa-carbidopa tablets by ATR-FTIR spectrometry. Pharm Dev Technol. 2007. https://doi.org/10.1080/10837450701481249.
13. Talebpour Z, Haghgoo S, Shamsipur M. 1H nuclear magnetic resonance spectroscopy analysis for simultaneous determination of levodopa, carbidopa and methyldopa in human serum and pharmaceutical formulations. Anal Chim Acta. 2004. https://doi.org/10.1016/j.aca.2003.10.081.23.
14. Lettieri M, Emanuele R, Scarano S, Palladino P, Minunni M. Melanochrome-based colorimetric assay for quantitative detection of levodopa in co-presence of carbidopa and its application to relevant anti-Parkinson drugs. Anal Bioanal Chem. 2022. https://doi.org/10.1007/s00216-021-03804-8.
15. Brenner KP, Rose-Pehrsson SL. Performance evaluation of a colorimetric hydrazine dosimeter. Report NRL/MR/6110–94–7491, Order No. AD-A281249 Naval Res. Lab., Washington, DC, 1994. https://apps.dtic.mil/sti/citations/ADA281249. Accessed 27 June 2022.
16. Rani A, Kumar M, Tuli HS, Abbas Z, Prakash V. Synthesis and spectral studies of 4,4′-(hydrazine-1,2-diylidenedimethylylidene)-bis-(2-methoxyphenol) and its transition metal complexes with promising biological activities Asian J. Chem. 2020. https://doi.org/10.14233/ajchem.2020.22703.
17. Rüger N, Fassauer GM, Bock C, Emmrich T, Bodtke A, Link A. Substituted tetrazoles as multipurpose screening compounds. Mol Diver. 2017. https://doi.org/10.1007/s11030-016-9711-x.
18. Vickers S, Stuart EK. Spectrofluorometric Determination of Carbidopa [L-(−)-α-Hydrazino-3,4-dihydroxy-α-methylhydrocinnamic Acid] in Plasma. J Pharm Sci. 1973. https://doi.org/10.1002/jps.2600620940.
19. Weerawatanakorn M, Wu JC, Pan MH, Ho CT. Reactivity and stability of selected flavor compounds. J Food Drug Anal. 2015. https://doi.org/10.1016/j.jfda.2015.02.001.
20. González CG, Mustafa NR, Wilson EG, Verpoorte R, Choi YH. Application of natural deep eutectic solvents for the "green" extraction of vanillin from vanilla pods. Flavour Frag J. 2017. https://doi.org/10.1002/ffj.3425.
21. Ong JJ, Pollard TD, Goyanes A, Gaisford S, Elbadawi M, Basit AW. Optical biosensors-illuminating the path to personalized drug dosing. Biosens Bioelectron. 2021. https://doi.org/10.1016/j.bios.2021.113331.
22. Palladino P, Brittoli A, Pascale E, Minunni M, Scarano S. Colorimetric determination of total protein content in serum based on the polydopamine/protein adsorption competition on microplates. Talanta. 2019. https://doi.org/10.1016/j.talanta.2019.01.095.
23. Torrini F, Scarano S, Palladino P, Minunni M. Polydopamine-based quantification of albuminuria for the assessment of kidney damage. Anal Bioanal Chem. 2021. https://doi.org/10.1007/s00216-021-03192-z.
24. Scarano S, Pascale E, Palladino P, Fratini E, Minunni M. Determination of fermentable sugars in beer wort by gold nanoparticles@polydopamine: a layer-by-layer approach for Localized Surface Plasmon Resonance measurements at fixed wavelength. Talanta. 2018. https://doi.org/10.1016/j.talanta.2018.02.044.
25. Scarano S, Palladino P, Pascale E, Brittoli A, Minunni M. Colorimetric determination of p-nitrophenol by using ELISA microwells modified with an adhesive polydopamine nanofilm containing catalytically active gold nanoparticles. Microchim Acta. 2019. https://doi.org/10.1007/s00604-019-3259-2.
26. Palladino P, Bettazzi F, Scarano S. Polydopamine: surface coating, molecular imprinting, and electrochemistry - successful applications and future perspectives in (bio)analysis. Anal Bioanal Chem. 2019. https://doi.org/10.1007/s00216-019-01665-w.
27. Pesez M, Petit A. Recherche et dosage de l'hydrazine Bulletin de la Société chimique de France. 1947;14(1–2):122–3.
28. Watt GW, Chrisp JD. A spectrophotometric method for the determination of hydrazine Anal. Chem. 1952. https://doi.org/10.1021/ac60072a044.
29. Malone HE. The Determination of Hydrazino-Hydrazide Groups Chapter 3 – Colorimetric and Spectrophotometric methods. Pergamon Press, Headington Hill Hall, Oxford, 1970 https://doi.org/10.1016/B978-0-08-015871-6.50008-4.
30. Baymak MS, Zuman P. Equilibria of formation and dehydration of the carbinolamine intermediate in the reaction of benzaldehyde with hydrazine. Tetrahedron. 2007. https://doi.org/10.1016/j.tet.2007.04.034.
31. González-Baró AC, Pis-Diez R, Parajón-Costa BS, Rey NA. Spectroscopic and theoretical study of the o-vanillin hydrazone of the mycobactericidal drug isoniazid. J Mol Struct. 2012. https://doi.org/10.1016/j.molstruc.2011.10.026.

32. Wang L, Su Q, Wu Q, Gao W, Mu Y. Synthesis of new substituted benzaldazine derivatives, hydrogen bonding-induced supramolecular structures and luminescent properties. C R Chim. 2012. https://doi.org/10.1016/j.crci.2011.12.006.
33. Chourasiya SS, Kathuria D, Wani AA, Bharatam PV. Azines: synthesis, structure, electronic structure and their applications. Org Biomol Chem. 2019. https://doi.org/10.1039/c9ob01272a.
34. Walash MI, Ouf AA, Salem FB. Colorimetric determination of sympathomimetic amines methyldopa and noradrenaline. J AOAC Int. 1985. https://doi.org/10.1093/jaoac/68.1.91.
35. Salem FB. Colorimetric Determination of Certain Sympathominetic Amines. Anal Lett. 1985. https://doi.org/10.1080/00032718508069100.
36. Vickers S, Stuart EK, Hucker HB. Further studies on the metabolism of carbidopa, (-)-L-alpha-hydrazino-3,4-dihydroxy-alpha-methylbenzenepropanoic acid monohydrate, in the human, Rhesus monkey, dog, and rat. J Med Chem. 1975. https://doi.org/10.1021/jm00236a004.
37. Dose K. Catalytic decarboxylation of α-amino-acids. Nature. 1957. https://doi.org/10.1038/179734b0.
38. Tolosa E, Martí MJ, Valldeoriola F, Molinuevo JL. History of levodopa and dopamine agonists in Parkinson's disease treatment. Neurology. 1998. https://doi.org/10.1212/WNL.50.6_Suppl_6.S2.